PHASE TRANSFORMATION IN PLATINUM-IRON-COPPER TERNARY SYSTEM

M. SHAHMIRI

PH. D. THESIS

THE UNIVERSITY OF ASTON IN BIRMINGHAM

1983

University of Aston in Birmingham

Title: Phase Transformation in Platinum - Iron - Copper Ternary System

Name: Mohammad Shahmiri

Degree: Ph.D. Thesis

Year: 1983

SUMMARY

The presence of a distinct compound in the Pt-Fe-Cu system at Pt_2FeCu composition was hypothesised by Nemilov in 1944, but the compound (Tulameenite) was first identified by Cabri et al in natural alloys from the platinum placer deposits of the Tulameen river in British Columbia.

The present research was initiated to determine the Pt-Fe-Cu phase diagram in the Pt_2FeCu region and thus to determine the composition range of Tulameenite and its compositional and structural changes during different thermal treatments using synthetic material.

Primary investigations have revealed that the compound is a single phase disordered f.c.c. solid-solution above 1178°C. On quenching, it transforms, probably by a martensitic transformation, to an ordered tetragonal structure. Multiple twinning on {101} habit planes avoids any macroscopic shape change due to the ordering. The twinned structure is unstable, and thermal treatments produce stress-relief recrystallization accompanied by deformation twins and grain-boundary fractures as further stress-relief mechanisms.

Tulameenite forms an extensive single phase region of solid-solution continuous with the binary region based on the compound FePt. At lower temperatures the stoichiometric compound Pt_2FeCu enters a two-phase field comprising a non-stoichiometric compound together with an ordered cubic phase.

The transformation to this two-phase structure occurs by different precipitation mechanisms which are accompanied by recrystallization of the matrix in some cases.

KEY WORDS : ORDER; DISORDER; TULAMEENITE; PLATINUM ALLOY; LONG-RANGE ORDER; RECRYSTALLIZATION

LIST OF CONTENTS

List of Figures		Page 4
List of Tables		16
1	Literature survey	17
1.1	Introduction	17
1.2	Common types of ordered alloys	18
1.2.1	Binary ordered alloys	18
1.2.2	Ternary ordered alloys	19
1.3	Theoretical treatments of superlattice	23
1.4	Detection of ordering processes	25
1.5	Superlattice and x-ray diffraction	27
1.5.1	Long-range order in $AuCu_3$	28
1.6	The Cu-Pt binary phase diagram	29
1.6.1	Around CuPt stoichiometric compound	31
1.6.2	Summary	34
1.7	The Fe-Pt binary phase diagram	34
1.7.1	Summary	36
1.8	The Cu-Fe binary phase diagram	40
1.8.1	Summary	40
1.9	The Pt-Fe-Cu ternary phase diagram	42
1.10	Mineralogical survey	43
2	Experimental procedures	48
2.1	Alloy preparation	48
2.2	Heat-treatment	50
2.2.1	Homogenization treatment	50
2.2.2	Continuous cooling	51

2.3	Recrystallization treatments of Pt_2FeCu	page 53
2.4	Specimen preparation	54
2.4.1	Metallographic specimens	54
2.4.2	Specimens for electron microprobe analysis	54
2.4.3	Transmission Electron Microscopy (T.E.M.) specimens	54
2.5	X-ray diffractometry	58
2.6	Electron Microprobe Analysis	58
3	Experimental Results	60
Introduction		
Section I	Ternary stoichiometric compound Pt_2FeCu	60
3.I.1	Differential thermal analysis(D.T.A)	60
3.I.2	X-ray diffraction	60
3.I.3	Measured and calculated densities	64
3.I.4	Electron Density Maps (E.D.M)	65
3.I.5	Measurements of the Long-range order (L.R.O.) parameter	71
3.I.6	Microstructural features of Pt_2FeCu	75
3.I.6.1	Transmission Electron Microscopy(T.E.M)	81
3.I.7	Recrystallization mechanisms	106
3.I.7.1	Activation energy measurements	106
3.I.7.2	Optical Microscopy	113
3.I.7.3	Transmissiom Electron Microscopy	127
3.I.7.4	Scanning Electron Microscopy	134
3.I.8	Grain-boundary fracture	139
Section II	Isothermal section at 1000°C	143
Section III	Isothermal section at 600°C	166

		page
4	Discussion	
4.1	Ternary stoichiometric compound	192
4.2	Isothermal sections of ternary phase diagram	222
5	Conclusions	238
6	Future work	241
7	Acknowledgement	243
8	references	244

List of Figures

Fig.1	The unit cells of the ordered systems	page 2
Fig.2	The Cu-Pt binary phase diagram[27]	33
Fig.3	The Fe-Pt binary phase diagram[27]	38
Fig.4	Constitution diagram of Fe-Pt system[39][40]	39
Fig.5	Microstructures of the FePt compound[45]	39
Fig.6	Phase diagram of the Pt-Fe system for 0 to 48% Iron[41]	39
Fig.7	Phase diagram of Cu-Fe binary system[27]	41
Fig.8	Photomicrograph of a complex Tulameenite grain (Grain B.C.D)[55]	46
Fig.9	The Pt-Fe-Cu ternary system : synthetic compounds are denoted by squares, natural samples by closed circles[55]	47
Fig.10	Compositions of Tulameenite (at%)[56]	47
Fig.11	Typical x-ray diffractometer trace of Pt_2FeCu	63
Fig.12	Electron Density Map of Pt_2FeCu	70
Fig.13	The cross-section of the Pt_2FeCu specimen	72
Fig.14	Variation of (L.R.O) parameter with time temperature	74
Fig.15	As-cast microstructure of the Pt_2FeCu . Etched . x180.	77
Fig.16	Appearances of dark and bright bands in cored structure of the Pt_2FeCu x300	77
Fig.17	Secondary Electron Image of the central region of the homogenized Pt_2FeCu, three months at 1200°C. Etched. x700	78

Fig. 18	Higher magnification of Fig. 17 x4200	page78
Fig. 19	Optical micrograph of the homogenized specimen of Pt_2FeCu, 10 days at 1400°C and quenched. Etched. x170	79
Fig. 20	Polarized light micrograph of the central parts of Fig. 19. Etched. x600	79
Fig. 21	Ordered domain microstructures of the Pt_2FeCu near the edge of the specimen. Optical image. Etched. x110	80
Fig. 22	Montage of bright-field micrograph of the Pt_2FeCu with S =0.29 x67K	83
Fig. 23	Bright-field micrograph of the interior area of the ordered domain in "A" of Fig. 22 x200K	84
Fig. 24	Dark-field image of Fig. 23 operating reflection $\{110\}$ x200K	84
Fig. 25	Bright-field micrograph of the two growing ordered domains in adjacent to a twinned band. x80K	87
Fig. 26	Bright-field micrograph of the three different sizes of internally twinned ordered domains. x60K	87
Fig. 27	Bright-field micrograph showing orthogonal ordered domains. x60K	88
Fig. 28	Bright-field image of the orthogonal order domains. x34K	88
Fig. 29	Bright-field micrograph of Pt_2FeCu, showing different sets of twinning. x80 K	91

Fig.30	Superlattice dark-field image of Fig. 29, operating reflections $\{110\}$ x 80K	Page 9
Fig.31	a) Selected area diffraction pattern of figure 29 b) The index of the S.A.D.P. of fig 31(a)	92
Fig.32	A sterographic projection showing the twin orientation relationships of fig.29	93
Fig.33	Bright-field image of internally twinned ordered domain x80K	95
Fig.34	Dark-field image of fig 34 using $\{001\}$ superlattice reflection x80K	95
Fig.35	S.A.D.P. of figure 33	96
Fig.36	Indices of the S.A.D.P. of fig. 35	97
Fig.37	A sterographic projection showing the twin orientation-relationships of fig.33	98
Fig.38	Sterographic projections showing the angular disparities when the structure is twinned on a) (101), b) $(\bar{1}01)$, c) (011) and d) (110) planes	101
Fig.39	Schematic representation of the ordered tetragonal domains with alternate C-axes in adjacent domains	105
Fig.40	The reciprocal lattice of the Pt_2FeCu showing the Fundamental and Superlattice reflections	105
Fig.41	The fraction recrystallized vs annealing time for the Pt_2FeCu	110

Fig.42	Avrami plot for the recrystallization of the Pt_2FeCu	Page1
Fig.43	Arrhenius plot for determination of activation energy for recrystallization of the Pt_2FeCu	112
Fig.44	Grain-boundary nucleation and growth of the recrystallization grains, 5 minutes at 1000°C. optical micrograph. Etched x135	114
Fig.45	Similar area to Fig.44 Etched x185	114
Fig.46	Optical micrograph showing the nucleation of the recrystallized grains at the junctions of the twinned bands. Etched x350	116
Fig.47	Similar area to fig 46 x300	116
Fig.48	Thickening of the domains, one hour at 1000°C. Optical image. Etched x350	117
Fig.49	Similar area to fig 48. Etched x420	117
Fig.50	Polarized light micrograph showing the advance of the recrystallized grains towards the favourable orientations. Etched x420	119
Fig.51	Similar features to fig 50 . . Etched x420	119
Fig.52	Optical micrograph of Pt_2FeCu specimen, annealed at 1000°C for 1000 hours, showing the recrystallized grains at the central regions. Etched x27	120

Fig.53 Similar to Fig 52, but showing the unaltered original twinned structures along the edges of the sample. Etched x180 Page120

Fig.54 Optical micrograph of the fully recrystallized area of the sample, annealed 1000 hours at 1000°C showing normal grain structures and annealing twins. Etched x66 122

Fig.55 Optical micrograph of the recrystallized grains annealed at 1000°C for 1000 hours, revealing different sets of deformation and annealing twins. Etched x168 122

Fig.56 Optical micrograph of the deformation twins inside a recrystallized grain, annealed for 1000 hours at 1000°C. Etched x420 124

Fig.57 Corresponding polarized light micrograph of fig 56. Etched x420 124

Fig.58 Optical micrograph showing the population of the deformation twins around the triple junctions and their absence in the vicinity of the grain-boundary fracture. Etched x336 126

Fig.59 Optical micrograph of the fully recrystallized area of the sample, annealed for 3000 hours at 1000°C. Thermally etched x135 126

Fig.60 a) Bright-field image of three recrystallized grains x54K — Page 127

b) A sterographic projection showing the orientation relationships of three recrystallized grains — 128

Fig.61 Bright-field image of the partially recrystallized sample (Arrows A_1, A_2) and the original twinned structures x34K — 131

Fig.62 Dark-field image of the dotted area of fig 61, using $\{110\}$ superlattice reflections x80K — 132

Fig.63 Dark-field image of figure 61, using $\{220\}$ fundamental reflection x34K — 132

Fig.64 A sterographic projection showing the orientation relationships of Fig.63 — 134

Fig.65 A section of a sterographic projection showing the orientation of the new grains — 135

Fig.66,67 Backscattered electron image of the recrystallized grains and their corresponding channelling patterns x600 — 136

Fig.68 a) Backscattered electron image of recrystallized grains and twinned microstructure x2400 — 138

b) The twinned structure revealed by backscattered electron mode x2400 — 138

Fig.69 Scanning electron micrograph of the inter-crystalline fracture. Thermally etched x755 — 141

Fig.70 Scanning electron micrograph, showing the vertical displacement of grains G2 and G3. Thermally etched x150 Page 141

Fig.71 Optical Micrograph of the grain-boundary fractures. Thermally etched x540 14

Fig.72 Optical micrograph showing the ejections of the small grains. Etched x168 14

Fig.73 The Pt-Fe-Cu ternary isothermal sections at 1000°C 146

Fig.74 Dimensional changes of the ordered tetragonal single phase along the Pt_2FeCu-PtFe line 151

Fig.75 Optical micrograph of alloy 46 showing the attack of the recrystallized grains towards the original twinned matrix. Etched x168 154

Fig.76 Optical micrograph of alloy 47 showing partially recrystallized basket structures. Etched x336 154

Fig.77 Optical image of the recrystallized alloy 45. Etched x42 155

Fig.78 Optical micrograph of the recrystallized alloy 50 showing the deformation twins. Etched x270 155

Fig.79 Plate-like and grain boundary precipitations of the β_0-phase in γ''_D matrix. polarized light micrograph of alloy 2. x135 157

Fig.80 Fine twinning inside the β_0 phase plate-like precipitates of alloy 2. x168 Page157

Fig.81 Optical micrograph of alloy 8 showing the β_0 (light areas) and γ'_D (dark areas) of the ($\beta_0 + \gamma'_D$) phase mixtures. Etched x84 159

Fig.82 Optical micrograph of alloy 11 showing the β_0 (light areas) and γ'_D (dark areas) of the ($\beta_0 + \gamma'_D$) phase mixtures. Etched x84 159

Fig.83 Optical micrograph of alloy 18 showing the Fe-rich particles embedded in the Cu-matrix unetched x108 162

Fig.84 Polarized light micrograph of alloy 22, single phase Fe-rich, showing normal grain structures and some irregularly shaped annealing twins. Etched x420 162

Fig.85 Bright-field optical micrograph of alloy 32 (γ'_D phase) showing sub-grain boundaries. Etched x168 164

Fig.86 Dark-field optical micrograph of the same area as Fig.85. Etched x168 164

Fig.87 Optical image of alloy 32, showing similar features to Fig.85. Ion-beam etched. x336 165

Fig.88 Optical micrograph of alloy 32. Interference contrast. Ion-beam etched. x336 165

Fig.89 The Pt-Fe-Cu ternary isothermal section at 600°C Page167

Fig.90 Optical micrograph of alloy 41 showing primary recrystallized grains, nucleation and growth of the secondary recrystallization and deformation twins. Etched x168 173

Fig.91 Similar feature to that of fig 90. Alloy 40 Etched x42 173

Fig.92 Optical micrograph of alloy 5 showing grain-boundary and plate-like precipitations of the γ_0'' phase in the β_0 phase matrix. Etched x420 175

Fig.93 Microstructure of the γ_0'' phase plate-like precipitation in β_0 phase matrix of alloy 4. Etched x420 175

Fig.94 Optical micrograph of the ternary compound Pt_2FeCu decomposition and appearances of γ_0'' phase along the edge of the sample. Lightly etched x33 177

Fig.95 Higher magnification of fig.94 showing the precipitation of the γ_0'' phase. Etched x336 177

Fig.96 Normal recrystallized grain-structures of the central regions of fig.94 showing deformation twins. Etched x108 178

Fig.97 Polarized light micrograph of fig.96 showing the change of contrast of the deformation twins. Etched x108 178

Fig.98 Cellular and plate-like decomposition in alloy 8. Optical micrograph. Etched x420 Page180

Fig.99 Microstructure of alloy 10 showing the stoppage of the cellular decompositions when having encountered plate-like precipitations. Optical image. Etched x420 180

Fig.100 Optical image of the growth of the cellular precipitation towards the interior parts of the neighbouring grains. Etched x135 181

Fig.101 Polarized light micrograph of Fig 100 showing the original twinned structure. Etched x135 181

Fig.102 Microstructure of the twinned structures of fig.100 showing basket weaved and particle precipitations on them. Etched x420 182

Fig.103 Polarized light micrograph of fig.102 showing the precipitations on the twinned bands. Etched x420 182

Fig.104 Optical micrograph of alloy 12 revealing plate and particle precipitations in the vicinity of the advancing cellular interphase. Etched x420 184

Fig.105 Similar precipitation morphologies to Fig.103. Alloy 10. optical micrograph Etched x420 184

Fig.106	Optical micrograph of the central and outside regions of alloy 12 showing recrystallized grains and plate-like precipitations. Etched. Interference contrast mode. x42	Page 186
Fig.107	Recrystallization, deformation twins and phase separation mechanisms in alloy 10. Optical micrograph. Etched x168	186
Fig.108	Optical micrograph of alloy 22 showing, Eutectoid-type, plate-like and cellular precipitation mechanisms. Etched x168	188
Fig.109	Eutectoid-type, plate-like and cellular precipitations in alloy 26. Optical micrograph. Etched x168	188
Fig.110	Microstructure of alloy 28 showing the grain-boundary and Widmanstätten precipitations. Optical image. Etched x420	190
Fig.111	Polarized light micrograph of Fig.110 showing the plate-like precipitations in twin orientations. Etched x420	190
Fig.112	Unit cell of the ordered tetragonal Pt_2FeCu	199
Fig.113	Dark-field image of the "as-quenched" specimen showing the relaxation of the stress-relief twinning. $\{110\}$ super-lattice reflection operating 200K	208
Fig.114	Advance of the recrystallized grain towards the original twinned structure.	216

Fig.115 Twinning mechanism produced by Shear Page 218

Fig.116 Proposed binary Pt-Cu alloy system around PtCu 233

Fig.117 Possible contribution of the stoichiometric CuPt to the interior part of the Pt-Fe-Cu system 234

Fig.118 Space model of the Fe-rich corner of the Pt-Fe-Cu ternary system between 1000°C and 600°C 236

Fig.119 Space model of the ordered tetragonal single phase field based on binary FePt compound and its compositional shifts of the two-phase field between 1300°C-600°C. 237

List of Tables

		page
Table 1	Electron Microprobe Analysis of Tulameenite[55]	46
Table 2	X-ray diffraction powder data[55]	47
Table 3	Values of n and k in Avrami Relation	107
Table 4	Data for Arrhenius plot obtained from the fraction recrystallized curves of Pt_2FeCu	108
Table 5	Chemical composition, lattice parameter and $^c/_a$ ratio of the alloys used for 1000°C section	147
Table 6	Chemical composition, lattice parameter and $^c/_a$ ratio of the alloys used for 600°C	168

1. LITERATURE SURVEY

1.1 Introduction

In most substitutional solid-solutions, the constituent atoms are arranged more or less at random on the atomic sites of the lattice. In solutions of this kind the only major effect of a change in temperature is to increase or decrease the amplitude of thermal vibration. But there are some solutions which have this random structure only at elevated temperatures. When these solutions are cooled below a certain critical temperature T_c, each kind of constituent atoms arrange themselves in an orderly, periodic manner on one particular kind of lattice site and as a result, a new unit cell may be then defined in terms of atoms that are all of one kind. This kind of transformation which is often observed in the vicinity of certain well-defined atomic ratio , e.g., AB, A_3B, A_2BC and A_6BC is commonly termed as superlattice or superstructures.

The concept of order-disorder transformation was anticipated by Kurnakov et al [1] . They interpreted some physical property changes after long annealing with compositions around AuCu and Au_3Cu to the formation of superlattice. In 1919, Tammann[2] explained the behaviour of Au-Cu alloys in Nitric Acid by suggesting that the Copper and Gold atoms occupy certain lattice sites. The first direct evidence of ordering was obtained by Bain[3] in 1923. He interpreted the extra lines in x-ray diffraction patterns of annealed $AuCu_3$ as due to the formation of a

superlattice. Before proceeding into the nature of the order-disorder transformation, some of the more common ordered alloys will be outlined.

1.2 Common types of ordered alloys

What follows are the typical and well-known ordered binary and ternary alloys in metallic systems. Although the Strukturberitch system for classifying metallic structures is now no longer completely adequate [5], its symbols are still widely used to designate superlattice structures.

Accordingly these symbols will be used where appropriate.

1.2.1 Binary ordered alloys

(i) Type $L1_2$

The ideal chemical composition of this structure is AB_3 and is based on the face-centred cubic lattice with A atoms at the corners and B atoms in the centres of the faces of the unit cell, as shown in Figure 1(a).

Alternatively, if f.c.c. lattice is regarded as being comprised of four simple cubic sub-lattices, then the superlattice can be described as having A atoms on one sub-lattice and B atoms on the other three. The structure has a simple cubic space lattice. Typical examples of the $L1_2$ superlattice are $AuCu_3$, $FePt_3$, Fe_3Ni and Ni_3Pt.

(ii) Type $L1_0$

The ideal composition of this structure is AB and it is

also based on the f.c.c. lattice. It has either all A or all B atoms occupying alternate (001) planes as shown in Figure.1(b). The term face-centred tetragonal is frequently applied to this structure to distinguish it from other tetragonal structures. AuCuI, FePt, NiPt and CoPt are the typical examples of $L1_0$

(iii) Type B_2 (or $L2_0$)

This is also known as the CsCl structure. The structure is based on the body-centred cubic lattice with A atoms at the cube corners and B atoms at the body-centred position as shown in Figure.1(c). Some examples are FeAl, CuZn (beta-Brass), and FeCo.

(iv) The AuCu II Superlattice

Between about 380°C and 410°C the stable AuCu superlattice has an orthorhombic structure made up of ten $L1_0$ type cells arranged as shown in Figure.1(d). At intervals of five subcells in the [010] direction, the type of atom on a given (001) plane changes. Repetition of this unit cell gives rise to a "one dimensional long period superlattice" (l.p.s.), with the period 2M=10. A slight expansion of the lattice occurs in the direction of the periodicity so that the b/a ratio is about 1.003 while the c/a ratio remains about 0.92 as in AuCuI.

1.2.2 Ternary ordered alloys

There are several possibilities regarding the atomic distribution in an ordered lattice of a three component alloy system. For example, if a third element like C

replaces element B in an AB superlattice, then one can imagine that the arrangement of A on its sub - lattice could remain undisturbed while C is distributed on the sub-lattice of B . While C is distributed randomly, the structure will be the same as the superlattice, but if C is distributed on the B sub-lattice in an ordered manner a new superlattice is formed. In this section previous work on"three ordering component"ordering will be reviewed to provide a background for the investigation of ternary superlattice in the Pt-Fe-Cu system.

Although ordering from b.c.c. solutions has received more attention than ordering from f.c.c solutions in ternary ordered alloys, the latter will be discussed only as the former is not relevent to the present investigation.

Although there has been a large amount of research on the ternary system of form Au-Cu-X and some other, principally by Raub, Kester and Sehbert [5] . There have been few studies of actual distribution of different atoms on the crystal lattice. Ternary ordered systems have been detected at the ideal compositions ABC_2 and A_6BC. The case ABC_2 will be discussed below.

Gantois [6] replaced the Cu in AuCu II with up to 12.5 % Ni and from x-ray diffraction intensity measurements, predicted that the Ni atoms replaced Cu atoms in the ternary system.

Bialas et al [7] and Koster [8] succeeded in detecting an $L1_2$ superlattice by x-ray photographic methods for alloys around the composition Cu_2NiZn. Koster proposed that Zn atoms were at cube corners and Cu and Ni were randomly distributed at the face-centres.

Hirabayashi et al [9] attempted to obtain more conclusive evidence for the atomic arrangements in Cu_2NiZn by single-crystal Neutron-diffraction. They considered the three possible structures shown in figure .1(e). Model A is fully ordered with a tetragonal structure, while models B and C are partially ordered and cubic.

Direct evidence for ternary ordering has been found by Nagasawa [10] using the composition $AuCu_2Pd$ and Au_2CuPd. He detected extra electron diffraction reflections at (100) and (011) positions as well as (001) and (110) in films of $\left[100\right]$ orientation prepared by evaporation.

As it is obvious from the above description, ternary ordering from f.c.c solutions is not so common. Two examples based on the tetragonal $L1_0$ structure have been established in the Au-Cu-Pd system.

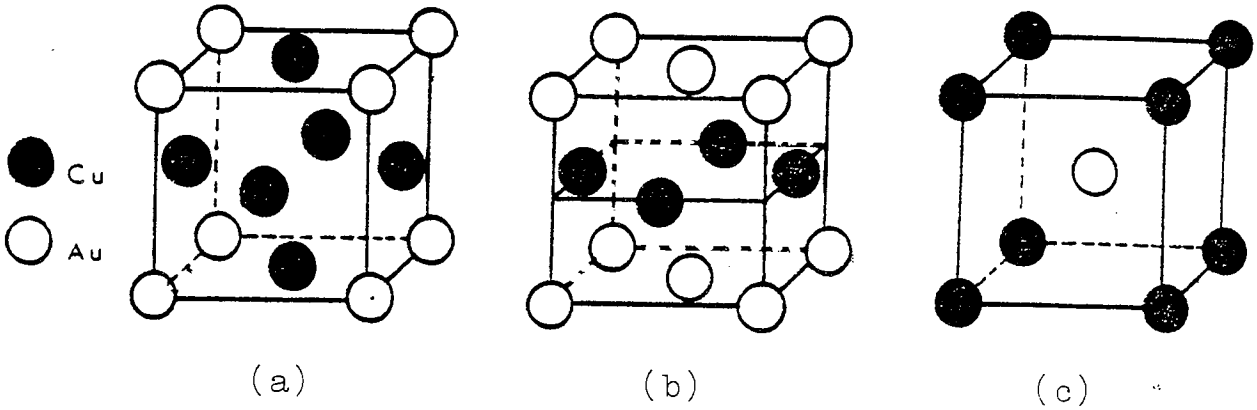

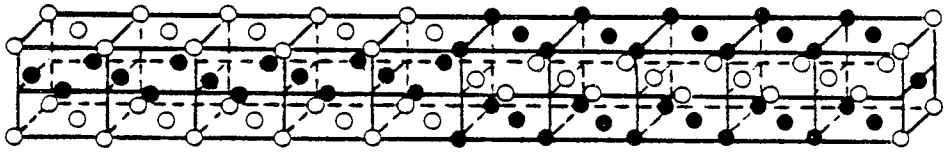

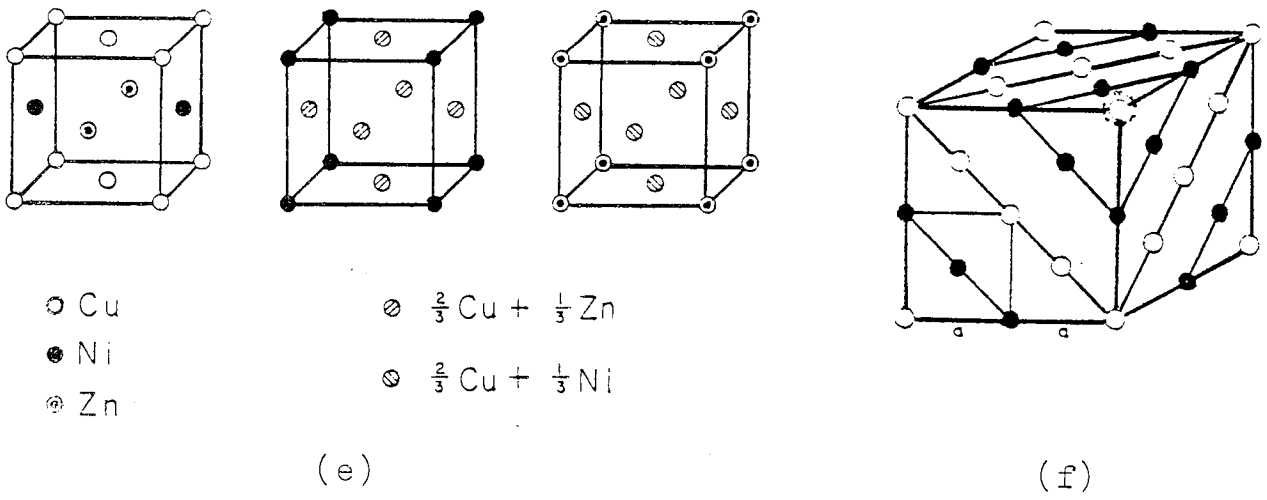

Fig 1- Unit cells of the ordered systems of;

a)- $L1_2$

b)- $L1_o$

c)- $L2_o$

d)- AuCu II

e)- possible structures of Cu_2NiZn

f)- $L1_1$

1.3 Theoretical treatments of superlattice

In this present work no theoretical investigations were made so the theoretical background of order-disorder transition will be briefly explained.

Theoretical treatments of order-disorder transformation are traceable on three different bases;

1) Interatomic forces among the constituent atoms
2) Atomic size differences of the pure components
3) Electronic effects.

Early investigators who had taken interatomic forces of the constituent atoms as the main force, responsible for the ordering transformation, had their models modified by Bragg and Williams (B-W)[11][12] where the concept of the long-range-order (L.R.O) was introduced. Their approach assumes that the ordering energy is proportional to the long-distance order in the crystal and expresses the latter by a (L.R.O) parameter, S

$$S = \frac{P-r}{1-r} \qquad (1.1)$$

Where P is the probability that an A atom occupies its correct sub-lattice site, and r is the fraction of total sites occupied by A atoms. The parameter S varies from 0 to 1 for disordered and perfect ordered structures respectively.

After the publication of their results (B-W), Bethe[13] pointed out that the ordering energy acting on any

particular atom depends on the interactions between very close neighbours only, whereas Bragg and Williams assumed that the energy acting on any particular atom depends on the distribution of all the other atoms in the crystal.

Bethe[13] , offered an alternative theory for the ordering energy, based on first nearest neighbour interactions and introduced the concept of the short-range-order (S.R.O). In simple terms if unlike atoms tend to attract each other then S.R.O is formed and the S.R.O is the determining factor in the subsequent L.R.O attraction.

Another important factor which had been neglected by (B-W) and Bethe's theories was introduced in a model by Hume Rothery, et al[14][15] which is based on lattice strains to account for the ordering phenomenon. They postulated that strains are produced when atomic species with different atomic sizes are present in the matrix. The tendency to reduce these strains provides the necessary driving force that causes ordering.

A little later came the Brillouin Zone theory as applied to ordering with which Muto [16] showed that the energy of conduction electrons can be lowered by introducing a new periodicity into the lattice such that the corresponding Brillouin zone will touch the Fermi surface.

If, however, a random structure undergoes an ordered transformation, then just as new lines occur on the x-ray

diffraction pattern, new planes of energy discontinuity are formed in the wave-number space. Hence, the extra superlattice reflections can be represented by the formation of new Brillouin zone boundaries.

To summarise, none of the above mentioned theories can satisfactorily explain the order-disorder transformation and weaknesses are easily observed in them.

For example, it is possible to obtain a zero value for L.R.O parameter for highly ordered alloys such as AuCuII and although Hume-Rothery's proposed model can explain an ordering process in the Au-Cu binary alloy system, it fails in the case of Mg_3Cd or Fe-Co.

Introduction of the Brillouin zone theory could explain the ordering transformation such as AuCuII[17] , but is unable in the case of CuPt compound, so it can be concluded that after nearly seventy years of Tammann's postulation, it is only the combination of these theories that can satisfactorily explain any given transformation.

1.4 Detection of ordering process

Almost all the standard techniques have been employed to study superlattice formation.

The technique which is used to test some of the thermodynamic parameters is that of thermal measurements. These methods quantify the change in internal energy following the atomic rearrangements accompanying the ordering process. Sykes and Jones[18] used these techniques to investigate the order-disorder transformation in Cu_3Au compound.

Electrical resistance is also very dependent upon the degree of order since the conduction modes are vastly altered by imperfections in the crystalline lattice. A disordered alloy results in a high resistance; when ordering is complete the irregularities disappear, giving rise to a low resistance. By combining domain size with resistivity measurements, Jones and Sykes[18] have shown that the resistivity is linearly related to the inverse of the domain size.

Many metallographic studies have also been carried out on numerous different systems. In recent years, optical microscopy has been superceded by transmission electron microscopy and many of the predicted structures viewed directly. Fisher and Marcinkowski[19] have extended the stacking fault contrast theory with TEM of Whelan and Hirsch[20] to include the case of APB contrast of domain structures, which until then had not been detected.

Field-Ion-Microscopy has also been employed to observe the ordering in the systems with high atomic numbers, e.g. CoPt[21] and Ni_4Mo[22]. Progress in this field has been

made possible by means of a detailed image contrast theory, which enables one to distinguish between the atomic species.

Neutron diffraction has been employed for systems such as Ni_3Mn[23] since the difference in the scattering power of the components is insufficient to produce superlattice reflections with x-ray diffraction and Iron-Aluminium alloys have been studied by means of the Mössbauer spectroscopy, but one of the most frequently used techniques to investigate order-disorder transformations is that of the x-ray diffraction technique.

1.5 Superlattice and x-ray diffraction

The change in atom arrangement which occurs on ordering produces changes in a large number of physical and chemical properties and as mentioned before, the existence of ordering may be inferred from some of these changes. However, the only conclusive evidence for a disorder-order transformation is a particular kind of change in the x-ray diffraction pattern of substance. Evidence of this kind was first obtained by Bain[3], in Cu-Au solid-solution system having the composition $AuCu_3$. Since that time, the same phenomenon has been discovered in many other alloy systems.

As it will be seen later on x-ray diffraction techniques have been used to construct the electron density map of the compound Pt_2FeCu, so at this stage it is appropriate to discuss this technique in more depth.

As was mentioned earlier, Cu-Au system is the most investigated of all the other systems regarding superlattice formation, so to discuss the application of the x-ray diffraction technique, the examples will be from the Cu-Au system.

1.5.1 Long-range order in $AuCu_3$

The Au and Cu atoms of $CuAu_3$, above the critical temperature of about 390°C are arranged in the random manner of a f.c.c lattice. Below that temperature the Au atoms in a perfectly ordered alloy occupy only the corner positions and the Cu atoms the face-centred positions of the cubic unit cell.

The atomic scattering factor of the "average" gold-copper atom is given by

$$f_{av} = (\text{atomic fraction Au})\, f_{Au} + (\text{atomic fraction Cu})\, f_{Cu},$$

$$f_{av} = \tfrac{1}{4} f_{Au} + \tfrac{3}{4} f_{Cu}$$

There are four "average" atoms per unit cell, at 000, $\tfrac{1}{2}\tfrac{1}{2}0$, $\tfrac{1}{2}0\tfrac{1}{2}$, $0\tfrac{1}{2}\tfrac{1}{2}$. Therefore the structure factor is given by

$$F = f\, e^{2\pi i(hx+ky+lz)}$$

$$F = f_{av}\left[1 + e^{\pi i(h+k)} + e^{\pi i(h+l)} + e^{\pi i(k+l)}\right]$$

and this becomes;

$F = 4f_{av} = (f_{Au} + 3f_{Cu})$ for hkl unmixed

$F = 0$ for hkl mixed

We therefore find, as might be expected, that a disordered alloy produces a diffraction pattern similar to that of any f.c.c metal, say pure Au or pure Cu. No reflection of mixed indices are present.

For a completely ordered alloy, each unit cell now contains one gold atom at 000, and three copper atoms at $\frac{1}{2}\frac{1}{2}0$, $\frac{1}{2}0\frac{1}{2}$, $0\frac{1}{2}\frac{1}{2}$,

$$F = f_{Au} + f_{Cu}\left[e^{\pi i(h+k)} + e^{\pi i(h+l)} + e^{\pi i(k+l)}\right]$$

$F = (f_{Au} + 3f_{Cu})$, for hkl unmixed,

$F = (f_{Au} - f_{Cu})$, for hkl mixed,

The ordered alloy thus produces diffraction lines for all values of hkl, and its diffraction pattern therefore resembles that of a simple cubic substance.

The diffraction lines from the planes of the unmixed indices are called fundamental lines, since they occur at the same positions and with the same intensities in the pattern of the ordered and disordered alloys. The extra lines which appear in the pattern of an ordered alloy, arising from the planes of mixed indices, are called superlattice lines and their presence is direct evidence that ordering has taken place.

As it was shown in the above discussion, all the superlattice lines are much weaker than the fundamental lines, since their structure factors involve the difference, rather than the sum, of the atomic scattering factors of each atom.

1.6 The Cu-Pt binary system

Both Copper and Platinum are f.c.c metals and upon mixing and from its melting point of 1083°C , Copper forms a continuous series of disordered f.c.c solid-solution with platinum right up to the latter's melting point of 1772°C.

All the preliminary investigations which had been based on the electrical, magnetic, thermal analysis and lattice parameter measurements were collected by Hansen et al[27] and are shown in figure 2. These measurements have proved the existence of total solid-solubility of alloys covering the entire binary compositional variation when annealed at and quenched from above 850°C.

Of particular interest in the system are solid-state transformations which occur at much lower temperatures than the solidus. Over a very wide range of compositions, order-disorder transformation occurs in the Cu-Pt binary alloys.

Johannson et al[28] by means of the electrical resistivity measurements and x-ray diffraction technique found three major different stoichiometries around which the ordering phenomena occurs, which are Cu_3Pt, CuPt and $CuPt_3$.

Other investigators, i.e., Linde[29], Schneider et al[30] and Tang [31] tried to clarify the crystal structure and the compositional stabilities of the different stoichiometric and non-stoichiometric compounds in the system, but they all added more ambiguity to the existing results as far as the crystal structure determinations were concerned.

In the above mentioned studies, crystal structure determinations were made on the basis of the x-ray powder diffraction patterns and consequently, owing to the weakness in intensity of superlattice reflections, conflicting results were obtained.

The most comprehensive investigation in the Cu-Pt alloy system was carried out by Müda et al[32] and Wu, et al[33]. They used single-crystal samples of different compositions and analysed them by means of electron microscopy and electron diffraction and obtained some well defined results. They all agreed that in the Cu-Pt binary system below 812°C three types of ordering transformations, based on Cu_3Pt, CuPt and $CuPt_3$ occurs. Both the Cu_3Pt and $CuPt_3$ superlattices are f.c.c of the $L1_2$ (Cu_3Au) type, with critical temperatures of about 645°C (at 22.5 at % Pt) and 670°C respectively.

1.6.1 Around $Cu_{0.5}Pt_{0.5}$ stoichiometry

The Cu-Pt system, at the 35-55 at % Pt range, has a unique superstructure at temperatures below 812°C(= T_c for the stoichiometric ratio , CuPt). An ordered rhombohedral lattice is formed from the disordered f.c.c. The deformation of the cube is along a (111) body diagonal giving rise to the $L1_1$ type structure, Figure. 1 (f) . This configuration, or superlattice is crystallographically unique; no ordered alloy is known to be isomorphous with it. The random distribution of atoms within the f.c.c

cell is regularly arranged by the ordering process, so that the copper and platinum atoms segregate on alternate layers of the (111) planes. This superlattice is unusual in that the average number of unlike nearest neighbours of a copper and platinum atom is not altered by the transition from the disordered to the ordered configuration and it is only the proportion of the second-nearest neighbours which is changed.

Apart from the early studies of Linde[29] and Walker[34], the only reported attempt at a microscopic examination of the CuPt is due to Corke, et al[35] by means of T.E.M. The extreme difficulty of thinning the samples of CuPt appears to have discouraged further attempts, though some T.E.M micrographs of ordered and deformed CuPt have been published by Paris et al[36].

Later on Irani and Cahn[37] carried out the most detailed studies of ordering characteristics of CuPt, near the CuPt composition, using x-ray diffraction, optical microscopy (in conjunction with polarized light), high voltage electron microscopy and dilatometry.

From their interpretations, it can be concluded that:

a)- Ordering in stoichiometric CuPt takes place at all temperatures by a nucleation and growth mechanism. During ordering, ordered and disordered phases co-exist.

b)- Samples slowly cooled through the critical temperature order in the form of coarse macrotwins, internally subdivide by microtwins.

Although Irani's et al[37] results seem valid enough, Hisatsune et al[38], could not detect the gradual shifts of the x-ray lines at high temperatures, though both agree on the low temperature mechanism.

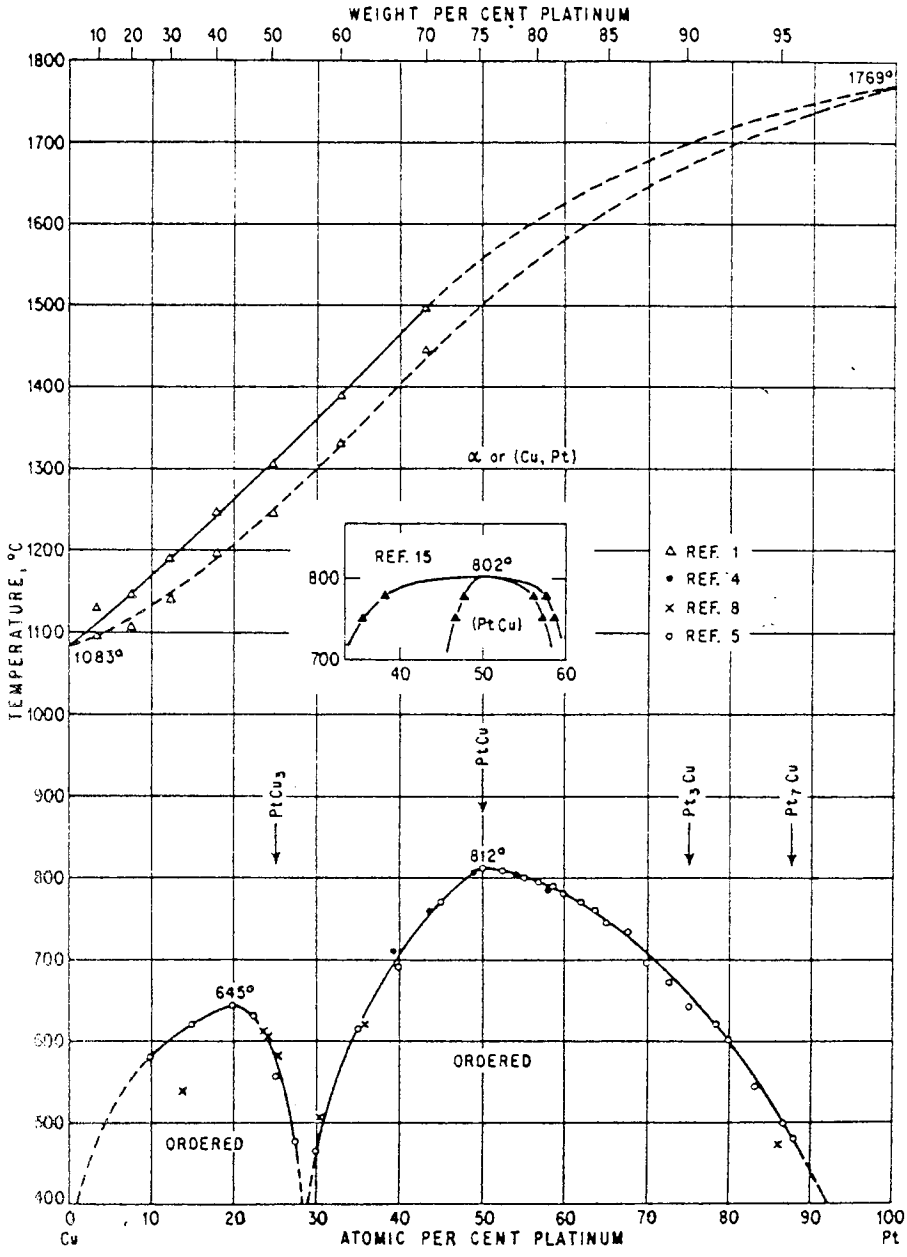

(27)

Fig.2 - The Cu-Pt binary phase diagram

1.6.2 Summary

In the Cu-Pt alloy system, order-disorder transitions have been found to take place over a wide range of compositions. These ranges of order corresponding approximately to 10-26, 35-55 and 60-80 at % Pt have been recognised. These ranges of order have been confirmed by x-ray, electrical resistivity measurements and microscopic techniques. The compositions Cu_3Pt, CuPt and $CuPt_3$ are the predominant phases, which are included in these ranges of order respectively.

1.7 The Fe-Pt binary phase diagram

Iron and platinum form a continuous range of solid-solution at high temperatures. At lower temperatures, O/D transformations which are based on Fe_3Pt ,FePt and FePt take place and introduce narrow miscibility gaps in the phase diagram.

The results of the early investigations have been collected by Hansen et al[27] and are shown in Figure.3.

After the publications of the preliminary investigations, there were areas of ambiguity in the phase diagram especially in the region of 32-40 at% Pt, i.e., although the Fe_3Pt is a well established phase, Hansen's et al diagram does not clarify its relationship with the narrow two-phase-field based on the FePt compound.

On this basis, Vlasov et al[39][40] studied the single-crystal samples of varying compositions in this range and believed that the samples annealed for more than 150 hours at 700°C had two types of structures; a cubic based on Fe_3Pt and a tetragonal based on the FePt compositions. This structural data gave rise to their proposal that between the FePt and Fe_3Pt superlattices the diagram is a eutectoid type figure 4. They believed that after long annealing the alloy with 32 at % Pt had a two-phase structure and it consisted of a cubic phase with Fe_3Pt type order and $a = 3.776\ A^{o}$ and a tetragonal phase with FePt order structure and $a = 3.784A^{o}$, $c = 3.737A^{o}$ and $c/a = 0.988$.

In the alloy with 35 at % Pt structural changes occur in the process of quenching and annealing from 750°C: the formation of tetragonal nuclei in the cubic matrix creates an elastic stress, they grow until they impinge and form a complex microstructure of alternating domains with perpendicular C-axes. These domains are parallel to $\{110\}$ type, figure. 5

The compositional limits of the ordered region based on FePt is well defined in figure 3 although, according to Crangle and Shaw [41], the high Pt side is more restricted. The characteristic banded structure of FePt was first observed metallographically by Isaac and Tamman [42] in 1907. In a later study Nemilov [43][44] showed that FePt alloys quenched from within the single phase region had

banded structures while alloys quenched from above the single phase region had a finer microstructure of ripples or small platelets.

Lipson et al[45] carried out a more thorough study of FePt and identified the structure as tetragonal. They also found that the disordered state could not be retained by quenching. Similar microstructural features to that of Nemilov's were also observed by Lipson et al[45] and are shown in figure 5.

Crangle and Shaw[41] studied the Pt-rich region of the system based on $FePt_3$ compound from room temperature right up to 1400°C. They used the conventional x-ray diffraction technique to investigate the lattice parameter changes due to compositional changes and finally proposed a revised phase diagram of the Fe-Pt system for compositions between 0.48 at % Fe. Their proposed diagram is shown in figure 6.

1.7.1 Summary

Both preliminary and up to date Cabri et al[46], studies of the binary alloy system of Fe-Pt confirm the existence of the O/D transformations in the system which are based on the stoichiometric compounds of Fe_3Pt, FePt and $FePt_3$. The compositional variations, the critical temperatures and the phase relationships of the Fe_3Pt and $FePt_3$ with FePt **are** still questionable, but the majority of authors seem to agree that in the region which is based

on FePt compound, there exists a very narrow two-phase field of the cubic plus tetragonal mixture.

Another dispute has arisen amongst some authors about the retention of the disordered structure of the FePt on quenching the samples from above the critical temperature. Isaac, Nemilov, Craf and Lipson could not suppress the disordered state on quenching, whereas[47] reported that this mechanism is indeed possible. Even today this problem exists and there seems to be no clear answer to the problem.

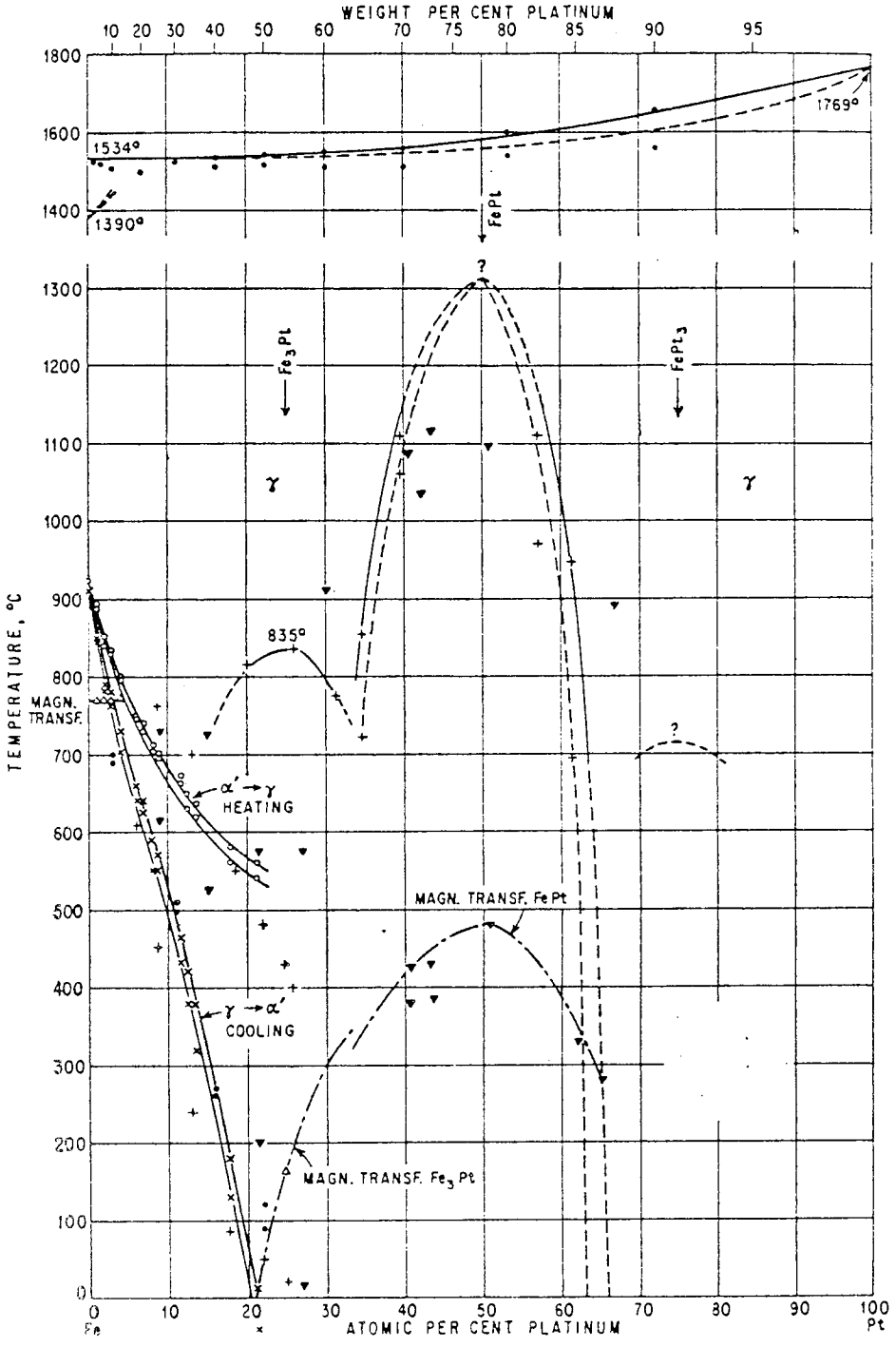

Fig 3- The Fe-Pt binary phase diagram[27]

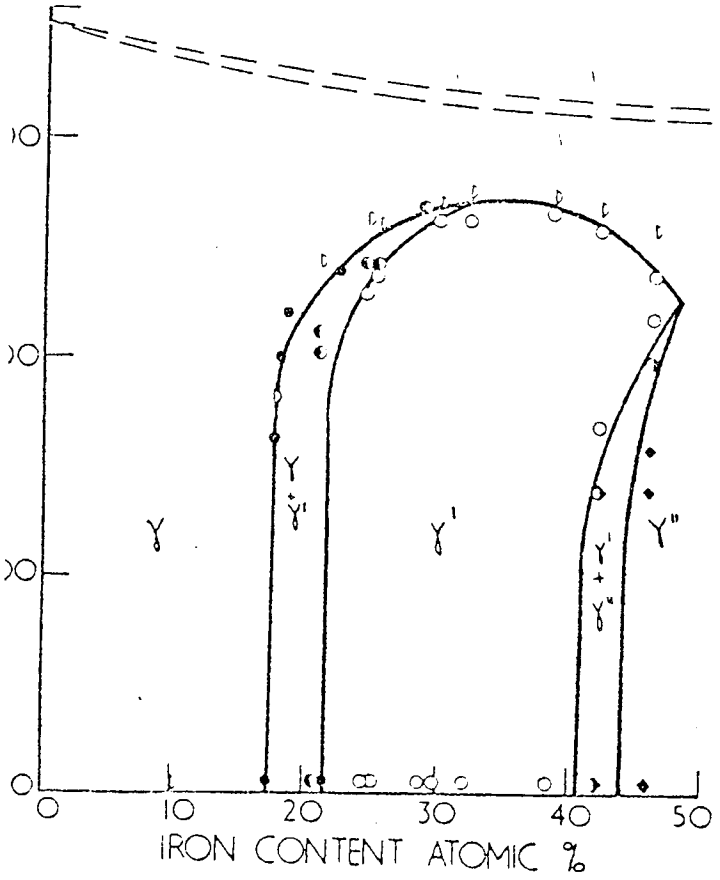

Fig 6- Phase diagram of the Pt-Fe system for 0 to 48 % Fe (41).

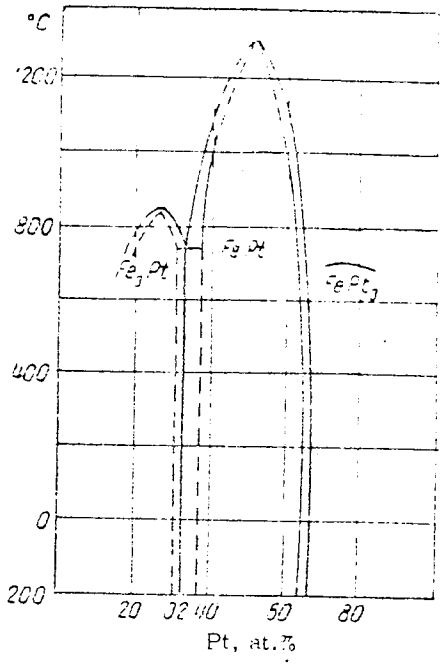

Fig 4- Constitution of Fe-Pt (39)(40).

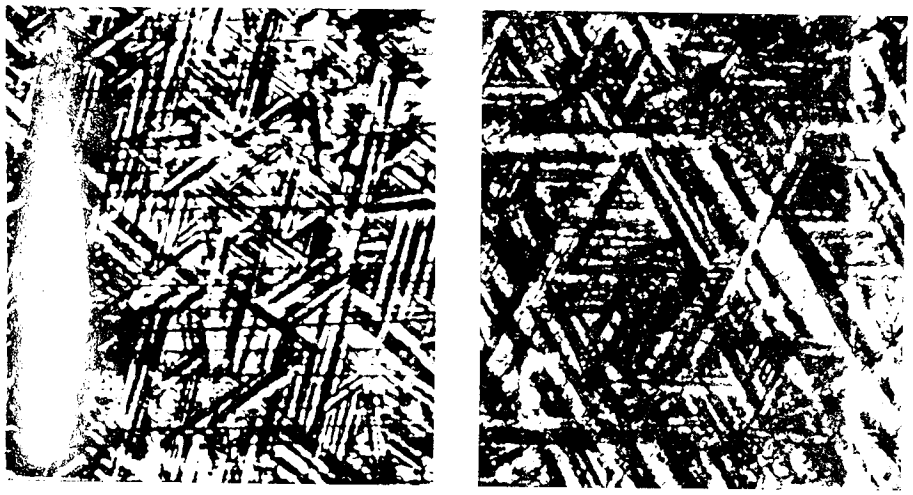

a b

Fig 5- Microstructures of FePt compound (45);

a)- 5 minutes at 1500°C ; cooled at 30°C/sec

b)- 5 minutes at 1400°C ; cooled at 30°C/sec

1.8 The Cu-Fe binary phase diagram

There is neither an intermediate nor order-disorder transition in the Cu-Fe binary system which is shown in figure.7, Hansen et al,[27].

The solid-solubility of Fe in Cu is very small at low temperatures but increases to several per cent at $\sim$1070°C. The solubility of Cu in α-Fe is so small it extends to a maximum of $\sim$ 8 at % in γ-Fe.

The temperature given for the eutectoid reaction of $\gamma \rightleftarrows \alpha +$Cu differs widely because of a great hysteresis between heating and cooling. On cooling the temperatures of 791°C, 820°C, 824°C and 755°C [48,49,50,51] and on heating, 850°C, 856°C and 860°C [49,50,52] were obtained. There is also conflicting reports for the peritectic reaction involving the δ-phase, i.e., 1477°C and 1484°C are recorded by [51][49] respectively.

The lattice spacings of the Cu solid-solution have been measured by Anderson, et al [53] who found them to increase almost linearly with Fe to a = 3.6092Å at the solid-solubility limit at 1025°C.

1.8.1 Summary

Although the Cu-Fe binary system is one of the oldest binary diagrams, it seems to be the least informative one regarding:

a)- The exact limits of the solid-solubilities of Cu in Fe or vice versa

b)- The precise temperatures of the eutectic, eutectoid and pretectic reactions.

So in the present investigations, whenever necessary the binary data of figure. 7 will be used.

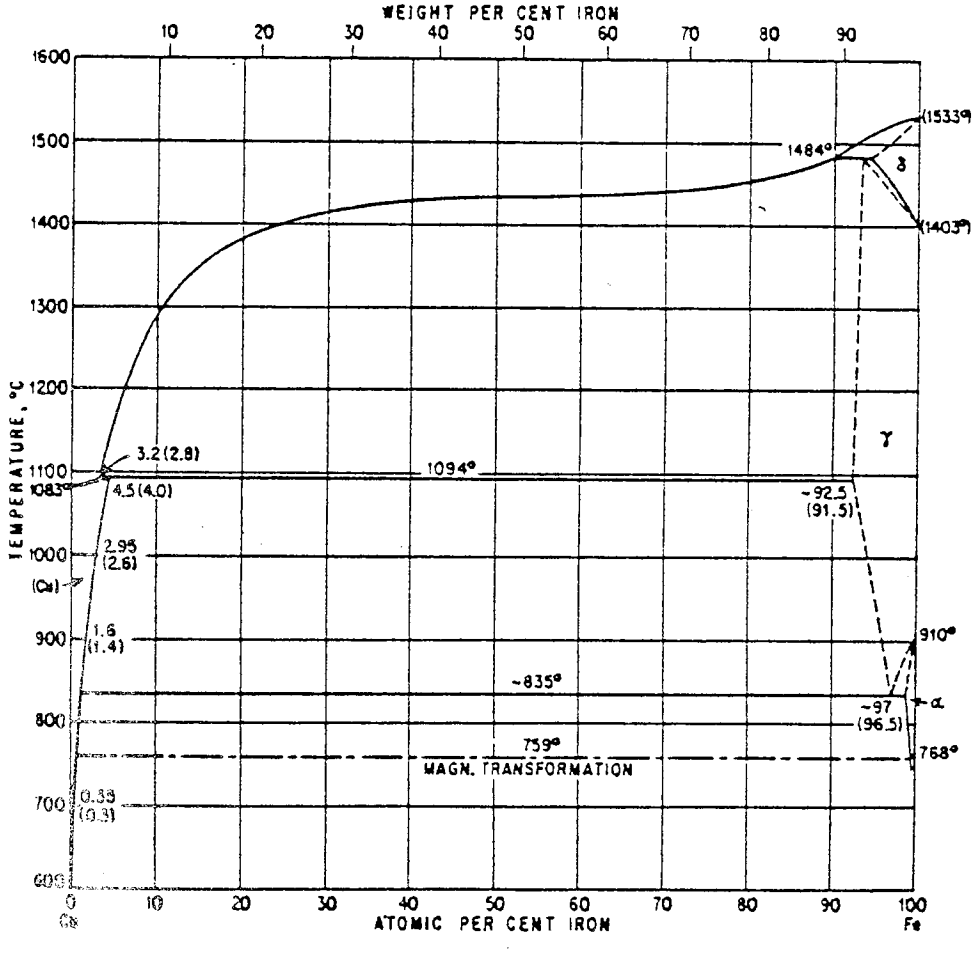

Fig.7 phase diagram of Cu-Fe system (27)

1.9 The Pt-Fe-Cu ternary phrase diagram

As far as we are concerned, there is only one published report on the ternary phase relationships in Pt-Fe-Cu system, which was published in 1944 by two Russian workers Nemilov and Rudnitskii[54] . They used thermal analysis, hardness measurements, electrical resistivity and optical metallographic techniques to carry out their investigations.

They were the first people to state the existence of the compound Pt_2FeCu (50% Pt, 25% Fe and 25 at% Cu) in their thermal analysis and microstructural studies.

In their conclusions, they stated that with the exception of that part of the diagram, low in platinum, at approximately 20 at% Pt, all the alloys were solid-solutions at high temperatures. On lowering the temperature, and decomposing the solid-solutions, apart from the compound already known from the binary systems of Pt-Fe and Pt-Cu, approximately at 1200°C, a solid compound Pt_2FeCu is formed. The compound Pt_2FeCu forms continuous regions of solid-solutions both with excess platinum and with the compound PtFe. With the compound PtCu, the Pt_2FeCu forms a limited region of solid-solutions on the PtCu side. The region of solid-solution of Pt_2FeCu in PtCu extends to approximately the composition, 10 at% Fe, 40 at% Cu and 50 at% Pt.

In the direction of the Fe-Cu binary system, the Pt_2FeCu solid-solution region is very limited, reaching only to 45 at% Pt, passing beyond this into the heterogeneous region, arising from the decomposition of a solid-solution forming Pt_2FeCu and a solid-solution of Platinum, Iron and Copper, near to 33 at% Pt.

Considering further the region of ternary solid-solutions, extending from 33 to 20 at% Pt and near to the Fe-Cu edge of the diagram, lies a heterogeneous region.

They finally concluded that the Pt-rich corner of the ternary phase diagram is a region of continuous solid-solutions.

As it can be seen from the above discussion, this report does not give a great deal of useful information about the phase relationships, phase boundary, order-disorder transformations in this system of alloys. No attempts were made to study the system on the isothermal sections, but only the solidus and liquidus contours of the phase relationships.

1.10 Mineralogical surveys

The most comprehensive studies of the (PGM) are due to Cabri et al [41,55] who analysed different samples from placer and primary deposits as well as synthetic alloys Fe-Pt binary alloys and the ternary compound Pt_2FeCu.

In their studies of (PGM), they found new minerals in placer deposits along the valleys of the Tulameen and Silkameen rivers in South British Columbia, Canada. One of the new minerals, an alloy of Platinum, Iron and Copper which had the composition Pt_2FeCu was found and has been named Tulameenite for its locality.

Tulameenite occurs associated with cubic Fe-Pt natural alloys as a rounded to irregular area up to about 400μm in diameter, as a free grain, or as grains with complex inclusions, figure.8.

They studied some optical and physical properties of this new mineral and in some cases the stoichiometric composition of Pt_2FeCu was synthesized for further studies.

Their microprobe analysis on eight Tulameenite grains are shown in Table.1 and some are plotted on a ternary Pt-Fe-Cu ternary diagram, figure.9. The average microhardness value of 442 $^{kg}/_{mm}2$ was obtained for Tulameenite when a 50 g load was used.

They also measured the lattice parameter of the Pt_2FeCu by x-ray diffraction on the natural and synthetic samples. Their analysis show that the Tulameenite has a tetragonal structure cell of a = 3.891Å , and c = 3.577Å dimensions. Table.2 shows their x-ray diffraction data.

They finally concluded that the Tulameenite has a range of composition with minor Ir replacing Pt with Ni replacing Fe. Experiments along the PtFe-Pt_2FeCu line indicate that the maximum substitution of Fe for Cu in Tulameenite is between $Pt_2Fe_{1.68}Cu_{0.32}$ and $Pt_2Fe_{1.28}Cu_{0.72}$.

The mineral concentrates from the Tulameen district were further studied by Shahmiri et al[56] where the (PGMs) occurred as discrete grains and nuggets up to 2-3mm in diameter. Cubic platinum-iron (Pt_3Fe) formed the bulk of the PGMs, with Tulameenite as a minor intergrown phase. Electron-probe microanalysis of Tulameenite gave compositions clustered around the Pt_2FeCu point in the ternary phase diagram isothermal section as shown in Figure 10, pointing to limited solid-solubility.

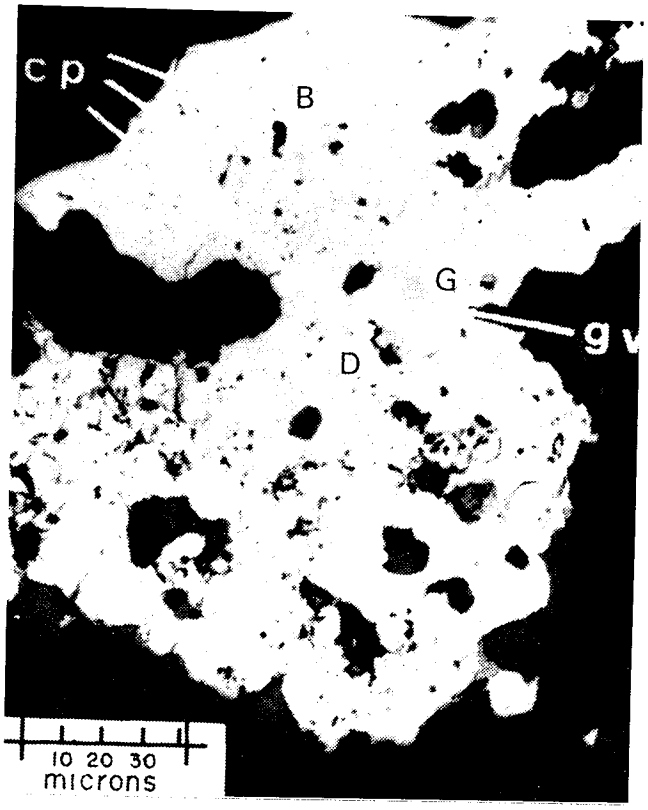

Fig 8- Photomicrograph of a complex Tulameenite grain (grain ,B, G ,D) (55).

Sample, locality & no. of analyses	weight per cent -- average and range						Total	Formula
	Pt	Ir	Fe	Cu	Ni	Sb		
tulameenite								
Grain A (G.D.) Tulameen R. (10)	76.65 75.5-77.6	not detected	10.55 8.6-12.3	6.95 5.7-8.3	3.77 3.0-4.7	2.07 1.6-2.9	99.99	$Pt_{2.04}(Fe_{0.98}Cu_{0.56}Ni_{0.34}Sb_{0.08})_{\Sigma=1.96}$
Grain B (G.D.) Tulameen R. (9)	74.87 70.7-76.9	not detected	8.39 6.4-9.8	9.38 6.9-11.9	3.52 2.1-4.6	3.52 2.7-5.0	99.68	$Pt_{2.00}(Fe_{0.78}Cu_{0.76}Ni_{0.32}Sb_{0.14})_{\Sigma=2.08}$
Grain 5 Similkameen R. (10)	73.98 73.56-74.78	1.99 1.98-1.99	10.38 9.80-11.09	13.13 12.18-13.99	not detected	not detected	99.48	$(Pt_{1.94}Ir_{0.06})(Cu_{1.06}Fe_{0.94})_{\Sigma=2.00}$
Grain 9 Similkameen R. (10)	73.68 72.12-75.09	1.95 1.94-1.96	11.22 10.13-12.05	11.25 10.15-13.09	not detected	not detected	98.10	$(Pt_{1.98}Ir_{0.06})(Fe_{1.04}Cu_{0.92})_{\Sigma=1.96}$
Grain 1 (#2258) Area A-Tul. R. (8)	76.66 76.19-77.19	0.22 0.22-0.22	11.94 11.43-12.14	8.66 8.45-8.98	0.50 0.49-0.51	1.40 1.31-1.50	99.40	$(Pt_{2.06}Ir_{0.006})(Fe_{1.12}Cu_{0.72}Sb_{0.06}Ni_{0.04})_{\Sigma=1.94}$
Grain 1 (#2258) Area B-Tul. R. (8)	77.24 77.00-77.55	0.20 0.18-0.21	12.21 12.12-12.28	8.43 8.29-8.56	0.51 0.49-0.53	1.23 1.14-1.30	99.82	$(Pt_{2.06}Ir_{0.006})(Fe_{1.14}Cu_{0.70}Sb_{0.06}Ni_{0.04})_{\Sigma=1.94}$
Grain 1 (#2258) Area C-Tul. R. (9)	77.31 76.91-78.12	not detected	11.23 10.40-12.45	9.17 8.70-9.43	0.60 0.58-0.64	1.04 0.96-1.20	99.35	$Pt_{2.08}(Fe_{1.06}Cu_{0.76}Ni_{0.06}Sb_{0.04})_{\Sigma=1.92}$
Grain 1 (#2258) Area D Tulameen River (10)	77.83 76.93-78.33	0.25 0.24-0.25	12.87 12.59-13.07	8.01 7.87-8.15	0.56 0.52-0.58	0.65 0.59-0.70	100.17	$(Pt_{2.06}Ir_{0.006})(Fe_{1.20}Cu_{0.66}Ni_{0.06}Sb_{0.02})_{\Sigma=1.94}$

Table 1- Electron Microprobe analysis of Tulameenite (55).

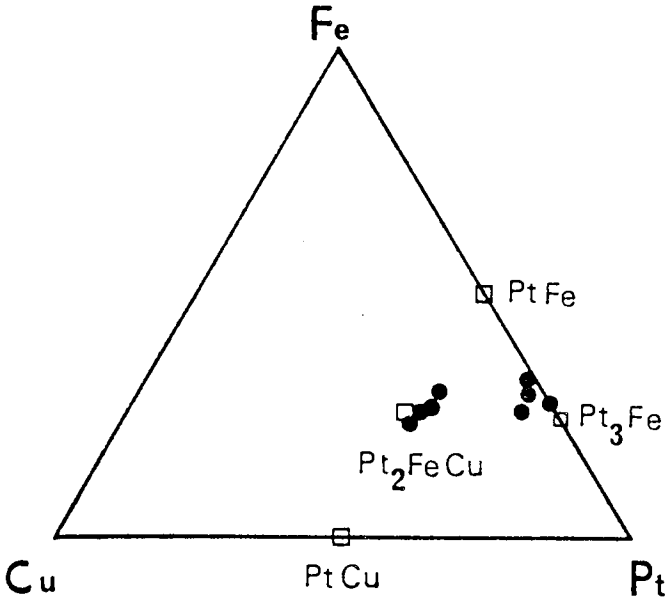

Fig 9- The Pt-Fe-Cu ternary system. Synthetics are denoted by squares. Natural by closed circles (55).

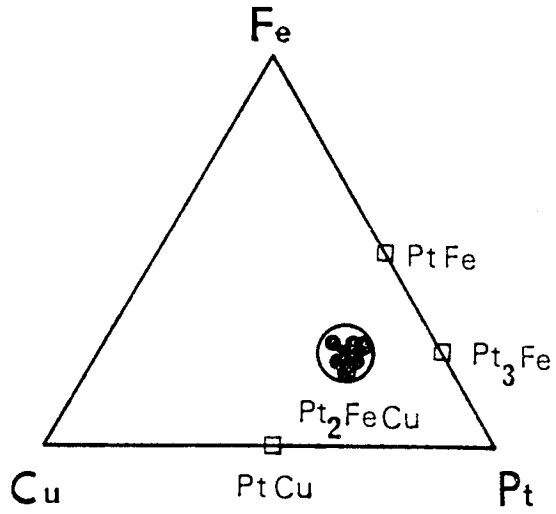

Fig 10- Composition of Tulameenite(at%) (56).

Tulameenite (gr. #5) a=3.891(2) c=3.577(2)Å				Pt_2FeCu a=3.885(1) c=3.588(1)Å			PtFe a=3.847(1) c=3.715(1)Å			
I	d_{meas}	d_{calc}	$hk\ell$	I	d_{meas}	d_{calc}	I	d_{meas}	d_{calc}	$hk\ell$
3	3.569	3.576	001	3	3.568	3.588	3	3.690	3.715	001
4	2.753	2.751	110	4	2.746	2.747	3	2.714	2.720	110
10	2.179	2.181	111	10	2.180	2.181	10	2.195	2.194	111
7	1.946	1.945	020	6	1.942	1.942	4	1.918	1.923	020
2	1.789	1.788	002	4	1.794	1.794	3	1.857	1.857	002
4	1.709	1.709	021	4	1.707	1.708	3	1.707	1.708	021
3	1.500	1.499	112	4	1.502	1.502	3	1.534	1.534	112
4	1.375	1.375	220	4	1.374	1.373	3	1.361	1.360	220
5	1.317	1.317	022	7	1.319	1.318	5	1.338	1.336	022
2	1.285	1.284	221	3	1.283	1.282	4	1.280	1.282	030
1	1.230	1.230	130	4	1.229	1.228	2	1.243	1.238	003
			003	1	1.196	1.196	3	1.218	1.216	130
8	1.163	1.163	131	9	1.163	1.162	9	1.156	1.156	311
							6	1.127	1.127	113
8	1.093	1.094	113	8	1.096	1.096	6	1.098	1.097	222
							1/2	1.068	1.067	230
							5	1.042	1.041	023
6	1.016	1.016	{023	3	1.018	1.018	6	1.018	1.017	132
			{132	6	1.014	1.013				
3b	0.9730	0.9728	040	5	0.9713	0.9712	5	0.9626	0.9618	040
2b	0.9433	0.9438	140	6	0.9420	0.9422	5	0.9324	0.9311	041
2b	0.9175	0.9172	230	5	0.9157	0.9157	6	0.9180	0.9157	223
			223	6	0.9022	0.9020	5b	0.9088	0.9068	330

Table 2- X-ray diffraction powder data , after (55).

2. EXPERIMENTAL PROCEDURES

2.1 Alloy preparation

To study the phase relationships in the Pt-Fe-Cu ternary diagram, alloys with different compositions were made up. The locations of these alloys were chosen to cover the entire system. No binary alloys were synthesized as the previous existing studies seemed adequate .

The spectrographically pure element, platinum, iron and copper were used to synthesize the alloys. Electron microprobe and chemical analysis of the pure elements showed no significant impurities. Pure powdered elements were weighed out in quantities sufficient to prepare one gram alloys of the desired compositions.

At first, attempts were made to compact and sinter these alloys, so a very small die-set was designed to give cylindrical shaped samples 3 mm in diameter.

When each alloy was weighed from pure elements , they were mixed for 2 hours in a cylindrical drum mixer , revolving horizontally about its axis.For compaction no lubricant was added to the powders. Lubrication of the die walls was carried out by brushing on a saturated solution of stearic acid in diethylether.

Six different platinum-rich alloys were prepared with this technique and were sintered for four weeks in a vacuum furnace at 1050 ± 2°C under a low partial pressure of argon gas.

These sintered alloys were subsequently quenched in water and analysed by the E.P.M.A. technique to check their homogenity. Surprisingly, an area big enough for E.P.M.A. analysis could not be found due to a great deal of porosity. This technique was then abandoned and the alternative technique of melting and casting was employed to prepare the remaining alloys.

To melt these alloys a non-consumable electrode vacuum-arc furnace was used. At first, the weighed powdered alloys were compacted in the designed die-set to avoid any dispersion of the powdered samples during melting.

These compacted samples were placed in the vacuum chamber of the arc-furnace. The chamber was evacuated to a pressure of 10^{-5} torr and then high purity Argon was introduced. This was repeated three times and finally before melting under a low pressure of Argon, a titanium getter was melted for ten minutes to absorb the residual gases.

The alloys were repeatedly turned over and remelted again to improve their homogenities. These alloys were weighed before and after final melting and the weight losses were found to be negligable. All the alloys were prepared by the above-mentioned technique.

2.2 Heat treatment

2.2.1 Homogenization treatment

When the alloys were melted by means of the vacuum- arc furnace, some of them were randomly selected and composition profiles obtained by E.M.P.A. to determine the state of homogenity. Platinum-rich alloys showed more segregation compared with the copper and iron-rich alloys although they were remelted several times to improve their homogenity, it seemed that a much longer annealing time was needed than anticipated.

The alloys were placed in silica tubes which were evacuated three times to 10^{-4} torr and each time back filled with argon gas. Finally, after the last evacuation, each tube was back filled with argon and then sealed off. On average, about 20 alloys were placed in each tube and ceramic beads were used to separate the alloys to avoid any diffusion during the annealing.

These tubes were placed inside a muffle furnace operating at $1200^{\circ}C \pm 5^{\circ}C$.

Following fracture of the silica tubes in the initial work, possibly due to vaporisation of absorbed or combined water from the ceramic, the evacuation procedure was modified. In this case, when the tubes were joined to the main glass body and after the evacuation, the tubes were heated up by a Bunson burner from outside to evaporate the water

from the inside of the tubes which was then trapped by means of a liquid N_2-cooled cold trap. Finally when the cold-trap was being used, the tubes were sealed off.

Due to the breakages of the silica tubes, some alloys, mainly Cu and Fe-rich alloys were totally oxidized and were abandoned. The rest of the alloys and some newly made ones were sealed off inside the silica tubes and were placed inside the muffle furnaces at 1200°C ± 5°C for three months. These tubes were finally quenched in iced water and alloys were checked for their degree of homogenization and seemed uniform enough to carry out the further heat-treatments (the compositional variation of 0.5% was measured from the different regions of a sample). A total of 22 randomly selected alloys were analysed for this purpose.

2.2.2 Continuous cooling

The second stage of the heat-treatments was continuous cooling of already homogenized samples.

The homogenized alloys were cut in half and each half was sealed off inside the silica tubes as mentioned above. The tubes were placed in two separate muffle furnaces at 1200°C ± 5°C for one week then slowly cooled at 10°C/day. One set of alloys reached 1000°C in twenty days and was then held for a further period of three months and finally quenched.

The second set of alloys was continuously cooled at 10°C/day to 600°C and were kept at this temperature for six months and finally quenched in iced water.

To study the ternary compound Pt_2FeCu in greater detail, 10g of the compound was synthesized from its stoichiometric ratios. The compound was melted in the vacuum-arc furnace and was homogenized for three months at 1200°C ± 5°C.

During the course of the present investigation, when some more compound was required the following technique was employed, as the previous homogenization heat treatment was rather time consuming.

It had been emphasized that the silica tubes should not be used at temperatures higher than 1200°C. Attempts were made to back fill the tube by the right amount of the inert gas to keep the outside and inside pressure in balance to prevent the collapse of the tube at the temperatures higher than 1200°C.

By trial and error it was found that if the tube was back filled by Argon to 0.2 bar it could withstand annealing temperatures up to 1400°C without collapsing, but the tube changed its diameter from 25mm to 45mm at 1400°C and while still under partial pressure.

This technique was then employed and the compound was homogenized for 10 days at 1400°C.

To check the chemical composition of the compound after homogenization treatments, chemical analysis was carried out on two small pieces of the sample, which were cut from top and bottom of the master sample and the following results were obtained.

Pt	76.42 Wt% 76.58 Wt%
Fe	10.81 Wt% 11.02 Wt%
Cu	12.74 Wt% 12.60 Wt%

2.3 Recrystallization treatments of the Pt_2FeCu

To study the recrystallization mechanism, four pieces, each of one gram weight were cut from the homogenized materials. They were subjected to two hours annealing at 1250°C and rapidly quenched in iced water. Four isothermal temperatures of 1000°C, 900°C, 800°C and 700°C were selected for recrystallized treatments.

These samples were given heat-treatments of 2 to 3000 hr duration in the vacuum-furnace with the quenching facilities. Some of these samples were also subjected to shorter or longer heat treatments in order to study the recrystallization mechanism. After each heat-treatment they were quenched in water and optical photographs of the original surfaces were taken. Standard procedures were employed to obtain the recrystallized fraction, and subsequently the activation energy of the recrystallization mechanism.

2.4 Specimen preparation

2.4.1 Metalography specimen

To examine the microstructural features of the alloys, Optical microscopy was used. Samples were hot mounted in conductive bakelite, mechanically ground and polished to $\frac{1}{4}$ μm finish.

Such a fine polish could not remove some of the scratches and although a repeated "etching and polishing" technique was used, scratch marks were still observed after the final etching.

These scratches proved to be more difficult to remove in the two-phase samples especially if one-phase was copper-rich.

2.4.2 Specimens for electron microprobe analysis

For the electron microprobe analysis, the samples which were used for optical metallography were used. After initial grinding down to 240 grit size, they were polished down to 1 μm by means of the vibratory polisher to ensure adequate flatness of the samples.

2.4.3 Transmission electron microscopy specimens

To examine some of the microstructures of the compound Pt_2FeCu, different thin foils with different treatments were examined under the T.E.M. Because of the high atomic number thin specimens were required ($\sim$100 nm thick) and this could have been achieved by electropolishing technique. On the other hand,the resistance of platinum and its alloys

to chemical attack has long been known and therefore a satisfactory electropolishing solution was difficult to find.

The first step taken was to use the solutions which had been used for the pure platinum. A highly viscous, acidified $CaCl_2$ solution at $-35^{o}C$ with an AC potential applied across the electrodes was used

The alternating potential repeatedly depolarises the surface, but partial self-rectification takes place and so the sample slowly dissolves. Among the other solutions which failed were 10% aqueous solution of KCN under AC conditions and concentrated chromic acid solution which are excellent polishes for iridium .

The modified solution of Croke et al[57] was also tried. It consisted of 100 ml saturated solution of calcium chloride to which had been added, in order, 73 ml distilled water, 45 ml concentrated hydrochloric acid, 25 ml 70% perchloric acid and 1 gram cuprous nitrate. This solution was the best out of all the solutions previously tried but out of ten attempts, two samples only gave satisfactory thin foils.

Later on Irani et al[58] modified Croke's solution to only 4.5 ml HCl. Both of the latter techniques were applied to our system and in spite of sustained attempts, only a few of the samples were sufficiently electron- transparent to be used.

An alternative technique for the production of thin foils is Ion-beam thinning .

Discs of 3mm diameter were spark-machined using a tubular electrode and then ground on grade 1200 silicon carbide to a thickness of 100 - 200 μm. The thin sample was then placed between two tantalum specimen holders and fitted inside the Ion-beam chamber. The energy of the Ions were 3-5 KeV and the time required to thin down the samples suitable for T.E.M. observation was 3-72 hours.

The Ion-beam thinning procedure was carried out with Ion-tech Ltd equipment (Super Microlap Mark 2,Model B306). In this equipment two Ion guns are employed to bombard both sides of a disc specimen at the same time. This prevents sputtered atoms recondensing on the other side of the specimen.

The incident Ion-beam angle was $\sim$ 40 degrees and when a small hole appeared in the sample,the angle was reduced to $\sim 10^{o}$ relative to the specimen surface for final thinning.

There are a few effects which must be taken into consideration when the Ion-beam is used:

1)-The heat produced during the thinning procedure ($\sim 90^{o}C$) could affect the structure and chemical composition of the specimen,if there is a phase transformation within the heating range.

2)- The energy of the incident Ions is important since a high energy beam causes overheating.

3)-Preferential sputtering occurs whenever a Multicomponent system is subjected to Ion-bombardment.Due to different

partial sputtering yields of the individual components an altered surface layer and consequently surface roughness will develop.

4)-Preferential sputtering could result in surface enrichment of the component (usually heavier component) for the alloys and intermetallic compounds.

When a thin foil, produced by Ion-beam thinning is viewed under T.E.M. some artifacts may be observed due to the thinning procedure which could result in a misinterpretation of the micrographs.

When etching was required,(e.g. for optical microscopy) the following solutions were employed.

1-An acid-ferric-chloride (10 gr Fe_3Cl, 25 ml HCl, 250 ml methanol).

2- Aqua-regia, full strength (20 c.c conc. Nitric acid and 80 c.c. conc. hydrochloride acid).

3- Nital, (2% solution of HNo_3 in ethanol).

4- Ammonium persulphate.

The main etching solution was Aqua-regia of different strength and temperature. The tetragonal single phase region alloys were etched in boiling hot aqua-regia for 2-10 min, whereas for the the two phase or three phase alloys,a cold solution and a time of 20 secs,was needed.

In some special cases where chemical etching seemed to produce microstructures unrelated to the metallurgical structure,the ion-beam technique was used as an etching technique.

2.5 X-ray diffractometry

An x-ray diffractometer using Co-K_α radiation and an Iron-β-filter was used throughout the present investigations to measure the lattice parameters and determine the crystal structure of the stoichiometric Pt_2FeCu, and to make measurements of the long-range order parameters.

Lattice parameters were obtained from the diffractometer measurements on samples scanned at one degree per minute. Super-pure aluminium samples were used to calibrate the instrument and each time its lattice parameter was reproducable to 0.001Å.

To obtain the true values of the lattice parameters, standard correction procedures were undertaken. For cubic and tetragonal unit cells the $Cos^2\theta$ correction function[59],[60] was employed. Whenever the integrated intensity measurements were required, either a planimeter was used on peaks on graphically recorded data or integrated intensities were measured directly by numerical data output from a computer-controlled diffractometer step scan. A scan rate of $0.1^\circ/_{min}$ was used for the latter.

2.6 Electron Microprobe Analysis

Electron microprobe analysis was carried out with a Cambridge Instruments "Microscan Five" microanalyser to determine the chemical compositions of the alloys under study. The normal procedure in microanalysis is to compare the count rate for the given element, first from the area on the

sample under analysis then from a standard of the pure element. The ratio of the count rates from the unknown and the standard is the basic experimental measurement.

All measurements were obtained using 20 kev accelerating voltage and a beam current of 50 nA. Pure elemental standards were employed and the analyses were carried out using the L_α lines of Pt (λ = 1.3130 Å) and the K_α lines of Fe and Cu (λ = 1.9360 Å, and 1.5405 Å respectively).

Pt	L_α
Fe	K_α
Cu	K_α

A computer correction program based on that of Duncomb and Jones(61) was used to correct the x-ray intensity data for absorption, fluorescence and atomic number effects.

3. EXPERIMENTAL RESULTS

Introduction

In the present study, the results will be presented in three sections; the first section, dealing with the results of the investigation of the ternary stoichiometric compound Pt_2FeCu, then sections two and three dealing with the constructed isothermal ternary sections at 1000°C and 600°C respectively.

Section I

Ternary stoichiometric compound Pt_2FeCu

3.I.1 Differential thermal analysis (D.T.A)

D.T.A was employed to study any changes which could occur during the cooling and heating of the homogenized sample of Pt_2FeCu. The following heating and cooling rate was adopted;

1) Heat to 1300°C at 7°C/min
2) Cool to 1100°C at 1°C/min
3) Cool to 900°C at 2°C/min
4) Cool to room temperature at 5°C/min

During heating a significant endothermic reaction was observed to have taken place. The temperature at the start of this reaction was 1168°C. On cooling one significant exothermic reaction was observed starting at a temperature between 1178°C and 1170°C and ending between 1152°C and 1140°C.

3.I.2 X-ray diffraction

An x-ray diffractometer using cobalt K_α-radiation (λ = 1.7902A°) and an Iron-β-filter was employed to measure the

lattice parameters and later to determine the crystal structure of the Pt_2FeCu.

The observed x-ray traces had similar patterns despite the fact the samples had following treatments;

a) As-cast (no heat-treatments)

b) Cast, then solution-treated at 1200°C for three months and rapidly quenched.

c) Samples of b) ordered-annealed at 1000°C, 900°C, 800°C and 700°C for 2,4, ..., 3000 hours and subsequently quenched after each anneal.

d) Elemental powder, compacted and sintered at 1000°C for three months and quenched

e) As a), then homogenized at 1500°C for six hours and either quenched or slowly cooled to room temperature.

A typical x-ray diffractometer trace is shown in Figure 11. In none of the traces were major angular shifts of any reflections observed and only the relative intensities altered depending on the thermal-treatments.

In all traces, apart from the fundamental lines, there existed certain mixed index reflections, e.g. (001), (110), etc. The presence of these reflections revealed that an ordering transition had occurred in these alloys to produce a superlattice based on the face-centred structure cell. Therefore, taking the D.T.A results into consideration, it was deduced that the compound transformed to an ordered-phase from the disordered phase between 1174°C-1146°C(T_c).

Although some of the x-ray traces were taken from the samples which were subjected to different heat-treatments above T_c, further attempts were made to retain the disordered phase by rapid quenching. All attempts failed and even the fastest quenched samples, on the subsequent x-ray analysis, showed the presence of the superlattice reflections.

It appeared that Pt_2FeCu had similar behaviour to the binary compound PtFe which according to [45] orders on quenching from the above $\sim 1300^{o}C$. On this basis, it seems that the disordered structure above T_c cannot be retained on quenching.

Although the x-ray traces of the Pt_2FeCu have been indexed by Cabri et al [55] (Card No 26-528), a Bunn chart was used to index the x-ray traces which corresponded to a face-centred tetragonal lattice.

The structure cell was confirmed as tetragonal and the true lattice parameters were determined as follows for the as-quenched sample;

$$a = 3.895A^{o} \qquad c = 3.595A^{o} \qquad {}^{c}/_{a} = 0.923$$

Cabri et al [55] measured the lattice-parameters but did not report any crystal structure determination, so it became necessary to determine its structure. This was achieved by plotting the Electron-density maps (E.D.M) from the calculated and measured intensities of two different materials, as-quenched and the fully ordered ones. To achieve such plots, some preliminary steps had to be taken.

Figure 11. Typical x-ray diffractometer trace of Pt_2FeCu.

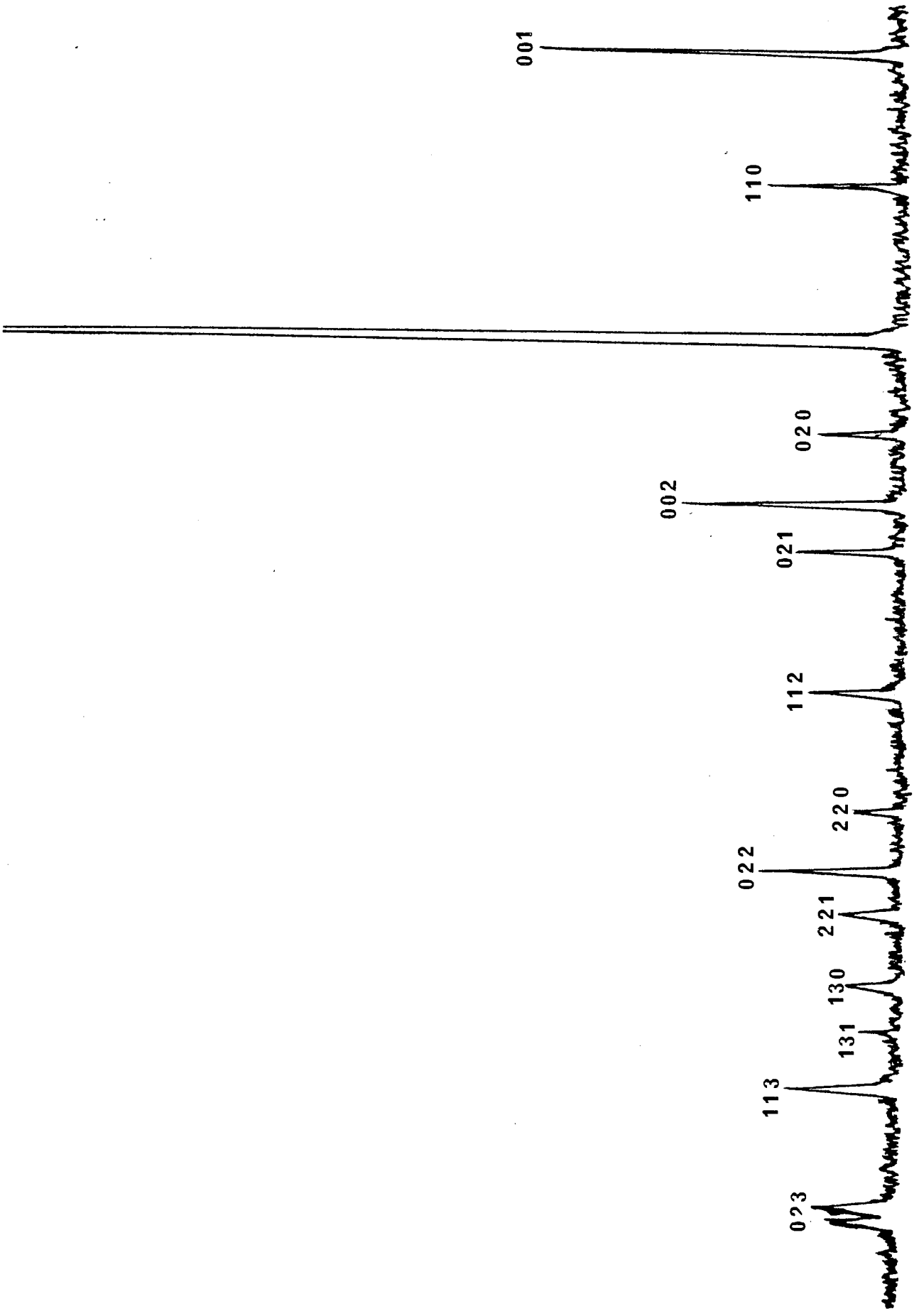

3.I.3 Calculated and measured Densities

The following equation (62) was used to calculate the density of the Pt_2FeCu;

$$\rho = \frac{\text{Weight}}{(V_{Pt} + V_{Fe} + V_{Cu})} \quad \ldots\ldots\ldots(1)$$

By substituting the relevant values , $\rho = 15740\ Kg/m^3$ can be obtained.

The density value is related to the number of the atoms in unit cell according to;

$$\rho = \frac{n \cdot \bar{A}}{V \cdot N} \quad \ldots\ldots\ldots(2)$$

where:

ρ = Density , n = number of atoms in unit cell, V = volume of the cell, N = Avogodro's number and $\bar{A}$ = Mean atomic weight of the atoms.

The mean atomic weight of the atoms is calculated from the atomic percentages, P_1, P_2 and P_3 of the elements comprising the compound and the atomic weights, A_1, A_2 and A_3 with the formula;

$$\bar{A} = \frac{P_1 A_1}{100} + \frac{P_2 A_2}{100} + \frac{P_3 A_3}{100} \quad \ldots\ldots\ldots(3)$$

When all the known values are substituted in equation (2) the $n = 4$ is obtained which shows that there are four atoms per unit cell.

The value of $14930\ Kg/m^3$ was also obtained for the measured density.

3.I.4 Electron Density maps (E.D.M)

The purpose of plotting the E.D.M was to identify the positions of the Pt, Fe and Cu atoms in Pt_2FeCu. Two important factors had to be taken into consideration; firstly the anomalous scattering factor[62] and secondly, that an insufficient number of reflections were available on the x-ray diffraction patterns to construct accurate three-dimensional maps.

To overcome these difficulties a decision was made to use Co-radiation and project the whole content of the structure cell onto the (hk0) plane.

During the first stage, a model was adopted which allocated the fractional coordinates (000), $(\frac{1}{2}\frac{1}{2}0)$ to platinum, $(\frac{1}{2}0\frac{1}{2})$ to copper and finally $(0\frac{1}{2}\frac{1}{2})$ to iron atoms.

The structure factors of the fundamental and superlattice reflections were calculated as;

$$F_f = 2f_{Pt} + (f_{Cu} + f_{Fe}) \text{ .... Fundamental lines ... (4)}$$

$$F_s = 2f_{Pt} - (f_{Cu} + f_{Fe}) \text{ ...Superlattice lines .... (5)}$$

When the thermal vibrations of the contributing atoms are taken into consideration, the true form of the atomic scattering factors would be:

$$f = f_o e^{-M} \quad \text{..... (6)}$$

where the values of f_o are tabulated[62] and;

$$M = B \left(\frac{\sin\theta}{\lambda}\right)^2 \quad \text{..... (7)}$$

Where;

$$B = \frac{6.h^2.T}{M.K.\Theta^2}\left[\Phi(x) + \frac{x}{4}\right] \qquad \ldots\ldots\ldots(8)$$

Where in equation (8);

h = Planck's constant ,T = absolute temperature, M= mass of the vibrating atom, K = Boltzman's constant, Θ = Debye characteristic temperature of the substance (tubulated) and $x = \frac{\Theta}{T}$ or $\Phi(x) = \Phi\left(\frac{\Theta}{T}\right)$ where $\Phi(x)$ is also tabulated[62].

The quantity B can be calculated when the appropriate values are substituted in equation (8)

$$B = \frac{1.15\times10^4\times T}{A\times\Theta^2}\left[\Phi(x) + \frac{x}{4}\right] \qquad \ldots\ldots\ldots(9)$$

By substituting equations (9),(8) and (7) in equation (6) we have;

$$f = f_o \exp - \left\{ \frac{1.15\times10^4\times T}{A\times\Theta^2} \right\} \left[\Phi(x) + \frac{x}{4}\right]\left(\frac{\sin\theta}{\lambda}\right)^2 \qquad \ldots\ldots(10)$$

If the room temperature is taken as $t=19^{\circ}C$,it is possible to calculate individual values for M ,for the contributing atoms;e.g.,for platinum,

$$M = \left(\frac{1.15\times10^4\times292}{195.09\times230^2}\right)\left[\Phi\left(\frac{230}{292}\right) + \frac{230}{988}\right]\left(\frac{\sin\theta}{\lambda}\right)^2 \qquad \ldots\ldots(11)$$

so finally;

$$M_{Pt} = 0.3302\left(\frac{\sin\theta}{\lambda}\right)^2 \qquad \ldots\ldots\ldots\ldots\ldots(12)$$

$$M_{Fe} = 0.3428\left(\frac{\sin\theta}{\lambda}\right)^2 \qquad \ldots\ldots\ldots\ldots\ldots(13)$$

$$M_{Cu} = 0.5268\left(\frac{\sin\theta}{\lambda}\right)^2 \qquad \ldots\ldots\ldots\ldots\ldots(14)$$

Therefore the modified structure factors would be;

$$F_s = 2 f_{oPt} \exp\left[0.3302\left(\frac{\sin\theta}{\lambda}\right)^2\right] - \left\{ f_{oFe} \exp\left[0.3428\left(\frac{\sin\theta}{\lambda}\right)^2\right] + f_{oCu} \exp\left[0.5268\left(\frac{\sin\theta}{\lambda}\right)^2\right]\right\} \quad \text{----------(15)}$$

$$F_f = 2 f_{oPt} \exp\left[0.3302\left(\frac{\sin\theta}{\lambda}\right)^2\right] + \left\{ f_{oFe} \exp\left[0.3428\left(\frac{\sin\theta}{\lambda}\right)^2\right] + f_{oCu} \exp\left[0.5268\left(\frac{\sin\theta}{\lambda}\right)^2\right]\right\} \quad \text{----------(16)}$$

The three dimensional E.D.M. can be plotted by the application of the following equations(63)(64);

$$\rho_{\{X,Y,Z\}} = \frac{1}{V} \sum\sum\sum F_{\{hkl\}} \exp 2\Pi i \{hx+ky+lz\} \quad \text{....(17)}$$

When the crystal lattice is centro-symmetrical, in expanding the exponential function the sine terms vanish and if the (hk0) projection is desired, equation (17) will reduce to;

$$\rho_{\{X,Y\}} = \frac{1}{A} \sum\sum F_{\{hk0\}} \cos 2\Pi \{hx+ky\} \quad \text{.....(18)}$$

In equation (18) A is the area of the plane of the projection and F_{hk0} are the structure factors.

The second attempt to plot the E.D.M. was based on the measured values of the structure factors. The intensity of any reflection when measured by the x-ray diffractometer is given by (63)(64).

$$I = |F|^2 \rho \left(\frac{1 + \cos^2 2\theta}{\sin^2\theta \cos\theta}\right) e^{-2M} \quad \text{.....(19)}$$

From the equation (19), the structure factor can be calculated as;

$$F = \sqrt{\frac{I}{\rho \left\{ \frac{1 + \cos^2 2\theta}{\sin^2\theta \cos^2\theta} \right\} e^{-2M}}} \qquad \ldots\ldots\ldots\ldots (20)$$

In equation (20) I= intensity of the diffraction peak, ρ = multiplicity factor, $\left(\frac{1+\cos^2 2\theta}{\sin^2\theta \cos^2\theta}\right)$ = Lorentz-polarization factor, and M= temperature factor given by equation (12), (13) and(14).

The measured values of the integrated intensities were inserted in equation (20) and subsequent results were finally used in equation (20) to plot the E.D.M. from the measured values of the intensities.

The calculated and measured electron-density maps proved to be identical and are shown in figure 12.

The four corners sites (00) and the centre of the projection plane $(\frac{1}{2}\frac{1}{2})$ can easily be identified as occupied by the platinum atoms, but it was not possible to discriminate between Fe and Cu atoms as occupants of the $(\frac{1}{2}0)$ or $(0\frac{1}{2})$ positions.

When these two-dimensional sites are considered in three dimensions, the following atomic sites of the structure cell can be detected (000) and $(\frac{1}{2}\frac{1}{2}0)$ to platinum and $(\frac{1}{2}0\frac{1}{2})$ or $(0\frac{1}{2}\frac{1}{2})$ sites belong to either Iron or Copper atoms. An immediate interpretation was that copper and iron are randomly distributed with the platinum atoms at the fixed atomic sites,and so the ordering transition is due to the platinum tendency to have ordered arrangements with Copper and Iron.

In the present research no attempts were made to obtain any structural information, regarding the disordered phase of the Pt_2FeCu, but based on, a)- Cabri's et al [55] report that the copper atoms substitute for iron atoms in the PtFe binary compound and b)- the latter has a disordered f.c.c. structure, therefore it seems quite safe to assume a similar disordered structure for the Pt_2FeCu compound where the resultant face-centred tetragonal is due to ordering in this system. Although the system is a ternary compound its behavior is nevertheless expected to be similar to the AuCu[62], PtCo[65] and PtFe[45] binary metallic systems.

X-ray diffraction has been used extensively to investigate the ordering mechanism in the aforementioned systems. In the Pt_2FeCu case, as the tetragonal lines appeared to be in their final positions and no disordered material was found, it is impossible to draw any conclusion regarding the nature of the mechanism based on the x-ray analysis.

Fig 12- Electron Density Map of Pt_2FeCu

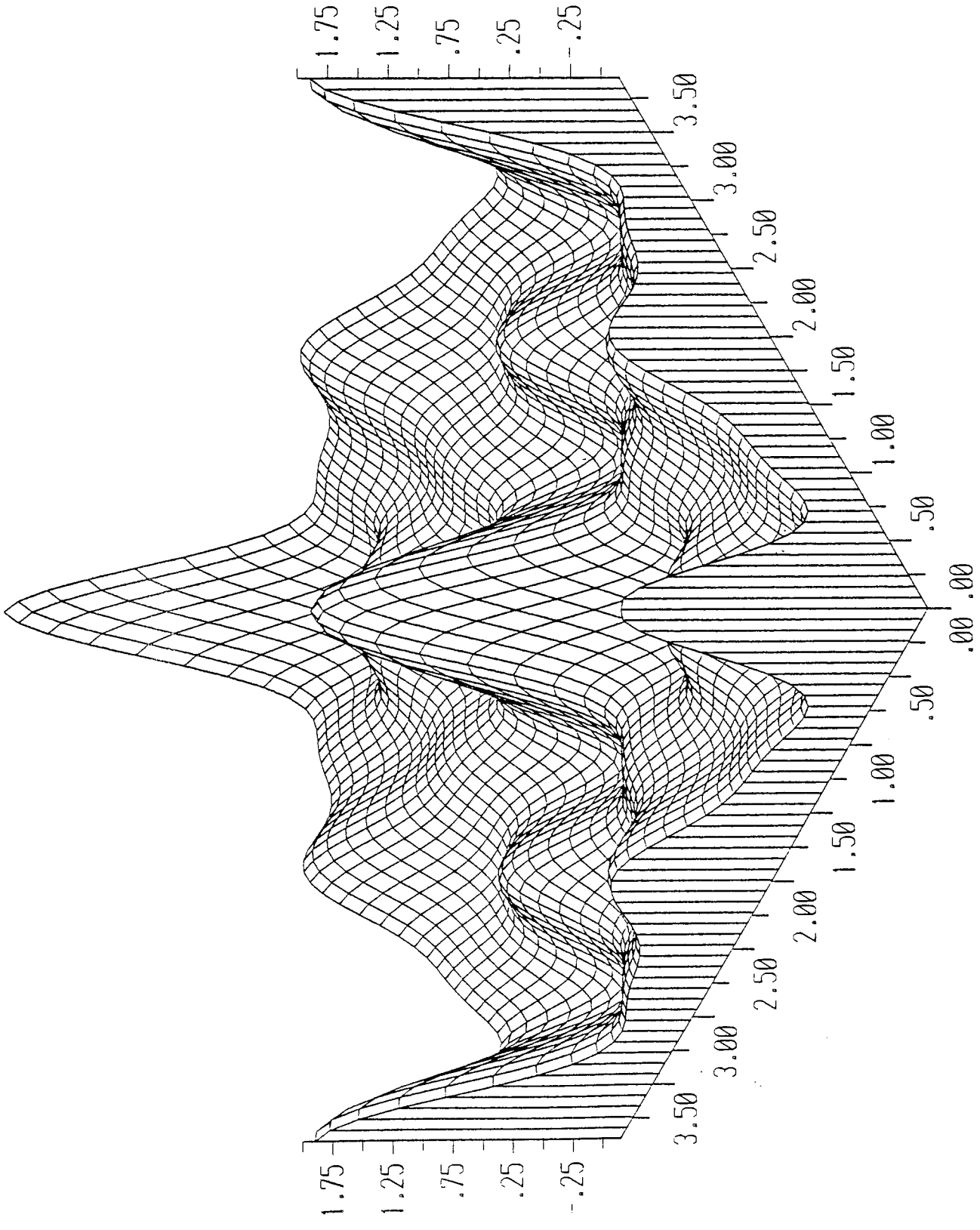

3.I.5 Measurements of the Long-Range order(L.R.O) parameter

X-ray diffraction techniques have been used to measure the variations of the L.R.O parameter (S-parameter) with time and temperature.

The degree of order can be determined from the following expression proposed by Keating and Warren(66)

$$S^2 = \left[\frac{P_s}{P_f}\right] \frac{\left[\rho F \exp -2M \left(1+\cos 2\theta\right)/\sin^2\theta \cos\theta\right]_f}{\left[\rho F \exp -2M \left(1+\cos 2\theta\right)/\sin^2\theta \cos\theta\right]_s} \quad \ldots\ldots(21)$$

where $\frac{P_s}{P_f}$ is the ratio of the intensity of the superlattice reflection to that of a fundamental reflection, ρ is the multiplicity, F is the structure factor, M is the Debye temperature factor, λ is the wavelength of the x-rays and θ is the Bragg angle of reflection.

By this technique S was found to be 0.41 for a sample subjected to three months solution-treatment at 1200°C (above T_c) and rapidly quenched. When measuring the S values a whole surface cross-section of the specimen was exposed to the incoming x-rays and the (110) superlattice and (220) fundamental reflections were used.

Such a high value of S, not only indicates that the ordering has occurred upon quenching,but also the material possesses high ordered configuration. In other words 41% of the ordering transformation has taken place which clearly would indicate the high rate of ordering and growth of the ordering centres compared with the S=0 which is expected for a similarly treated material.

When such a sample was viewed under a optical microscope very interesting microstructural alternations were observed. The central regions of the material had the most complex twin characteristics and the outside regions (near the edges) showed less complex twinned morphologies.

It was thought that such microstructural variations which usually accompany the ordering reactions[58,68,69,70,71] should be directly related to the local-variation of the S-parameter and so it was decided to measure the S-values locally, but as the grains were not big enough for the individual measurements the following procedure was adopted.

The cross-section of the sample for these measurements had a circular shape, figure 13.

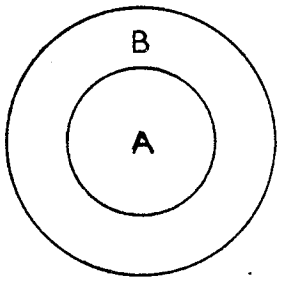

Figure 13- The cross section of the Pt_2FeCu specimen

The S-values were measured for the central region (hereafter area "A" in figure 13) while the outer circle was being masked and vice versa for the "B" and the following values were obtained.

Area A	S= 0.63
Area B	S= 0.29

From the two measured values of the S, it was quite clear that the area A had a much higher ordered arrangement than

area B and the observed complex twinned microstructures at these regions were directly related to such high value of S.

To study the variation of S with time and temperature, similar measurements were made on the samples which were used to study the recrystallization mechanism.

Whole cross sections of the sample were exposed to the x-rays. In other words, the S-values were actually the averaged L.R.O. parameters.

Figure 14 shows the variation of the S-parameters with time and temperature. The process of ordering progresses very rapidly at the start and gradually slows down on prolonged order- annealing. In other words, the rate of ordering is directly proportional to the temperature and time which equilibrium state is reached.

Figure 14. Variation of Long-range order-parameter with time and temperature.

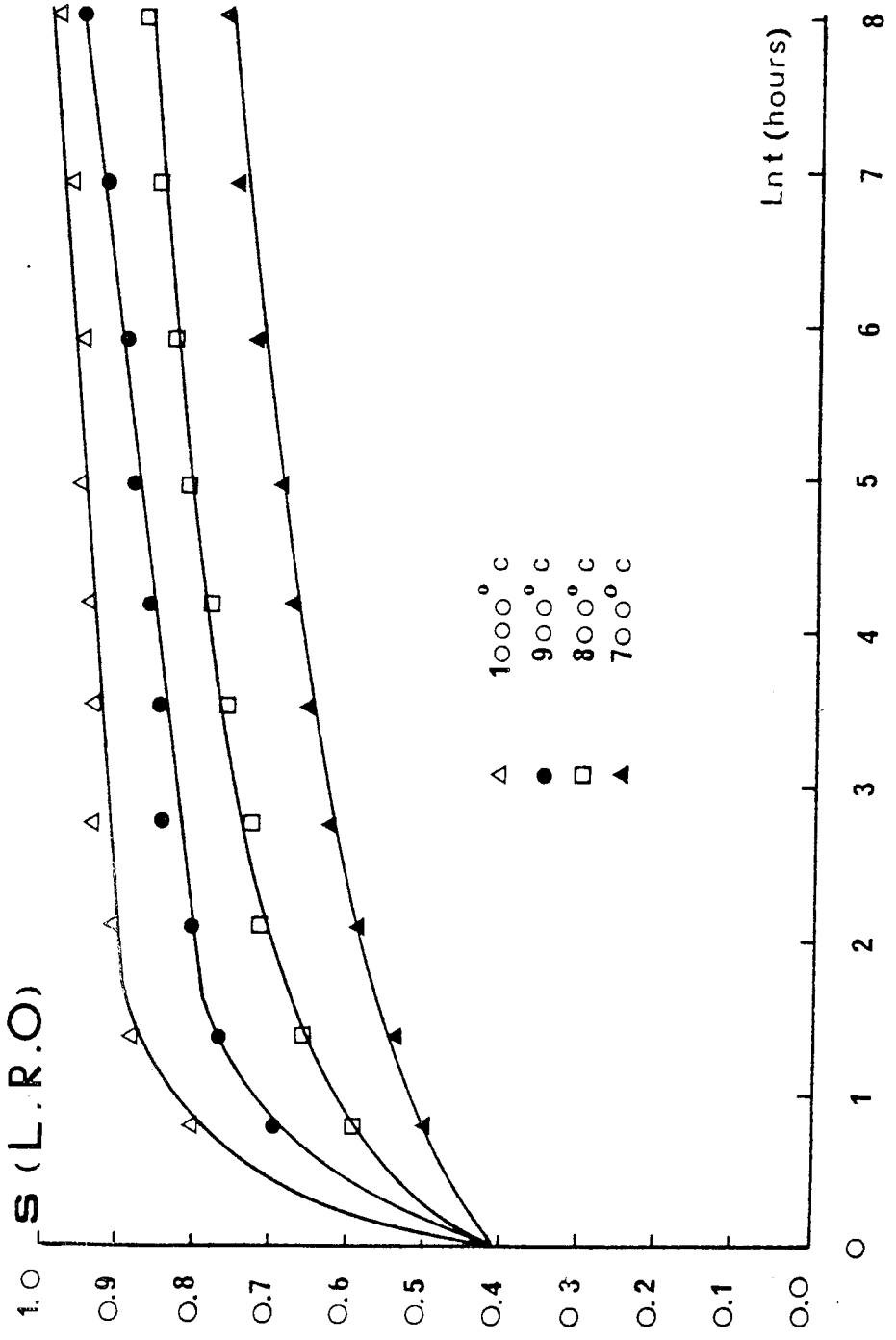

3.I.6 Microstructural features of Pt_2FeCu

Depending on the heat-treatments used, different microstructures were observed when samples were viewed with optical/electron microscopy.

The as-cast sample which was the result of the melting and casting without any heat-treatment, showed a typical cored-dendritic structure, with the Pt-rich cored dendrites set in a mixture of iron and copper-rich interdendritic phases (Figure 15). When these cored structures were magnified several times, very fine dark and bright bands were also observed, Figure 16. These bands were irregularly distributed and were more frequent at the central region of the specimen.

To eliminate the cored structure and homogenize the samples which had ~15-20% compositional variations, they were subjected to the following solution-treatments;

1)- At 1200°C for three months.

2)- At 1400°C for 10 days.

At the end of each treatment, the samples were rapidly quenched in iced water and their homogenuity was confirmed by means of the E.P.M.A, (~0.5% compositional variations).

Figures 17 and 18 are the secondary electron images of the sample, treated at 1200°C for three months. Each grain seems to be completely divided into narrow, parallel bands which in turn are also divided by much finer parallel bands. The width of these bands at this condition varied between 8-11 μm.

Figures 19 and 20 are the optical micrographs of the sample annealed at 1400°C for ten days, which show similar microstructures to that of figures 17 and 18 but the width of the bands varies between 26-14 μm in the latter case.

These micrographs, i.e., figures 17,18,19 and 20 are taken from the central parts of the specimen, when areas near the edges of these specimens are viewed,a less complex band microstructures are observed and this is examplified in figure 21.

Similar band-structures have also been observed in such metallic systems as AuCu[69][71][45] and PtFe[45] where ordering reactions produce a crystal lattice with the lower symmetry than the disordered phase and are termed stress-relief twinning. Therefore, based on our x-ray diffractions and D.T.A results, the conclusion can be drawn that these observed bands are actually twinned-bands in the system formed during the ordering transformation. More evidence of this is presented later.

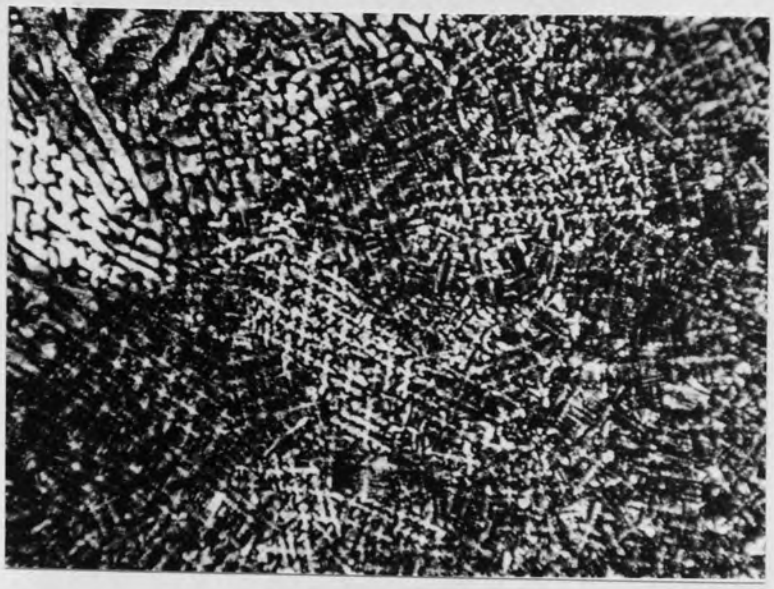

Fig 15- As-cast microstructure of the Pt_2FeCu.Etched. x180

Fig 16- Appearances of dark and bright bands in cored structure of the Pt_2FeCu. Etched. x300

Fig 17- Secondary Electron Image of the central region of the homogenized Pt_2FeCu, three months at 1200°C. Etched . x700

Fig 18- Higher Magnification of Fig.17 x4200

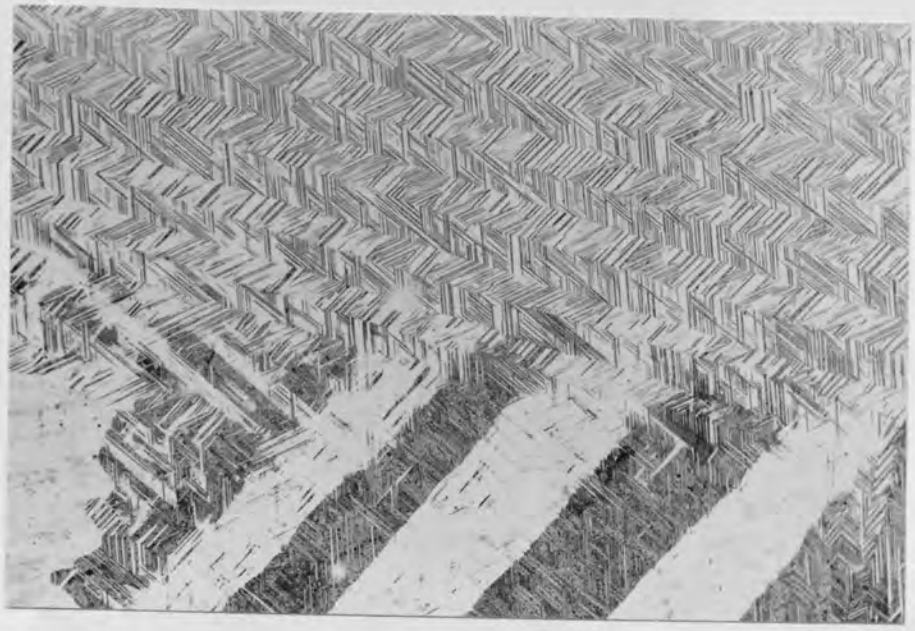

Fig 19- Optical micrograph of the homogenized specimen of Pt_2FeCu, 10 days at 1400°C and quenched. Etched. x170.

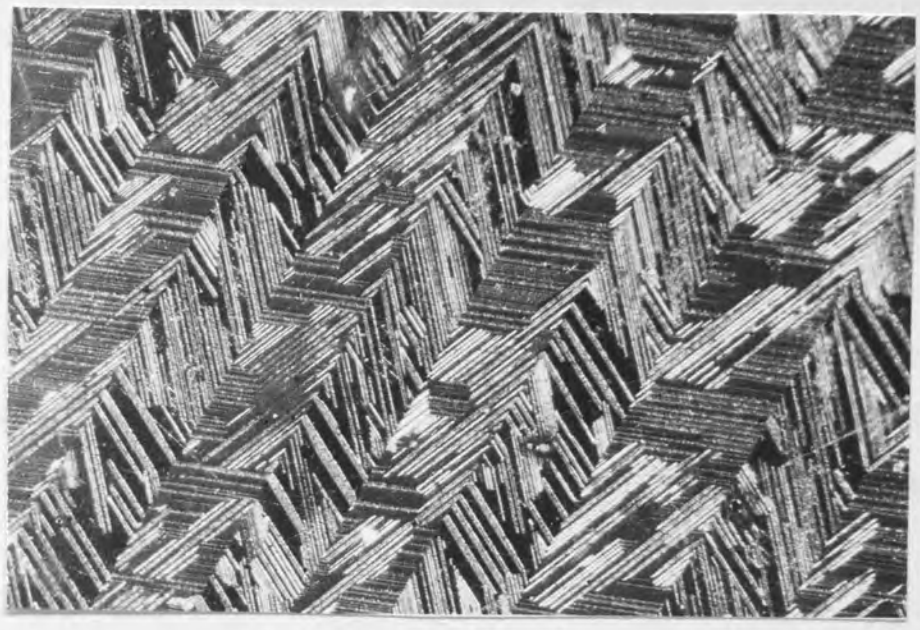

Fig 20- Polarized light micrograph of the central parts of Fig.19. Etched. x600.

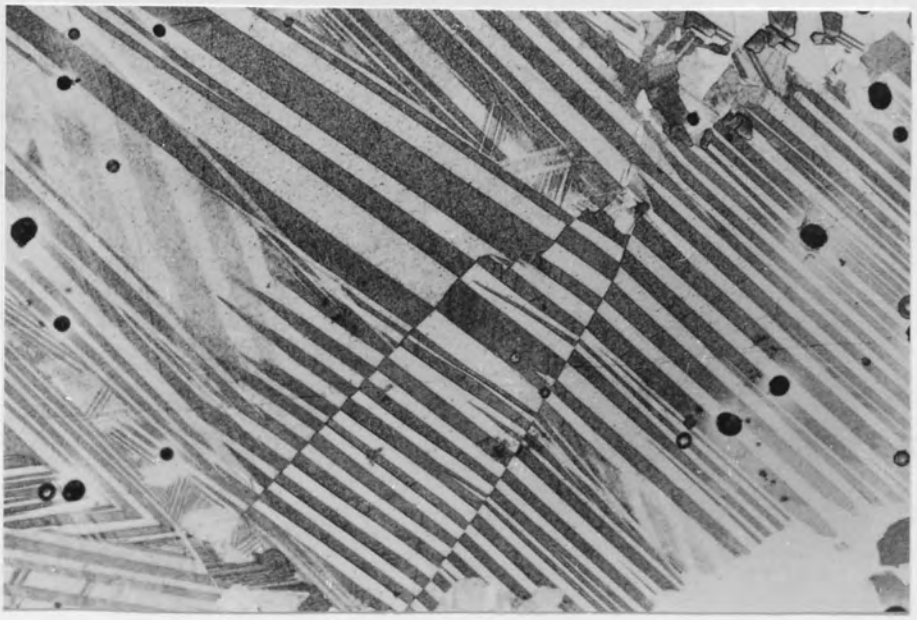

Fig 21- Ordered domain microstructures of the Pt_2FeCu near the edge of the specimen. Optical image. Etched x110

3.I.6.1 Transmission Electron Microscopy (T.E.M.)

To fully investigate the nature of the twin-bands in different regions of the sample, thin foils which were prepared either by ion- bombardment or electro-polishing techniques,were examined with a JEOL 100 B T.E.M. operating at 100 KeV.

Initial stages of the ordering transformation could not be investigated due to its high rate of the reaction, but it was thought that the variations of the S-parameter (S = 0.63 and S = 0.29 for the central and outside region of the sample quenched after three months at 1200°C) could yield some information regarding the ordering mechanism, especially the areas with S = 0.29.

T.E.M examinations were also carried out on the samples with different heat-treatments which will be mentioned in the appropriate sections. First the results of the T.E.M examinations of the as-quenched state will be presented;

a)- As- quenched state,

a.1) From S = 0.29 region

Thin foils of as- quenched material were prepared from the sample which was quenched from 1200°C (above T_c) after a three month homogenization treatment.

Figure 22 is a montage of bright- field micrographs from near the free surface where S = 0.29. In this picture two

big bands with varying width and another smaller one which make an angle of 40-50 degrees with them can be seen. Two ordered domains with different sizes have already grown with the "twin- band" feature inside them on either side of one of the bands. At this stage it appears that the growth of these ordered domains towards the disordered matrix have been suppressed by quenching. Another interesting feature is the presence of another "twinned-band" inside the bigger bands in the vicinity of the ordered domains. These twin-features are perpendicular to each other and make an angle of 60° to the growing ordered domains.

Further evidence was obtained when one of the larger domains was examined at higher magnification.

Figure 23 is a bright-field micrograph of the interior region of one of the ordered domains of figure 22.The foil's normal is $\langle 110 \rangle$ zone and figure 24 is the high-resolution dark-field image obtained when a $\{110\}$ super-lattice reflection was used showing the presence of the very fine ordered particles or plates of approximately 570-780 A° in size. In comparison with B.F image,it appears that the internally twinned ordered domains are actually comprised of very fine ordered particles or plate in twin-orientation relationships. Although not conclusive, the presence of these particles could confirm the nucleation and growth mechanism of the ordering reaction to a certain extent.

Fig 22- Montage of Bright-field micrographs of Pt_2FeCu with S = 0.29 67K

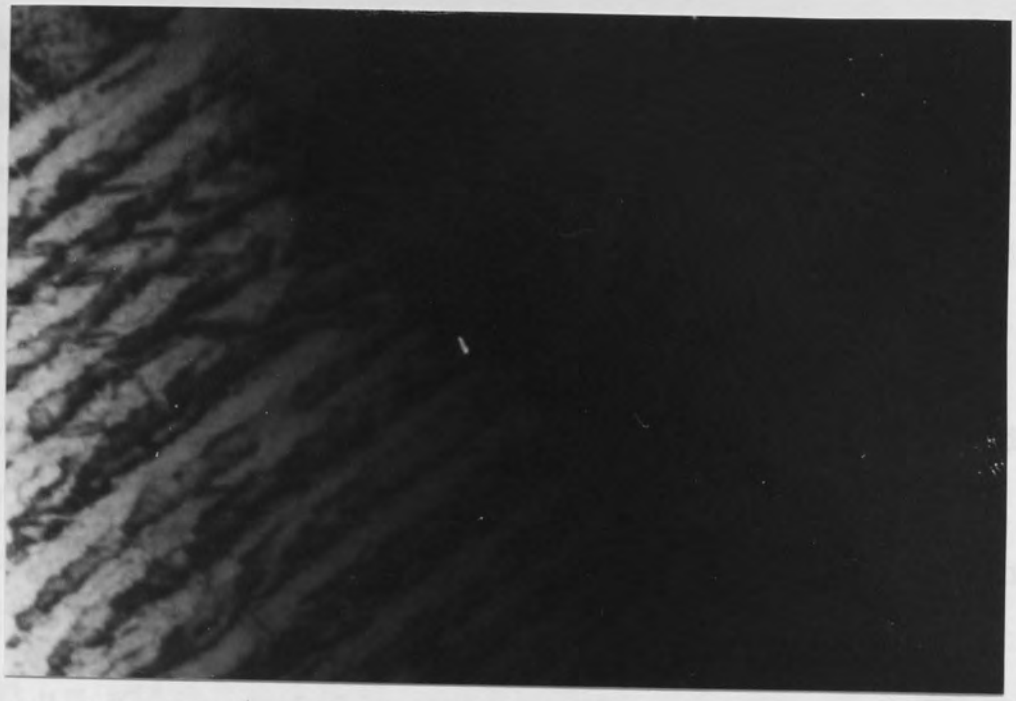

Fig 23- Bright-field micrograph of the interior area of the ordered domain in "A" of Fig. 22. x200K

Fig 24- Dark-field image of Fig. 23 .Operating reflection {110}. x200K.

Similar behaviour was also observed where two of such ordered domains were formed in the neighbourhood of a larger band as is shown in the bright-field micrograph of figure 25 . It is also interesting to note their zig-zag interfaces.

Further evidence of the presence of the nucleation and growth were observed and this case is shown in figure 26 . In this micrograph three different ordered domains can be observed; a large domain of 2.5 μm width, internally twinned (0.03 μm width) and another smaller domains of different sizes where they are also internally twinned with totally different orientation to that of the larger domain.

It is difficult to draw a firm conclusion as to whether the larger domain was in the process of re-absorbing the smaller domain (similar to the coelescence mechanism in normal precipitation mechanism) to decrease the surface energies or any other mechanism, but nevertheless these different domains of varying size can be thought to have been initiated via a nucleation and growth mechanism as the result of ordering transformations.

It appears that the interface of the larger domain with the smaller domain show some feature similar to interfacial dislocations. As there is no practical knowledge of the dislocation configurations in this system, no further comment is possible.

a.2) From S = 0.63 region

The thin foils of these regions showed the most interesting and complex microstructures.

Figures 27 and 28 are two bright-field images where orthogonal domains with different sizes can be observed . In these cases where the domains make an angle of 90^{o} to each other no sign of coelescences can be observed.

Based on these micrographs, it seems that the ordered domains with different orientations have grown from different ordering centres and come into contact with 90^{o} angle. It is worth noticing the absence of features which are thought to be interface dislocations in these micrographs.

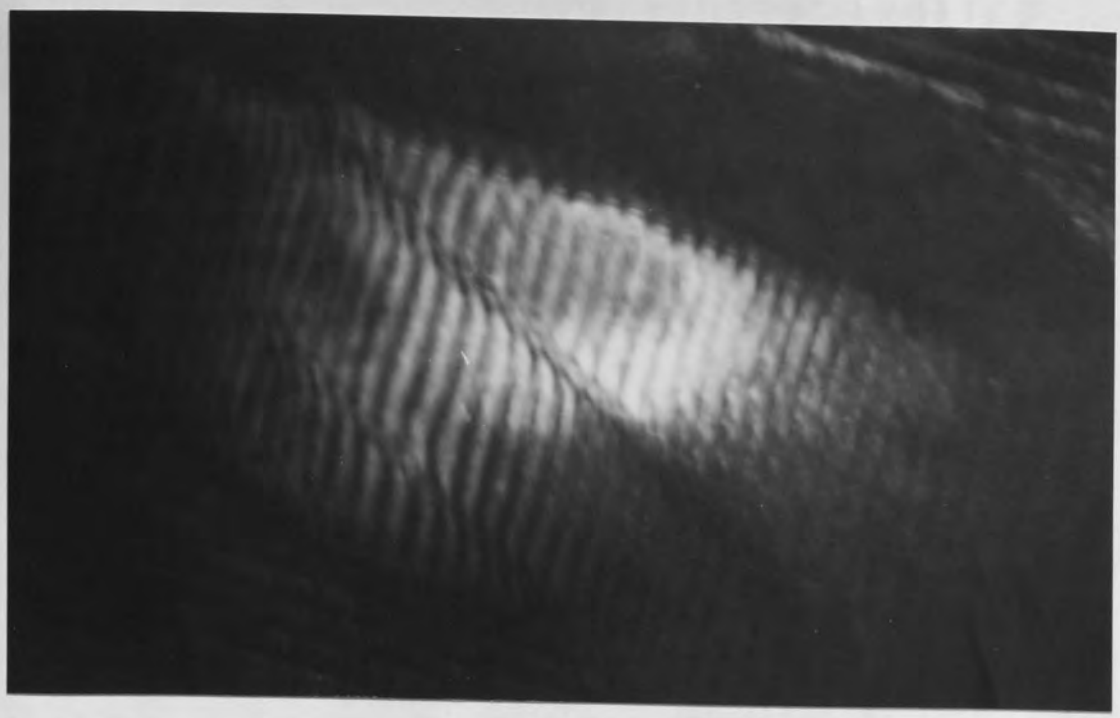

Fig 25- Bright-field micrograph of the two growing ordered domains in adjacent to a twinned band x80K

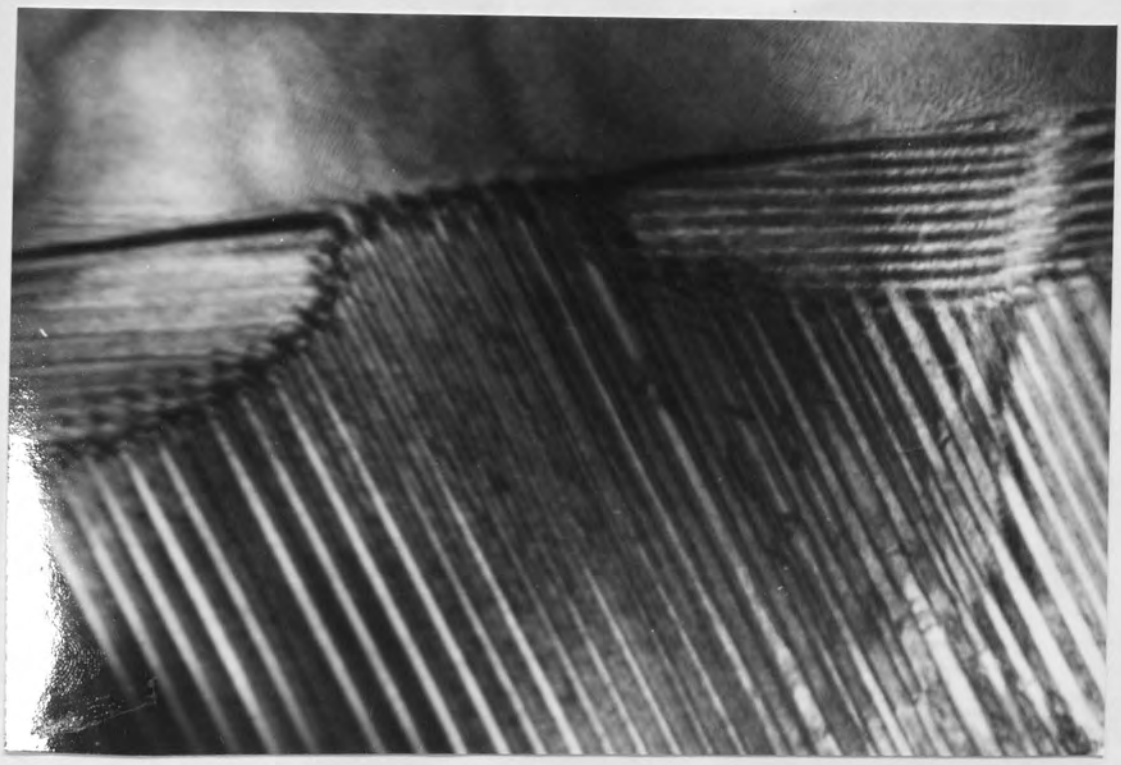

Fig 26- Bright-field micrograph of the three different sizes of internally twinned ordered domains x60K

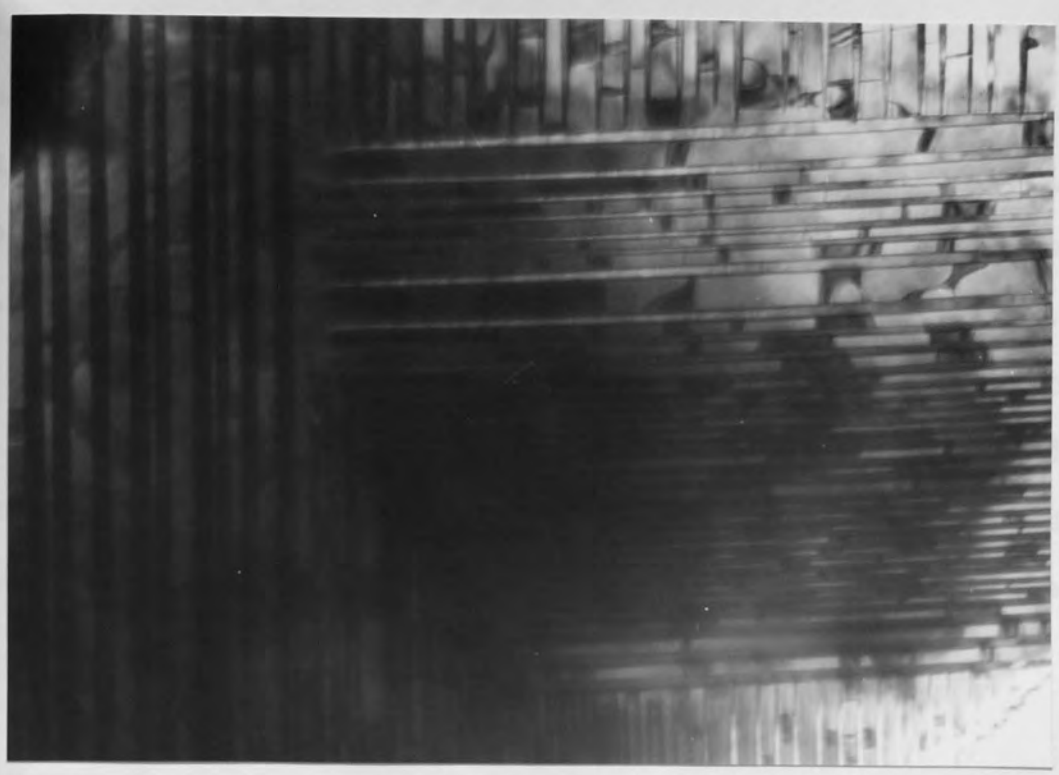

Fig 27- Bright-field micrograph showing Orthogonal ordered domains. x60K

Fig 28- Bright-field image of the Orthogonal order domains x34K

Figure 29 is another typical bright-field micrograph of an area of the sample with S = 0.63 produced by electro-polishing technique. Four big twin bands ($\sim$0.7 μm width), internally twinned ($\sim$0.05 μm) and three smaller bands ($\sim$0.3μm width), which are also internally twinned (0.03μm) can be observed. The selected area diffraction pattern of the above micrograph is shown in figure 31 with its indexing. Trace analysis of the traces, A,B,C, and interface plane yielded the following orientation relationships (figure 32).

1) Trace A (110) plane
2) Trace B (101) plane
3) Trace C (011) plane
4) Interface plane (101) plane

Furthermore, the (101) and (011) planes are equivalent in the tetragonal structure cell, thus the true relationships are:

Trace A (110)

Traces B,C,I (101)

Similar relationships have been obtained in systems such as AuCu [71], PtCo [70] and PtFe [45] where $\{110\}$ planes are twin planes. Therefore, according to the trace analysis, the $\{110\}\langle 110\rangle$ is the twinning mode in the Pt_2FeCu. Figure 30 clearly shows the twinning arrangements where a dark-field image of a $\{110\}$ type superlattice is used. This micrograph reveals that the orientation of the twinned structures have alternated regularly, thus implying that the alternate bands have the same crystal structure and orientations. Taking the tetragonality of the structure into account, the C-axes are lying in a alternate manner in the plane of the foil.

The Bright bands in the dark-field image are actually tilted $\sim 27^{\circ}$ relative to the foil surface.

The whole twinning features observed are actually the ordered domains in the twin-relationships bounded by $\{110\}$ type planes and C-axis in each domain is set nearly at right angles to that of its adjacent domain. Therefore when a dark-field image, using a superlattice reflection is obtained, these ordered domains light up alternatively, depending on their C-axis orientations.

Fig 29-Bright-field micrograph of Pt_2FeCu, showing different sets of twinning. x80K

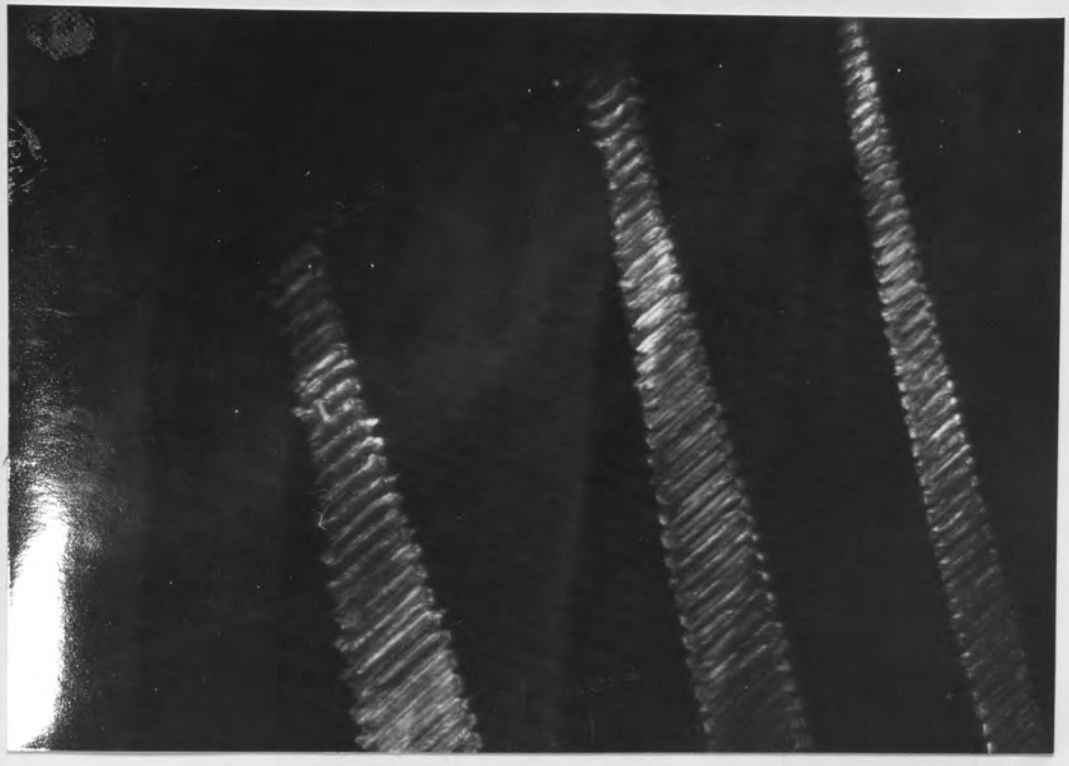

Fig 30- Superlattice dark-field image of Fig. 29, operating reflections $\{110\}$ x80K

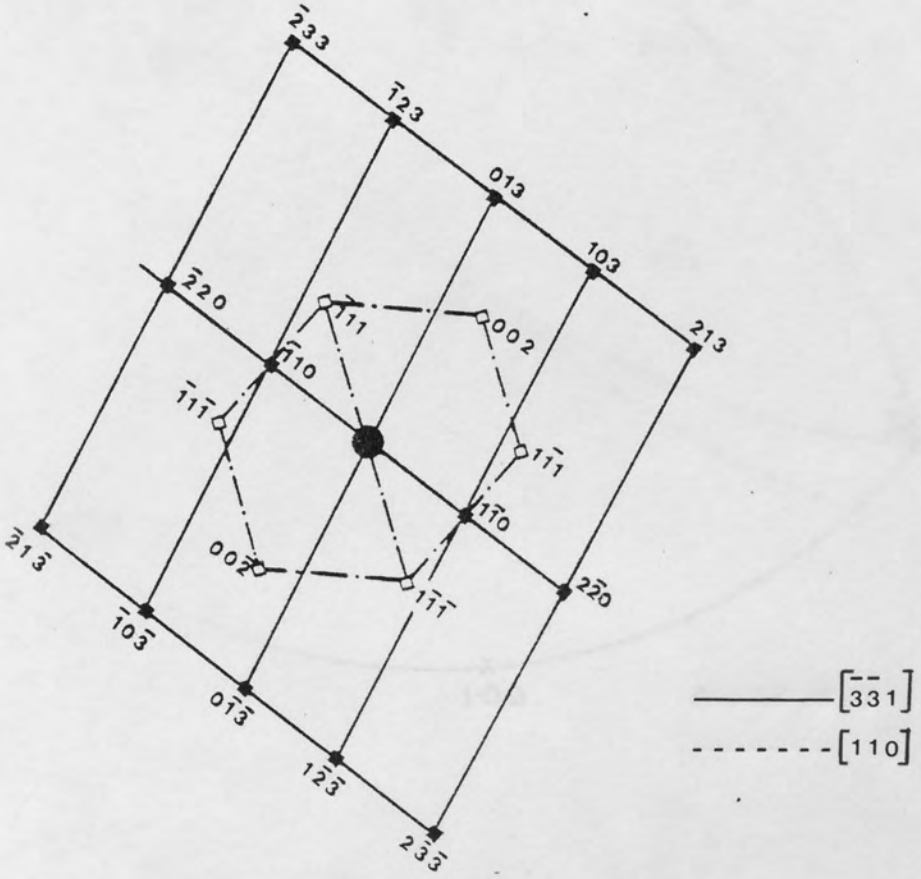

Fig 31- a) Selected area diffraction pattern of Fig. 29

b) Indexing

Figure 32- A sterographic projection, showing the twin orientation relationships of Figure.29.

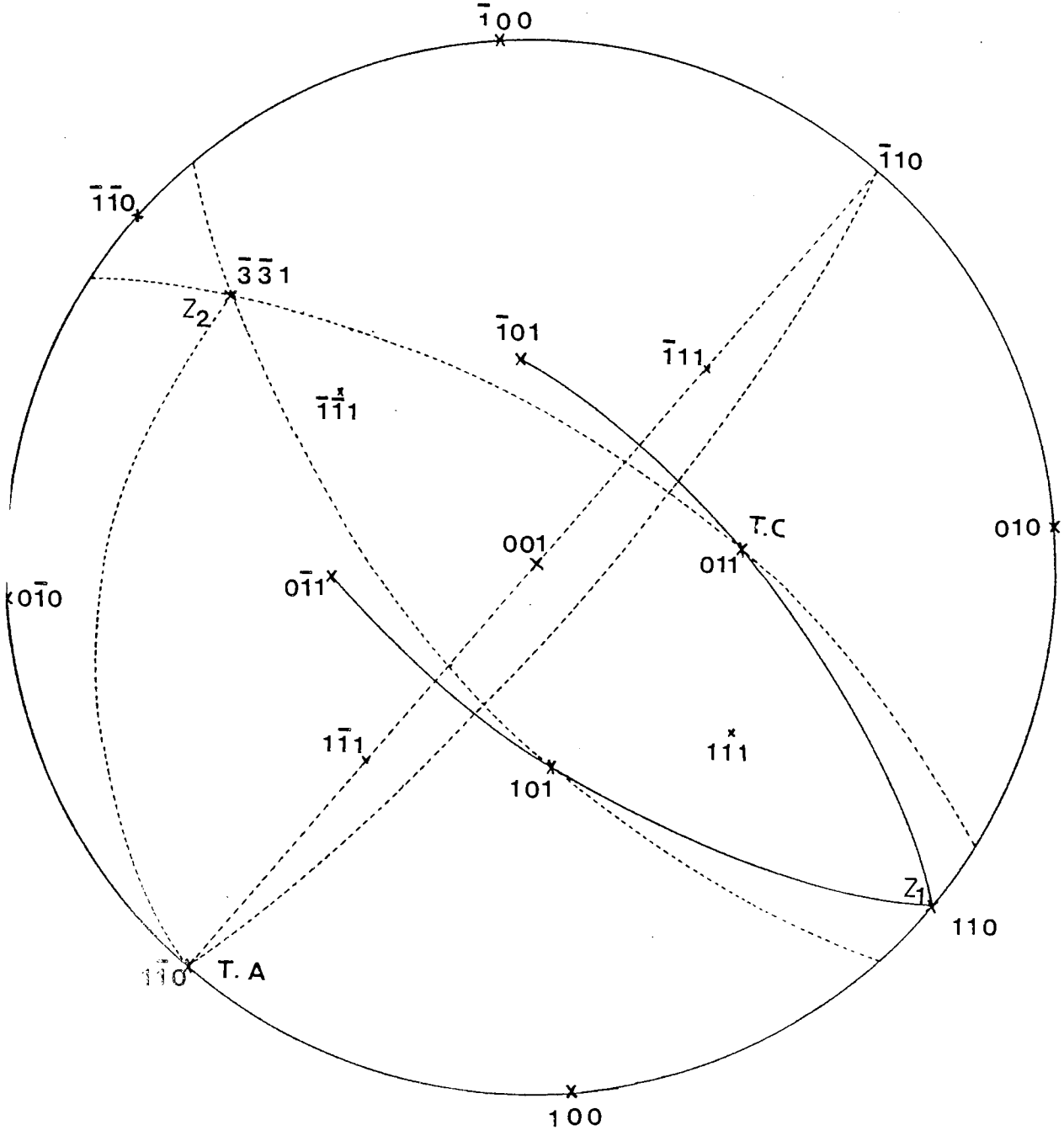

Further evidence for the arrangements of the ordered domains was obtained and is shown in figure 33. This is another typical bright field image and as it is observed the larger band is internally twinned. The S.A.D. P of the figure 34 and its indexing are shown in figure 35. The diffraction pattern is comprised of two $[010]$ and an $[001]$ zones.

Figure 34 shows the dark-field image of the figure using the (001) superlattice reflection. The bright bands in the dark-field image clearly show the ordered domains with alternate C-axis, lying in the plane of the foil and the dark-bands indicate the other ordered domain variants with their a-axis at nearly right angles to the neighbouring domains. Again, identical orientation relationships to the ones already obtained exist in this situation, figure 37.

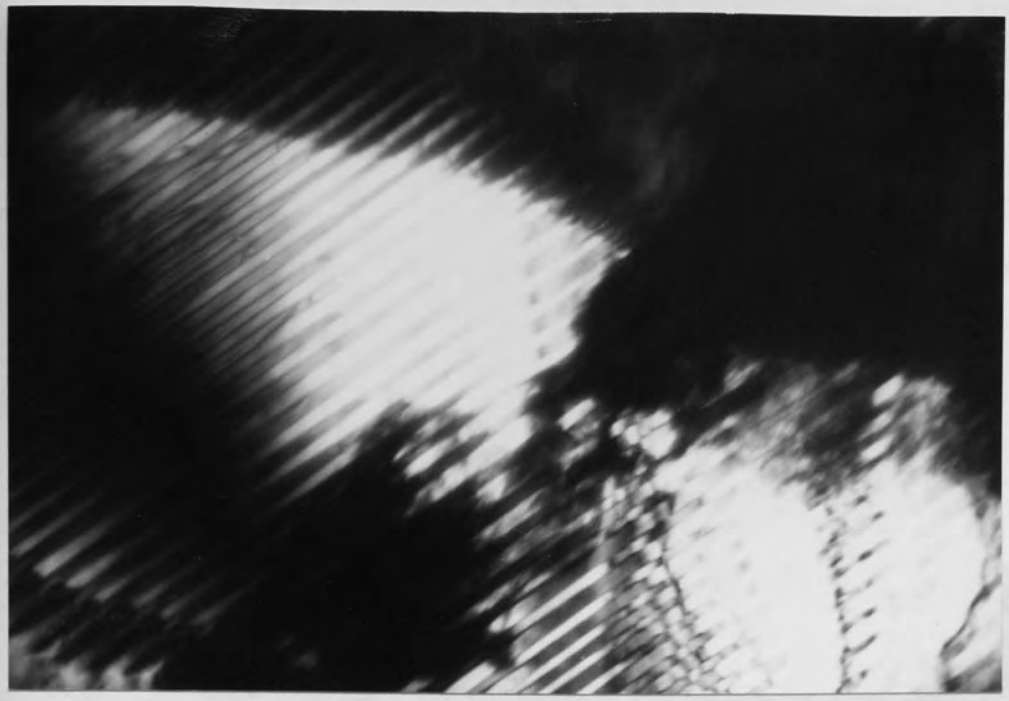

Fig 33- Bright-field image of internally twinned ordered domain x80K

Fig 34- Dark-field image of Fig.33 using $\{001\}$ superlattice reflection x80K

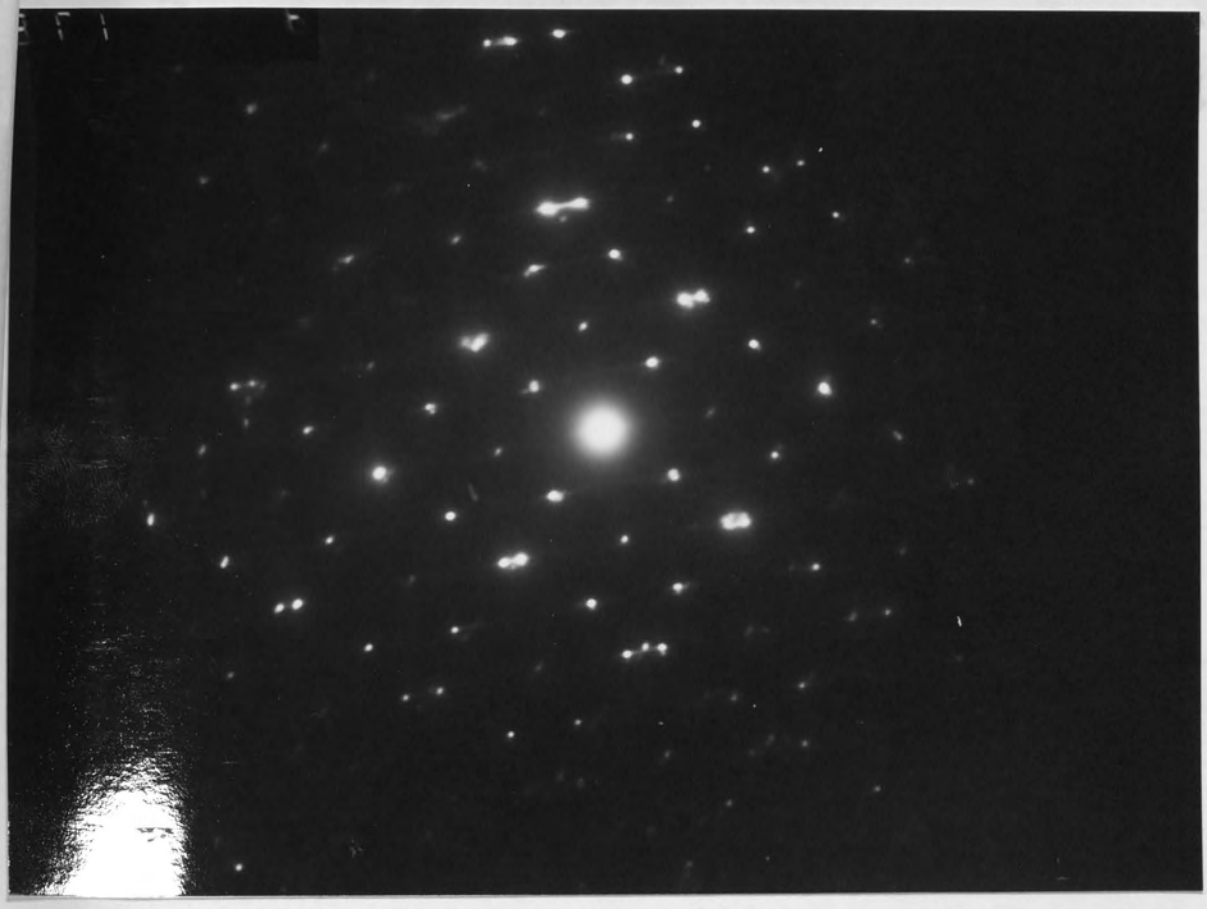

Fig 35- S.A.D.P. of figure 33

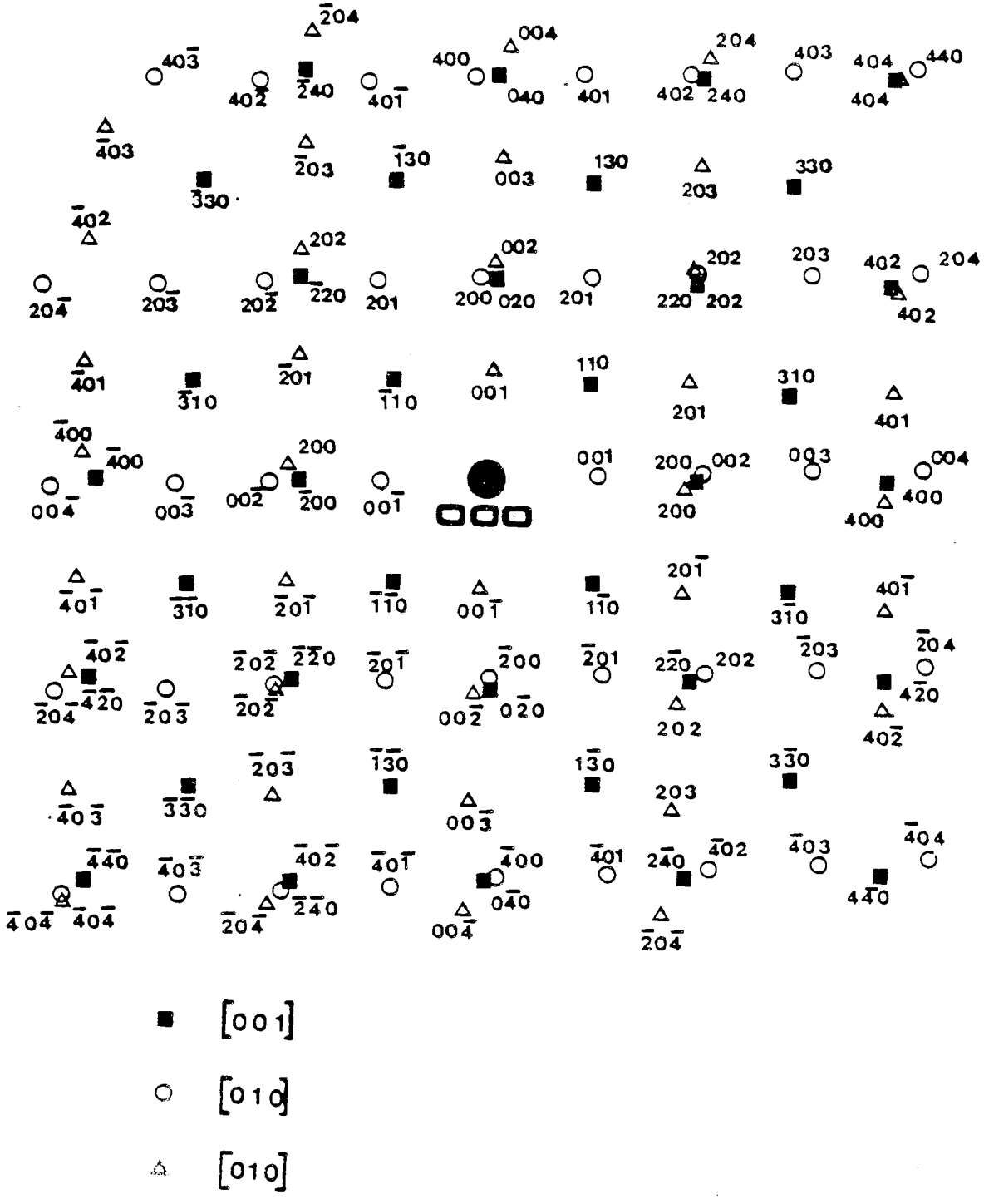

Fig 36 - Indexing of S.A.D.P. of Fig. 35

Figure 37-A stereographic projection showing the twin orientation relationships of Figure. 33.

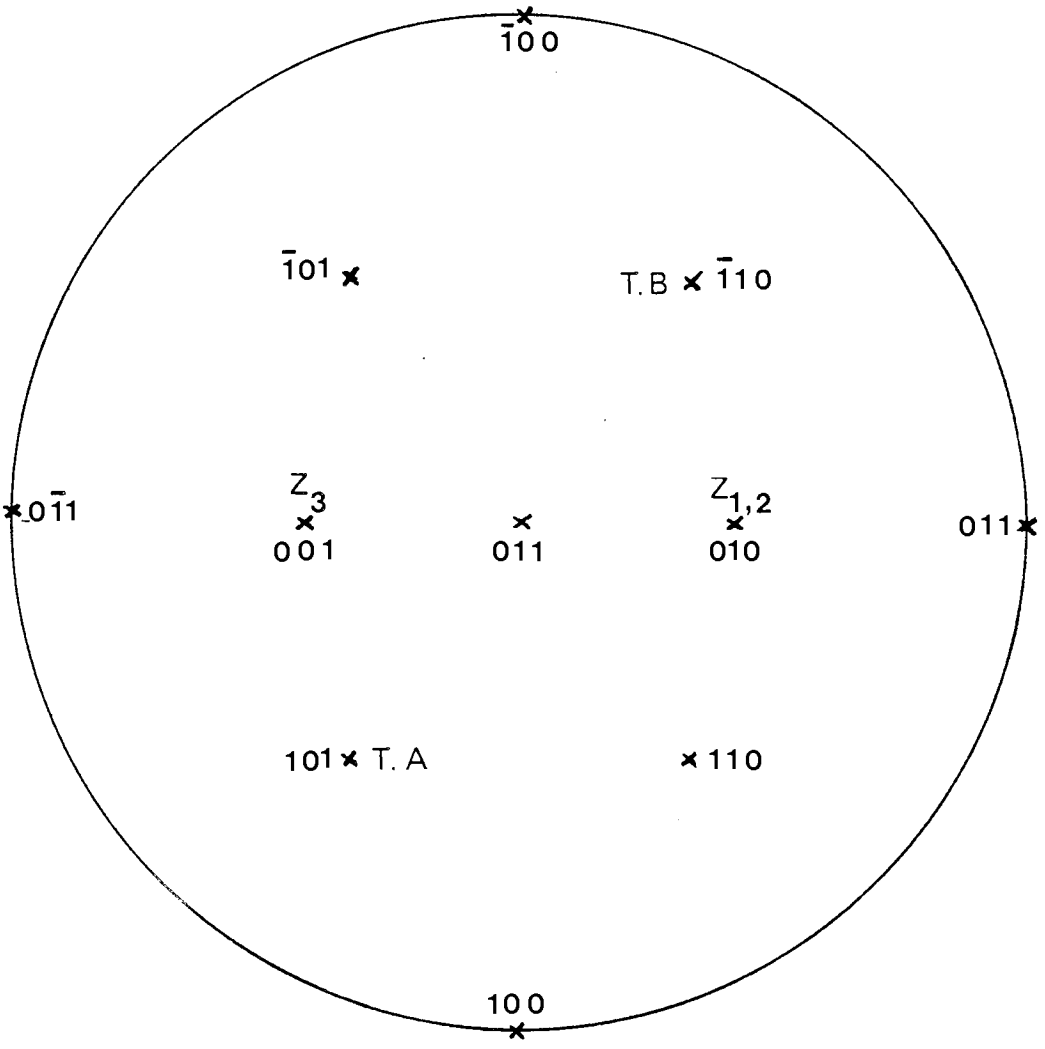

At first it appeared that the ordered domains had their C-axis at right angles to each other, but close examination of the S.A.D. P (figure 36) proved it otherwise and some angular disparities existed among them. In order to understand the true misorientation angles in the low index planes a stereographic projection of the tetragonal Pt_2FeCu cell was constructed.

Figure 38(a) is the (101) projection of the Pt_2FeCu in which the matrix is twinned on (101) plane(twin indices are shown by T_1). As it can be seen the following planes are parallel and there exist different degrees of misorientations among other planes .

a) $(1\bar{1}1)_M \parallel (111)_{T_1}$ $\quad$ $(111)_M \parallel (1\bar{1}1)_{T_1}$

b) $(010)_M \parallel (0\bar{1}0)_{T_1}$ $\quad$ $(0\bar{1}0)_M \parallel (010)_{T_1}$

If such a twinned structure is twinned on the other variant of the twin plane, i.e., $(\bar{1}01)$, figure 38(b) is obtained. The $(\bar{1}01)_M$ in figure 38(a) is brought to the centre of the projection through the rotation of $\backsim 85^\circ$ and the other indices (M, T_1) are also brought to their new positions. Twinning on $(\bar{1}01)_M$ plane produced further angular disparities, but similar planes to that of figure 38(a) are still parallel (T_2)

a) $(\bar{1}11)_M \parallel (\bar{1}\bar{1}1)_{T_2}$ $\quad$ $(\bar{1}\bar{1}1)_M \parallel (\bar{1}11)_{T_2}$

b) $(0\bar{1}0)_M \parallel (010)_{T_1}$ $\quad$ $(0\bar{1}0)_{T_1} \parallel (010)_{T_2}$

c) $(010)_M \parallel (0\bar{1}0)_{T_1}$ $\quad$ $(010)_{T_1} \parallel (0\bar{1}0)_{T_2}$

When the twinned structure in figure 38(a) was twinned once more on (011) plane, figure 38(c) was obtained. In this case further angular disparities developed, but still the following planes were parallel:

a) $(\bar{1}11)_M \parallel (\bar{1}11)_{T_1}$ $\quad$ $(1\bar{1}1)_{T_1} \parallel (111)_{T_2}$

If the crystal is twinned only on (110) plane no angular disparities are developed and such a case is shown in figure 38(d).

It appears that the twinning on (101),$(\bar{1}01)$,$(10\bar{1})$ and (011) planes would keep the combinations of $\{111\}_M$, $\{111\}_{T_1}$ and $\{111\}_{T_2}$ planes parallel and create different degrees of misorientation angles among other planes. The measured angular disparities based on figure 36 are in agreement with the values obtained from the sterographic projections.

Based on the aforementioned observations it is possible to illustrate the arrangements of these twinned-orientated ordered domains. This situation is shown in figure 39.

Figure 38 - Sterographic projections showing the angular disparities when structure is twinned on

a) (101)

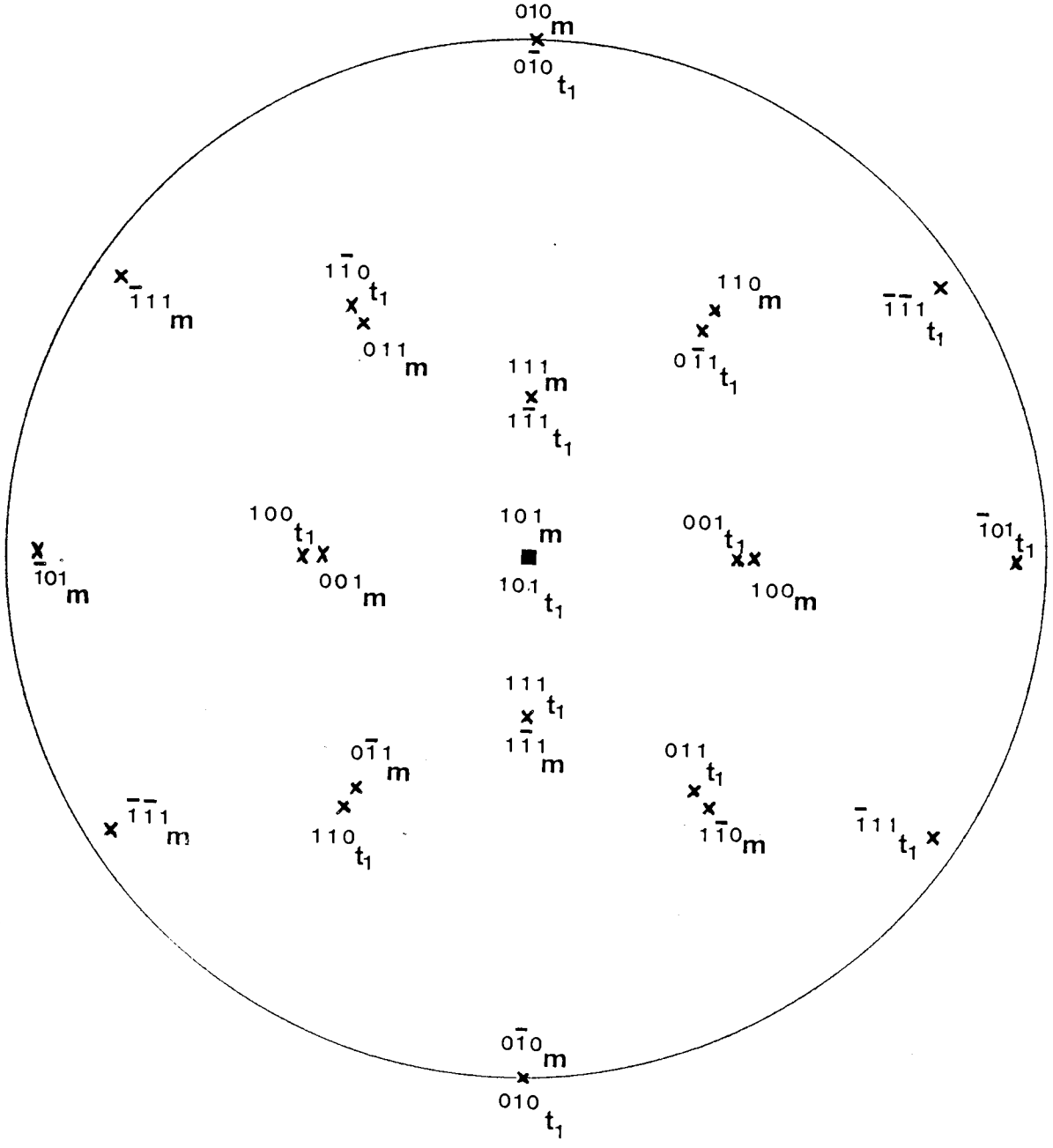

b) $(\bar{1}01)$

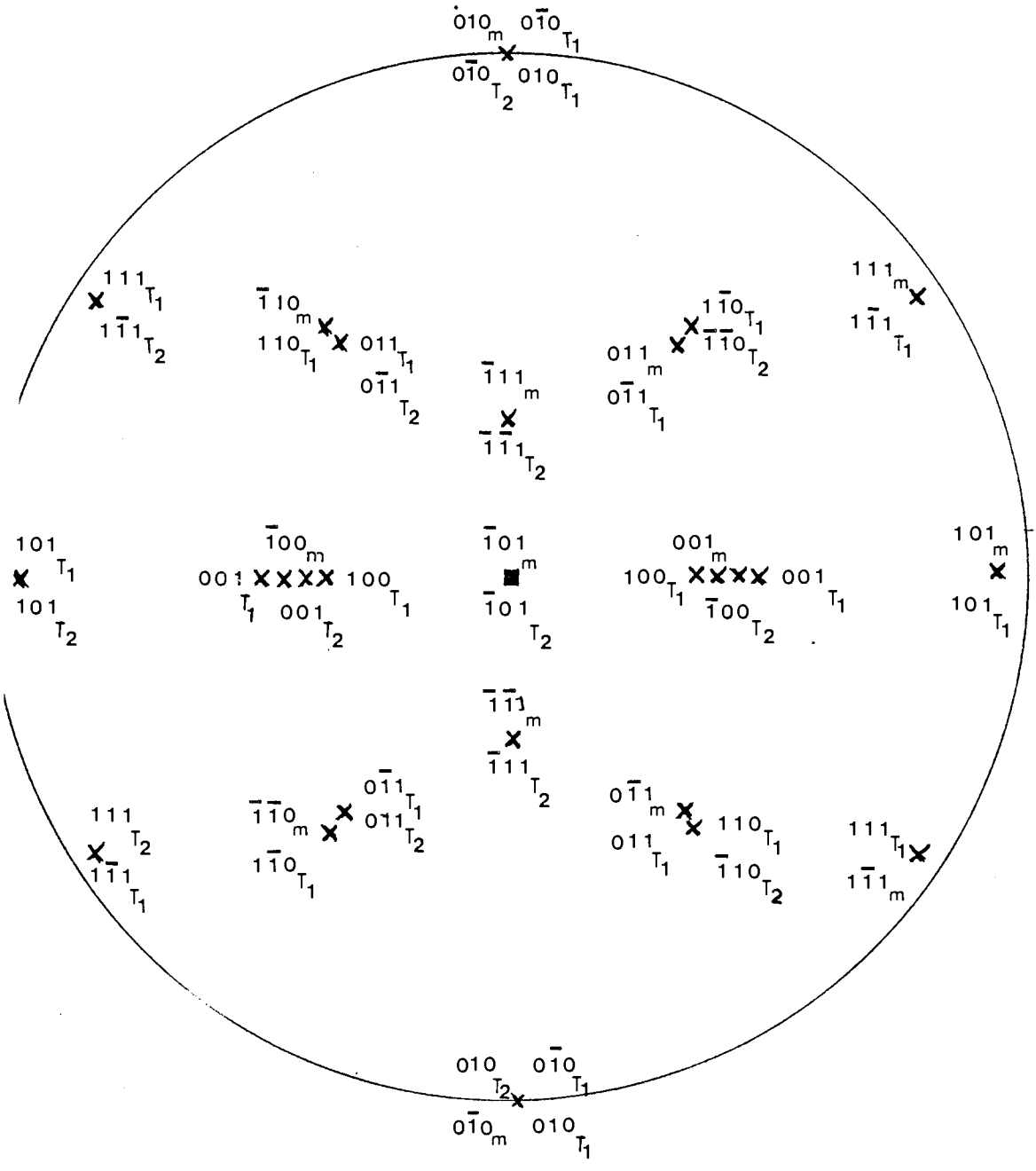
010 m 0$\bar{1}$0 T1
0$\bar{1}$0 T2 010 T1
111 T1
1$\bar{1}$1 T2
$\bar{1}$10 m
110 T1
011 T1
0$\bar{1}$1 T2
$\bar{1}$11 m
$\bar{1}$$\bar{1}$1 T2
1$\bar{1}$0 T1
$\bar{1}$$\bar{1}$0 T2
011 m
0$\bar{1}$1 T1
111 m
1$\bar{1}$1 T1
101 T1
101 T2
$\bar{1}$00 m
001 T1
100 T1
001 T2
$\bar{1}$01 m
$\bar{1}$01 T2
001 m
100 T1
001 T1
$\bar{1}$00 T2
101 m
101 T1
$\bar{1}$$\bar{1}$1 m
$\bar{1}$11 T2
0$\bar{1}$1 T1
$\bar{1}$$\bar{1}$0 m
011 T2
1$\bar{1}$0 T1
0$\bar{1}$1 m
011 T1
110 T1
$\bar{1}$10 T2
111 T2
1$\bar{1}$1 T1
111 T1
1$\bar{1}$1 m
010 T2 0$\bar{1}$0 T1
0$\bar{1}$0 m 010 T1

c) (011)

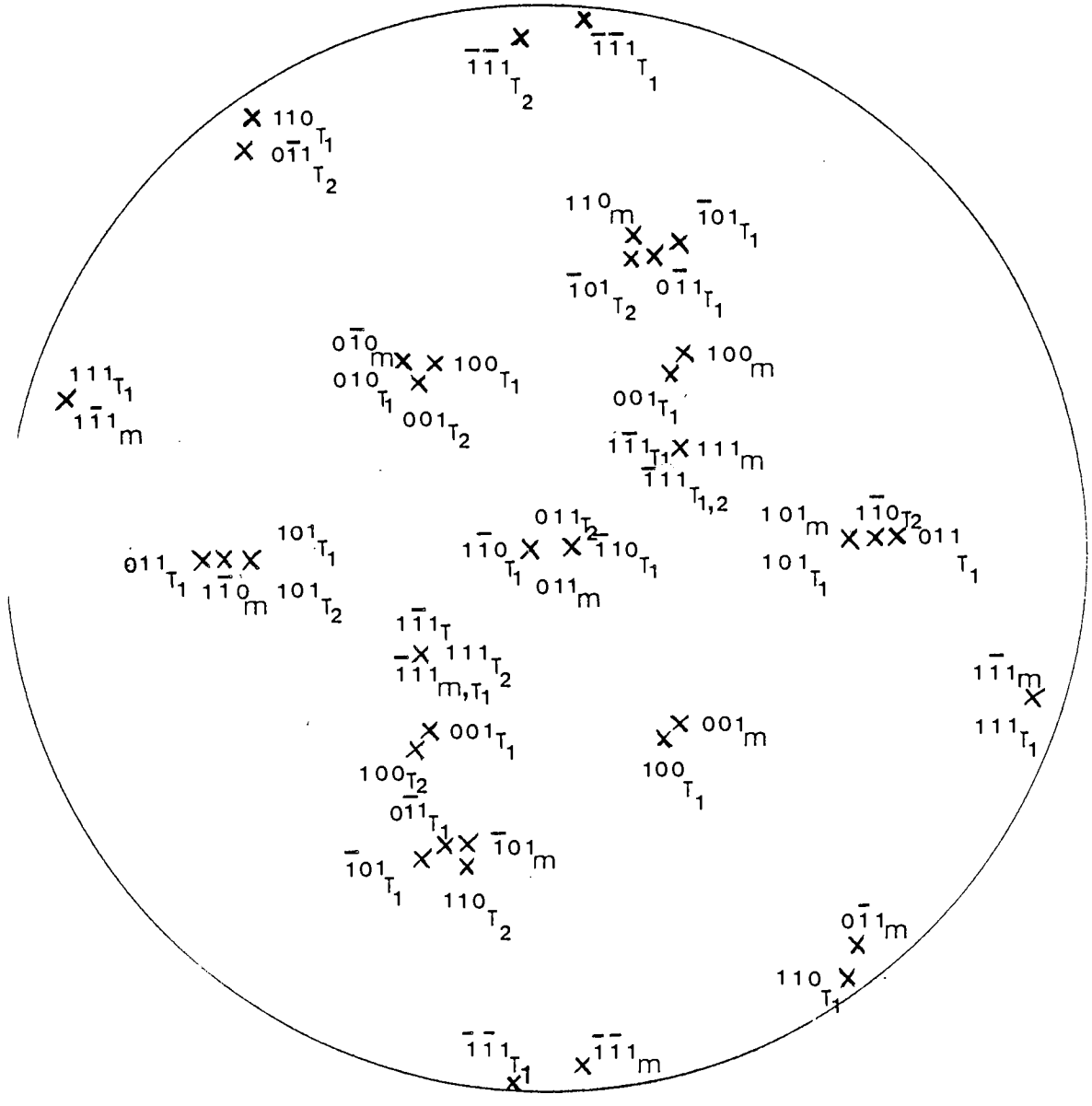
$\bar{1}\bar{1}\bar{1}_{T_2}$
$\bar{1}\bar{1}1_{T_1}$
110_{T_1}
$0\bar{1}1_{T_2}$
110_m
$\bar{1}01_{T_1}$
$\bar{1}01_{T_2}$
$0\bar{1}1_{T_1}$
$0\bar{1}0_m$
100_{T_1}
010_{T_1}
001_{T_2}
100_m
001_{T_1}
111_{T_1}
$1\bar{1}1_m$
$\bar{1}\bar{1}1_{T_1}$
111_m
$\bar{1}11_{T_1,2}$
011_{T_2}
101_m
$1\bar{1}0_{T_2}$
011_{T_1}
101_{T_1}
$1\bar{1}0_{T_1}$
011_m
$1\bar{1}0_m$
101_{T_2}
$1\bar{1}1_T$
$\bar{1}11_{T_2}$
$111_{m,T_1}$
$1\bar{1}1_m$
111_{T_1}
001_{T_1}
001_m
100_{T_2}
100_{T_1}
$0\bar{1}1_{T_1}$
$\bar{1}01_m$
$\bar{1}01_{T_1}$
110_{T_2}
$0\bar{1}1_m$
110_{T_1}
$\bar{1}\bar{1}1_{T_1}$
$\bar{1}\bar{1}1_m$

d) (110)

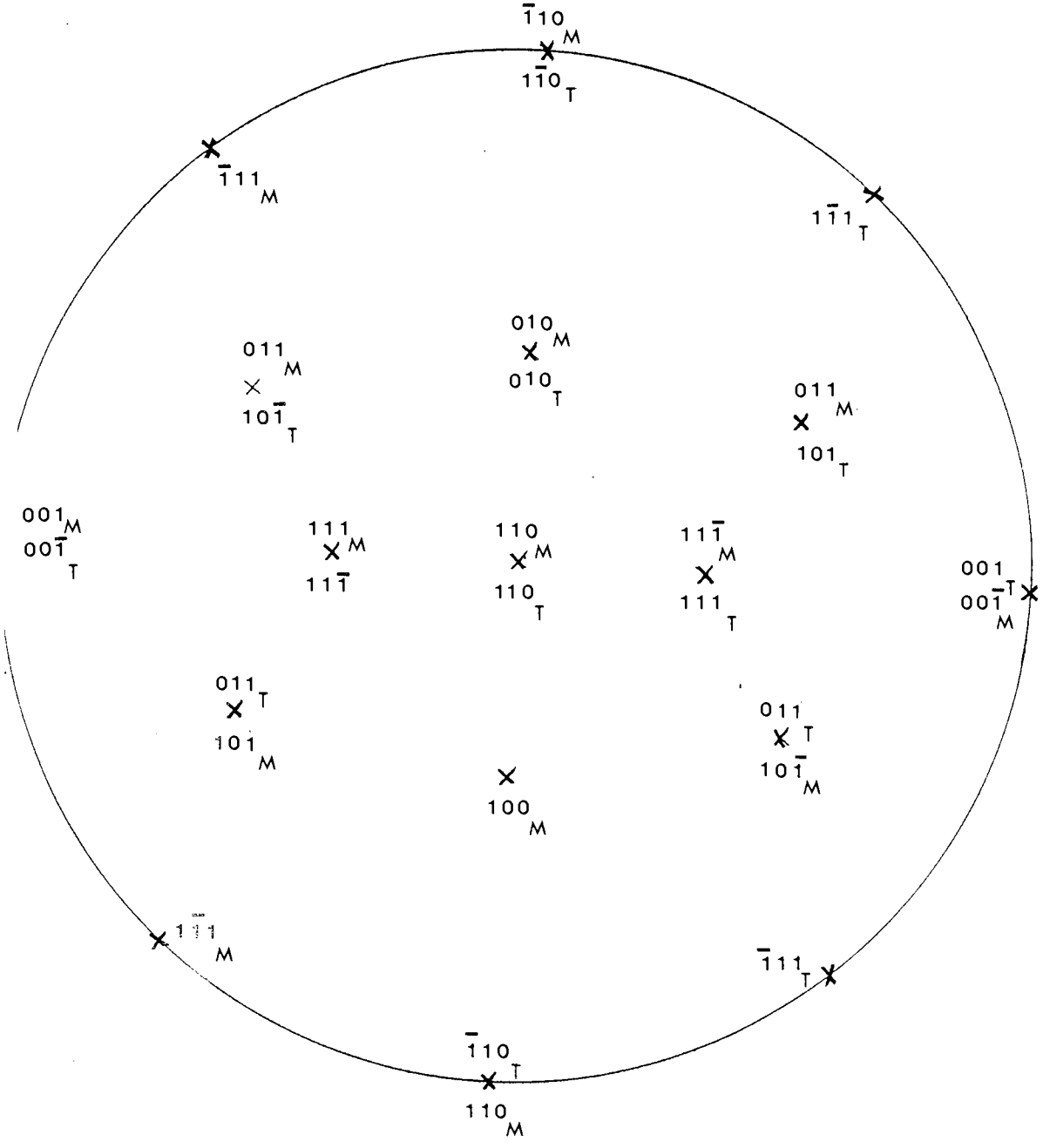
$\bar{1}10_M$
$1\bar{1}0_T$
$\bar{1}11_M$
$1\bar{1}1_T$
010_M
010_T
011_M
$10\bar{1}_T$
011_M
101_T
001_M
$00\bar{1}_T$
111_M
$11\bar{1}$
110_M
110_T
$11\bar{1}_M$
111_T
001_T
$00\bar{1}_M$
011_T
101_M
011_T
$10\bar{1}_M$
100_M
$\bar{1}11_M$
$\bar{1}11_T$
$\bar{1}10_T$
110_M

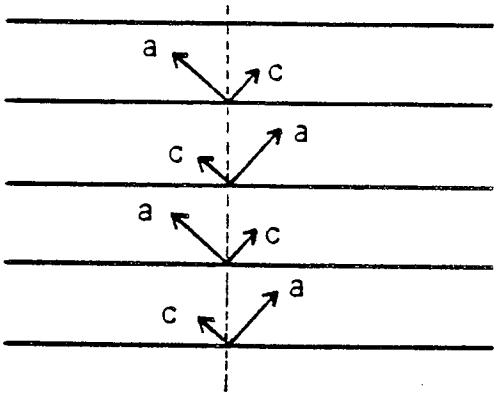

Figure 39 - Schematic representation of the ordered tetragonal domains with alternate C-axis in adjacent domains.

The reciprocal lattice of Pt_2FeCu which is constructed based on the x-ray and electron diffraction observations is shown in figure 40.

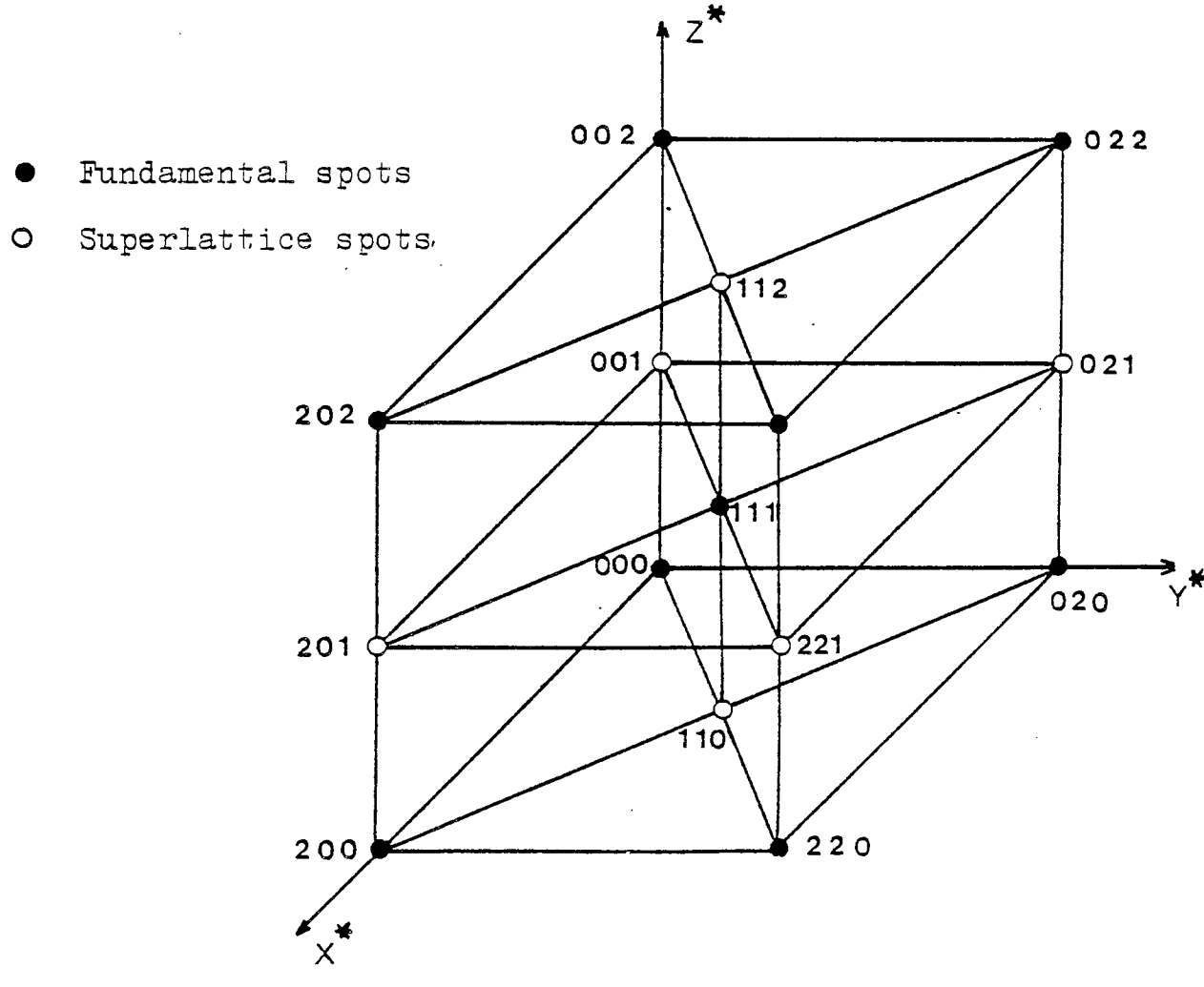

Figure 40 - The reciprocal lattice of Pt_2FeCu showing the fundamental and superlattice reflections.

3.I.7 Recrystallization mechanisms

During the course of different thermal treatments below the critical temperature, it was observed that recrystallization occurred. In the past, recrystallization of an ordered domain structure has only been observed on a few occasions [65,37,72] and there is much controversy, regarding the nature, orientation relationships and nucleation and growth mechanism. Therefore it was quite interesting to study such a mechanism in order to clarify some of the controversies and existing "models".

At first, the activation energy of the recrystallization mechanism was measured. For this purpose, four isothermal temperatures, 1000°C, 900°C, 800°C and 700°C, below the T_c were selected. Four samples were cut from the homogenized alloy and were subjected to 2,4, ..., 3000 hours heat-treatment and after each anneal, they were slowly quenched in water to avoid any grain boundary fracture (section 3.I.8). In some cases (especially at 1000°C), a shorter annealing time was required to study the recrystallization mechanism in detail.

3.I.7.1 Activation energy measurements

Many investigations of the kinetics of isothermal recrystallizations, have shown that the Avrami relationships is obeyed [73]. This is represented by an equation of the form:

$$f = 1-\exp(-kt^n) \qquad \ldots\ldots \quad (22)$$

Where f is fraction recrystallized after time t and k and n are constants[73]. If this is so, then a plot of $\ln \ln \left[\frac{1}{1-f}\right]$ versus ln t would be linear and from it values of k and n can be determined.

Figure 41 shows the plot of fraction recrystallized against ln t for different temperatures of heat treatment. The effect of temperature on recrystallization can clearly be observed, i.e., at 1000°C the material has reached 50% recrystallization stage in a matter of 72 minutes whereas at 700°C, it takes 350 hours to reach a similar stage. At 900°C and 800°C, the time of 7 and 23 hours are required to achieve 50% recrystallization.

Figure 42 shows the Avrami plot of $\ln \ln \left[\frac{1}{1-f}\right]$ versus ln t which was a straight line relationship up to f= 0.5 with another linear section for f>0.5. From this graph the values of the k and n for the two linear relationships can be determined and are given in table 3. These values were obtained by fitting straight lines to f<0.4 and f > 0.6

T°C	f<0.4		f>0.6	
	n_1	k_1	n_2	k_2
1000	0.95	58×10^{-2}	0.2	86×10^{-2}
900	0.75	15×10^{-2}	0.15	55×10^{-2}
800	0.71	6.8×10^{-2}	0.15	41×10^{-2}
700	0.72	1.17×10^{-2}	0.16	22.5×10^{-2}

Table 3- Values of n and k in the Avrami relation

This shows that the n increased with increasing temperature whereas k decreased. The actual value of n varies between 0.15-0.2 and 0.7-0.95.

Finally, the activation energy was measured from the time for 40% and 60% recrystallization and table 4 shows the relevant data which was used to plot ln t versus $\frac{1}{T}$ for these measurements.

$T^{o}C$	$1/T(K^{-1})$ $x10^{-3}$	Time (h) for recrystallization	
		40%	60%
1000	0.78	0.81	2.1
900	0.85	4.30	25.5
800	0.93	15	134
700	1.03	221	1808

Table 4- Data for Arrhenius plot obtained from the fraction recrystallized curves of Pt_2FeCu

The activation energy of the recrystallization was calculated from the following expression(89)

$$\mathcal{T} = A \exp\left(-\frac{Q_r}{R\,T}\right)$$

where $\mathcal{T}$ is the time at a given temperature required to recrystallize a certain percentage of the volume of material, A and R are constants and Q_r is the activation energy of recrystallization.

From the slopes of the Arrhenius plot the Q_r values were calculated and are shown in table 4(a) .

fraction recrystallized	KJ/Mole	eV/atom
f = 0.4	209.4	2.16
f = 0.6	249.5	2.57

Table 4(a)

Figure 41 - The fraction recrystallized vs annealing time for the Pt_2FeCu

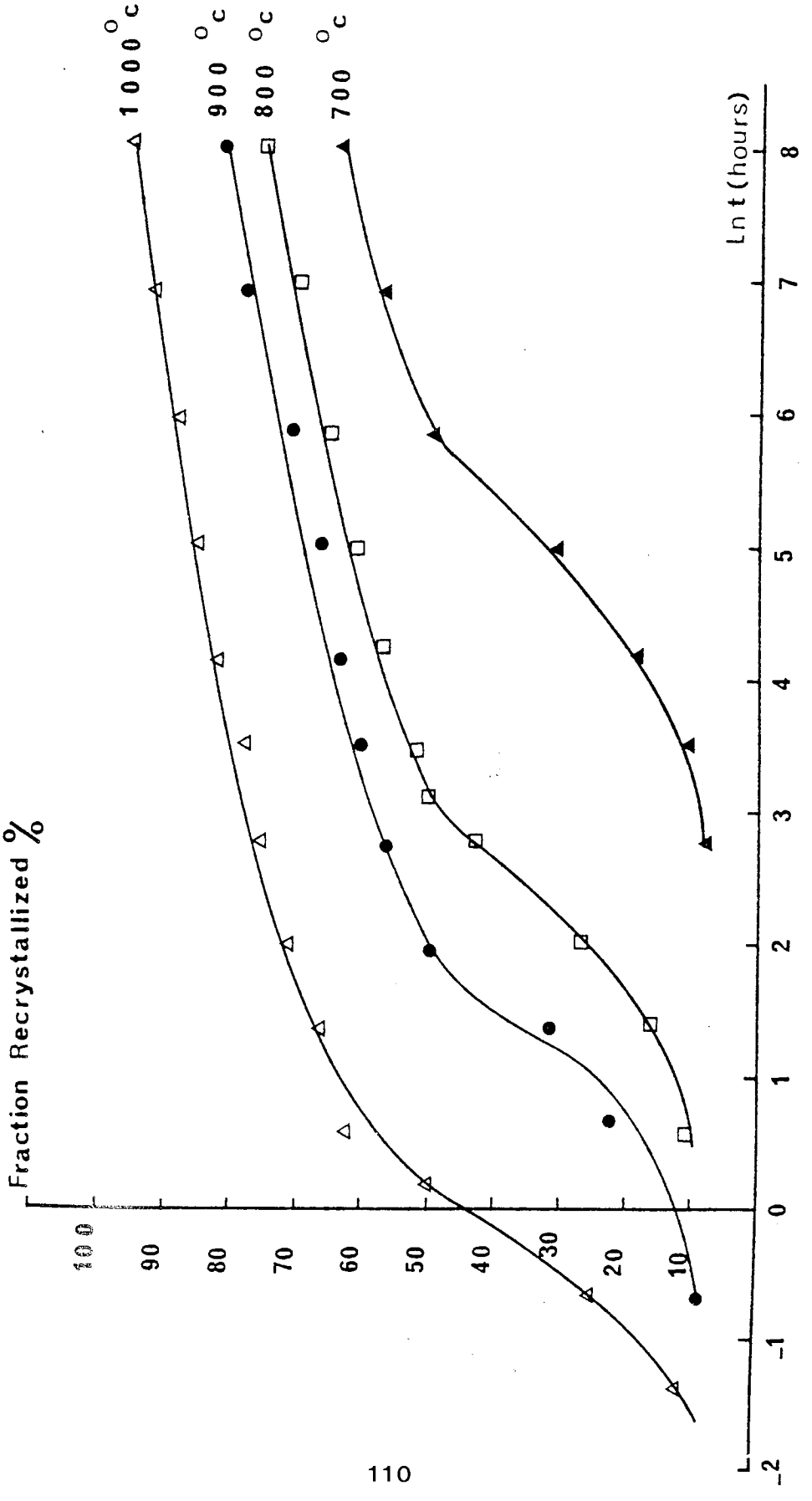

Fig 42 - Avrami plot for the recrystallization of Pt_2FeCu

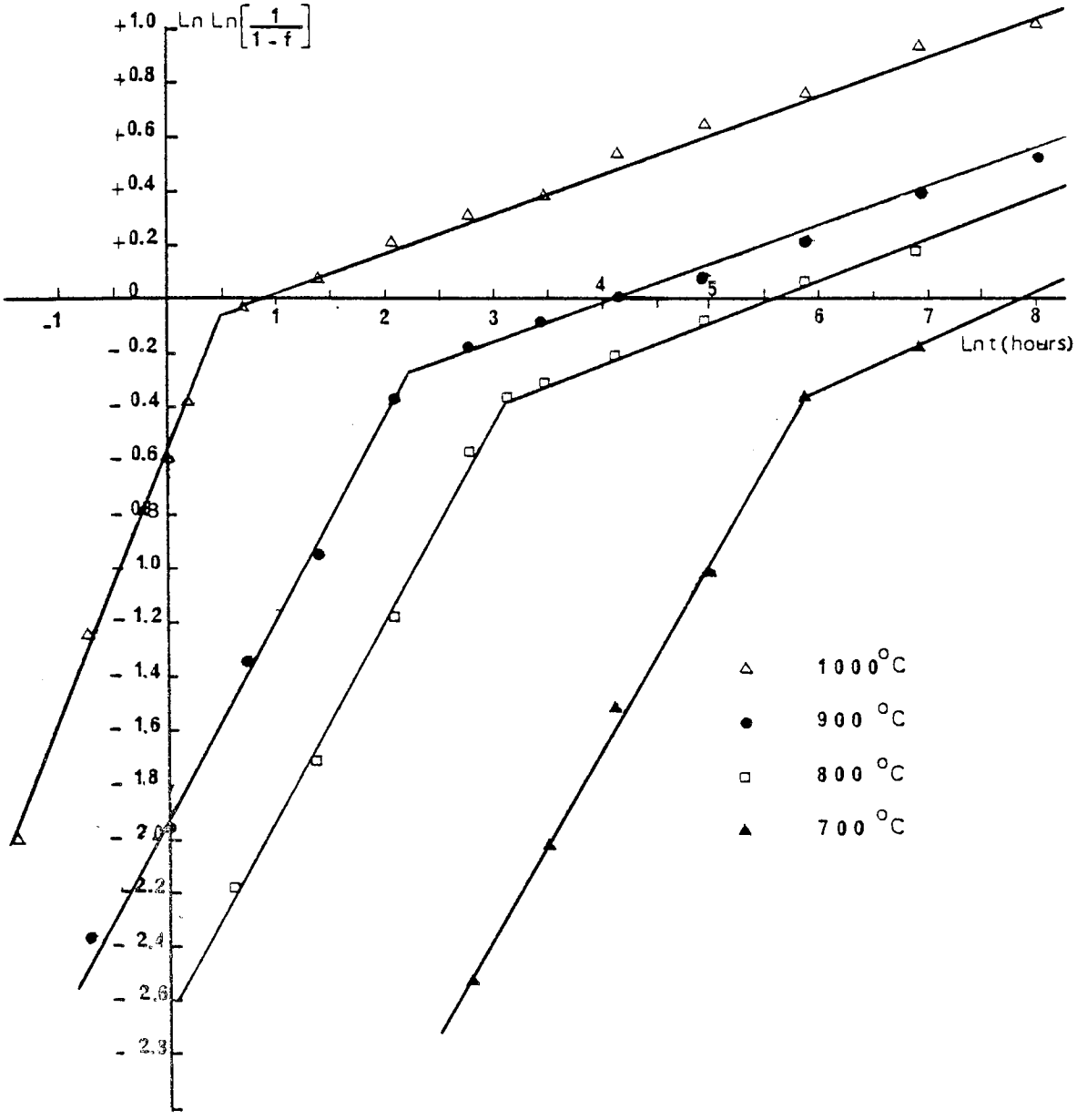

Figure 43 - Arrhenius plot for determination of activation energy for recrystallization of the Pt_2FeCu

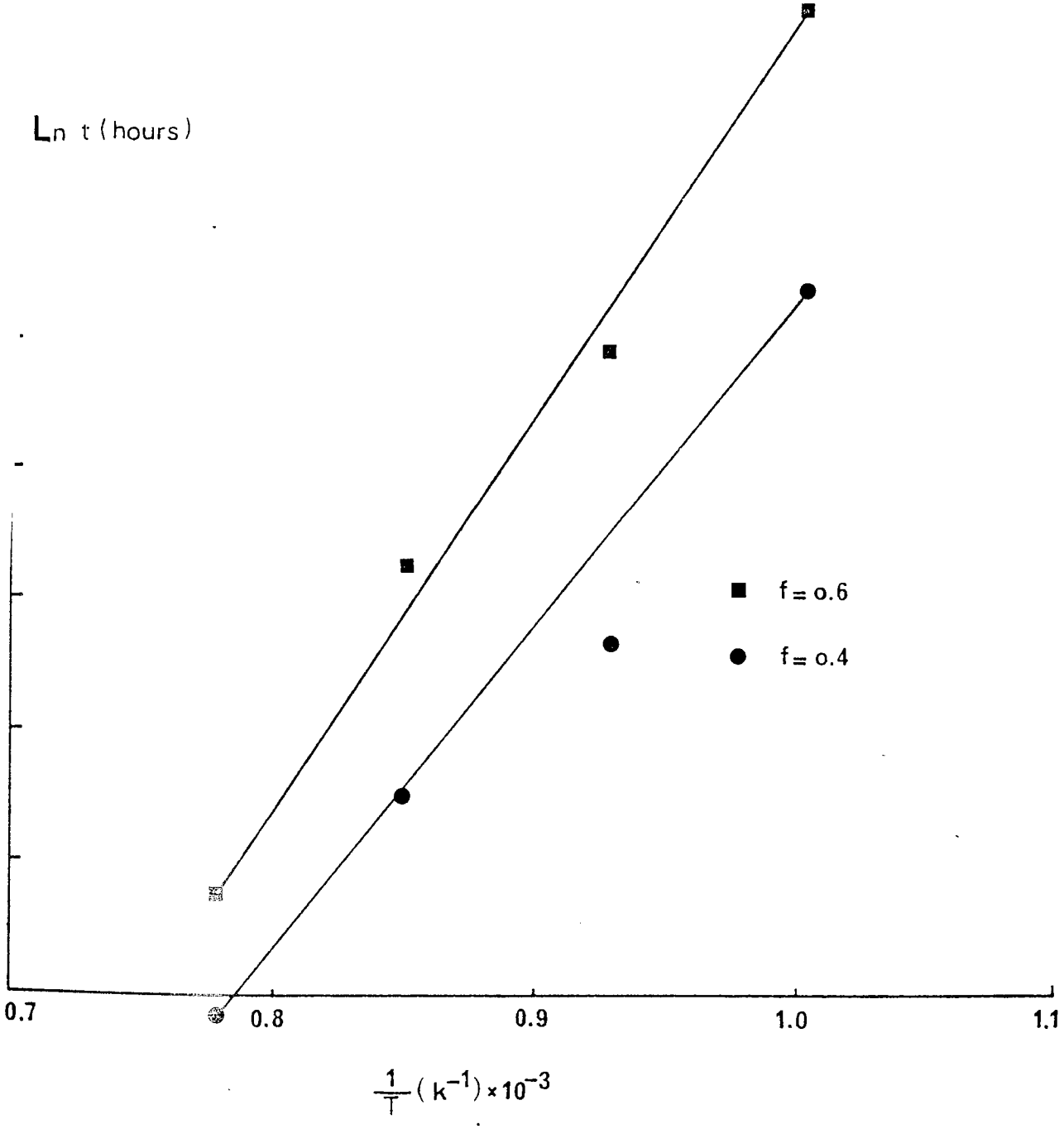

3.I.7.2 Optical microscopy

During the course of activation energy measurements of the recrystallization, the actual mechanism was closely examined by means of optical and electron microscopy at different stages. As the recrystallization mechanism proved to be identical for the samples subjected to different recrystallization treatments, only the experimental observation of the 1000°C isothermal heat-treatment will be represented below.

After only 5 minutes at 1000°C, the new grains appeared along the grain boundaries of the parent matrix. They were mostly observed at the central region and no new grains were observed near the edges of the sample, i.e., indicating a heterogeneous nucleation and growth mechanism.

Fig 44- Grain-boundary nucleation and growth of the recrystallization grains, 5 minutes at 1000°C. Optical micrograph. Etched. x135

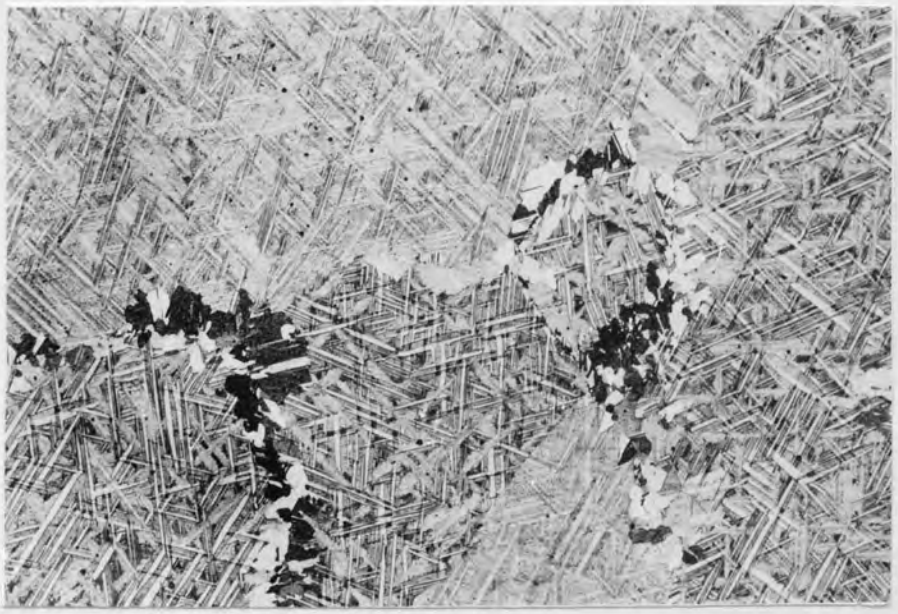

Fig 45- Similar area to Fig.44 .Etched X185

On the longer recrystallization treatments, it appeared that the grain-boundaries were not the only sites for the recrystallized nuclei,but the intersections of the twin-bands seemed to be also adopted as sites for recrystallization. These sites were clearly observable after 30 minutes at 1000°C and figures 46 and 47 show these sites.

After one hour of heat-treatments where the two afore-mentioned mechanisms were in progress, the third kind of morphological change was observed.Although no new grains appeared to have formed, some of the ordered domains seemed to be advancing into the adjacent materials. This mechanism shows a similar character to that of the stress-induced grain boundary migration where the parallel sided domain boundaries start to advance towards the neighbouring region with the wavy boundaries, similar to grain boundary bulging. Figures 48 and 49 examplifies such a mechanism.

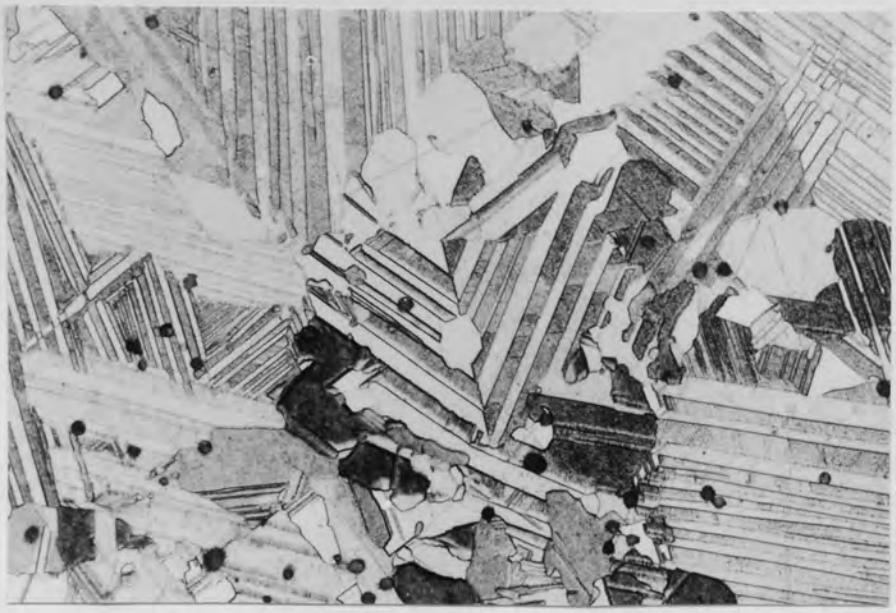

Fig 46- Optical micrograph showing the nucleation of the recrystallized grains at the junction of the twinned bands. Etched. x350

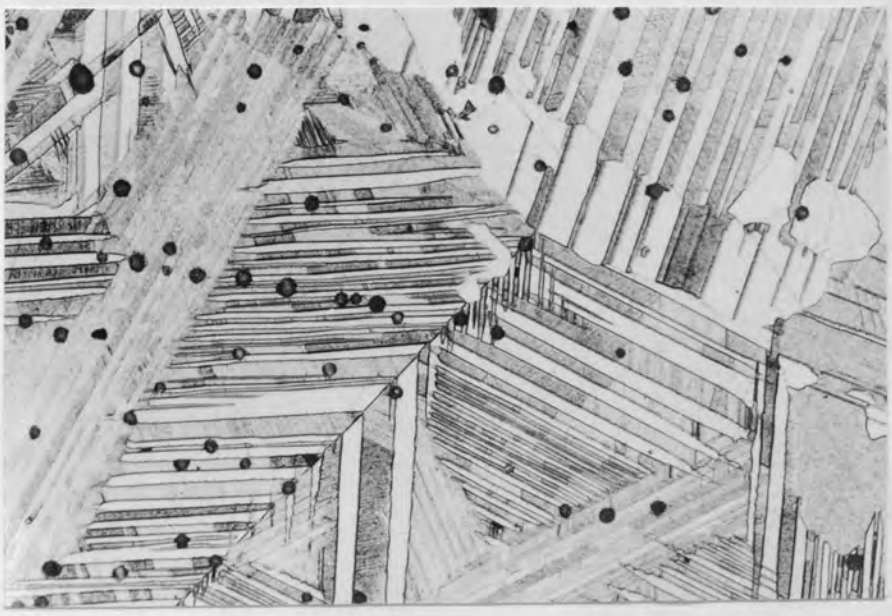

Fig 47- Similar area to Fig. 46. x300

Fig 48- Thickening of the domains, one hour at 1000°C.
Optical image. Etched. x350

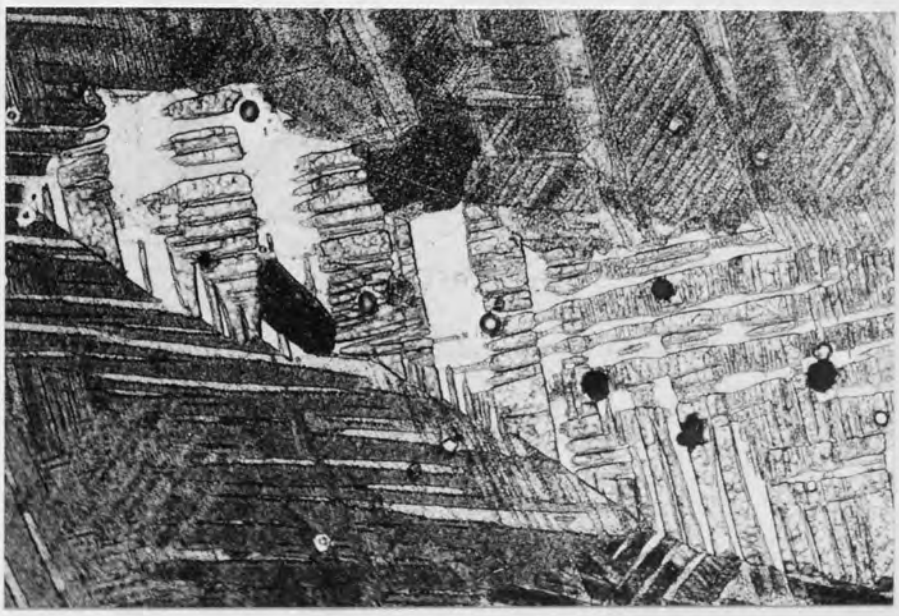

Fig 49- Similar area to Fig.48 . Etched. x420

.ring further heat-treatments, these three mechanisms
)ntinued to progress at the expense of the finely
winned matrix. Their growth appeared to be an orientation-
ependent mechanism,i.e., the new grains advanced toward
favourable orientation first. This effect is clearly
.een in figures 50 and 51 where the advancing fronts
are shown by arrows.

As in the normal recrystallization mechanism, it was expected to have a fully recrystallized material at a given time and temperature, but it proved otherwise.

The sample subjected to 1000 hours heat-treatments at 1000°C only reached 90% recrystallization and further annealing up to 3000 hours only produced a 95% recrystallized sample. The fully recrystallized region of the sample was the central parts where the original material had the most complex twinned microstructure. The only region of the material where the original microstructure was unaltered, seemed to be in the vicinity of the free surface (edges of the sample), figures 52 and 53.

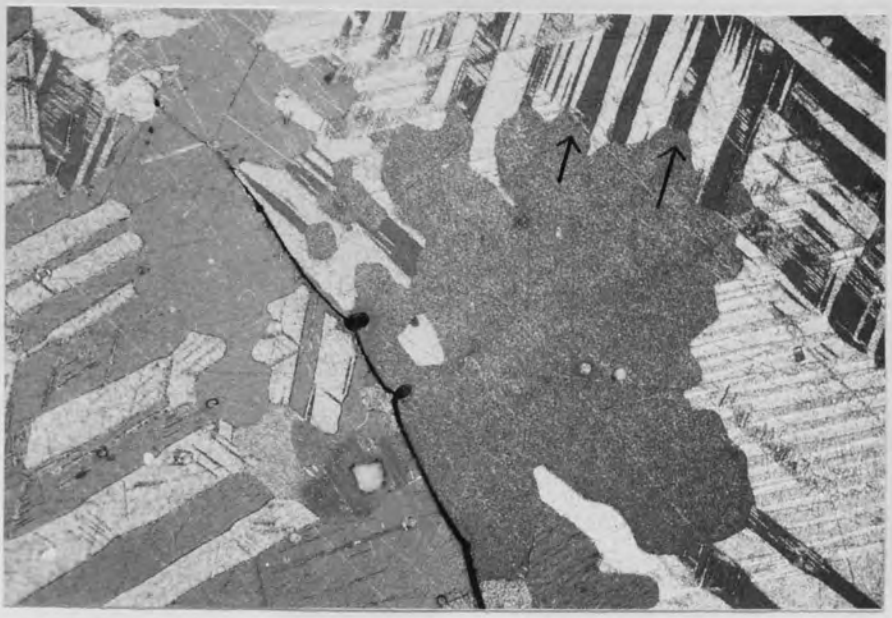

Fig 50- Polarized light micrograph showing the advance of the recrystallized grains towards the favourable orientations. Etched X420

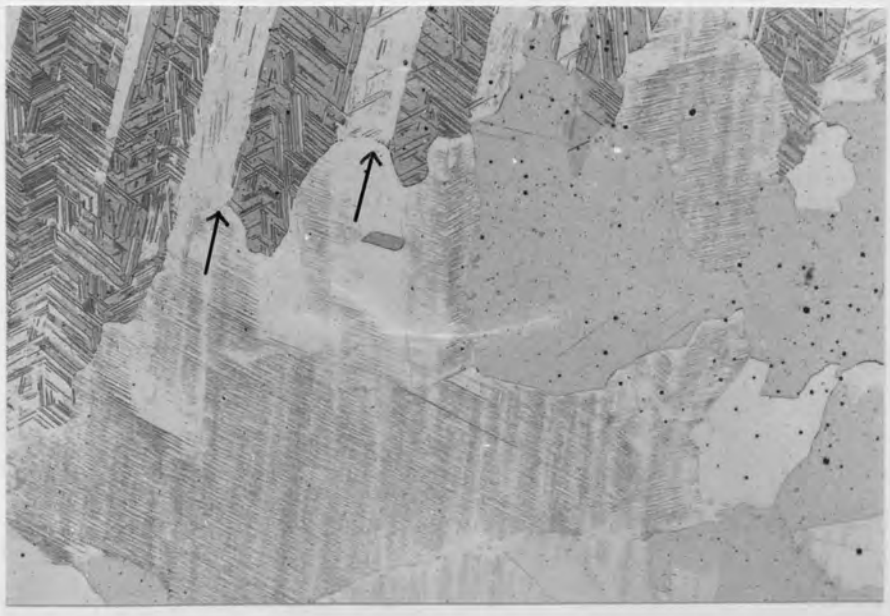

Fig 51- Similar features to Fig.50. Etched x420

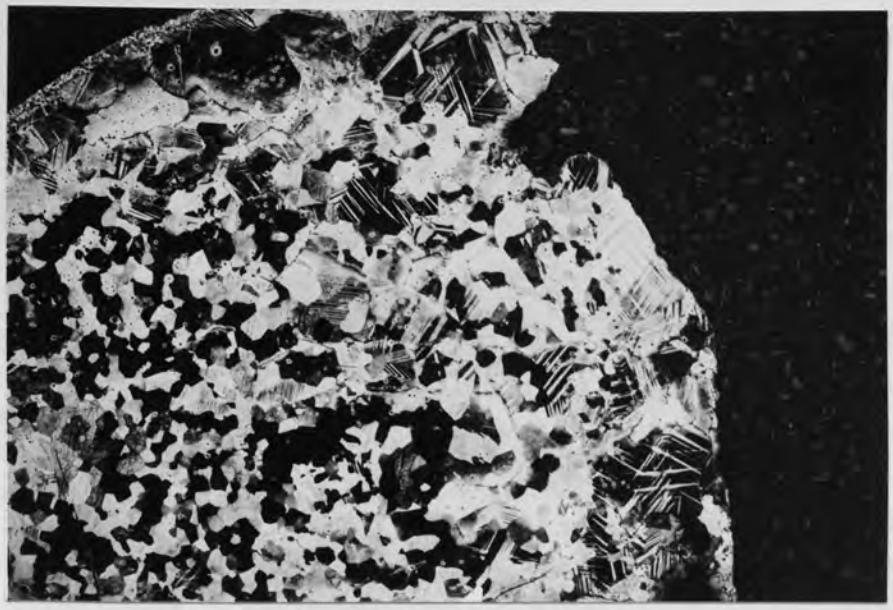

Fig 52- Optical micrograph of Pt_2FeCu specimen, annealed at 1000°C for 1000 hours, showing the recrystallized grains at the central regions. Etched. x27.

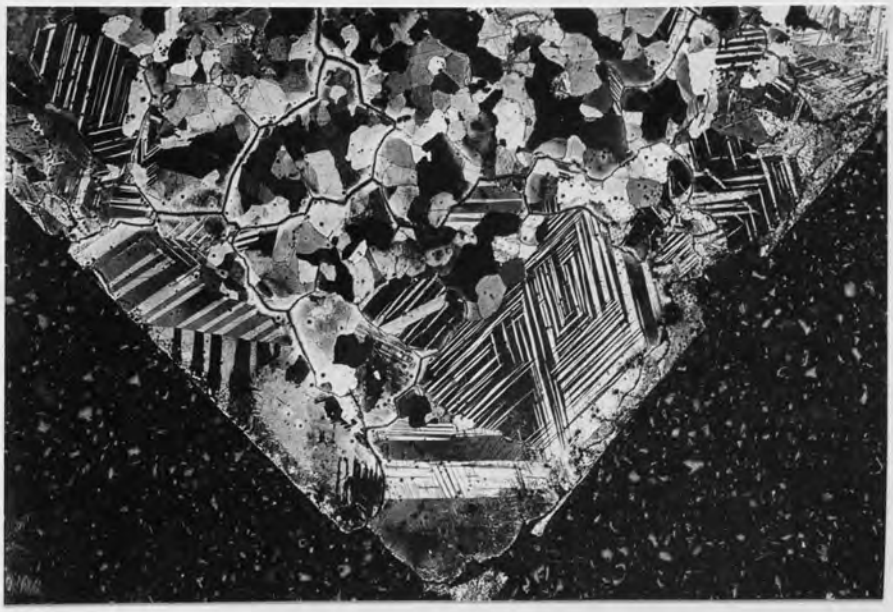

Fig 53- Similar to Fig.52, but showing the unaltered original twinned structures along the edges of the sample. Etched. x 180.

The recrystallized parts of the material had normal grain structures and showed some evidence of annealing twins, which were generally in the form of parallel-sided lamella. Annealing twins were not very frequent, i.e., there appeared to be approximately one twin to two grains, figure 54.

When these recrystallized grains were examined in detail, some additional markings interpreted as deformation twins were also observed which were distributed throughout the grains in an irregular manner. As a safeguard, to assure correct identification, the specimen was ground, polished and etched again and subsequently viewed with the polarized light microscope in which they showed twin characteristics.

Figure 55 is a typical area of the specimen which shows those narrow deformation twins in a relatively coarse grain about 0.4mm diameter. It appears that four sets of such twins are present in the grain plus an annealing twin. It is also interesting to note that:

1) Some of the twins end inside the grain
2) Some of the twins go right across the grain
3) Where the twins intersect each other there is no detectable displacement cross from one twinning plane to another of each twin
4) When the twins encounter the annealing twin their direction is changed; the original direction is resumed when they pass once more into the matrix.

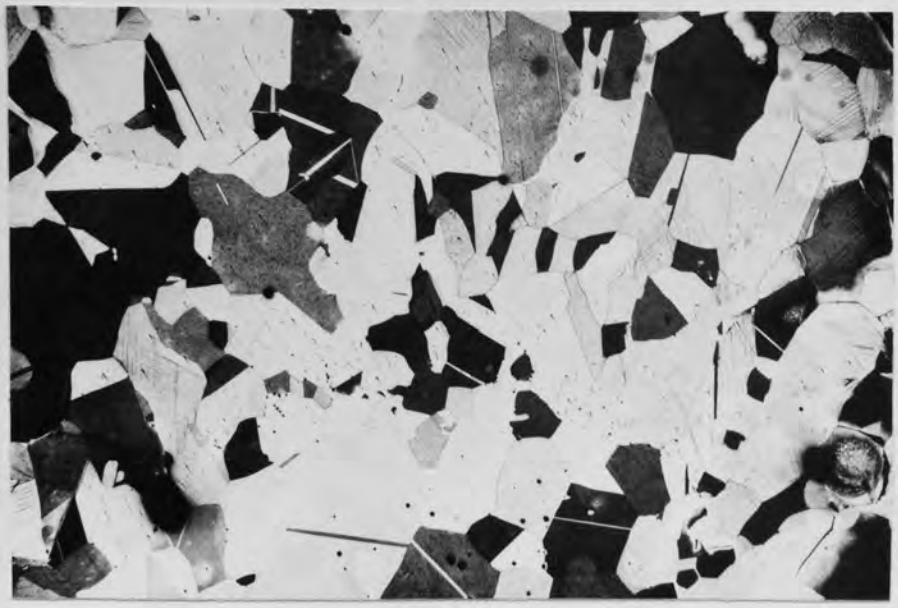

Fig 54- Optical micrograph of the fully recrystallized area of the sample, annealed at 1000°C showing normal grain structure and annealing twins. Etched. x66.

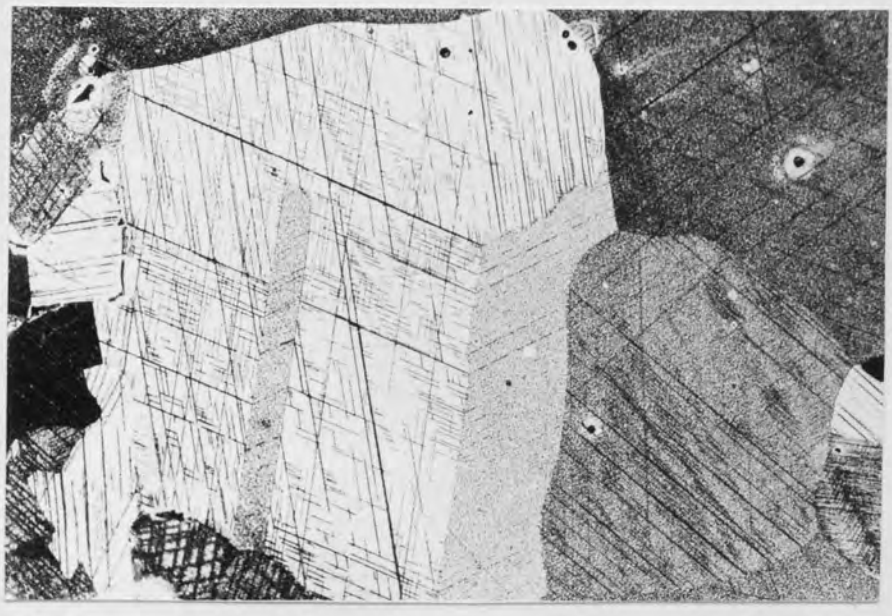

Fig 55- Optical micrograph of the recrystallized grains annealed at 1000°C for 1000 hours, revealing different sets of deformation and annealing twins. Etched. x168

Figure 56 is another area of the recrystallized specimen with similar features to that of figure 55 and figure 57 is a polarized light micrograph of the figure 56, showing change of contrast.

It is also interesting to note that the populations of the deformation twins were more when recrystallized grains formed a triple junction or normal boundaries and they were absent when fracture had occurred along the grain-boundaries, Figure 58 shows these features.

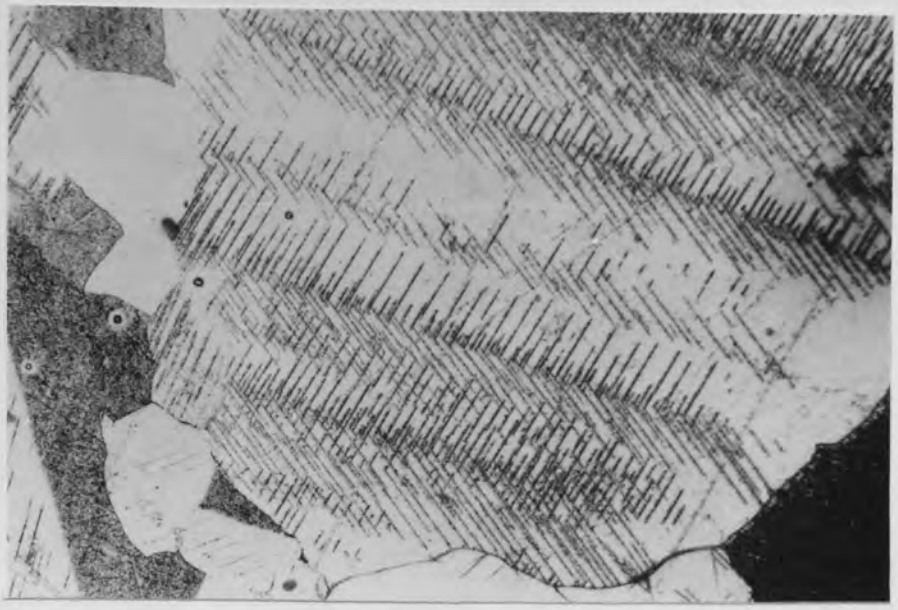

Fig 56- Optical micrograph of the deformation twins inside a recrystallized grain, annealed for 1000 hours at 1000°C. Etched . x420

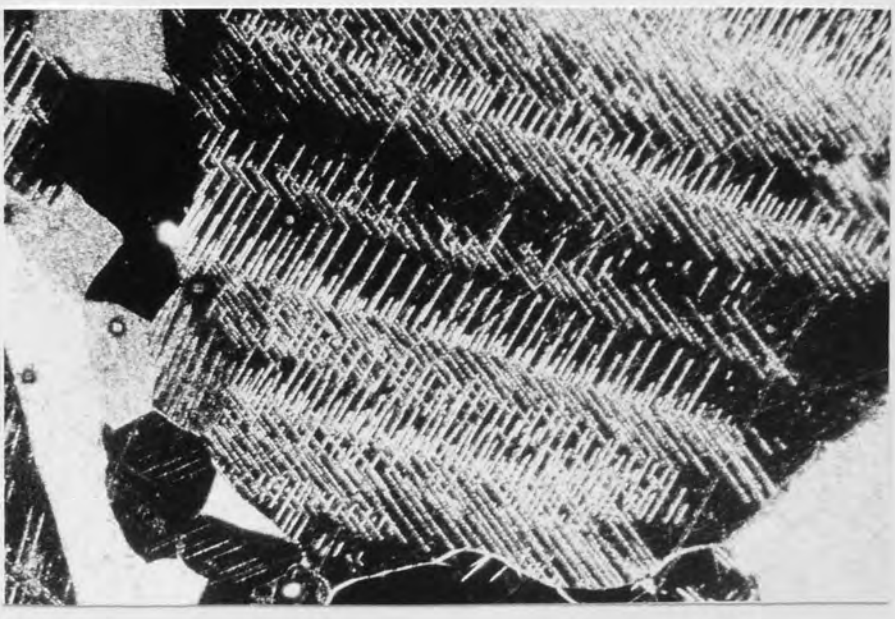

Fig 57- Corresponding polarized light micrograph of Fig.56 Etched. x420

When the sample was subjected to a longer recrystallization treatment, these deformation twins were totally absent and instead the specimen had normal grain structure with annealing twins, figure 59. Annealing twins have normal parallel-sided lamella, but in some cases they appeared differently.

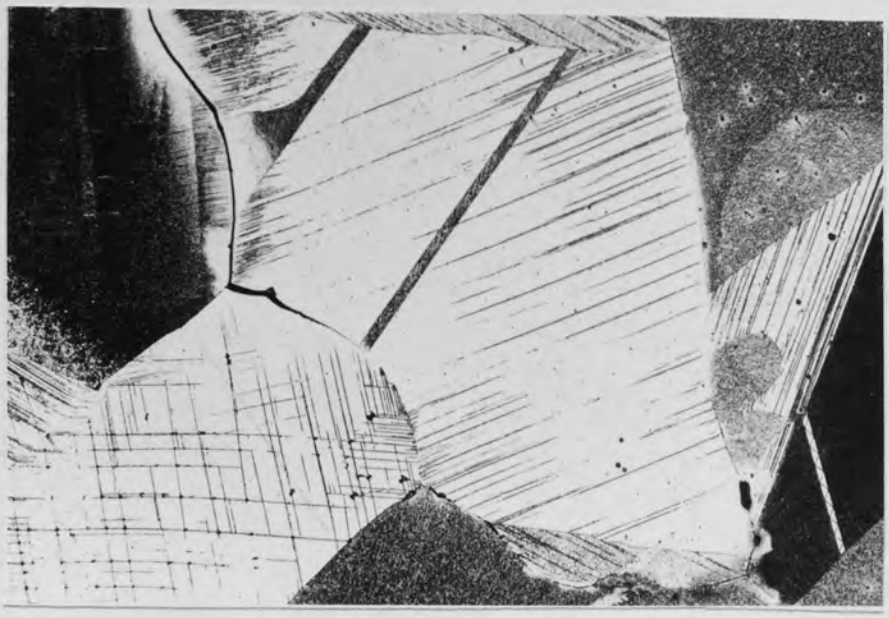

Fig 58- Optical micrograph showing the population of the deformation twins around the triple junctions and their absence in the vicinity of the grain-boundary fracture. Etched. x336.

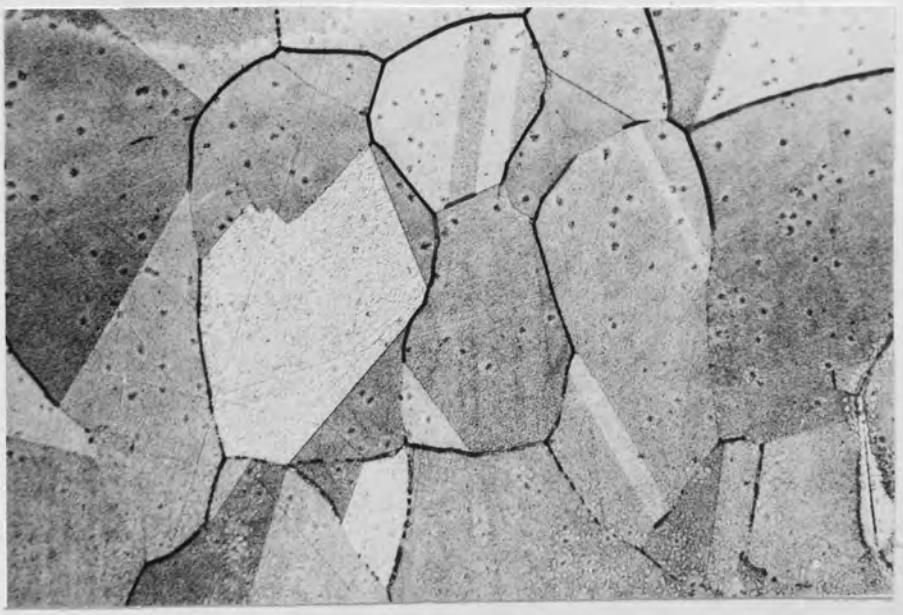

Fig 59- Optical micrograph of the fully recrystallized area of the sample, annealed for 3000 hours at 1000°C, Thermally etched. x135.

3.I.7.3 Transmission electron microscopy

It was mentioned earlier that the growth of the recrystallize grains were orientation-dependent. To fully investigate such a relationship , the T.E.M. examination would have been the ideal technique, but the difficulties in preparing a thin foil with both the twinned and recrystallized regions together proved it otherwise. Only on two occasions, by chance, such thin foils were prepared.

Figure 60(a) shows a bright-field micrograph of three fully recrystallized grains in addition to what seems to be deformation twins in grain '3'. The analysis of the S.A.D.P's confirmed the following orientations of the grains.

G_1 $[3\bar{1}1]$

G_2 $[\bar{1}0,3,1]$

G_3 $[0\bar{1}1]$

Fig 60(a)- Bright-field image of three recrystallized grains x54K

Figure 60(b)- A sterographic projection showing the orientation relationships of the three recrystallized grains.

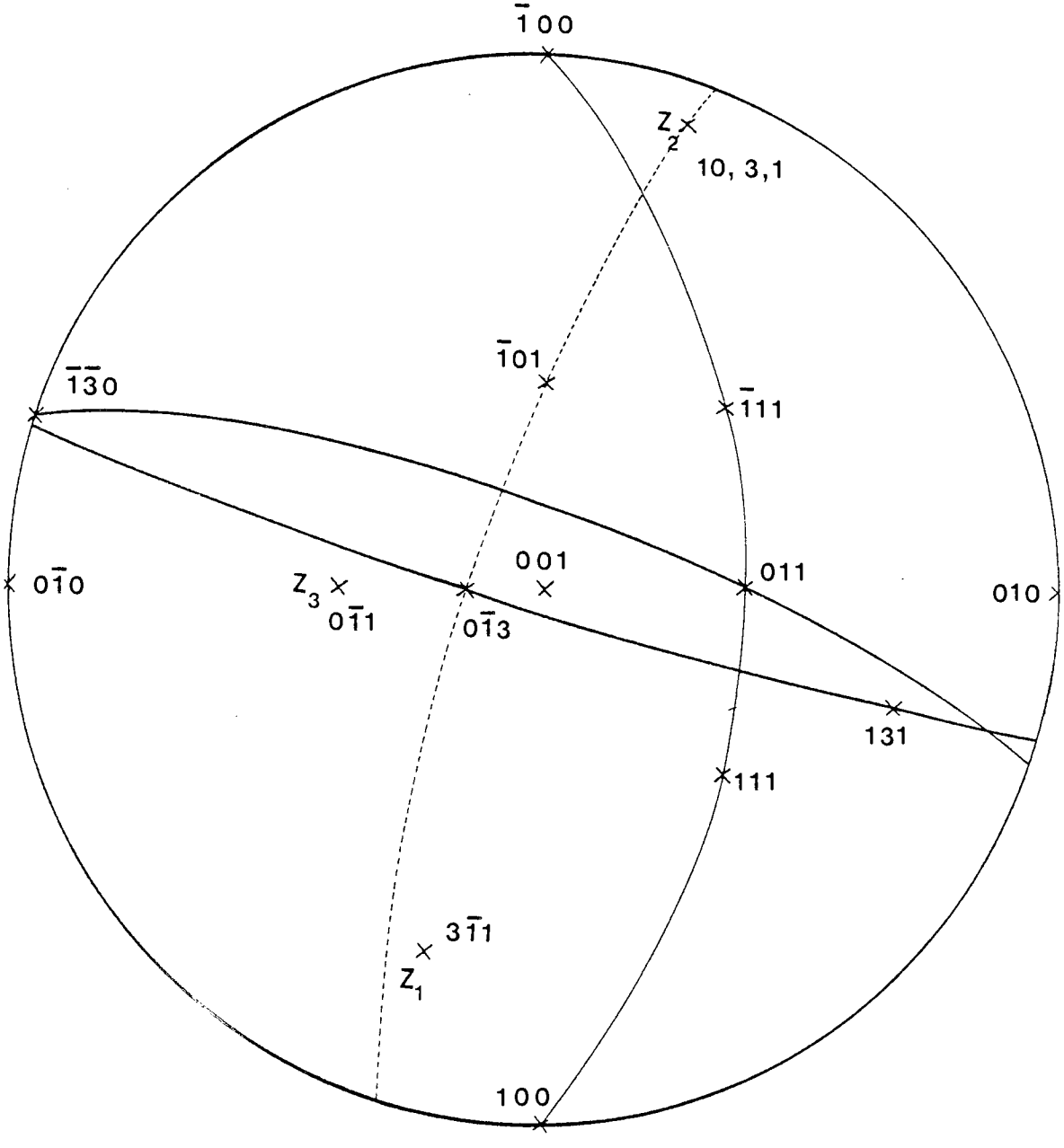

Based on these grain orientations and the trace analysis of Figure 60(b), the following relationships are obtained.

1) twin plane T_1 = $\{101\}$ type, 45° tilted
2) $[011]_{G_1} \parallel [011]_{G_3}$
3) $[133]_{G_2} \parallel [133]_{G_3}$
4) $[133]_{G_2}$ or G_3 is ~15° tilted away from $[011]_{G_1}$

Further supporting evidence was obtained when partially recrystallized samples were examined (one-hour at 1000°C).

Figure 61 is a bright-field micrograph where both the twinned and recrystallized regions can be observed. Although this micrograph does not reveal any information regarding the initial stages of the recrystallization, the orientation-dependency of the growth mechanism can clearly be observed. The recrystallized areas, shown by arrows A_1 and A_2 have advanced rapidly in the alternate twin-bands, but the central region, shown by double arrows B seemed to be hampered by the presence of an unfavourable orientation, although eventually the recrystallization process would swallow all these regions.

Similar twinning which has been observed in optical micrographs is also present in figure 61 with varying widths, Traces 'C'.

Figure 62 is a dark-field image of the dotted area of figure 61 when a $\{110\}$ superlattice reflection is used, whereas figure 63 shows another dark-field, obtained when

(220) fundamental reflection was operative. Similar arguments to that of the "As-quenched state" can be applied in this case, regarding the nature of these twin-bands. Further trace analysis also confirmed the $\{110\}\langle 110\rangle$ orientation-relationships. The finer twin markings inside the recrystallized regions seem to be similar to Trace.B in figure 63, i.e. $\{101\}$ types where the foil normal is $[1\bar{1}2]$.

Fig 61- Bright-field image of the partially recrystallized sample (Arrows A_1,A_2) and the original twinned structures. x34K.

Fig 62- Dark-field image of the dotted area of Fig.61, using $\{110\}$ superlattice reflections. x80K.

Fig 63- Dark-field image of Fig.61,using $\{220\}$ fundamental reflection. x34K.

Figure 64- A sterographic projection showing the orientation relationships of Figure 63.

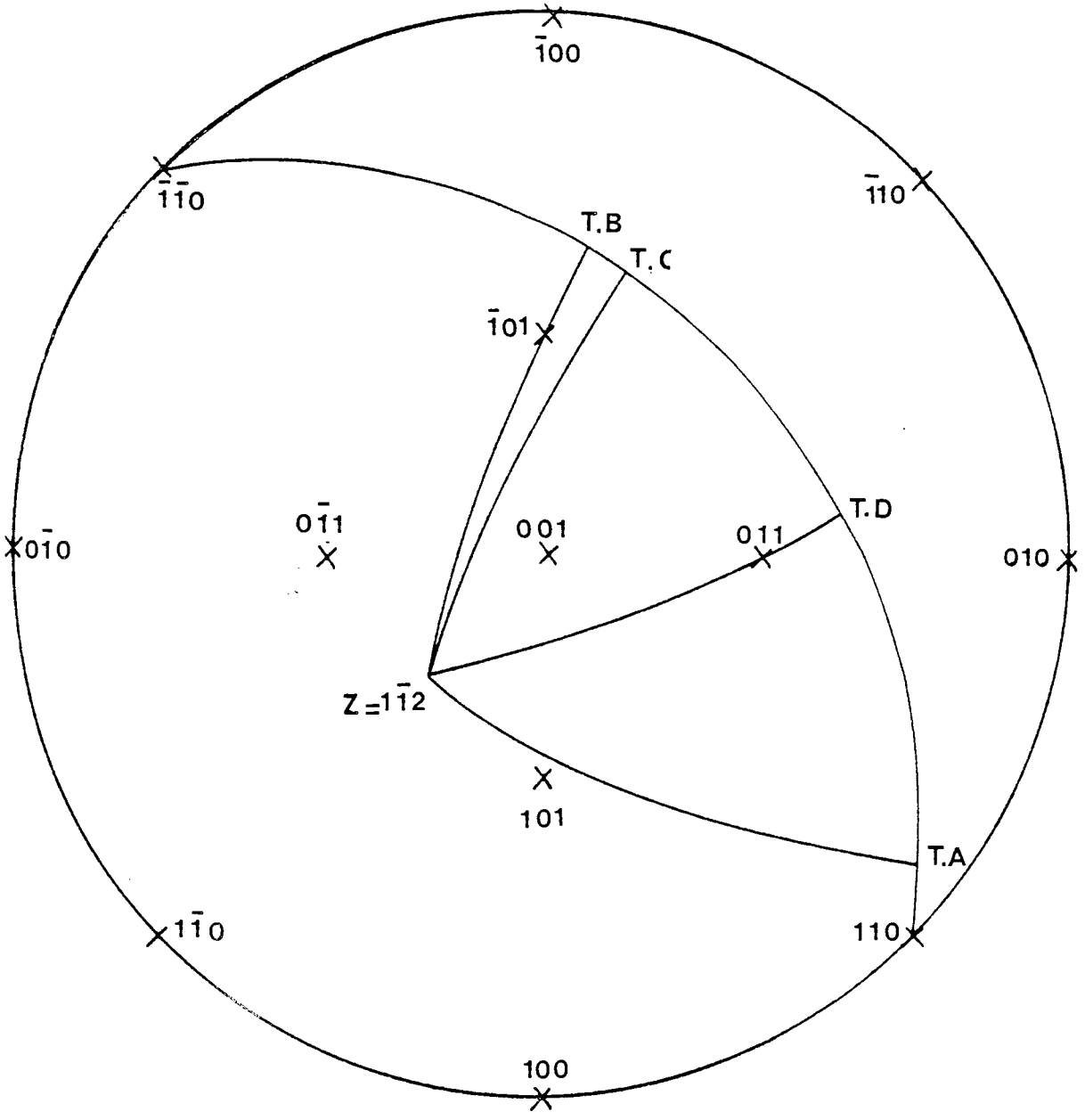

3.I.7.4 Scanning Electron Microscopy (S.E.M.)

Although some orientation relationships were obtained by means of the T.E.M. examinations, further evidence was needed to study this aspect in more detail.

The alternative technique of S.E.M. in the channelling pattern mode was used to solve the problem. To use such a technique the surface finish of the sample was very critical. As stated before no suitable electro-polishing solution could be used and Ion-bombardments produced too much surface topography. Therefore, mechanical polishing was adopted to produce the required surface.

A homogenized sample was subjected to one hour recrystallization heat treatment at 1000°C and was polished down to $\frac{1}{4}$ μm by standard techniques. To remove the remaining fine scratches "etch and polish" procedure was used for one week and although at the end, a scratch free surface was not produced, nevertheless it was thought to be good enough for the orientation relationship determinations.

Figures 66 and 67 show two areas of the sample with the twinned and recrystallized microstructures with their corresponding channelling patterns. Figure 65 shows the orientation relationships of recrystallized grains which all appear to be clustered around (101) pole (0.68-6.18 degree for $G_{1,2,3,5,6}$) and therefore confirming the existence of an orientation relationship between the twinned structure and the recrystallized grains.

Such relationships were also confirmed by means of the T.E.M examination, figure 61.

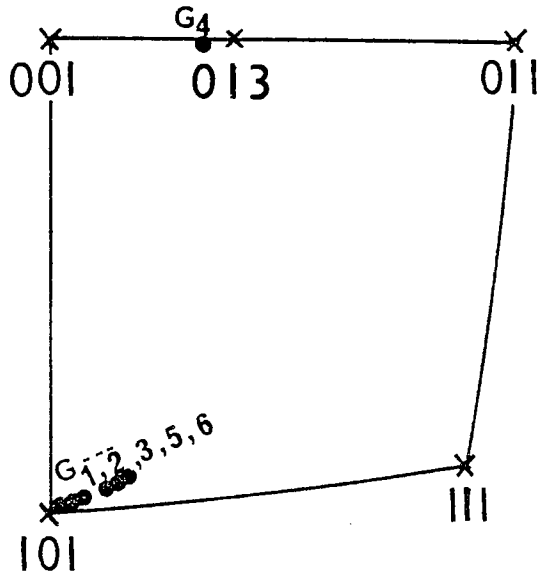

Figure 65 - A section of a sterographic projection showing the orientation of the new grains.

Figures 68 (a),(b) also shows the twinned structures obtained with the backscattered electron image mode.

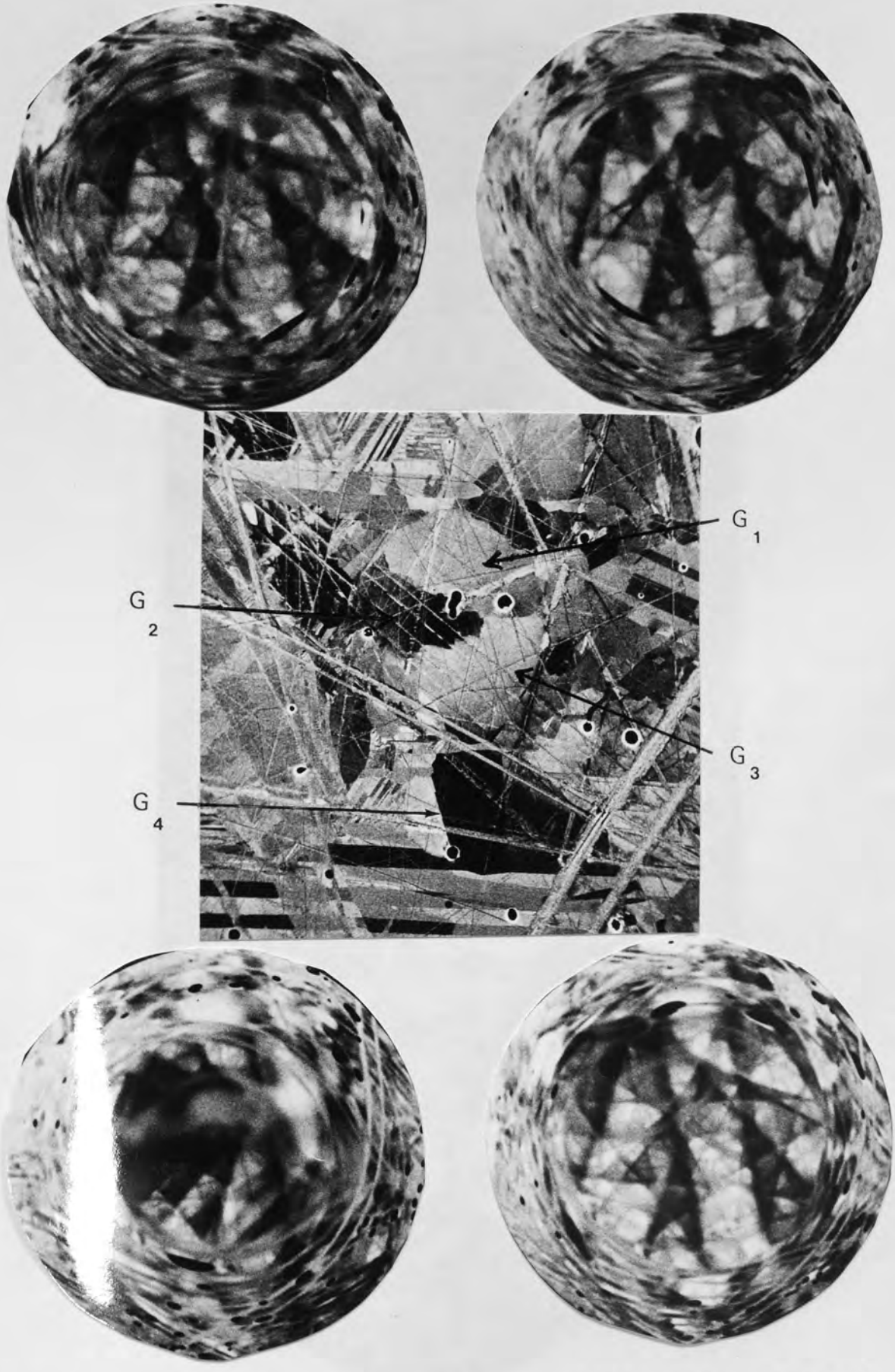

Fig 66- Backscattered electron image of the recrystallized grains and their corresponding channelling patterns x600

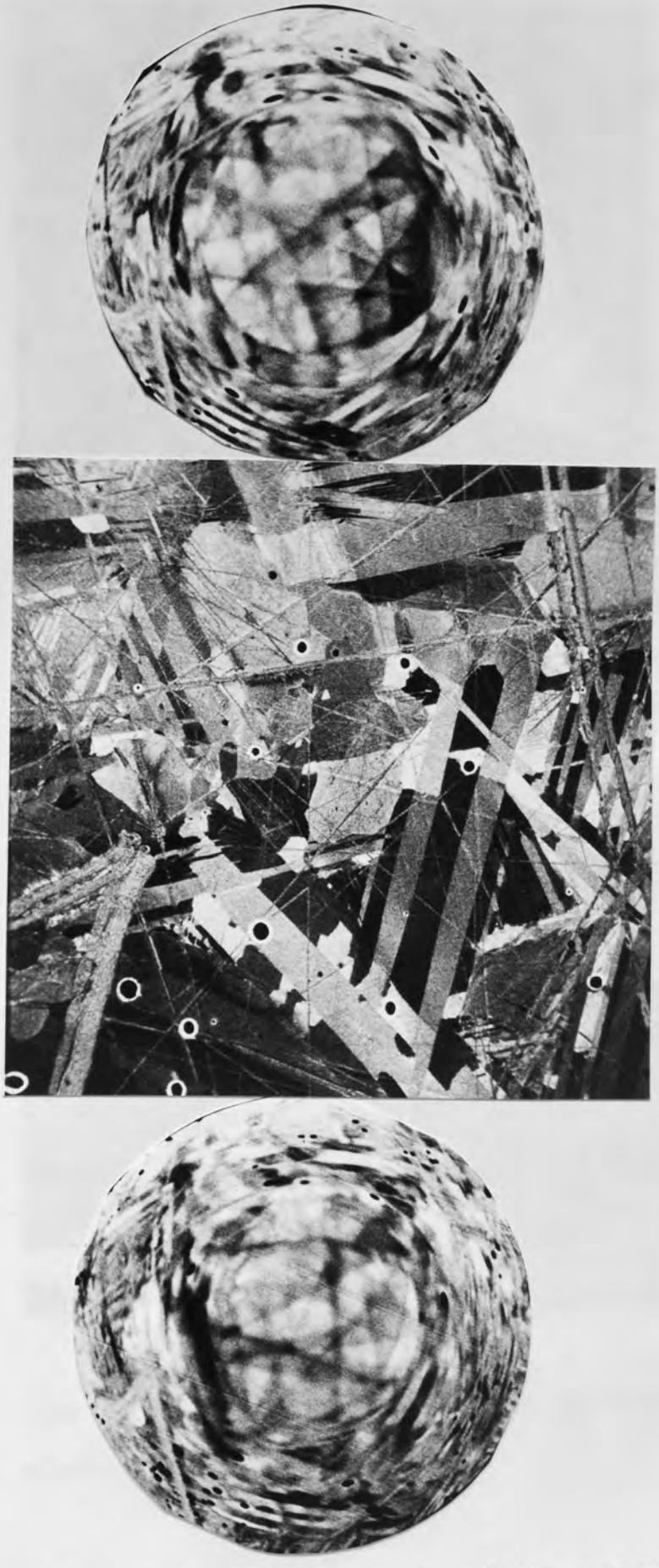

Fig 67- Backscattered electron image of the recrystallized grains and their corresponding channelling patterns x600

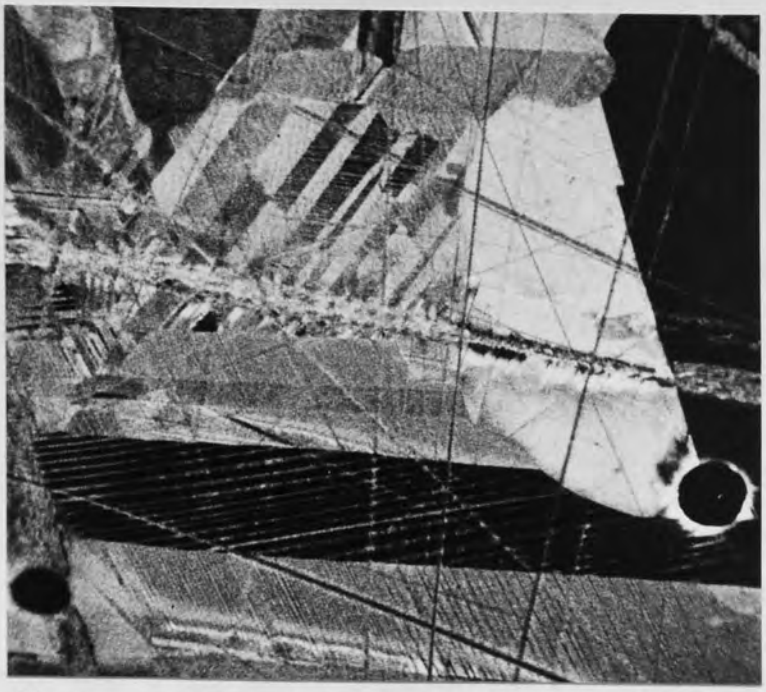

Fig 68 a) Backscattered electron image of recrystallized grains and twinned microstructure x2400

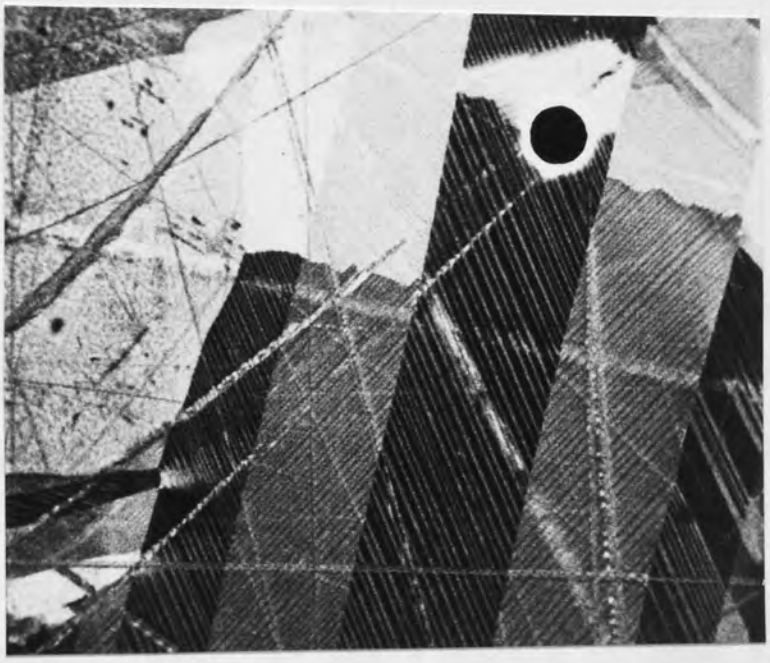

b) The twinned structure revealed by backscattered electron mode x2400

3.I.8 Grain-boundary fracture

When samples of Pt_2FeCu were rapidly quenched either from above T_c or below, very fine cracks appeared along some of the grain-boundaries. These cracks appeared to propagate or new cracks were initiated when samples were rapidly quenched several times.

Figure 69 shows the intercrystalline fracture between two grains, G_1 and G_2 where grain G_2 seems to be displaced normal to the surface. This effect can clearly be observed in figure 70 where G_2 and G_3 seem to be slightly higher than the rest of the grains. Some evidence of the twinned structure is also visible in this figure 70.

Figure 71 is the optical micrograph of a sample which has been quenched five times and shows the spread of these cracks.

To prevent this effect a much slower quenching rate was employed during the recrystallization studies but, nevertheless, some cracks appeared when the samples were subjected to frequent quenching, (figures 50 and 53).

Another unusual effect of the ejection of some of the smaller grains from the interior regions, in addition to the grains on the edges of samples, was also observed during the recrystallization studies. The ejection of the grains is shown in figures 72 and 52. In the vicinity of the ejected

grains, the deformation twins showed complex features as shown in figure 72. Similar features were also observed when material was slow cooled (inside the furnace from 1400°C to room temperature) but the grain-boundary fractures were not on the same scale as the quenched samples.

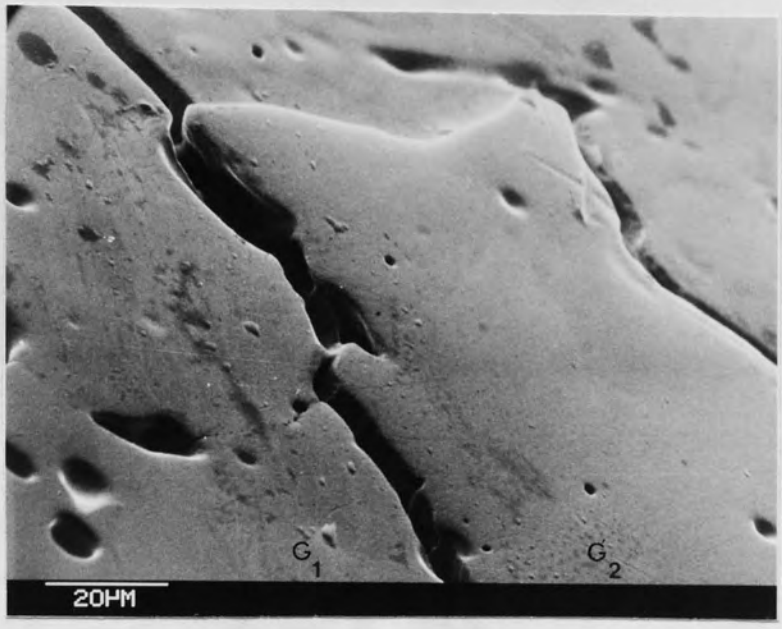

Fig 69- Scanning electron micrograph of the intercrystalline fracture. Thermally etched x775

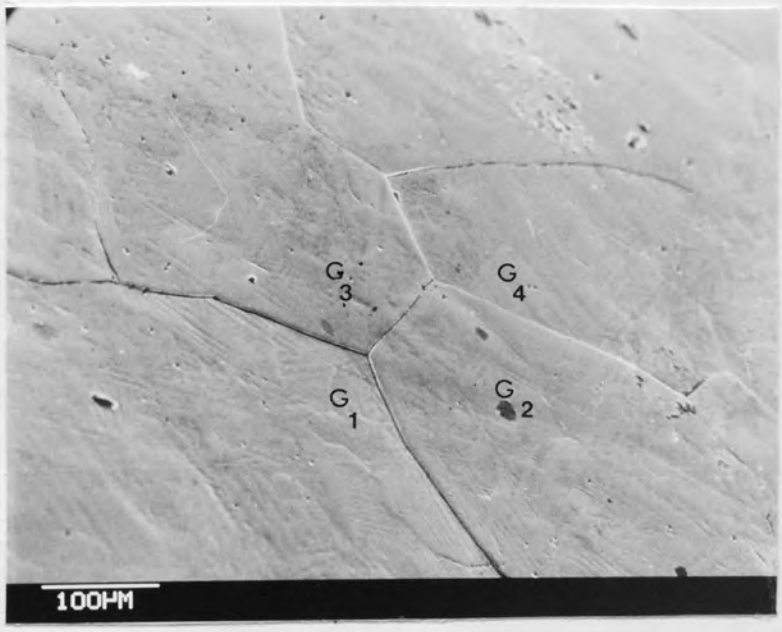

Fig 70- Scanning electron micrograph, showing the vertical displacement of grains G_2 and G_3. Thermally etched x150

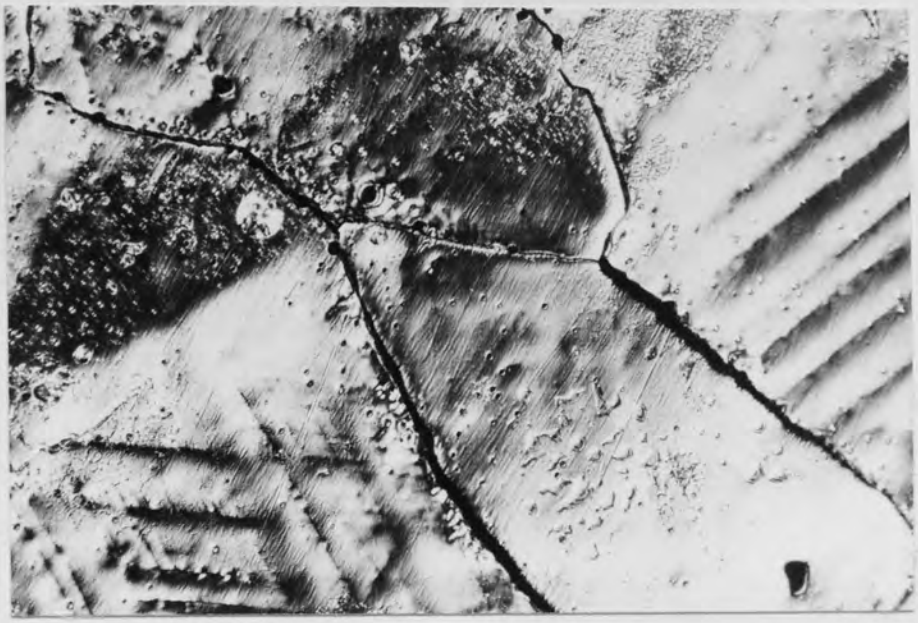

Fig 71- Optical micrograph of the grain-boundary fractures. Thermally etched x540

Fig 72- Optical micrograph showing the ejections of the small grains. Etched x168

section II

Isothermal section at 1000°C

The isothermal sections were determined from the x-ray diffractometer (lattice parameter measurements) and Electron Microprobe Analysis(chemical composition measurements) of the alloys under study. During E.P.M.A the following precodures were adopted in order to measure the true composition of coexisting phases;

a)- When the coexisting phase was relatively large, the chemical compositions of the adjacent areas of the interphase were measured.

b)- Second phase particles of less than 3 μm were not analysed.

In presenting the isothermal sections some measures were also taken in order to avoid needless repetitions and are as follows;

1)- No x-ray diffractometer traces are reproduced other than the trace shown in figure 11 which is truly representative of the other traces obtained.

2)- When a few alloys happened to have a similar micro-structure, only one representative of the group is shown.

3)- When some alloys happened to be in the single,two-phase or three-phase fields, only a minimum number of them which helped to construct the phase-boundaries are shown or mentioned.

4)- Numbering of alloys in the two sections are not corresponding number.

At this stage, it should be emphasized that the nature or formation mechanisms of the observed microstructures will not be discussed here as the present project was designed to investigate the stoichiometric Pt_2FeCu phase relationships with the other binary compounds and preliminary investigations of its structural changes.

Figure 73 shows the isothermal section at 1000°C of the ternary phase diagram. The section is constructed by combining the experimental results from the ternary alloys with the currently accepted constituting binary systems, Table 5 shows the compositions, lattice parameters and c/a ratios of the alloys, used to construct the 1000°C section. Below is a list of the Greek letters which have been used to designate the different phases in the ternary system;

Disordered f.c.c Pt-rich	γ''_D-phase
Ordered f.c.t	β_O-phase
Disordered f.c.c. Cu-rich	γ'_D-phase
Disordered f.c.c Fe-rich	γ_D-phase

Previous investigations in the Pt-Fe binary system have confirmed that below 1300°C, there exists a broad single phase region of an ordered tetragonal structure which is based on the PtFe Compound. In the present work it was found that at 1000°C and by addition of Cu, this region extends towards the interior part of the system and reaches the 50% Pt, 30% Cu and 20% Fe approximately. The variations of the Pt content in the β_O-phase is 38% - 58%.

X-ray traces of the alloys which are situated in the β_0-phase confirm the presence of the superlattice reflections and the tetragonality of their structure cells.

At the exact composition of 50%Pt, 25% Fe and 25% Cu, there exists a ternary compound (Tulameenite). Cabri et al [55] (alloy no 54) which as can be observed from Figure 73 forms a continuous region of solid-solution with the binary compound PtFe, with a = 3.895 A^o and c = 3.595 A^o compared with a = 3.847 A^o, c = 3.715 A^o, Cabri [55], for PtFe. The changes in lattice parameters can be studied in more detail when the dimensional changes are plotted along the line Pt_2FeCu-PtFe. Figure 74 shows the effect of the Cu addition along such a line which gives rise to the increase in a-parameter and decrease of c- parameter of the alloys. In the same figure the variation of c/a and the volume per atom changes can also be observed.

Figure 73 - The Pt-Fe-Cu ternary isothermal section at 1000°C.

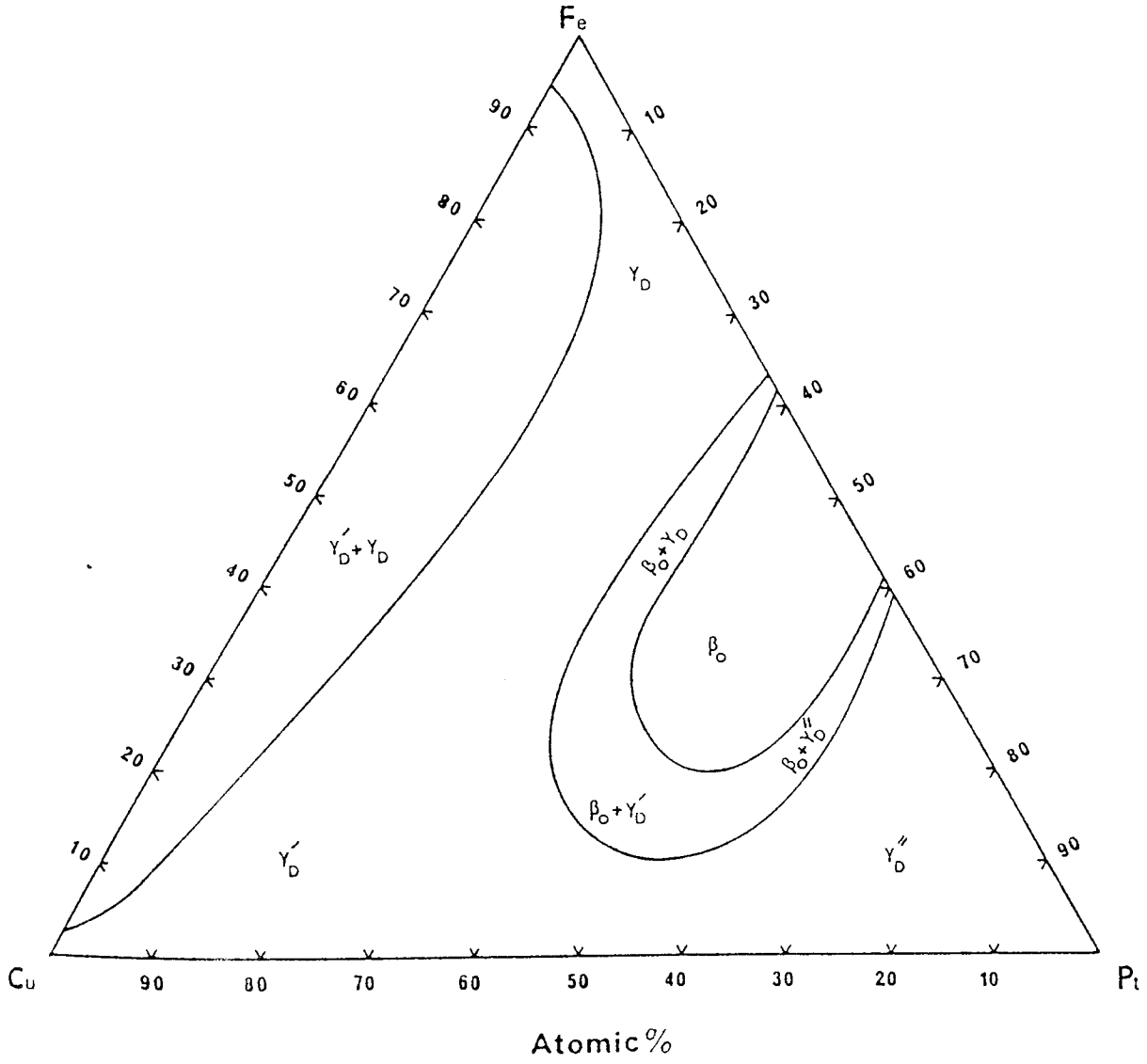

TABLE-5

Alloy No.	Overall Compositions(at%)			Phase separations (at%)			Lattice Parameters		c/a ratio
	Pt	Fe	Cu	Pt	Fe	Cu	a(A°)	c(A°)	
1	61.2	33.6	5.2	59.2	35.4	5.4	3.861	3.716	0.962
				61.9	33.0	5.1	3.866	-	-
2	61.5	27.7	10.8	59.3	30.5	10.2	3.882	3.645	0.939
				62.6	26.8	10.6	3.885	-	-
3	61.0	19.4	19.6	58.2	24.1	17.7	3.896	3.582	0.919
				62.3	17.9	19.8	3.847	-	-
4	57.7	17.2	25.1	55.9	20.8	23.3	3.883	3.613	0.931
				59.6	13.1	27.3	3.832	-	-
5	55.1	14.4	30.5	53.3	19.8	26.9	3.861	3.621	0.938
				56.3	11.1	32.6	3.791	-	-
6	50.8	14.4	34.8	49.8	20.2	30.0	3.869	3.596	0.929
				51.5	10.3	38.2	3.828	-	-
7	46.6	16.9	36.5	47.4	21.3	68.7	3.871	3.619	0.935
				45.6	12.3	42.1	3.794	-	-
8	43.7	20.1	36.1	45.3	23.1	31.6	3.874	3.621	0.935
				41.5	15.6	42.9	3.780	-	-
9	40.4	22.3	37.3	43.3	25.2	31.5	3.878	3.627	0.935
				38.1	19.2	42.7	3.767	-	-
10	38.4	25.7	35.9	41.4	27.3	31.3	3.875	3.631	0.937
				35.4	23.9	40.7	3.759	-	-
11	36.1	30.8	33.1	39.5	31.2	29.3	3.871	3.638	0.939
				33.4	30.2	36.4	3.731	-	-

Alloy No	Overall Compositions(at%)			Phase separations(at%)			Lattice Parameters		c/a ratio
	Pt	Fe	Cu	Pt	Fe	Cu	a(A^o)	c(A^o)	
12	36.1	37.5	26.4	38.3	37.2	24.5	3.864	3.642	0.945
				32.9	37.9	29.2	3.742	-	-
13	36.8	44.4	18.8	38.6	43.8	17.6	3.848	3.673	0.955
				33.2	35.5	31.3	3.763	-	-
14	37.1	52.3	10.6	39.0	51.5	9.5	3.828	3.686	0.963
				34.4	33.5	32.1	3.772	-	-
15	37.5	59.6	2.9	38.6	58.5	2.9	3.816	3.689	0.967
				36.1	61.2	2.7	3.788	-	-
16	5.7	12.2	82.1	3.3	4.6	92.1	3.678	-	-
				10.4	26.3	63.3	2.911	-	-
17	12.9	46.9	40.2	2.6	4.1	93.3	2.906	-	-
				16.3	61.4	22.3	3.637	-	-
18	8.1	51.4	40.5	1.8	3.2	95.0	3.631	-	-
				11.8	80.8	7.4	2.894	-	-
19	5.1	58.6	36.3	1.1	2.9	96.0	3.628	-	-
				7.1	87.8	5.1	2.882	-	-
20	1.8	49.1	49.1	0.5	2.8	96.7	3.622	-	-
				2.6	92.5	4.9	2.879	-	-
21	1.8	97.2	1.0	1.8	97.2	1.0	3.651	-	-
22	8.1	88.7	3.2	8.1	88.7	3.2	3.659	-	-
23	15.8	82.7	1.5	15.8	82.7	1.5	3.669	-	-
24	14.1	78.1	7.8	14.1	78.1	7.8	3.673	-	-

Alloy No.	Overall Compositions(at %)			Phase separations (at%)			Lattice parameters		c/a ratio
	Pt	Fe	Cu	Pt	Fe	Cu	a(A^o)	c(A^o)	
25	25.8	69.1	5.1	25.8	69.1	5.1	3.753	-	-
26	33.0	57.6	9.4	33.0	57.6	9.4	3.779	-	-
27	17.7	53.2	29.1	17.7	53.2	29.1	3.728	-	-
28	31.1	43.2	25.7	31.1	43.2	25.7	3.751	-	-
29	13.3	29.6	57.1	13.3	29.6	57.1	3.726	-	-
30	16.5	41.6	41.9	16.5	41.6	41.9	3.713	-	-
31	30.6	25.6	43.8	30.6	25.6	43.8	3.728	-	-
32	26.3	19.7	54.0	26.3	19.7	54.0	3.715	-	-
33	19.9	16.1	64.0	19.9	16.1	64.0	3.704	-	-
34	11.8	24.4	63.8	11.8	24.4	63.8	3.702	-	-
35	9.5	11.5	79.0	9.5	11.5	79.0	3.694	-	-
36	23.2	2.6	74.2	23.2	2.6	74.2	3.707	-	-
37	35.6	9.4	55.0	35.6	9.4	55.0	3.721	-	-
38	42.9	12.4	44.7	42.9	12.4	44.7	3.774	-	-
39	48.8	9.1	42.1	48.8	9.1	42.1	3.817	-	-
40	58.8	8.8	32.4	58.8	8.8	32.4	3.829	-	-
41	43.9	3.0	53.1	43.9	3.0	53.1	3.801	-	-
42	70.1	20.1	9.8	70.1	20.1	9.8	3.863	-	-
43	70.0	9.8	20.2	70.0	9.8	20.2	3.854	-	-
44	81.1	10.9	8,0	81.1	10.9	8.0	3.888	-	-
45	56.2	26.4	17.4	56.2	26.4	17.4	3.891	3.591	0.923
46	50.0	30.1	19.9	50.0	30.1	19.9	3.887	3.621	0.932

Alloy No.	Overall compositions(at%)			phase separations (at%)			Lattice parameters		c/a ratio
	Pt	Fe	Cu	Pt	Fe	Cu	a(A^o)	c(A^o)	
47	50.0	37.2	12.8	50.0	37.2	12.8	3.871	3.658	0.945
48	50.0	44.9	5.1	50.0	44.9	5.1	3.862	3.685	0.954
49	45.8	27.2	27.0	45.8	27.2	27.0	3.881	3.618	0.932
50	41.2	29.5	29.3	41.2	29.5	29.3	3.874	3.632	0.938
51	40.1	44.9	15.0	40.1	44.9	15.0	3.833	3.688	0.962
52	40.4	58.1	1.5	40.4	58.1	1.5	3.837	3.711	0.968
53	58.2	38.1	3.7	58.2	38.1	3.7	3.869	3.724	0.963
54	50	25	25	50	25	25	3.895	3.595	0.923

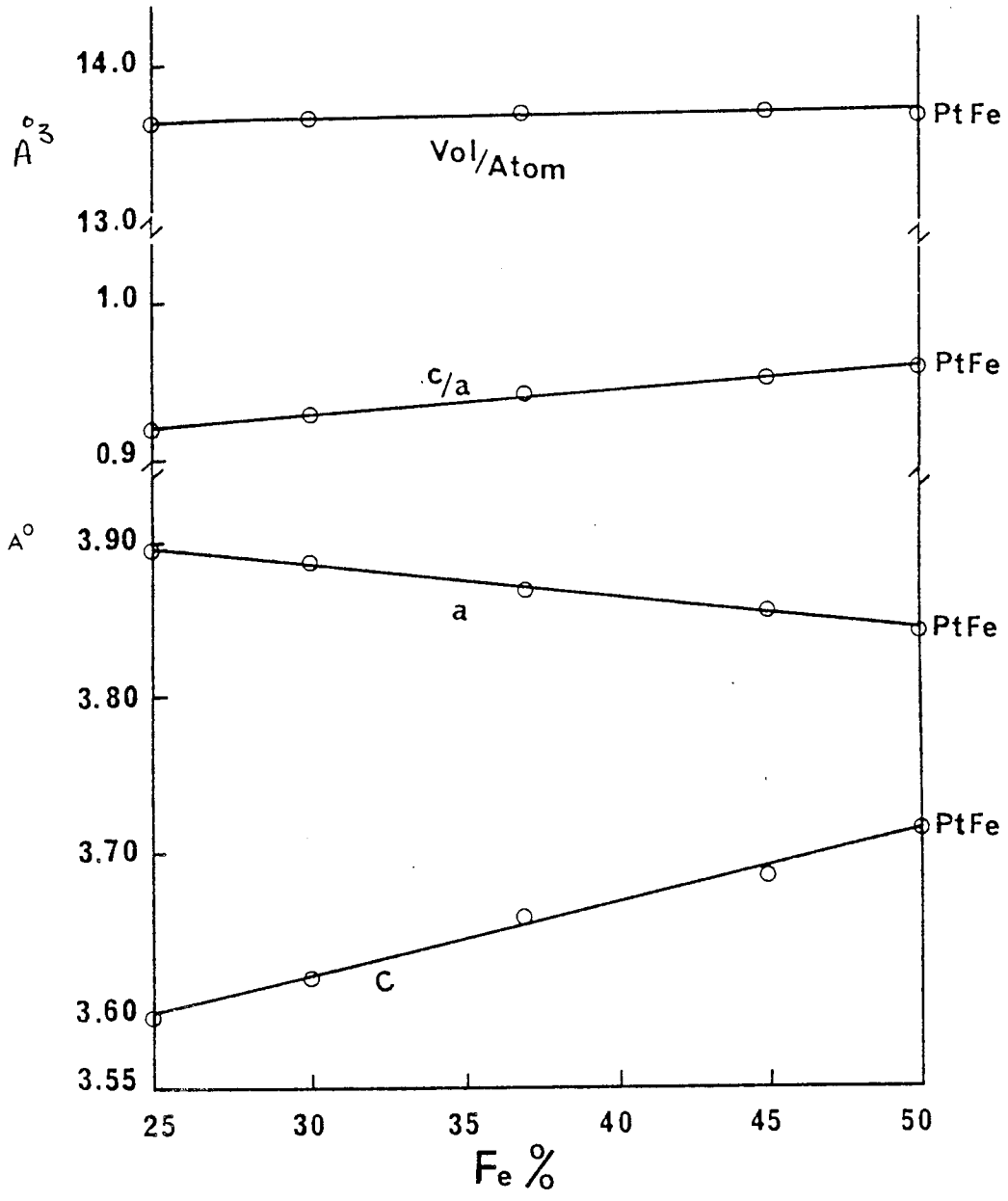

Figure 74 - Dimensional changes of the ordered tetragonal single phase along the Pt_2FeCu - PtFe line.

After the initial homogenization treatments, the alloys which are located in the β_o-phase region were slow cooled to 1000°C and held there for a further period of three months. Therefore, neither the initial microstructural features nor the O/D transformation were being studied. So the microstructures shown here are the end results of the above-mentioned heat-treatments.

The effect of the different heat-treatments on one of the alloys in β_o-phase (Stoichiometric Pt_2FeCu) has been studied in detail in section I. These studies have revealed that the recrystallization mechanism is the most dominant structural change which occurred on any heat-treatments below T_c. Equilibrium heat treatments made to establish the 1000°C isothermal phase diagram section also produced recrystallization of the tetragonal phase β_o in the off-stoichiometric Pt_2FeCu samples, but not all the alloys have been equilibrated for the same time. For example, figures 75 and 76 are optical micrographs of the alloys 46 and 47 which show that part of the twinned structures of the original material is still being consumed by the advancing new grains, whereas the alloys 45 and 50 are fully recrystallized under identical conditions.

Whether these alloys which are in the β_o-phase are partially or fully recrystallized, some additional features can also be observed. These features have an identical character to that of the stoichiometric alloy 54 (section 3.I.7.2) where they were found to be deformation twinning. These

features are shown by arrows in figures 75 and 76. These deformation twins are more pronounced in alloys 45 and 50 where the material is fully recrystallized, figures 77 and 78.

Fig 75- Optical micrograph of alloy 46 showing the attack of the recrystallized grains towards the original twinned matrix. Etched x168

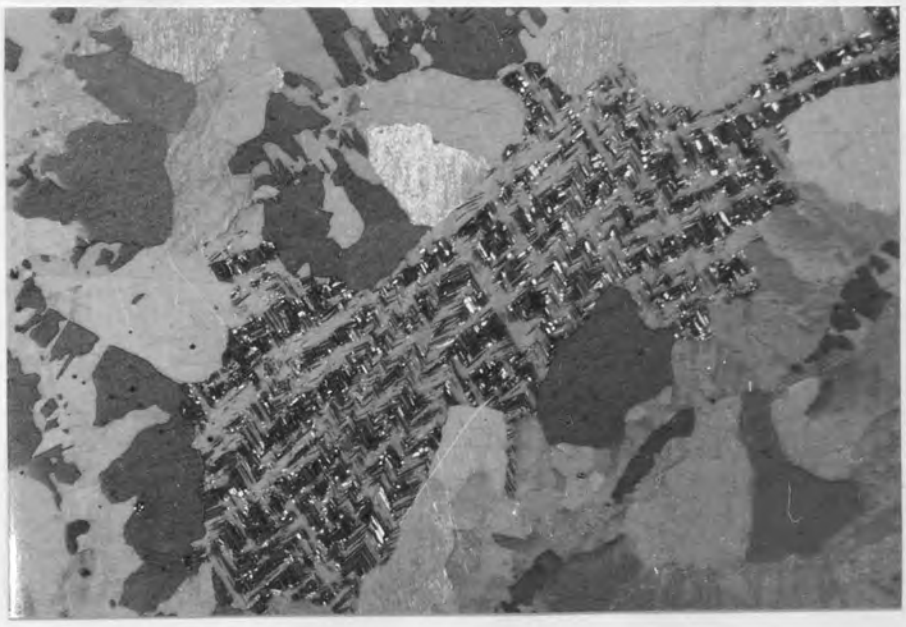

Fig 76- Optical micrograph of alloy 47 showing partially recrystallized basket weave structure. Etched. x336.

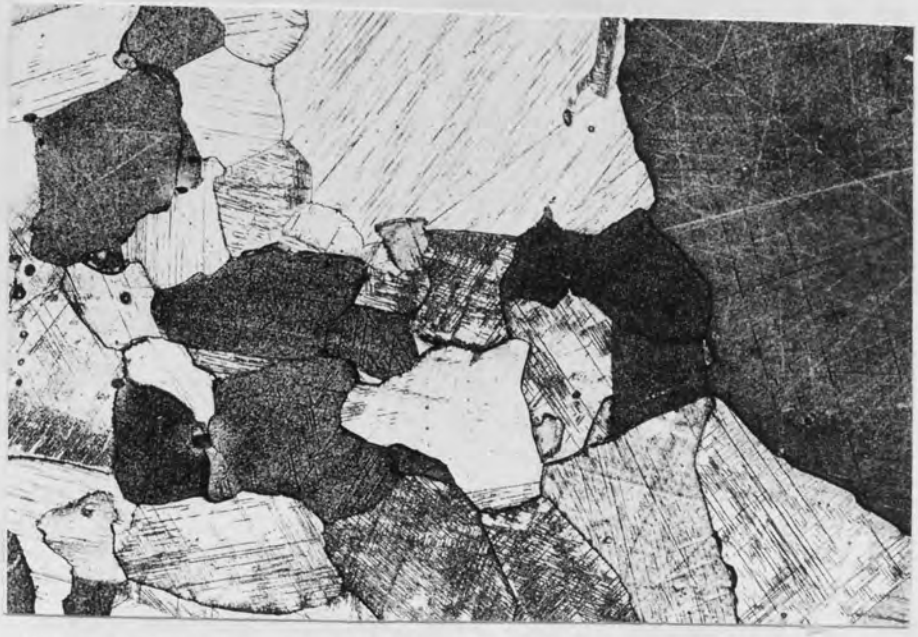

Fig 77- Optical image of the recrystallized alloy 45. Etched x42

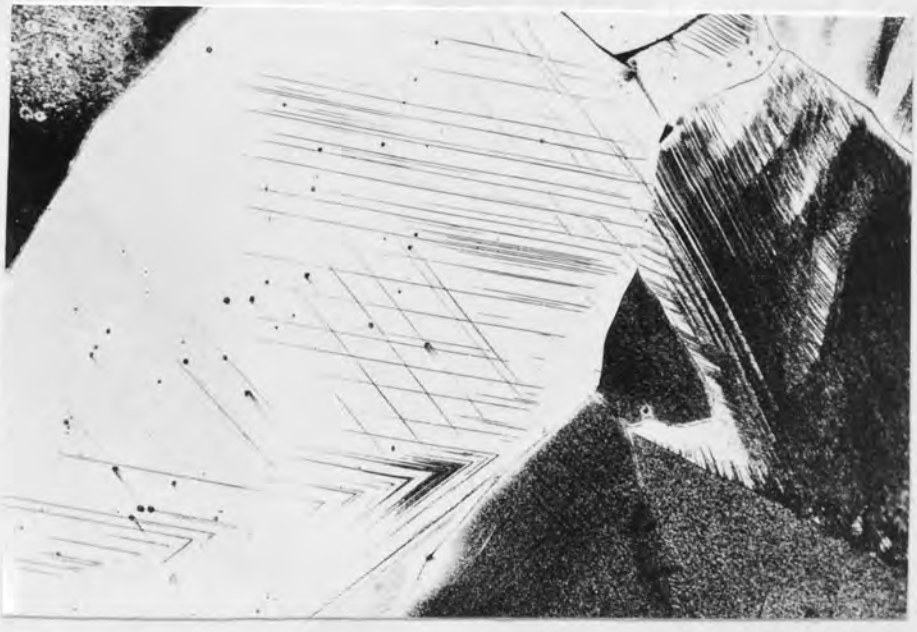

Fig 78- Optical micrograph of the recrystallized alloy 50 showing the deformation twins. Etched x270

The ordered tetragonal β_o-phase is separated from the γ_D, γ_D' and γ_D'' single phase regions by a wide two-phase field.

X-ray diffraction traces from alloy 1,2, ..., and 15 show two coexisting diffraction patterns, one belonging to the disordered f.c.c. phase and the other to the ordered tetragonal β_o phase.

Different microstructures were observed in this two-phase field. Most of the alloys had the γ_D''-phase as their major and β_o as the minor phase. The β_o-phase usually appears as either plate-like or discontinuous grain-boundary particles. Some evidence of the twinning was also observed inside the plates or particles of the β_o-phase. Figures 79 and 80 show these twinned features.

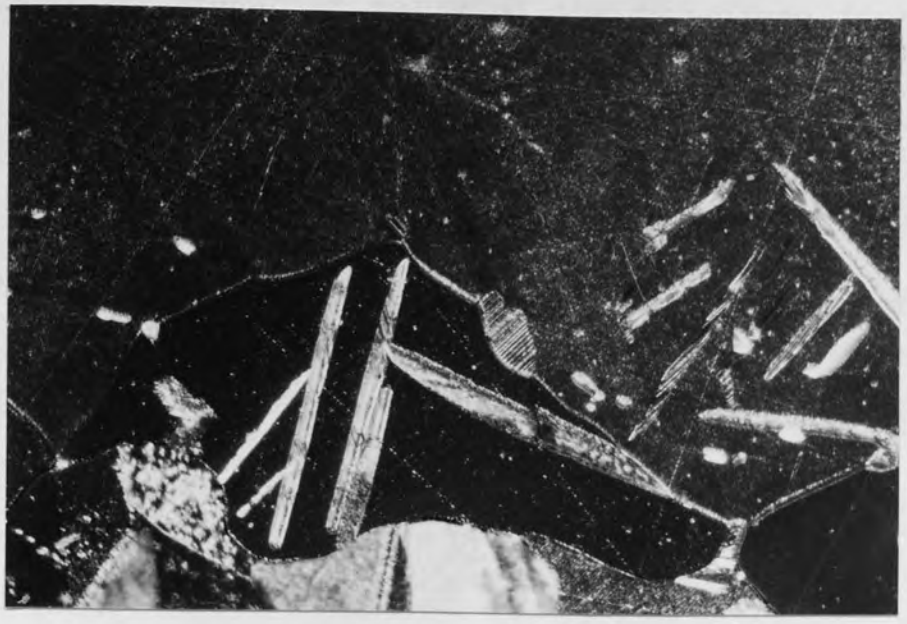

Fig 79- Plate-like and grain boundary precipitations of the β_0-phase in γ'' matrix. Polarized light micrograph of alloy 2. Etched. x135

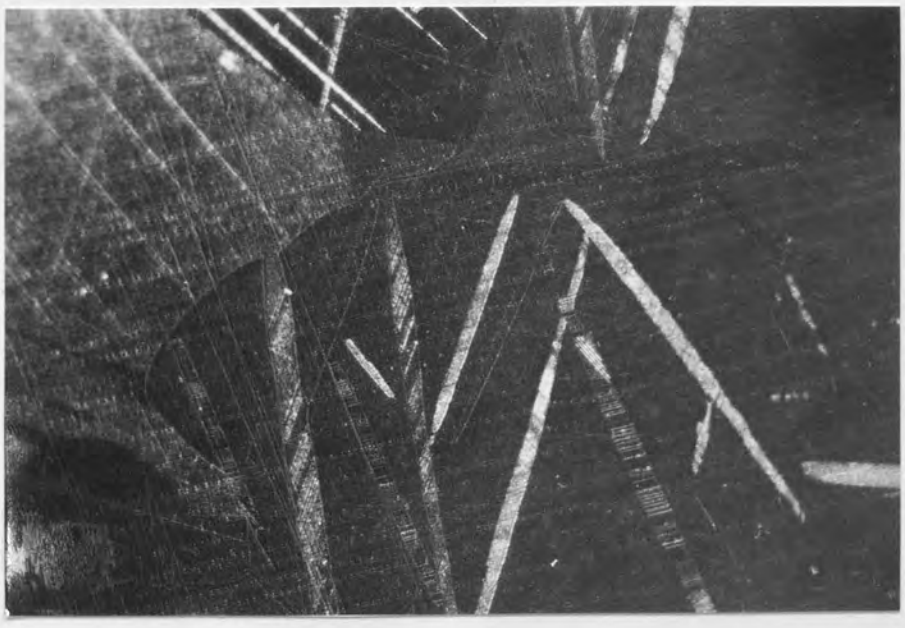

Fig 80- Fine twinning inside the β_0 phase plate-like precipitates of alloy 2. x168

The copper or iron-rich parts of the two-phase field, i.e., $\beta_o + \gamma'_D$ and $\beta_o + \gamma_D$ show similar microstructures. The two phases were nearly equally distributed in the samples studied. Figures 81 and 82 are the optical micrographs of typical areas of alloys no 8 and 11 where the alloys are comprised of the β_o-phase (light areas) and γ'_D or γ_D (dark areas). The β_o-phase appears to be irregularly distributed in the samples.

Fig 81- Optical micrograph of alloy 8 showing the β_0 (light areas) and γ'_D (dark areas) of the ($\beta_0+\gamma'_D$) phase mixtures. Etched . x84

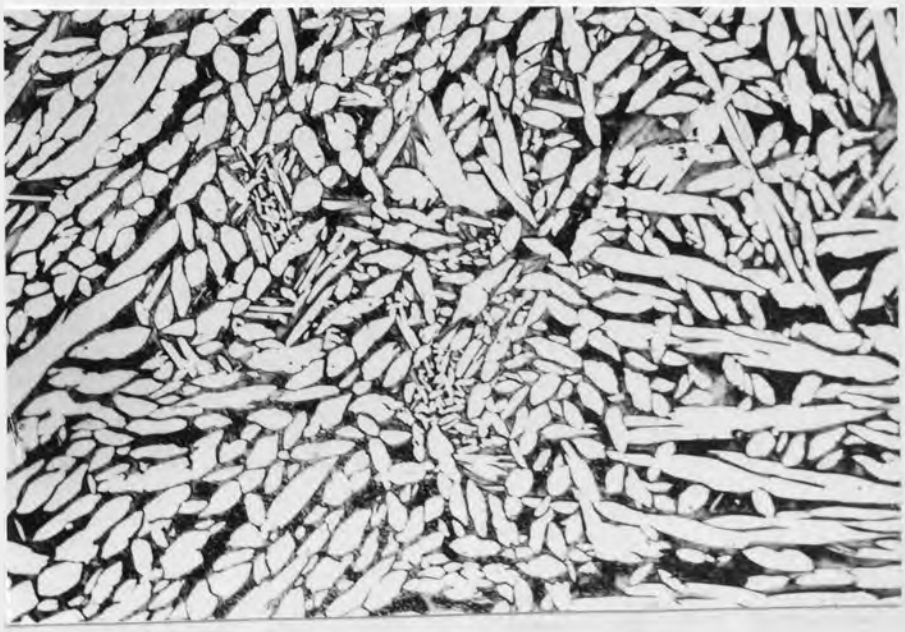

Fig 82- Optical micrograph of alloy 11 showing the β_0 (light areas) and γ_D (dark areas) of the($\beta_0+\gamma_D$) phase mixtures. Etched. x84

Between the single phases of γ'_D and γ_D there exists a two-phase field mixture of Cu and Fe-rich phases. The x-ray traces of the alloys in this phase field are comprised of the disordered f.c.c plus b.c.c. lines. Although these alloys were quenched from 1000°C, it was expected to retain the (γ-Fe). Nevertheless, it appears that the γ- Fe had transformed on quenching.

Figure 83 is typical of the structure in alloys 17,18,19 and 20 in this phase field. The Fe-rich particles (γ_D - phase) are embedded in a Cu-rich matrix.

The existence of such Fe-rich particles could be explained in terms of the applied heat- treatment. These alloys were homogenized at 1200°C where it is approximately 110°C above the copper melting point. It was thought that the addition of platinum and iron to copper should increase the latter melting point, therefore 1200°C was selected, but it was proved otherwise, i.e., the Cu-rich phase had melted during the homogenization treatment and subsequently solidified during slow cooling.

Apart from the β_D and the other two-phase fields in the 1000°C isothermal section, all other alloys were single phase solid-solutions of Pt , Fe and Cu. some of these alloys played an important part in determining the boundaries of the two - phase fields, so not all of these alloys are presented here, but their compositions and lattice

parameters of all single phase samples are given in Table 5. There follows a brief account of some of these single phase alloys.

Figure 84 is an optical micrograph of the γ_D region with a normal grain structure with some irregular annealing twins inside the grains.

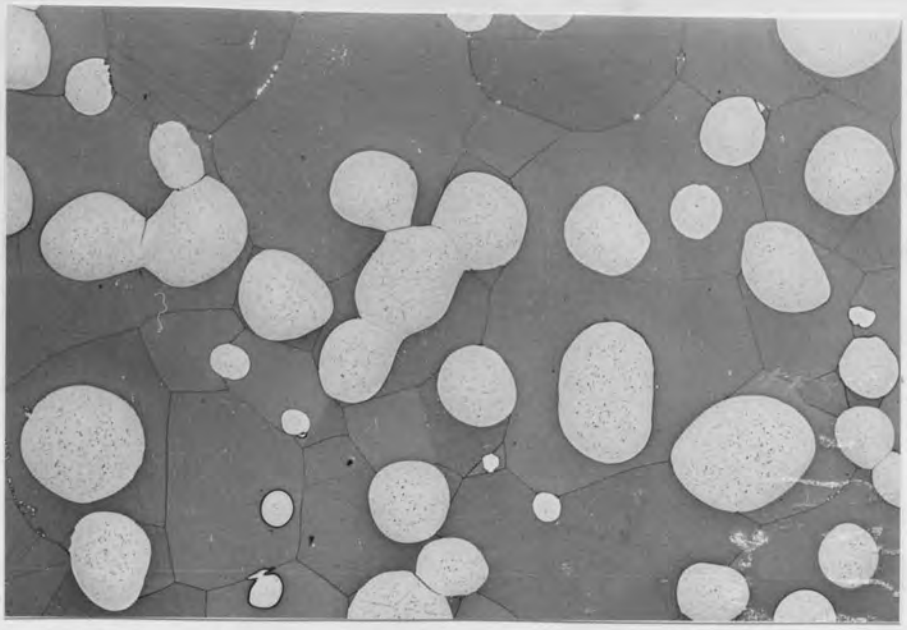

Fig 83- Optical micrograph of alloy 18 showing the Fe-rich particles embedded in the Cu-rich matrix. unetched x108

Fig 84- Polarized light micrograph of alloy 22, single phase Fe-rich, showing normal grain structures and some irregularly shaped annealing twins. Etched. x420

Another set of single phase alloys in γ'_0-region produced rather unusual microstructures, these were 38,37,36,33,34 32,31 and 29 and figure 85 shows a typical optical micrograph of alloy 32 in which each grain was subdivided by narrow parallel bands and some of these bands were irregularly distributed, Figure 86 is a Dark-field optical micrograph of figure 85.

In the first instance it was thought that the peculiar microstructures observed in these sets of alloys were the metallographic artifacts. To obtain the true microstructure, an ion-beam etching technique was employed and figure 87 and 88 show some typical microstructure of alloy 32 produced by this technique. These appear to be essentially similar to the structure shown in figures 85 and 86 indicating that they are real.

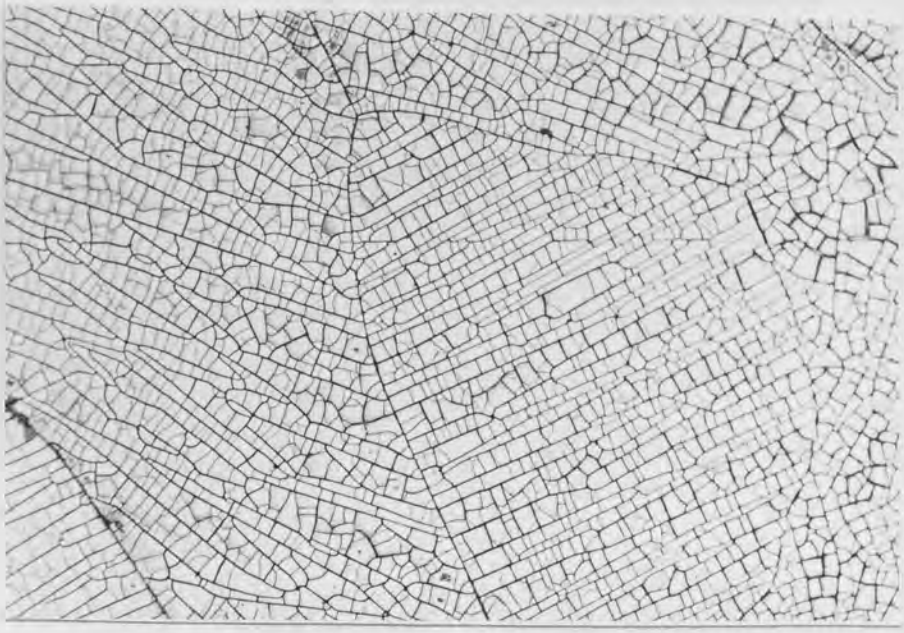

Fig 85- Bright-field optical micrograph of alloy 32(γ'_D phase) showing sub-grain boundaries. Etched. x168

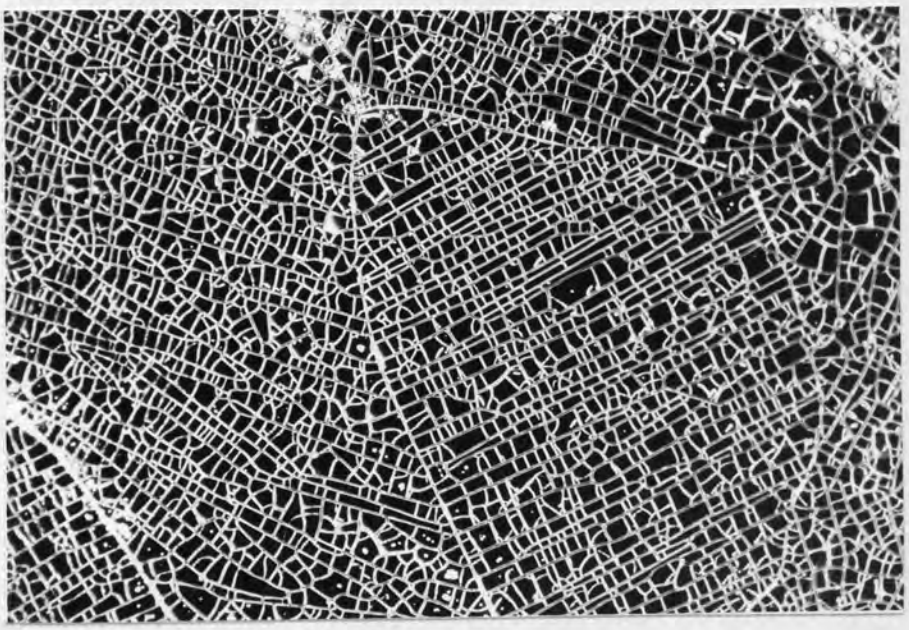

Fig 86- Dark-field optical micrograph of the same area as Fig.85. Etched. x168

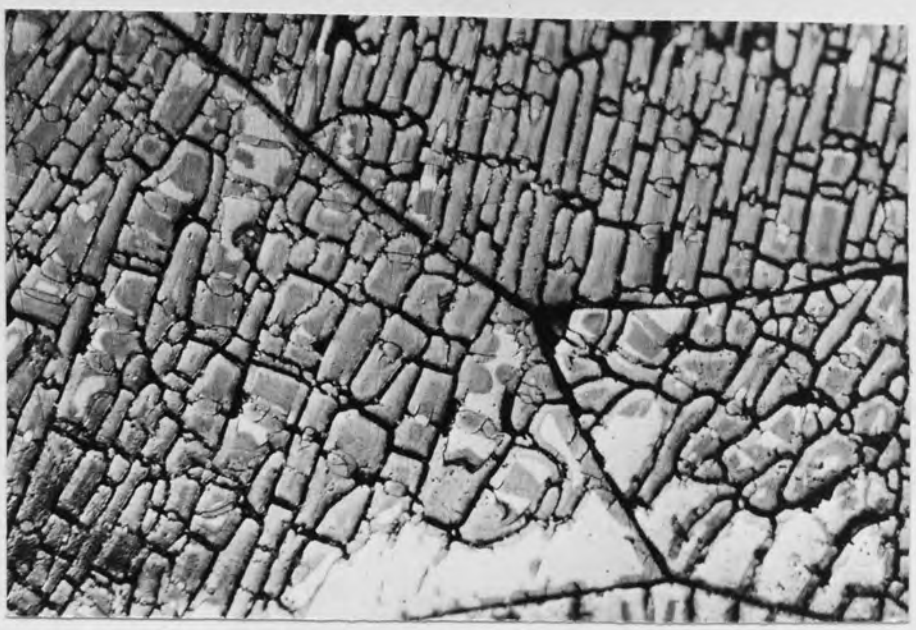

Fig 87- Optical image of alloy 32, showing similar features to Fig. 85. Ion-beam etched. x336

Fig 88- Optical micrograph of alloy 32, Interference contrast. Ion-beam etched. x336

Section III

Isothermal section at 600°C

The 600°C isothermal section was determined and similar measures to that of the 1000°C were also employed in presenting the results.

Table 6 shows the compositions and the lattice parameters of the alloys used to construct the isothermal section.

Figure 89 shows the Pt-Fe-Cu, isothermal section at 600°C constructed from the data of Table 6.

Figure 89 - The Pt-Fe-Cu ternary isothermal section at 600°C.

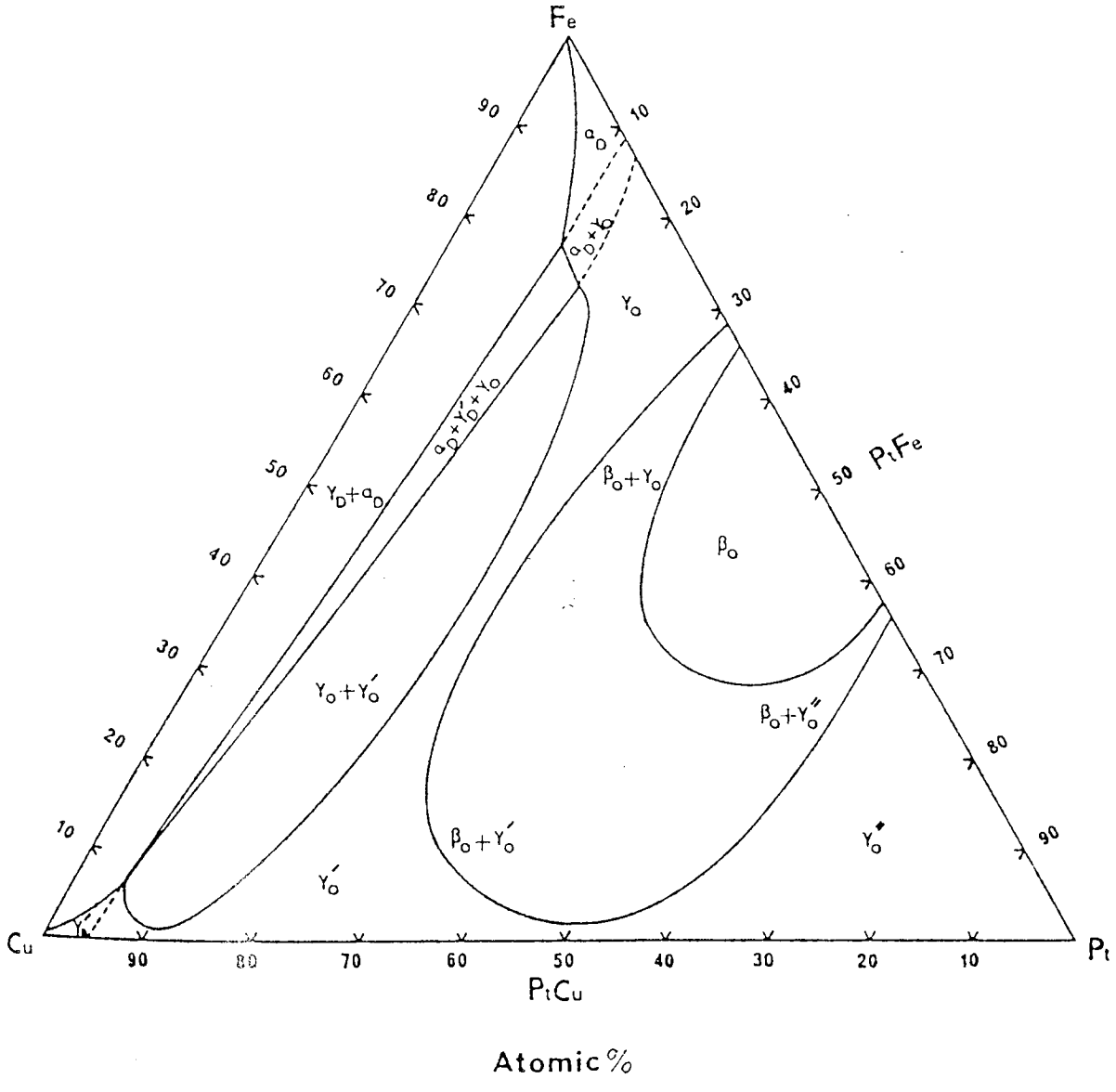

TABLE-6

Alloy NO.	Overall Composition (at%)			Phase separations(at%)			Lattice parameters		c/a ratio
	Pt	Fe	Cu	Pt	Fe	Cu	a(A^o)	c(A^o)	
1	80.2	9.8	10.0	80.2	9.8	10.0	3.886	-	-
2	69.2	21.6	9.2	69.2	21.6	9.2	3.877	-	-
3	71.4	8.9	19.7	71.4	8.9	19.7	3.864	-	-
4	63.2	32.7	4.1	61.8	34.0	4.2	3.869	3.692	0.954
				64.1	31.9	4.00	3.872	-	-
5	61.3	25.4	13.3	58.4	29.2	12.4	3.882	3.639	0.937
				63.8	21.8	14.4	3.858	-	-
6	57.1	20.8	22.1	52.4	28.2	19.4	3.897	3.606	0.925
				62.3	12.3	25.4	3.842	-	-
7	50.0	25.0	25.0	48.2	29.1	22.7	3.881	3.611	0.930
				58.9	5.4	35.7	3.821	-	-
8	47.4	26.3	26.3	46.6	30.3	23.1	3.886	3.622	0.932
				53.3	2.1	44.6	3.811	-	-
8A	63.6	6.5	29.9	63.6	6.5	29.9	3.829	-	-
9	33.6	7.2	59.2	33.6	7.2	59.2	3.754	-	-
10	49.8	28.8	21.4	45.7	30.8	23.5	3.881	3.631	0.936
				44.2	2.9	52.9	3.771	-	-
11	43.2	28.3	28.5	44.1	31.8	24.1	3.880	3.638	0.938
				39.2	6.1	54.7	3.767	-	-
12	42.3	30.9	26.8	43.2	32.4	24.4	3.878	3.639	0.938
				33.7	9.7	56.6	3.749	-	-
13	31.9	4.2	63.9	31.9	4.2	63.9	3.718	-	-

Alloy NO.	Overall Compositions(at%)			Phase separations(at%)			Lattice Parameters		c/a ratio
	Pt	Fe	Cu	Pt	Fe	Cu	a(A°)	c(A°)	
14	17.1	6.9	76.0	17.1	6.9	76.0	3.681	-	-
15	23.3	10.6	66.1	23.3	10.6	66.1	3.687	-	-
16	24.1	18.6	57.3	24.1	18.6	57.3	3.699	-	-
17	23.3	34.4	42.3	23.3	34.4	42.3	3.731	-	-
18	41.2	32.2	26.6	42.4	33.2	24.4	3.871	3.642	0.941
				27.1	19.2	53.7	3.720	-	-
19	38.8	35.3	25.9	40.0	35.8	24.2	3.861	3.652	0.946
				25.2	28.8	46.0	3.731	-	-
20	12.7	3.1	84.2	14.6	4.3	81.1	3.678	-	-
				9.6	1.6	88.8	3.661	-	-
21	18.7	25.2	56.1	21.4	29.6	49.0	3.724	-	-
				6.3	3.8	89.9	3.662	-	-
22	34.5	38.6	26.9	38.0	39.1	22.9	3.843	3.649	-
				24.8	37.3	37.9	3.739	-	-
23	14.5	21.9	63.6	21.9	37.6	40.5	3.693	-	-
				6.8	3.4	89.8	3.654	-	-
24	32.3	44.1	23.6	36.1	43.5	20.4	3.811	3.657	-
				25.4	45.3	29.3	3.755	-	-
25	18.9	40.5	40.6	22.1	48.8	29.1	3.729	-	-
				6.3	3.6	90.1	3.662	-	-
26	31.8	51.5	16.7	34.5	50.2	15.3	3.784	3.662	-
				27.7	53.7	18.6	3.763	-	-

Alloy No.	Overall Compositions(at%)			Phase separations(at%)			Lattice Parameters		c/a ratio
	Pt	Fe	Cu	Pt	Fe	Cu	a(A°)	c(A°)	
27	32.1	63.9	4.0	33.5	62.5	4.0	3.769	3.674	0.975
				30.5	35.4	34.1	3.772	-	-
28	15.6	42.2	42.2	20.2	59.9	19.9	3.747	-	-
				5.9	4.2	89.9	3.659	-	-
29	12.9	44.6	42.5	18.5	68.8	12.7	3.764	-	-
				5.4	5.2	89.4	3.657	-	-
30	23.5	56.0	20.5	23.5	36.0	40.5	3.762	-	-
31	24.4	64.8	10.8	24.4	64.8	10.8	3.769	-	-
32	11.9	64.1	24.0	11.1	77.3	11.6	3.199	-	-
				15.9	72.4	11.7	3.752	-	-
				5.1	5.8	89.1	3.656	-	-
33	9.9	47.5	42.6	10.4	76.1	12.4	3.189	-	-
				15.5	72.3	12.2	3.751	-	-
				5.0	5.7	89.3	3.656	-	-
34	2.1	50.1	47.8	3.1	94.9	2.0	2.884	-	-
				0.7	0.8	98.5	3.622	-	-
35	3.9	57.1	39.0	5.7	90.4	3.9	2.891	-	-
				1.5	1.6	96.9	3.628	-	-
36	5.4	48.4	46.2	7.8	85.1	7.1	2.902	-	-
				2.2	1.8	96.0	3.637	-	-
37	6.2	31.6	62.2	9.9	80.1	10.0	2.919	-	-
				3.9	3.3	92.8	3.649	-	-

Alloy No.	Overall Compositions(at%)			Phase Separations(at%)			Lattice Parameters		c/a ratio
	Pt	Fe	Cu	Pt	Fe	Cu	a(A^o)	c(A^o)	
38	35.8	60.9	3.3	35.8	60.9	3.3	3.771	3.679	0.976
39	35.4	51.2	13.4	35.4	51.2	13.4	3.784	3.662	0.968
40	50.0	45.5	4.5	50.0	45.5	4.5	3.853	3.679	0.955
41	50.0	33.7	16.3	50.0	33.7	16.3	3.873	3.619	0.934
42	60.1	36.8	3.1	60.1	36.8	3.1	3.851	3.692	0.959
43	42.2	44.3	13.5	42.2	44.3	13.5	3.838	3.667	0.955

At 600°C, the β_o-phase took more iron (~ 29%) and less copper (~ 21%) into the solution along the 50% platinum line. There was no expansion towards the γ''_o-phase, but at the same time it extended slightly towards the Fe-rich side of the system. As a whole it appeared that the β_o-phase rejected copper out of the solution. As the result of such compositional shifts, some of the alloys which were in β_o-phase at 1000°C had decomposed to a Copper-rich phase and off-stoichiometric tetragonal Pt_2FeCu at 600°C. Even more marked is a great change in the solubility of iron in the copper-rich γ'_o which caused the two-phase field to extend nearly to the Cu-Pt binary edge at ~50 at % Pt.

The alloys in the β_o phase field had typical recrystallized grain-structures with some evidence of the deformation twinnings within them. Additional features were also observed and they are due to the appearances of a second generation of new grains along the grain-boundaries of the recrystallized material. Although the majority of the grains seemed to have been formed by nucleation and growth at grain-boundaries, some of these new grains also appeared to have initiated from the deformation twinnings features, figures 90 and 91.

It has been mentioned in section 3.I.7 that the stress-induced recrystallization occurred in order to partially relieve the ordering stresses due to the ordering reaction.

Fig 90- Optical micrograph of alloy 41 showing primary recrystallized grains, nucleation and growth of the secondary recrystallization and deformation twins. Etched . x168

Fig 91- Similar feature to that of Fig. 90. Alloy 40. Etched. x42

The observed microstructures of the off-stoichiometric alloys in β_o-phase field indicated that a similar reaction occurs in off-stoichiometric alloys. Thus the presence of the new grains could be due to a secondary stress-induced recrystallization mechanism.

The ordered tetragonal single phase (β_o-phase) was separated from the γ''_o, γ'_o and γ_o-phase, by a two-phase field of $\beta_o + \gamma''_o$, $\beta_o + \gamma'_o$ and $\beta_o + \gamma_o$. This two-phase field consisted of the ordered tetragonal β_o-phase plus an ordered cubic (primitive) structure. The cubic phase extended and was close to the binary compound PtCu, but could not actually form a continuous region with it, since PtCu is known to have a different structure [58].

Varieties of microstructural features were observed in this two-phase field, depending on the compositions of the alloys. Further decomposition of the high temperature phases of the ordered tetragonal and disordered f.c.c seemed to have taken place via different precipitation mechanisms, i.e., continuous or discontinuous grain boundary precipitation, Widmanstätten plate formation (regular and irregularly distributed), eutectoid-type, basket weave type and finally cellular decomposition mechanisms.

Figures 92 and 93 are typical microstructures of the alloys located in the ($\beta_o + \gamma''_o$) two-phase field. The light areas are the γ''_o-phase which appear as a continuous grain boundary or plate-like precipitates and the darker areas are the β_o-phase matrix.

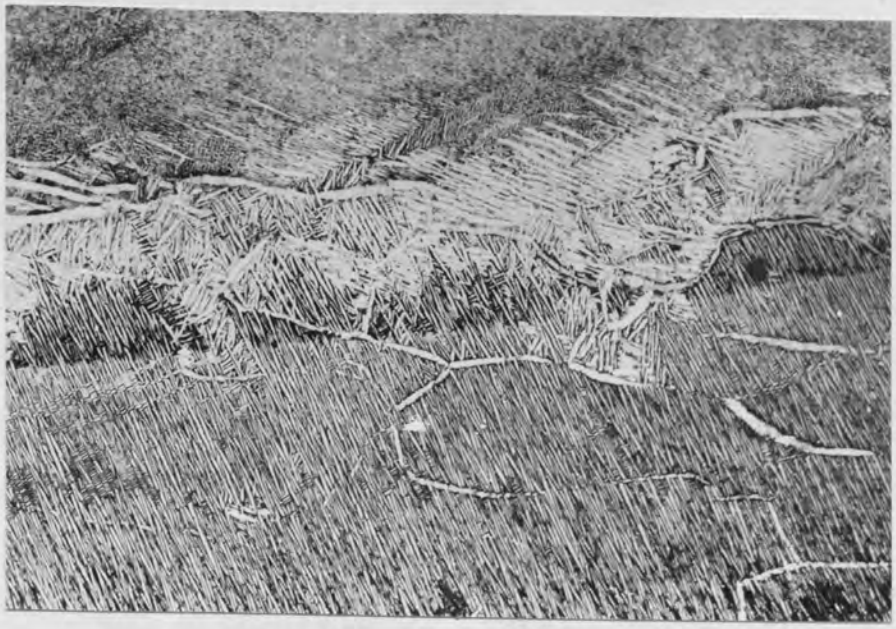

Fig 92- Optical micrograph of alloy 5 showing grain-boundary and plate-like precipitations of γ''_o phase in the β_o phase matrix. Etched.x420

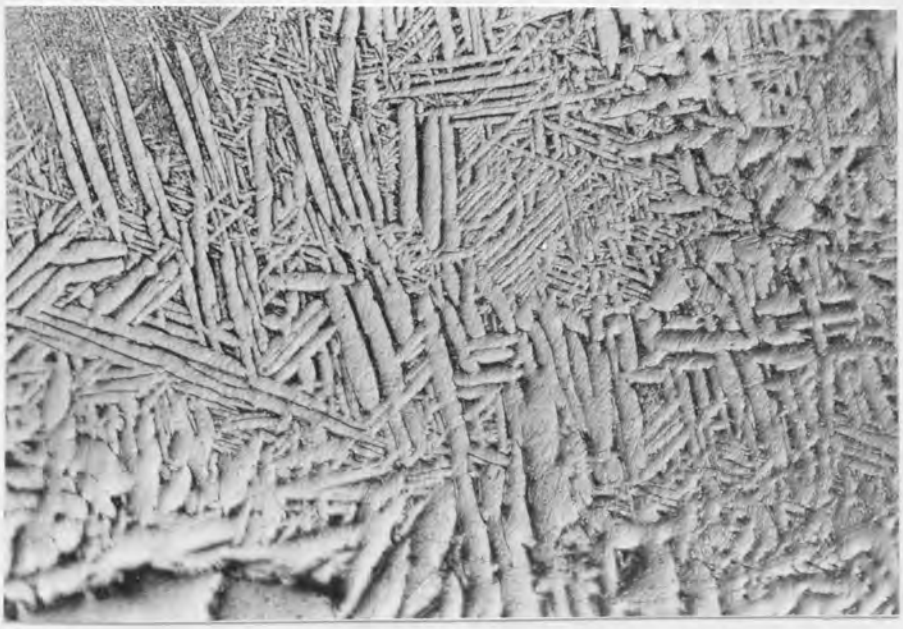

Fig 93- Microstructure of the γ''_o phase plate-like precipitation in β_o phase matrix of alloy 4. Etched. x420.

The high temperature stoichiometric compound Pt_2FeCu had decomposed on slow cooling and at 600°C it entered the $(\beta_o + \gamma_o'')$ side of the two phase field, alloy 7. The decomposition of alloy 7 took place in a very unusual manner. The central region of the specimen was a single phase region (average composition on the tie line, table 6) and only the outside region (near the free surface) had a two-phase mixture as is shown in figure 94. Figure 95 is a higher magnification of the edge of the specimen where the phase separation is clearly shown. The lighter areas are the γ_o''-phase and the darker regions are β_o-phase.

The central regions of the specimen have similar microstructures to those of the stoichiometric Pt_2FeCu, where the latter was subjected to 1000 hours recrystallization heat treatment at 1000°C . No traces of the coarse stress-relief twins were observed and the material had the normal grain structures with the deformation twins within them. Such microstructures most likely indicate the occurrence of recrystalliation mechanism in the alloy, figures 96 and 97.

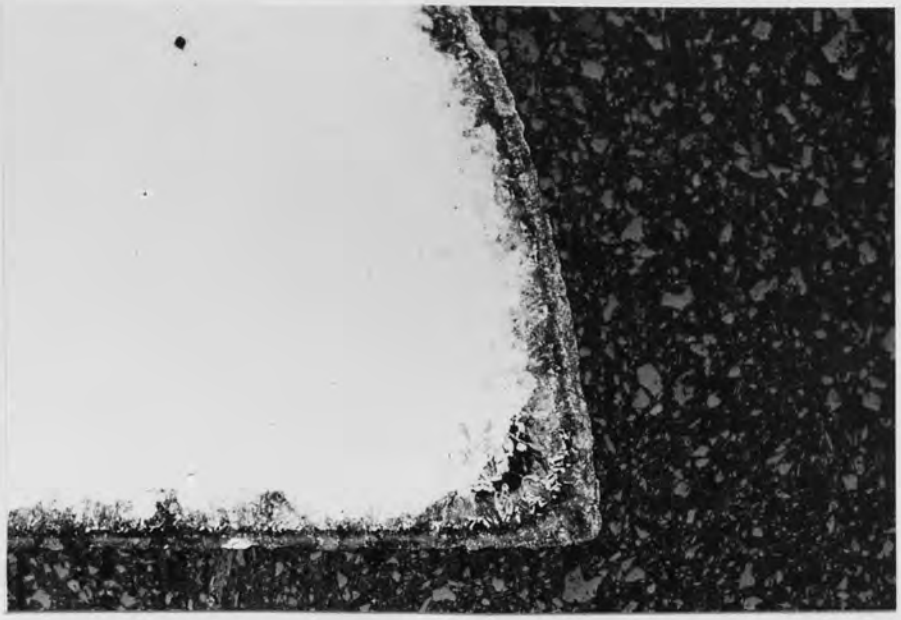

Fig 94- Optical micrograph of the ternary compound Pt_2FeCu decomposition and appearances of Y''_0 phase along the edge of the sample. Lightly etched. x33

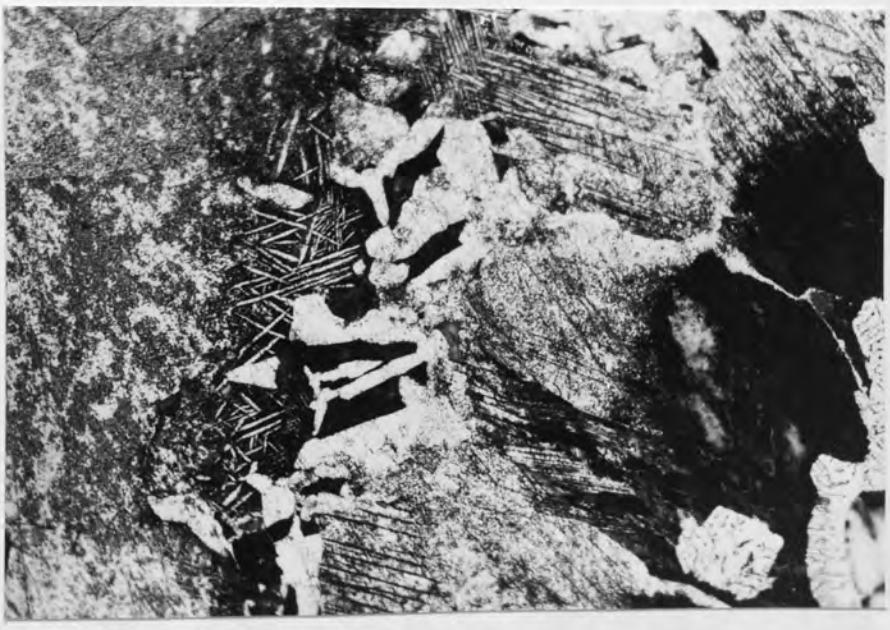

Fig 95- Higher magnification of Fig. 94, showing the precipitation of the Y''_0 phase. Etched .x336

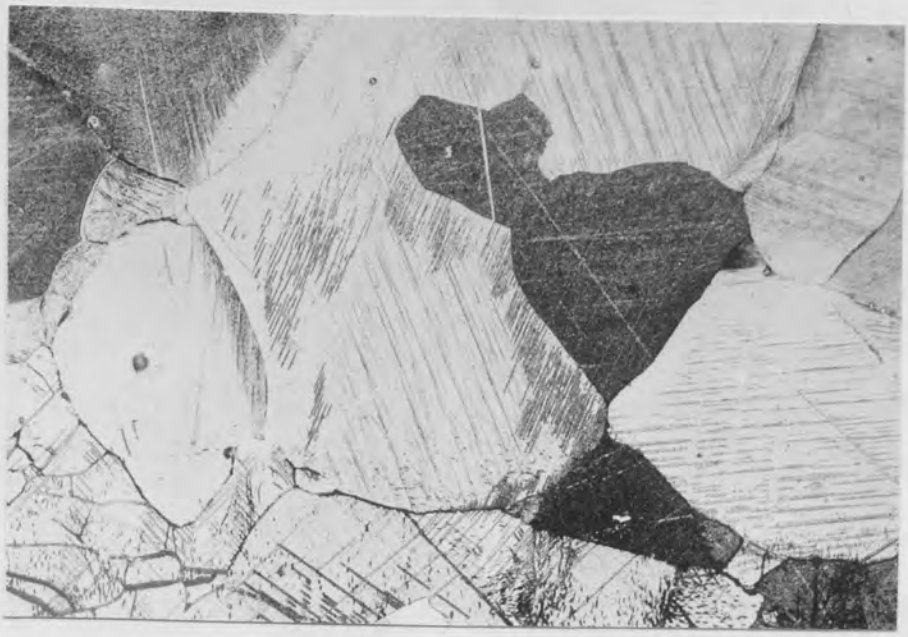

Fig 96- Normal recrystallized grain-structures of the central regions of Fig. 94 showing deformation twins. Etched x108.

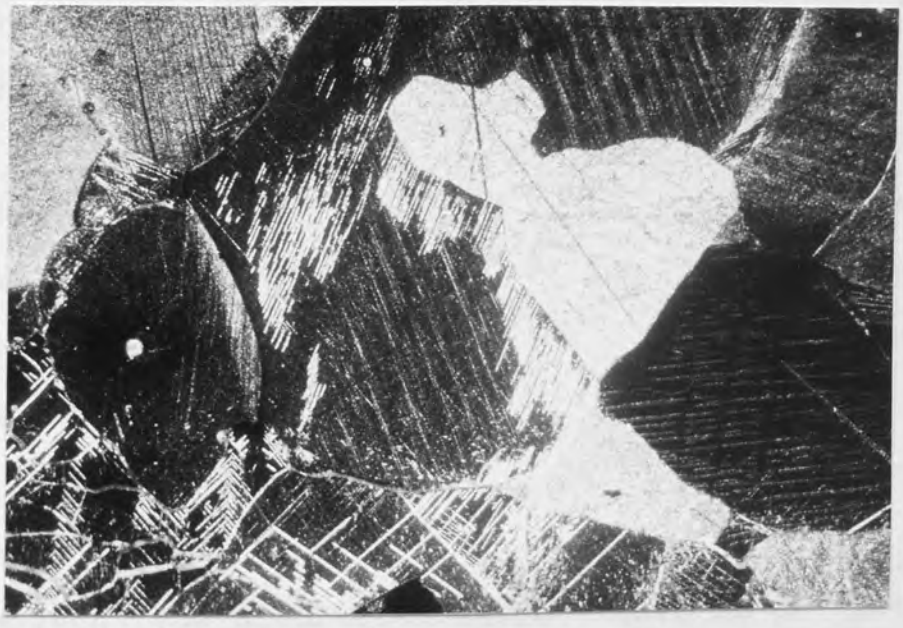

Fig 97- Polarized light micrograph of Fig,96 showing the change of contrast of the deformation twins. Etched.x108

Alloy No,6,8,10 and 12 produced the most interesting and complex microstructures in the two phase field. Similar to alloy 7, all of the phase segregation appeared to have occurred along the edges whereas the central regions of the samples also showed recrystallized structures.

Figure 98 shows a typical cellular precipitation in these alloys where the cells of ($\beta_o + \gamma_o'$) have already formed and grown to observable sizes. The dark areas are the γ_o'-phase and the lighter areas are β_o-phase. The growth of these colonies seemed to stop when the cells encountered another form of the precipitation mechanisms. Figure 99 clearly examplify such a mechanism.

Figure 100 shows a much clearer evidence of the cellular precipitations along the grain boundaries of the high temperature solid solutions and their growth towards the interior part of the grains of the matrix.

Close examination of the interior parts of the matrix, also reveal an interesting structure especially when viewed with the polarized light. Figure 101 shows such microstructure in which the twinned-bands structure of the grain is clearly visible. At higher magnifications other kinds of precipitate reaction in which fine particles of the γ_o' in addition to the basket-weaved type of precipitation exists in an alternate manner on the twinned structure. This is shown in figures 102 and 103.

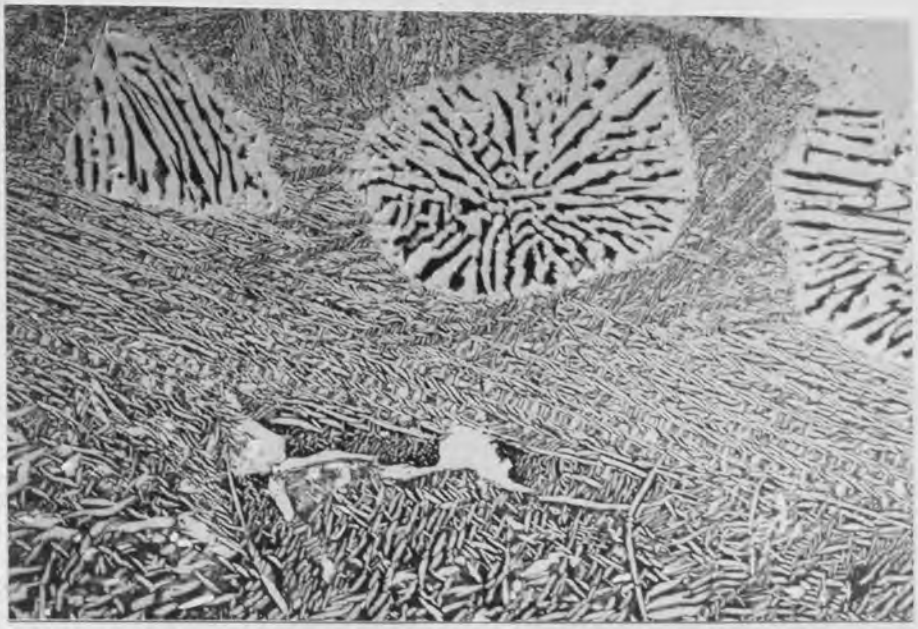

Fig 98- Cellular and plate-like decomposition in alloy 8. Optical micrograph .Etched. x420

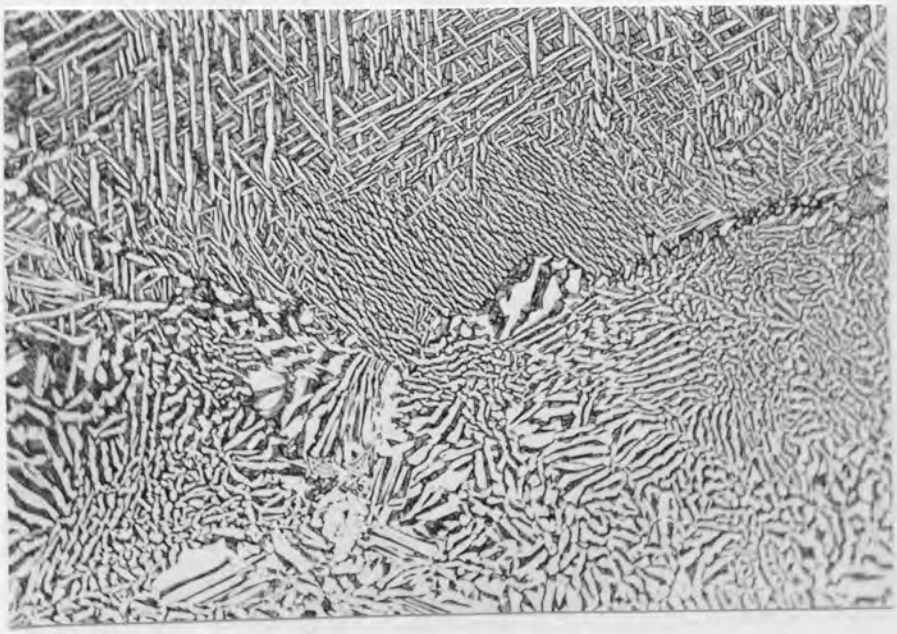

Fig 99- Microstructure of alloy 10 showing the stoppage of the cellular decompositions when having encountered plate-like precipitations. Optical image. Etched .x 420

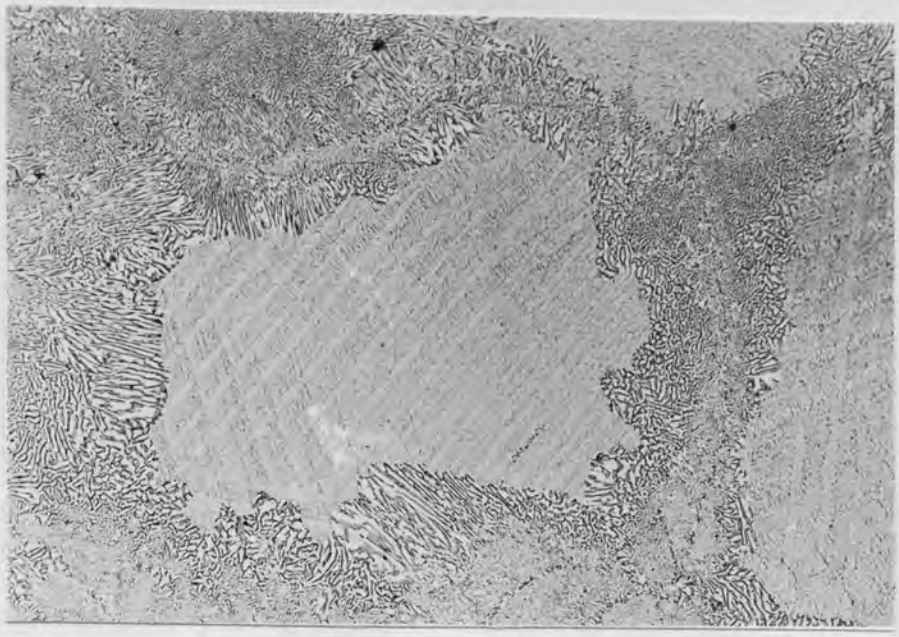

Fig 100- Optical image of the growth of the cellular precipitation towards the interior parts of the neighbounring grains. Etched. x135.

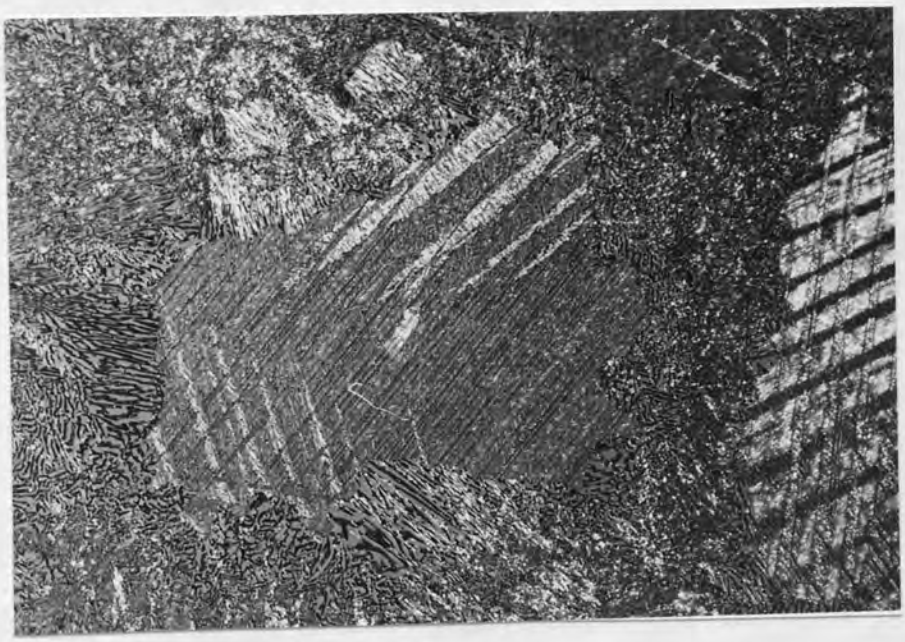

Fig 101- Polarized light micrograph of Fig.100,showing the original twinned structure. Etched.x135

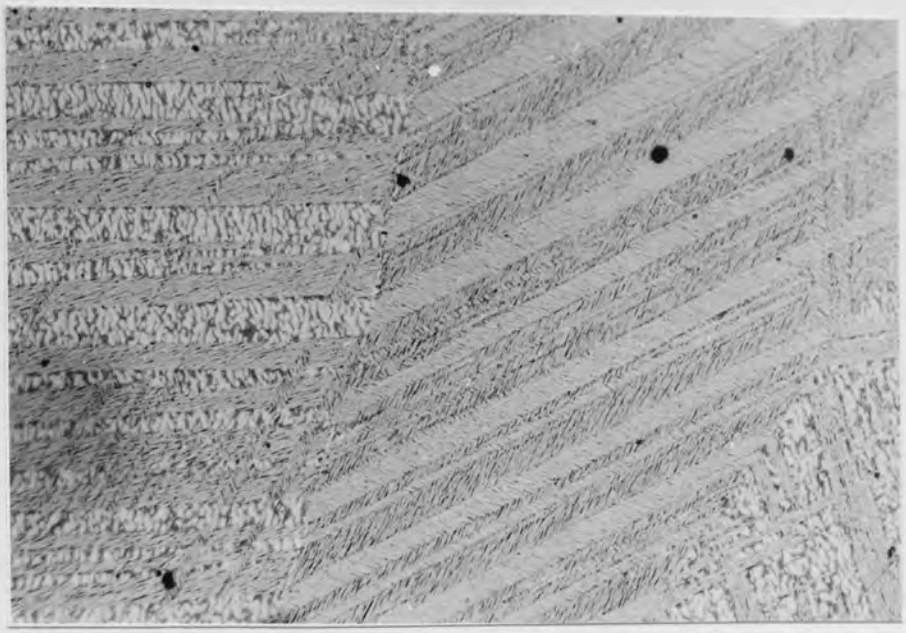

Fig 102- Microstructure of the twinned structures of Fig.100 showing basket weaved and particle precipitations on them. Etched. x420

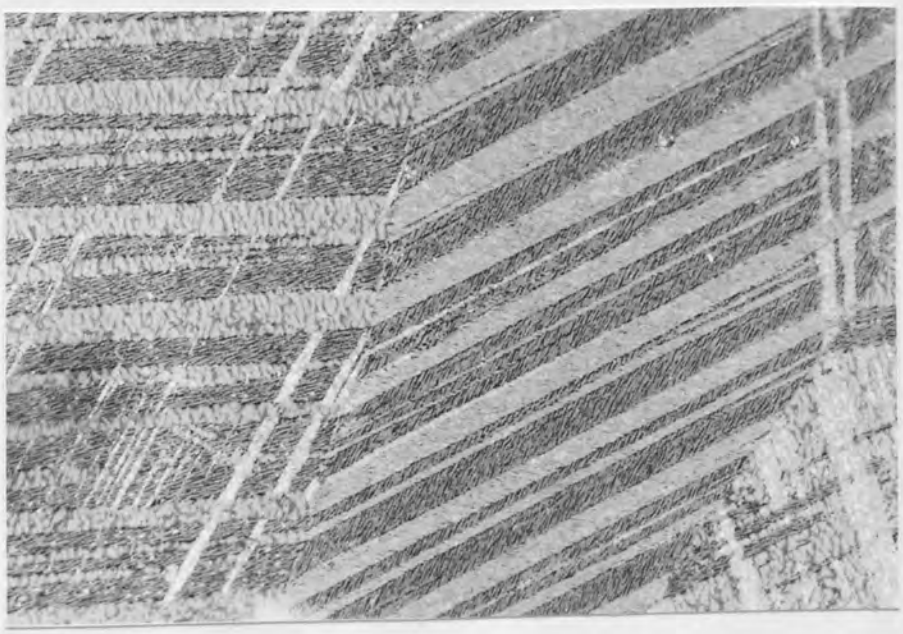

Fig 103- Polarized light micrograph of Fig 102 showing the precipitations on the twinned bands Etched. x420

Further evidence of such precipitation reaction was provided in Alloy 12, i.e., figure 104 where the complex twinned structure of the matrix, and the phase separations are clearly shown.

Figure 104 also shows that the growth of the lamellar colonies stops when the interface encounters another area with the twin morphologies which have very fine precipitate particles on them.

Plate-like precipitate on the original twinned structures were also observed in the vicinities of the lamellar cells. Figure 105 shows such a case in which the plates of β_o and γ'_o-phase have alternative arrangements.

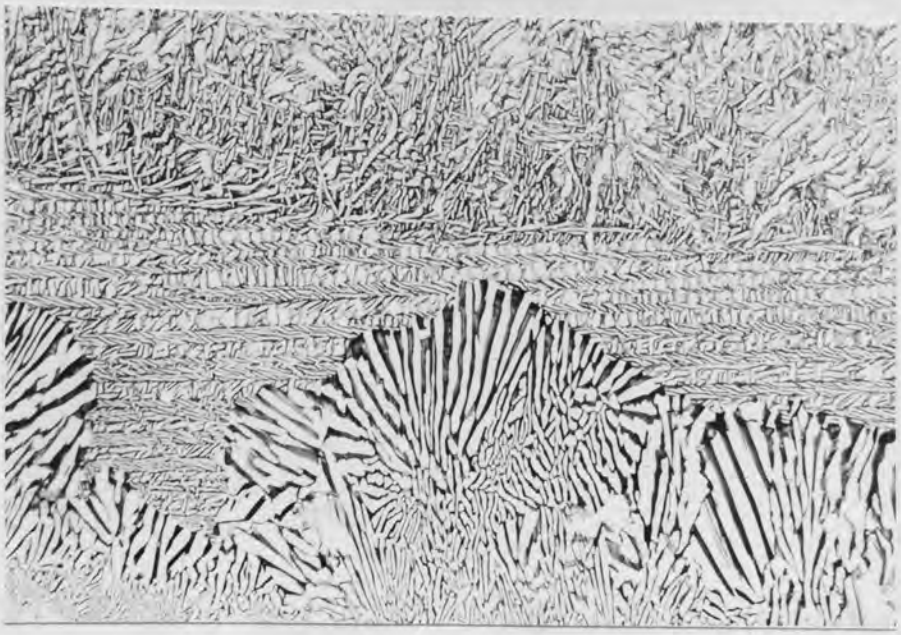

Fig 104- Optical micrograph of alloy 12 revealing plate and particle precipitations in the vicinity of the advancing cellular interphase. Etched .x420

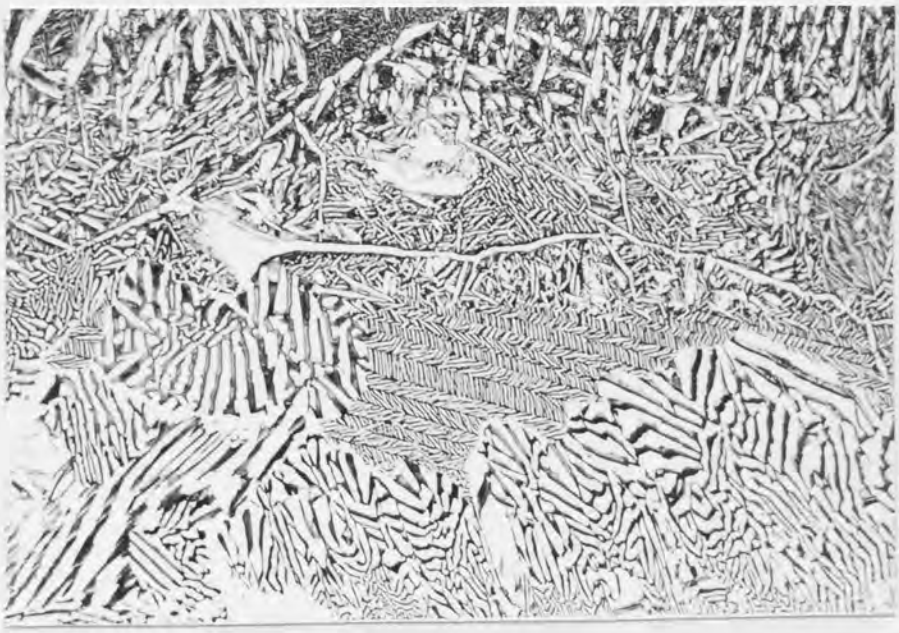

Fig 105- Similar precipitation morphologies to Fig.103. Alloy 10. Optical micrograph .Etched . x420

As was mentioned before, the recrystallization mechanism proved to be the most dominant structural change at the central region of these alloys. None of the alloys were fully recrystallized and some twinned structures similar to that of the as-quenched state of the stoichiometric Pt_2FeCu were also observed in the central regions. Figure 106 clearly shows the recrystallized grains and the plate-like precipitations (on the top left hand side) in alloy 12, and figure 107 also shows a similar situation to that of alloy 12 where the deformation twinning within the recrystallized grains are also shown.

Fig 106- Optical micrograph of the central and outside regions of alloy 12 showing recrystallized grains and plate like precipitations. Etched .Interference contrast x42

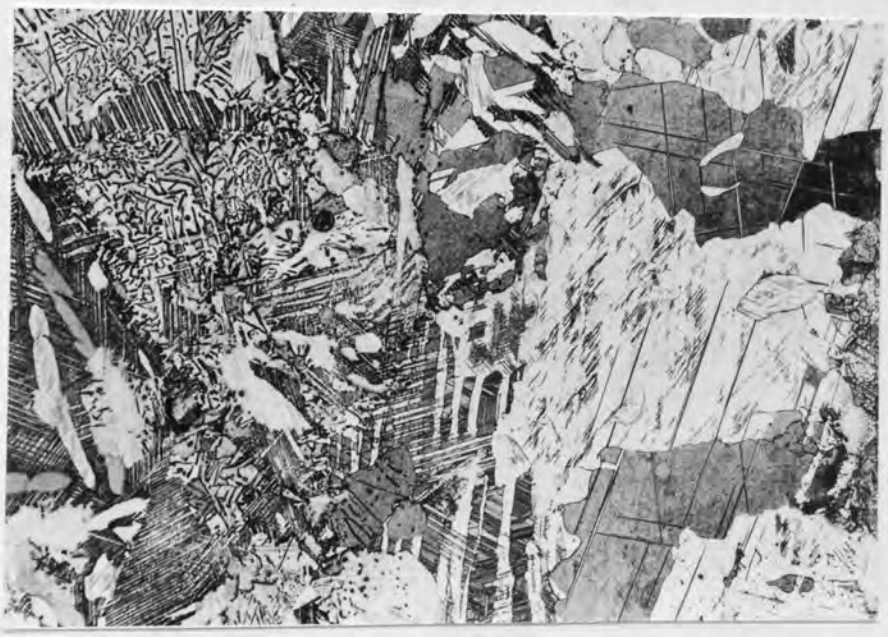

Fig 107- Recrystallization, deformation twins and phase separation mechanism in alloy 10. Optical micrograph. Etched. x168

Less complex structures were observed for the alloys in the (β_o + γ_o) side of the two-phase field, i.e., alloys 18,19,22,24,26 and 27. Neither recrystallization, nor the twinned structures were observed in this region, but the precipitation mechanisms similar to that of the (β_o + γ'_o) phase field seemed to be operative. The phase separation in these alloys took place throughout the samples, unlike the case of the two-phase (β_o + γ'_o) alloys where the phase separation occurred only along the free-surfaces.

Etching procedure of these alloys proved to be relatively easier than the (β_o + γ'_D), but on some occasions, etching and polishing had to be repeated several times to produce satisfactory results.

The phase separations of these alloys appeared to take place by the eutectoid-type, plate-like and cellular decomposition mechanisms, and figures 108 and 109 clearly show these structures. The light areas are the β_o-phase and the dark areas γ_o-phase.

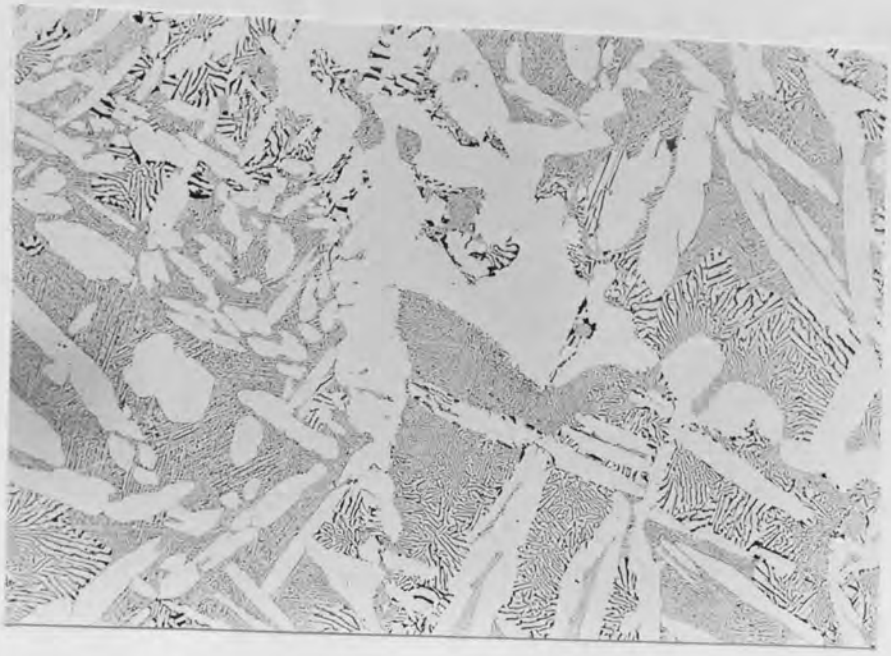

Fig 108- Optical micrograph of alloy 22 showing Eutectoid-type, plate-like and cellular precipitation mechanism. Etched. x168

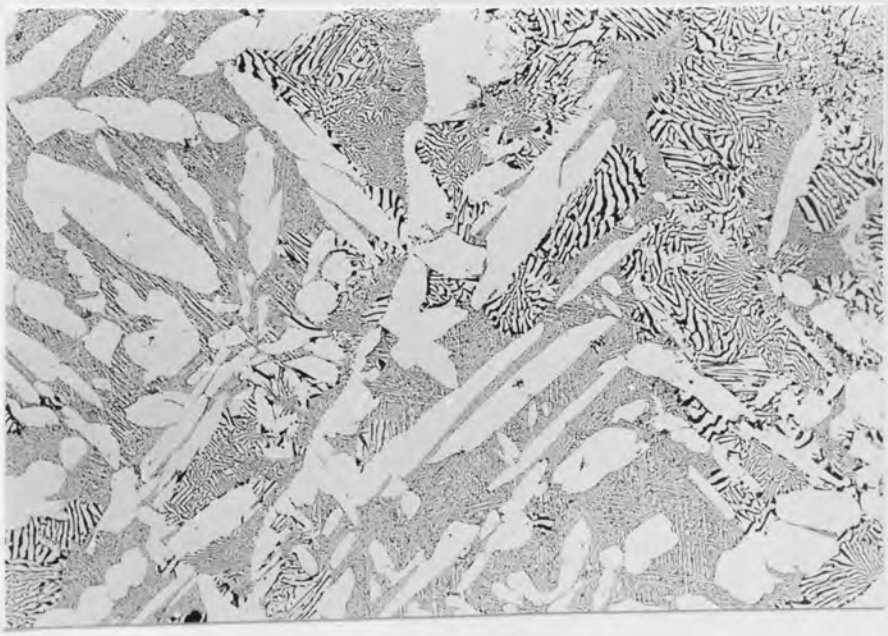

Fig 109- Eutectiod-type,plate-like and cellular precipitations in alloy 26. Optical micrpgraph. x168.

Between ~22% Pt and 25% Pt there existed a narrow single phase field continuous with Cu_3Pt and Fe_3Pt which could be considered either as γ_o or γ'_o-phase.

The alloys with less than 22% Pt were located in a two-phase field region with the primitive cubic structure cells. The (γ'_o + γ_o) phase field extended to approximately 70% Fe and 90% Cu towards the γ'_o and γ_o single phases respectively.

The phase separations in alloys 20,23,21,25,28 and 29 which lay in the (γ'_o + γ_o) phase-field occurred by two different mechanisms, continuous grain-boundary and plate-like (Widmanstätten) precipitations.

Figures 110 and 111 are the typical microstructures of these alloys where the aforementioned precipitations are clearly shown. The darker areas (plates) are γ'_o and lighter areas are γ_o-phases. The different orientation of γ'_o plates in twin variations within the same grain is particularly striking.

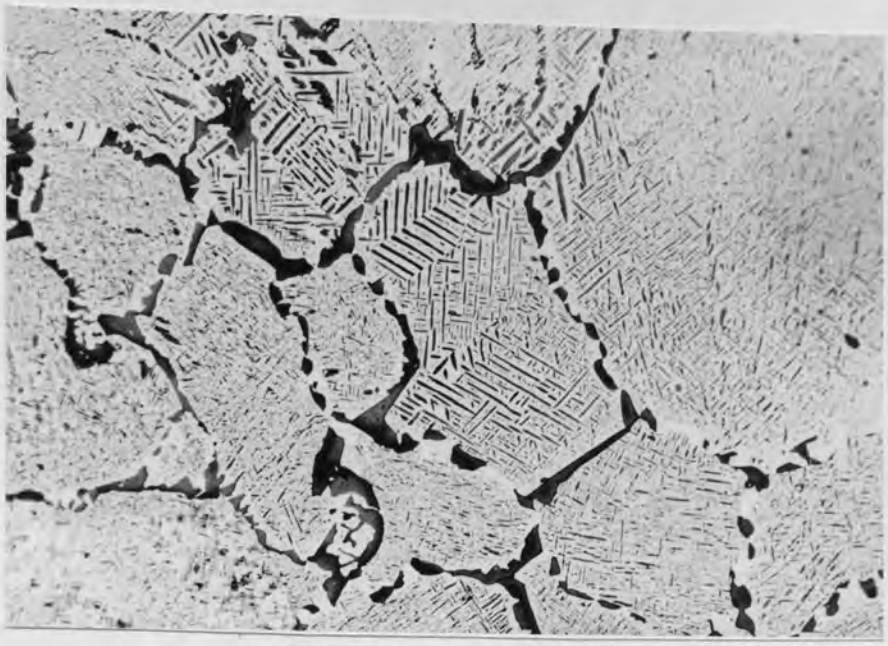

Fig 110- Microstructure of alloy 28 showing the grain-boundary and Widmänstatten precipitations. Optical image. Etched. x420.

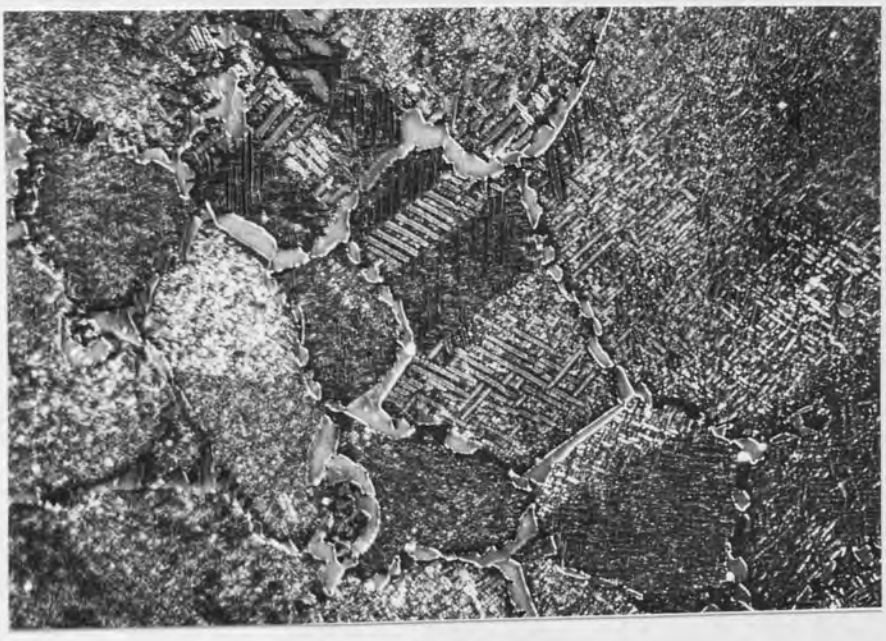

Fig 111- Polarized light micrograph of Fig.110, showing the plate-like precipitations in twin orientations Etched. x420.

Adjacent to the Cu-Fe binary system, there existed a ($\alpha + \gamma'_D$) two phase field where the alloys were comprised of disordered(α-phase) Fe-rich and disordered Cu-rich phases. Similar microstructures to that of the 1000°C section were observed, e.g., figure 83 for the ($\alpha + \gamma'_D$) phase field with Fe-rich particles embedded in Cu-rich matrix.

Between the two,two-phase fields of ($\alpha + \gamma'_D$) and the ($\gamma + \gamma'_o$), there appeared a three phase field of($\gamma_o + \alpha_D$)-Fe-rich and the γ'_o-Cu-rich.

4. DISCUSSION

4.1 Ternary stoichiometric Pt_2FeCu

Among natural occuring platinum-group metals (P.G.M) from different localities, Cabri et al[55] found a ternary compound containing 50 at % Pt, 25 at % Fe and 25 at % Cu. This mineral was named Tulameenite from the site of the find along the Tulameen River in Canada.

The formation of a compound at the Pt_2FeCu composition was first reported by Nemilov et al[54] in (1944) when they studied the synthetic ternary phase diagram of Pt-Fe-Cu alloys system, but no detailed investigations were undertaken.

Cabri et al[55] studied some of the optical and physical properties of this compound which can be summarised as follows;

1) Electron microprobe analysis of different natural grains has shown that Tulameenite has a range of composition and is based on the stoichiometric ratio of 2:1:1 of Pt, Fe and Cu respectively.
2) Tulameenite has a tetragonal unit cell with a=b= 3.891A^o and c=3.577A^o, but no crystal structure was reported.
3) Along the line of the binary compound PtFe-Pt_2FeCu, the Cu atoms substituted for Fe atoms on the PtFe crystal lattice.

In Cabri's et al [55] paper, no other compositional limitations of the Tulameenite was mentioned.

The present work which is stimulated by Cabri's report was undertaken to investigate the compositional limits of Tulameenite in synthetically prepared alloys of the Pt-Fe-Cu ternary system, especially with the binary compounds in Pt-Cu and Pt-Fe systems.

As the research proceeded the synthetically made stoichiometric Pt_2FeCu compound revealed rather interesting metallurgical structures. Therefore preliminary examinations were carried out to investigate some of these aspects.

Cabri et al [55] carried out their x-ray measurements on the sintered samples, slow cooled from 1200°C (sintering for 8 weeks) to 400°C and eventually air-quenched to room-temperature, but no attempts had been made to study the possible structural changes upon different thermal treatments, especially when they believed that Pt_2FeCu should have similar characteristics to those of PtFe where the latter suffers from ordering transformation at ~1300°C.

In our studies the Tulameenite samples were synthesised from their stoichiometric ratio and were given different thermal treatments.

Differential thermal analysis of the uniformed sample revealed that between 1174°C-1146°C there is a phase change. Different samples were annealed above the critical temperature for different durations and rapidly quenched into iced water to retain the high temperature structure. On the subsequent x-ray diffractometer traces the presence of the mixed indexed or superlattice reflections were pronounced, indicating that the material was suffering similar ordering transformation to that of the PtFe binary compound (45). Different attempts to retain the disordered phase met with no success and our fastest quenching ($\sim$1 second) could not suppress the ordering transformation. In other words, it was concluded that the material orders upon quenching.

The obtained x-ray traces were indexed (using the Bunn charts) and lattice parameters were measured on the face-centred tetragonal unit cell bases as follows;

$$a = 3.895\ A^{\circ} \qquad c = 3.595\ A^{\circ} \qquad {}^{c}/_{a} = 0.923$$

When ordering transformation took place in the binary PtFe compound, a layered structure was produced similar to AuCu (74) system, i.e. the Fe and Pt atoms occupied the $\{001\}$ planes in an alternate manner. From a structural point of view, the addition of the third element to such an ordered configuration has been the least investigated of the ordered ternary compounds and crystal structure determinations are mostly based on predictions. Therefore to overcome this problem and to investigate the mechanism of ordering in a "three components" system, the measured

and calculated intensities have been used to plot the electron-density maps (E.D.M) of the Pt_2FeCu. These plots have been shown in Figure 12. (identical plots have been obtained from both approaches and fully or partially ordered lattices).

The Pt atomic sites, due to its superior atomic number to that of Fe and Cu atoms, were easily visible, i.e., (000) and $(\frac{1}{2}\frac{1}{2}0)$. As far as Cu and Fe atoms were concerned, no differentiation could be made, although anomolous scattering effects had been taken into consideration , so it was concluded that Fe and Cu atoms were randomly distributed on the crystal lattice of Pt_2FeCu and remaining sites, i.e., $(\frac{1}{2}0\frac{1}{2})$ and $(0\frac{1}{2}\frac{1}{2})$ could be occupied by either Cu or Fe atoms.

The validity of the above conclusion was further strengthened when the following steps were taken and fully exploited on the basis of the x-ray and electron diffraction studies.

1) If either Cu or Fe atoms had occupied any specific lattice sites, it would have been expected that additional reflections such as (100), (010) would have appeared. Calculations of the relative intensities of these reflections based on the $F = f_{Cu} - f_{Fe}$ have proved that they would have intensities $<0.09\%$ of that of the strongest reflection in the x-ray traces (1785450 : 1707 ratio). Such low intensity reflections could not have been detected in any of our x-ray traces.

2) If these reflections were present, the electron diffraction pattern of the $[001]$ zone of the tetragonal cell, would also have additional reflections at (100) or (010). Close examination of such a (D.P) proved that this did not occur, e.g. figure 36.

Another way of approaching the problem is to allocate a given site, i.e., $(\frac{1}{2}0\frac{1}{2})$ to Fe atoms and $(0\frac{1}{2}\frac{1}{2})$ to Cu atoms. A simple geometrical calculation based on the atomic radii of the three components would yield:

$$a = 3.911\ A^{o} \qquad b = 3.952\ A^{o} \qquad c = 3.576\ A^{o}$$

which indicates that the unit cell is an orthorhombic one which would contradict the present x-ray/electron diffraction results. Therefore it has been conclusively proved that Fe and Cu atoms occupy the $(\frac{1}{2}0\frac{1}{2})$ and $(0\frac{1}{2}\frac{1}{2})$ sites of the unit cell in a random manner and three component ordering is absent.

Although no theoretical investigation has been carried out, the tendency of Pt atoms to order with Fe and Cu atoms can be explained on the factors given in section 1-3. The ordering energies in the superlattice formations are considered to have originated from the interatomic forces, atomic size differences or electronic effects of the constituting atomic species.

The Pauling electronegatives and Goldschmidt atomic diameter of three components of Pt, Fe and Cu are given below:

Electronegatives	Atomic sizes	Elements
2.1	2.775	Pt
1.7-1.8	2.579	Fe
1.8	2.556	Cu

The Pt atoms are more electronegative and much larger than Fe and Cu, which have similar properties. Therefore the superlattice which is based on Pt atoms would be expected to be more stable than those based on Fe and Cu. A similar explanation could be applied to the binary PtFe which has a higher stability than PtCu, which is indicated in their relative T_c values, figures 2 and 3.

The tendency of ordering of Pt atoms with Fe and Cu can also be traced from the nearest-neighbour concept and repulsion parameters [91] which are given below for the three components.

Pt	1.551
Fe	1.352
Cu	1.352

On this basis, due to ordering transformation, the Pt-Pt nearest neighbourhood is impossible due to its higher repulsion parameter. At the same time, the Pt-Cu and Pt-Fe bonding is stronger than the former one. As far as the Fe and Cu atoms are concerned (with the equal repulsion factors), they could wander in the crystal lattice.

Another ambiguity regarding the one ordering component can be removed due to the present investigations based on the (E.D.M) and Cabri's [55] lattice parameter measurements. It has been frequently suggested that if the ternary compounds, where one component ordering is operative, can reach the equilibrium state, one might be able to detect that the other two disordered species take an ordered configuration relative to each other or first component.

If this is the case, Cabri et al [55] would have been able to obtain an orthorhombic unit cell and not a tetragonal one considering that the natural grains of Tulameenite are in a much more perfect state of equilibrium compared with any synthetically made compounds.

No high temperature techniques have been used to study the disordered phase, but it has been presumed that the high temperature structure is a disordered face-centred cubic, although this cannot be proved by quenching. The evidence lies in the fact that a coarse-grained specimen shows groupings of x-ray reflections/electron diffraction spots such as (200) and (002) which can only be explained if the ordered tetragonal crystals had developed from a cubic crystal. Therefore based on the volume per atom concept a lattice parameter of a_D = 3.793 A^o can be obtained for the disordered f.c.c phase.

It is possible to calculate the theoretical lattice parameters of the ordered phase based on the above discussions and figure 112 shows the structure cell of the ordered tetragonal Pt_2FeCu with:

$a = b = 3.923\ A^{o}$ $\quad c = 3.609\ A^{o}$ $\quad {}^{c}/_{a} = 0.919$

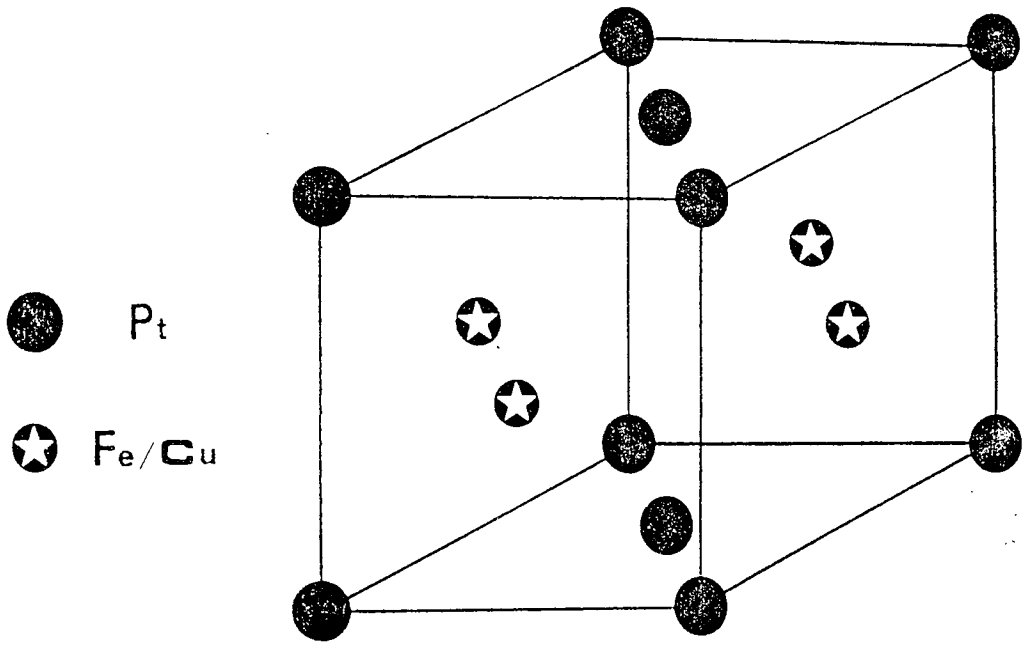

Figure 112 - Unit cell of the ordered tetragonal Pt_2FeCu

Another important feature of the Pt_2FeCu which was also investigated was the variation of the long-range-order parameter (S - parameter) with time and temperature.

Therefore, four samples were given different ordering treatments at four temperatures, 1000°C, 900°C, 800°C and 700°C.

At first the S-parameter was measured for the as-quenched sample after heating at 1200°C for three months. The measured value of S = 0.41 was obtained for such a sample in comparison to S = 0 as was expected. Therefore, such a measurement revealed that the material ordered on quenching and immediately after was in a highly-ordered configuration.

Similar procedures were undertaken for the other specimens which were given isothermal ordering treatments and the results of the variations of the S-parameter with time and temperatures are shown in figure 14.

It was concluded that the S-parameter variations were directly proportional to the time and the temperature in which the state of equilibrium was reached.

For the sample ordered-annealed for two hours at 1000°C the S-parameter reached the value of S = 0.79 in comparison to S = 0.49 for the 700°C. Eventually the equilibrium state was reached in about three months at 1000°C and at the same time a value of S = 0.76 was reached on ageing at 700°C.

if it were possible to retain the disordered phase,i.e., the starting points for these curves would have been from the origin (S = 0), then it can be seen that these curves vary exponentially with temperature and time. To measure the S-parameters, the whole cross-section of the small samples was exposed to the incoming x-rays, so these measured values are the average of long-range order over the exposed area.

Metallographic examination of the samples in the quenched state produced different morphologies,i.e., the central parts showed rather more complex "twin-band" features than anywhere else (section 3.I.6). These complex microstructures were associated with the ordering reaction, i.e., the S-parameter could be a local effect. Therefore as it has already been stated two different values of S = 0.63 and S= 0.29 were measured for the central and the outside region in a sample respectively. These variations of the S-parameter and the observed microstructural changes,indicated that the central parts possessed a higher state of ordered configuration than the other parts.

There could be different interpretations of the above mechanism, but nevertheless the heat loss during quenching played an essential role. It seemed that during quenching the samples from the disordered temperatures, surface heat was lost at a much faster rate than the central region. Therefore the heat was kept much longer in the central region than anywhere else and as the rate of ordering was so high, the central regions had aquired a higher degree

of order when either viewed metallographically or the S-parameter is measured.

This effect has already been stated in the previous studies without any explanation, e.g., Newkirk[65] believed that the surface of the specimen become ordered much faster than the interior parts and Okamura et al [75] when investigating the width of the domain boundaries in the $L1_0$ superlattice also found that the degree of order varied from S =0.9 to S =0.74 from the free surface to the interior parts of single ordered domain.

Although our findings in this respect appear to directly conflict with those of Newkirk and Okamura, the main issue that the degree of order is a positional parameter is generally agreed. Apart from the heat loss concept, there could be a number of reasons responsible for such an effect which are as yet unknown to us.

Metallographic examination of the Pt_2FeCu showed that different structures were obtained depending upon the previous thermal treatments. However, these microstructures can be categorized in three principle structures.

a)- cored- dendritic structure;

The cored-dendritic structure was produced as a result of primary solidification of the compound. Typically these structures showed platinum-rich cored-dendrites with a mixture of Fe-rich and Cu-rich interdendritic features. An

additional feature to the cored-structure was also observed, within some of the dendritic arms. These appeared as dark and bright bands which were distributed heterogeneously, but more were concentrated in the central regions. From the x-ray traces it is quite clear that these features are associated with the ordering reactions,i.e., twinning. Electron microprobe analysis confirmed the heterogenuity of the material (5-15% compositional variations).

These cored-structures were eliminated when the material was subjected to three months solution-treatments at 1200^{o}C and finally quenched in iced water. The homogenized material had $<$0.5 % compositional variations.

b) Twinning structure;

After homogenization treatments, samples when polished and etched were viewed under a microscope, coarse grains and within them the twin characteristic were also observed. The only observed difference was the thickness of the bands which varied from 8 to 26 μm depending on the applied heat-treatment.

The presence of these twins was more pronounced at the central region of a given sample and their population decreased from the central parts to the edges.

The appearances of these twin bands in similar systems where ordering reaction produces a crystal lattice with the lower symmetry is usually termed stress-relief twinning, i.e., the

mechanism by which the material releases the stress built up due to the ordering reaction, which produces the ordered tetragonal within the disordered f.c.c lattice. Before proceeding further, it is interesting to find out more about the nature and occurrences of twins at the initial stages of ordering reaction, i.e, the mechanism of ordering.

No information could be obtained regarding the nature of the ordering mechanism when differently heat-treated samples were examined by means of x-ray diffraction technique.

Although some minute positional shifts and the relative intensity variations were observed, the tetragonal lines appeared in their final positions and disordered reflections were observed. Thus it is impossible to draw any conclusion as to how these lines happened to be in their final positions (figure 11)

Further examinations of the areas of the samples with S =0.29 of the as-quenched state by means of T.E.M have revealed that the ordering reaction takes place via a nucleation and growth mechanism.

Two important factors, a) variation of the degree of order, b) the ordered domains with different sizes, can provide indirect , but not explicit support for such a mechanism.

In this type of ordering, the ordered phase form on the grain- boundaries or any other singularities of the disordered phase statistically. The ordered phase can choose any of the <100> orientations of the disordered lattice for further growth, i.e., c-axes of the tetragonal phase can align itself along any of <100>direction of the disordered cubic phase.

Based on the minimum lattice strain concept (table 7),it can be proved that the habit planes of an order domain in a disordered matrix should have : $\{110\}_D \parallel (101)_O$

Plane	Area A^{o2}	Possible coherency plane		Difference in area	%Difference in area
$\{100\}_D$	14.409	$\{100\}_D$	$(100)_O$	- 0.416	- 2.974
$\{110\}_D$	20.378	$\{100\}_D$	$(001)_O$	+ 0.793	+ 5.214
$\{111\}_D$	12.479	$\{111\}_D$	$(111)_O$	- 0.2901	- 2.380
$\{001\}_O$	15.202	$\{110\}_D$	$(110)_O$	- 0.588	- 2.973
$\{100\}_O$	13.994	$\{110\}_D$	$(101)_O$	+ 0.307	+ 1.487 *
$\{110\}_O$	19.789				
$\{101\}_O$	20.686				
$\{111\}_O$	12.184				

Table 7

O - ordered phase

D - Disordered phase

On subsequent growth, another factor which would determine the size of domains and the morphology of the product phase should also be taken into consideration. Such a factor can be obtained from a simple comparison between the lattice parameters of the two-phases, i.e., due to ordering transformation, 2.64% expansion and 5.2% contraction of the disordered cell occurs along the a and c axes respectively. Therefore a total amount of 3.46% lattice mismatch is created due to the tetragonality of the ordered phase within the disordered phase.

Therefore high stresses are created when these ordered domains continue to grow. These stresses can be short-range or long-range stresses, i.e., due to the tetragonality of the product and the way these ordered domains come into contact.

Detailed analysis of these twinned structures by means of T.E.M examinations has revealed that the c-axis of a given domain lies nearly perpendicular to that of the adjacent domain with some angular disparity, figures 29,35,38(a),(b) and 38(c). The evidence for such an arrangement was provided when the central-dark-field images of these ordered domains were obtained, using superlattice reflections of $\{110\}$ or $\{001\}$ types, figures 29 and 35. Trace analysis showed that the $\{101\}<101>$ twinning mode is operative in this system and the alternate bright and dark-bands contrast in the dark-field micrographs provided sufficient evidence to indicate that these bands have identical crystal structures and are in twin-orientation relationships, i.e. taking the

tetragonality of the ordered domains into account, the c-axes lie in an alternate manner and are bounded by {101} type planes which are common to both crystals.

This arrangement of alternating axes in these directions produces no macroscopic shape change on ordering, but long range stresses are set up due to the interaction of adjacent domains on each other.

However, it is also possible that such an arrangement may be due to the growth rather than mechanical twinning. If they were mechanical twins, then stress-relief provided by them should have resulted in a drop in hardness values, but previous studies[72,58,37] of hardness measurements showed a continous increase on order-annealing. Therefore it is more likely that these twins are of the growth type and can not provide much large relief for stress built up during heat-treatment. On the other hand, if these were mechanical twins, one would expect to have observed further twinning on any subsequent heat-treatments below T_c, but it was otherwise as the recrystallization mechanism proved to be the most dominant microstructural change observed.

Therefore, ordering stresses are partially relieved by growth type twinning, but further stresses are produced when ordered domains come into contact.

Considering the rate of the reaction and the improbability of the coelescence of the ordered domains in the short time ($\backsim$ 1 sec) available, these stresses could probably be relieved

by a stress-induced martensitic transformation on $\{101\}$ habit planes and in $\langle 110 \rangle$ directions to produce no macroscopic shape change.

Whatever their true nature might be, the term stress relief twinning has been used because they partially relieve the stresses of the early stages of the ordering reactions as the result of the anisotropy of the ordered domains in an isotropic matrix. Such a relief mechanism was clearly observed when the stresses from the bulk material were removed during the thin foil preparations. Figure 113 is the dark-field image of a typical structure where the twins have relaxed and appear to have discontinued before reaching the edges of the thin foils.

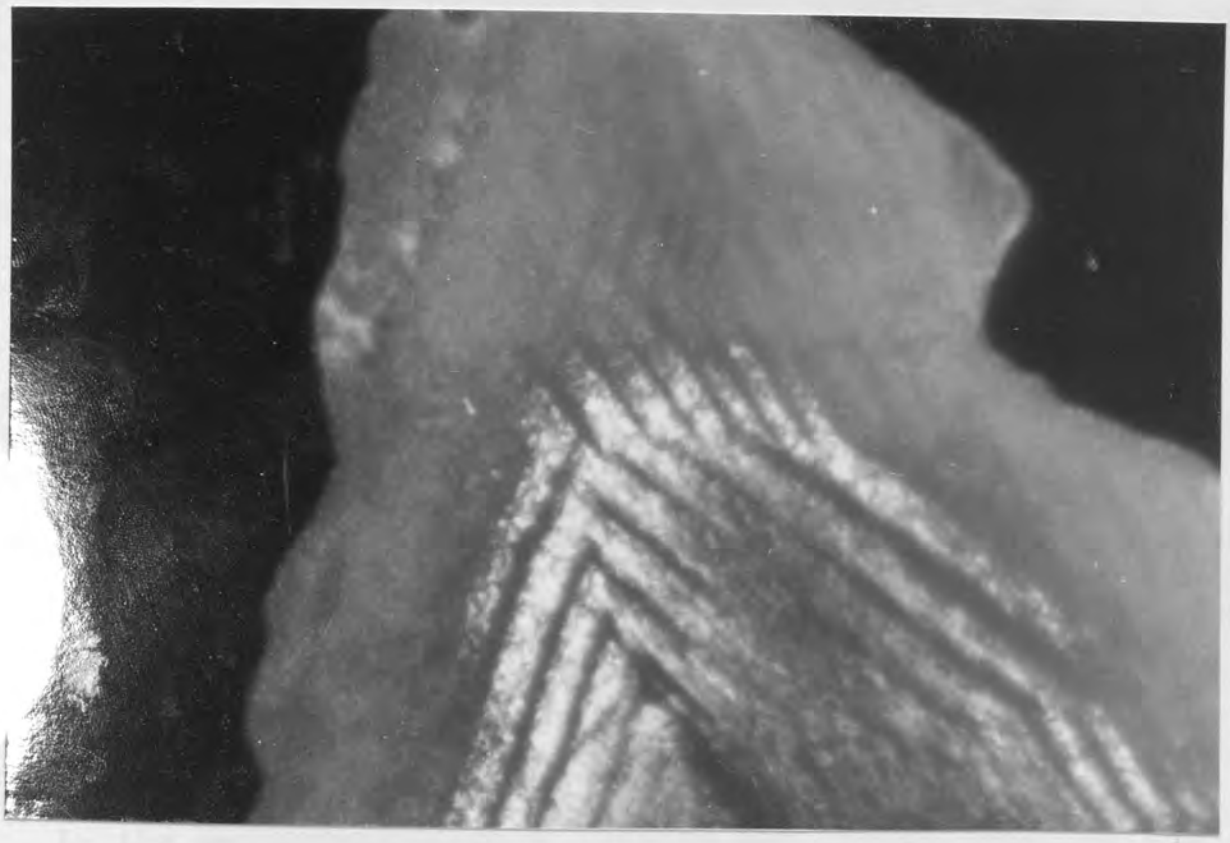

Fig 113- Dark-field image of the "as-quenched" specimen showing the relaxation of the stress-relief twinning. $\{110\}$ superlattice reflection. x200K

c) Recrystallized structure

The recrystallization mechanism proved to be the most pronounced structural change that took place when material was given order-annealing treatment below the T_c.

Before proceeding any further, one clear distinction must be made regarding the nature of such a reaction. Usually the recrystallization occurs when a deformed material is annealed at a suitable temperature. The driving force in this case is the stored energy in the material and the thermal treatments.

In the present case the samples were not subjected to any external deformations therefore the terms stress-induced recrystallization (S.I.R) has been adopted here for distinguishing purposes.

When partially ordered samples (quenched from 1200°C after three months, S_{ave} = 0.41) were annealed below the O/D transformation temperature, recrystallization occurred. The mechanism has been considered [58][65][72] as an alternative mechanism in which the ordering stresses are released, i.e., there is a competition between stress-relief twinning and recrystallization depending on the ordered-annealing treatments.

In the polycrystalline Pt_2FeCu during rapid ordering the material relieved the long-range stresses introduced by the constraint of neighbouring grains by twinning, but at the expense of accumulating a great deal of stored energy.

On the subsequent annealing below T_c, the S.I.R took over as a stress-relief mechanism to dissipate some of this stored energy.

S.I.R has been investigated in four temperatures of 1000°C, 900°C, 800°C and 700°C, and as the observed mechanism proved to be identical at each temperature, the 1000°C observations will be discussed below.

As a whole, three different sites for S.I.R have been observed. Two such mechanisms involved nucleation and growth of the new grains and the third one had similar characteristics to that of stress-induced-boundary migration (S.I.B.M).

These three S.I.R sites could be categorized in order of their appearance;

1) High angle grain boundaries; (Site I)
2) Twin band intersections; (Site II)
3) Thickening of the ordered domain boundaries (Site III)

It had been expected that the material would be fully recrystallized at a given time and temperature, but it proved otherwise. It was obvious that the delay times among the aforementioned mechanisms would yield different growth rates on the subsequent annealings, the region very close to the edges (figures 52 and 53) had kept their original twinned microstructures, after three months at 1000°C, whereas the central regions were fully recrystallized, as in figures 54 and 55.

The whole aspect of the S.I.R and as to why edges never recrystallized can be traced back to the ordering transformation which provided the driving forces for those mechanism.

The central region of the sample had much higher ordered configuration than any other areas of the quenched sample (S = 0.63). On the subsequent annealing below T_c, i.e., at 1000°C, the increase in the degree of order is very rapid, figure 14. Therefore more stresses are built up in the lattice. The increase in stresses could be either due to the increase in tetragonality or increase in the coherency strains between ordered domains. Somewhere between the start of the order- annealing and appearances of the new grains (5 minutes at 1000°C), the stress build up is so high that the material cannot cope with it, and as a result these stresses are relieved via a S.I.R mechanism. Depending upon the discontinuities of the ordered domains along the grain boundary preferential nucleation of these new grains take place there and they grow toward the interior parts of the twinned regions.

At the intersections of the ordered domains or antiphase boundaries within a grain, the orderly alternate arrangement of C-axes is disturbed. They thus represent regions of higher energy and are thermodynamically unstable. These high energy regions are the next most suitable sites for the nucleation and growth of new grain by S.I.R mechanism.

In general the energy of an antiphase domain in a given material depends on its orientation, so an increase in S-parameter on subsequent heat treatment increases the anti-phase domain boundary energies and a mechanism similar to the one proposed by Cahn et al[72] i.e., stress-induced boundary migration (S.I.B.M) takes place. In such a mechanism it has been suggested that the grain (or domain) with higher internal stresses is consumed by the grains containing lower stresses. This is unlikely in this case, but may be caused by stresses introduced by increased ordering or recrystallization elsewhere which are compensated by thickening of a domain with such an orientation that such stresses might be relieved. The advancing fronts of these so-called "thickened" domains closely resemble grain-boundary bulging, figures 48 and 49.

Despite the delay times or the growth rate differences of these mechanisms, they proceed to consume the original twinned structure as long as the driving forces which are created due to ordering reactions are supplied,i.e., when the degree of order S = 0.99 the recrystallization mechanism discontinues and 95% of the material has recrystallized at 1000^{o}C after 3000 hours annealing.

It was pointed out earlier that near the free surface the material kept its original twinned structure during the whole course of recrystallization. This effect may also be explained in terms of the ordering reaction, considering that some of the stresses components are zero unlike the central regions. So when degree of order increases upon the

subsequent heat-treatment, the stress build up is not as great as that near the central region and presumably the dislocation rearrangements can cope with such stresses. Therefore no recrystallization reactions are needed to release these small stresses.

The recrystallization grains have definite orientation relationships (at least in the early growth stages) with the twinned matrix. It was found that different orientation near the $\langle 101 \rangle$ were all adopted by new grains in one group and the twinned matrix. The directions actually make between 0.5- 6 degree angle with the exact $[101]$ direction, figure 65. Hence,it appears that the following relationships exist between the twinned and new grains.

$$\{101\}_T \quad \{101\}_R$$
$$\langle 101 \rangle_T \quad \langle 101 \rangle_R$$

The activation energy measurement of the recrystallization mechanism (2.16- 2.57 eV/atom) was found to lie between the self-diffusion energies of copper (2.06 eV/atom[85]) and iron (2.62 eV/atom[85]) or platinum (2.89 eV/ atom[86]). It also lies between the activation energies of diffusion of platinum in copper (1.64 eV/ atom[87]) and platinum in iron (3.03eV/ atom[88]).

Figure 42 was the Avrami plot for the recrystalliaztion which showed good linearity but with two distinct slopes.

The presence of two distinct slopes in such a plot and the

differing values of the measured activation energies may be taken as an evidence of at least two or three mechanisms for the recrystallization process.

The n values between 0.1 - 1.0 also confirm the occurrance of different stress-assisted recrystallization mechanisms (90).

At this stage it should be emphasised that it is not possible to attach much significance to the experimental activation energy for the recrystallization determined from the slope of an Arrhenius graph. The emprical activation energy obtained for the recrystallization should actually be comprised of different thermally active microscopic processes each with its own characteristic activation energies. This follows from the fact that nucleation continues to occur, in the twinned regions while earlier formed nuclei enter the growth stages. Hence, any such "overall activation energy" is a complex function of the activation energies for the two individual processes - both of which vary as recrystallization proceeds. At the very best, therefore, such an "overall activation energy" can only give limited indirect information about the fundamental controlling phenomena.

Additional features within the individual recrystallized grains and subsequently upon their impingements were also observed. These effects which showed contrast changes when

viewed under polarized lights, were more pronounced in the triple junctions of these grain boundaries indicating that deformation twins reformed in these new grains, figure 58. These twins have the characteristically narrow shape of deformation twins and extend as far into the recrystallized grain as the elastic stresses field which is responsible for their formation (Figure 55, 56 and 57).

The occurrence of these deformation twins can be traced back to the ordering reaction which appears to be responsible for most of the structural changes in the compound.

When recrystallization took place at the early stages of the order-annealing, the increase in the degree of order in the system, would create more stresses in the twinned region as well as the new grains. In other words, two opposite stresses with different magnitude have the boundaries of the recrystallized grains in between, one assisting and the other opposing their growth.

The imposed stresses upon the recrystallized grains from the twinned matrix, should have different components depending on the c-axes orientation in the alternate bands which eventually influence the mobility of the growing grains. Such a case is shown in figure 114 which is based on the figures 50, 51 and 61.

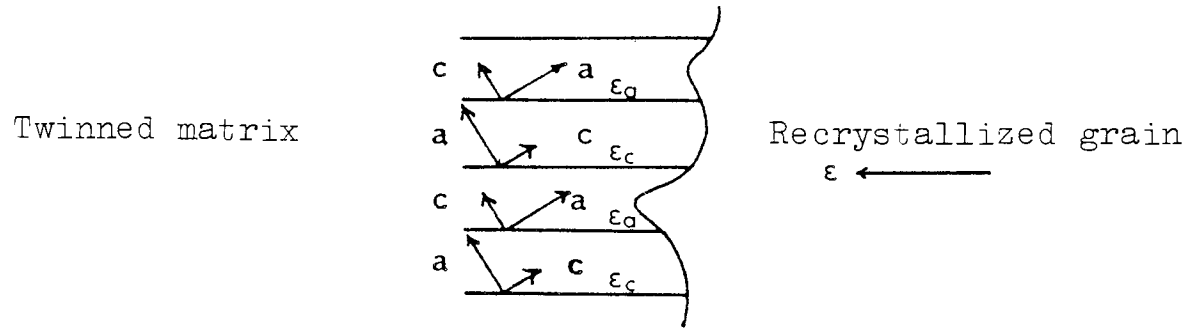

Figure 114 - Advance of the recrystallized grain towards the original twinned structure.

Based on the limited experimental observations, it appeared that the mobility of the growing grain boundaries is locally varied by the opposing stresses from the twinned matrix. Therefore deformation twins formed to accommodate the stress build up.

After eight hours order-annealing at 1000°C, the central regions of the specimen were fully recrystallized, although the degree of order had reached the value of s = 0.9 which indicate that the perfect order has not yet been established in the material. Therefore, further heat-treatments would still create more stresses plus additional ones due to the impingements of the recrystallized grains, each of which is a well ordered domain.

The correct identification of these markings (the deformation twins) were very critical as slip lines could have also produced similar effects on the surface. As a safeguard to assure correct identification, the sample was ground, polished and etched again and finally it was examined under a polarized light. The change of contrast of these markings

confirmed beyond any doubt that these lines were actually deformation twins.

These deformation twins showed some interesting features which can be summarised as follows and are based on figure 55.

1) - Some of the narrow twins (0.6 μm) end inside the grain
2) - Some of the broader twins (2.4 μm) go right across the grain
3) - Few of these twins also cross the annealing twin in a zig-zag manner.
4) - Some of the twins are actually parallel to the coherent interface of the annealing twins.
5) - Individual twins cross from one twin plane to another in which the process might be cross-twinning.

No attempt was made to investigate the true crystallographic nature of the deformation twins, but during the course of the T.E.M examinations, these twins happened to be in the field of view, figure 61. Trace analysis of the twin traces confirmed that $\{101\}$ plane as their habit planes, similar to the stress-relieve twinning habit planes, but the former is certainly produced by a shear mechanism.

The twinning which was produced in this manner can be illustrated when the elements of twins are;

$K_1 = (101)$, $\eta_1 = [10\bar{1}]$, $K_2 = (100)$ and $\eta_2 = [001]$

in terms of the face-centred tetragonal cell and is shown in figure 115. The a and x-axes are exaggerated in order to make the mechanism clearer.

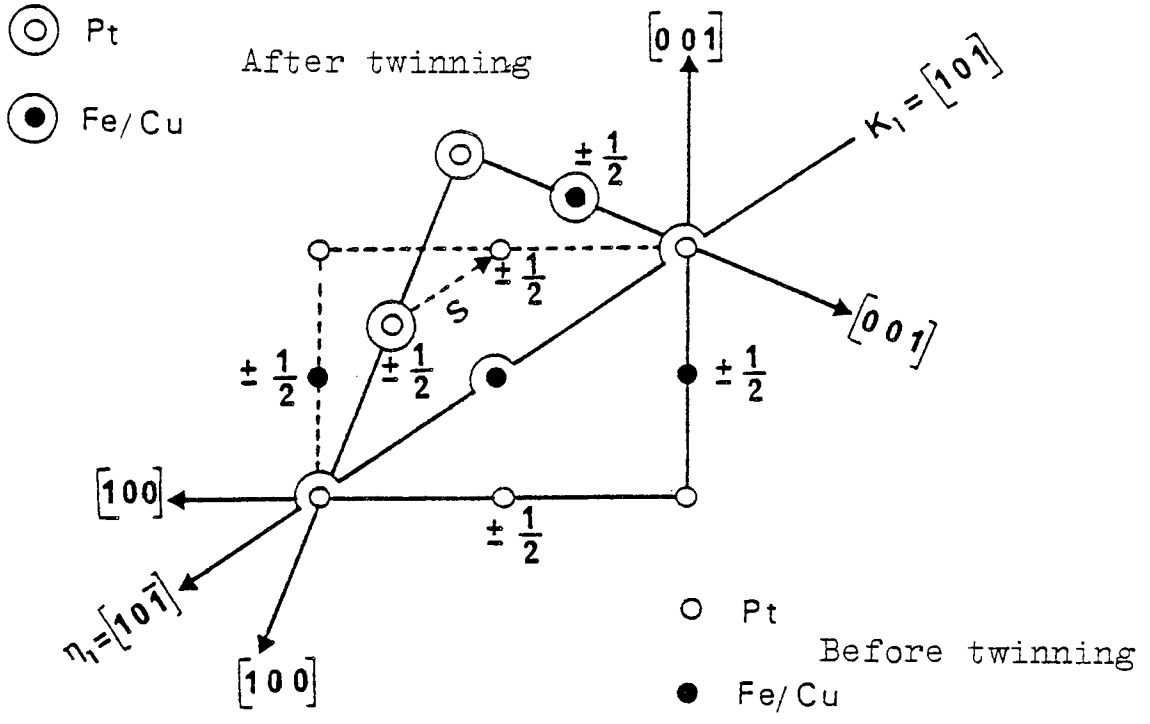

Figure 115 - Twinning mechanism produced by Shear

In this case both structures are twinned and it is clear that the twinning has been produced by a shear mechanism, where the amount of shear depends on the actual $^{c}/_{a}$ ratio. In this exaggerated case where $^{c}/_{a}$ = 0.66 the amount of shear is one third of the $[10\bar{1}]$.

The actual amount of shear can be obtained[76][77] :

$$2\phi = 2 \tan^{-1} {}^{c}/_{a} \qquad \ldots\ldots \quad (22)$$

$$S = 2 \cot (2\phi) \qquad \ldots\ldots \quad (23)$$

where the 2ϕ is the angle between the two undistorted planes during the shear and $^{c}/_{a}$ is the axial ratio.

When relevant data is substituted in equation (22) and (23):

$$2\phi = 85.41^{o}$$

$$S = 0.16$$

can be obtained. As the Pt_2FeCu compound is a non-cubic lattice, the stacking of the planes parallel to the composition planes, contain no repeat symmetry so that the twinning dislocations do not have a simple vector. Thus in the present case the twinning vector operating on each successive $\{101\}$ atomic layer is[76] .

$$b_t = \frac{2 (\gamma^2 - 1)}{(\gamma^2 + 1)} \langle 10\bar{1} \rangle \qquad \ldots\ldots \quad (24)$$

where b_t is the burger vector of twinning dislocations and γ is the axial ratio of the crystal, i.e. $^{c}/_{a}$ = 0.92. A simple calculation would yield $b_t = 0.16 \langle 10\bar{1} \rangle$ or $b_t = S\langle 10\bar{1} \rangle$ which would indicate that the movements of the twinning dislocations of $b_t = S\langle 10\bar{1} \rangle$ type on successive $\{101\}$ planes

could produce a twin lattice. Therefore the $\{101\}$ planes are the composition planes of the deformation twinning in the material.

In addition to the aforementioned reactions of the stress-relief mechanisms, when samples of the Pt_2FeCu were quenched, either from above or below the critical temperature, very fine cracks were observed on their surfaces. The cracks were originated along the grain-boundaries only and frequent quenching appeared to either propagate the existing ones or create fresh cracks.

Although during the recrystallization studies, specimens were slowly quenched to prevent the grain-boundary fracture and such measures greatly reduced the fracture, nevertheless in some samples these fractures appeared near the free surface of the recrystallized specimen.

Stress-relief by means of the recrystallizations is strictly possible only as long as the boundary migration is rapid in relation to the stress build up. As it was stated before, in the present case, the boundary migration is not compatable with the rapid stress build up and consequently the deformation twinnings occurs. Thus, clearly, migration of the recrystallized boundaries cannot be as rapid as to cope with this build up of strains and depending on the amount and localities of the stresses, the grain-boundary fracture provides the mode of stress-relief.

Therefore it is possible to draw the conclusion that the stress-induced recrystallization is not an alternative mechanism by which the ordering stresses are relieved. The recrystallization mechanism occurs after the initial stresses are partially relieved via the stress-relief twinning.

Primary recrystallization relieves the microstresses due to the domain structure. However as the small new grains grow larger they in turn introduce long-range stresses due to accidental unfavourable orientations of their c-axes. This is particularly important since they are better ordered than the original grains. Therefore additional mechanisms, i.e, deformation twinning and grain-boundary fracture are necessary to relieve the new stresses set up at unfavourable contacts.

However, material with high concentrations of deformation twins is also thermodynamically unstable and a fresh wave of recrystallization may be initiated at these points to reduce the elastic strain. Since grain growth is an inevitable consequence of continued annealing, a continuous cycle of recrystallization → grain growth + deformation twinning → recrystallization can be visualised in polycrystalline Pt_2FeCu. Limited evidence for at least one second wave of recrystallization was obtained in this study, (Figure 90 and 91).

This cracking of grain boundaries due to tensile stresses set up during recrystallization of the ordered material is very important when natural Tulameenite is considered.

Tulameenite frequently occurs as a vein or border to the more common mineral Ferroan platinum, Pt_3Fe, and is invariably penetrated by thin films of silicats or other rock-forming minerals, which appear to be grain-boundary accumulations. Other natural platinum alloys do not exhibit these features. If it is assumed that natural Tulameenite is formed from magmatic material cooling slowly from high temperature, then on passing through the ordering temperature the grains will become tetragonal, setting up stresses between themselves and contiguous cubic phases. Grain boundary fracture either directly or on subsequent recrystallization must take place and if this is above the melting point of the rock-forming minerals, these will be drawn into the fissures. This explanation of the mineralogical observations is evidence for a high-temperature formation for Tulameenite, and of its intergrown associated minerals, thus resolving a long-standing uncertainty[92].

Discussion of the ternary phase transformation of Pt-Fe-Cu

There is negligible information regarding the Pt-Fe-Cu ternary system. Even the constituent binary systems are not known with certainty.

The binary ordered alloys are cubic with $L1_2$, tetragonal with $L1_0$ and rhombohedral with $L1_1$ structures.

The isothermal sections at 1000°C and 600°C indicate that a continuous region of solid-solutions formed between Fe_3Pt and Cu_3Pt and between $FePt_3$ and $CuPt_3$ binary alloys.

The binary compound FePt formed a continuous region of solid-solution with Pt_2FeCu ternary compound where copper replaced iron atoms on the former crystal-lattice. The ordered tetragonal single-phase (β_o) based on FePt extends to 50% Pt, 20% Fe and 30% Cu approximately along 50% platinum line at 1000°C. On slow cooling to 600°C the β_o-phase field contracted and there was a shift towards the Fe-rich corner of the system. The same applied to the two-phase field which surrounds the β_o-phase field but the compositional shifts of the latter were more pronounced towards the Cu-rich corner than the Fe-rich.

As a consequence of such compositional shifts, the ternary compound was no longer a single phase and had decomposed to off-stoichiometric Pt_2FeCu and Pt-rich phases. The two phase field surrounding the β_o-phase extended right towards the binary compound CuPt but did not actually form a continuous region with it.

These observations are in agreement with the findings of Kornilov[78] who noted that, as general rule, the formation of continuous solid-solution between metallic compounds are favoured by the following conditions:

i) - Components should be isomorphous with similar lattice parameters

ii) - The same type of chemical bond should operate in each compound

iii) - The compounds should contain atoms from the same group of the periodic table.

iv) - The compound should have the same stoichiometric formula.

The observed microstructures of the alloys in the β_o-phase field, either at 1000°C or 600°C, strongly indicate that the stress-induced recrystallization together with the deformation twins were the most predominant structural changes which occurred in this phase field. The presence of these features can be interpreted in a similar manner to that of the stoichiometric case (Section 4.1) where these features were proved to be the stress-relief mechanisms as a result of ordering transformation.

At 600°C in addition to the normal recrystallized grain structures and the deformation twins, some other features which strongly resembled a nucleation and growth mechanism along the recrystallized grain boundaries were also observed. As no structural or compositional changes were detected between the matrix and the new grains, it appeared that the secondary stress-relief recrystallization had occurred along some of the matrix grain boundaries, figures 90 and 91.

It is doubtful whether one can capitalize on figures 91 and 90 to draw any firm conclusion, however, if one does, these features may be explained in terms of the ordering stresses.

The alloys in the β_o-phase field have all undergone ordering transformation. Apparently the initial stresses were relieved via stress-relief twinning and primary stress- induced recrystallizations accompanied by the deformation twins. On slow cooling the rates of all of the structural or compositional changes are drastically reduced. Such an effect was clearly observed for the time needed to establish the near perfect equilibrium degree in the stoichiometric Pt_2FeCu at 700°C. If the extrapolation is a meaningful concept in this case, it can take several years to achieve an equilibrium state at 700°C, whereas it takes nearly three months at 1000°C to reach a similar state.

If a similar explanation can be applied in the off-stoichiometric cases, it appears the driving force for any other changes (e.g. the exaggerated grain growth) has been greatly reduced. Thus when the degree of order (considering its positional dependency) and subsequently the stresses are continuously increasing, the fresh nucleation and growth of the secondary-induced recrystallization is kinetically more favourable mechanism to reduce the energy of the system.

The decomposition of the high temperature supersaturated solid-solution of the off-stoichiometric Pt_2FeCu and the disordered f.c.c structures takes place via a precipitation mechanism with a variety of the morphological appearances depending on their compositions.

At 1000°C and in the vicinity of the γ''_D-phase, the ordered tetragonal phase is the minor phase and appears as plate-like or discontinuous grain boundary precipitates with twinning features which are presumably formed in order to accommodate the growth stresses of the anisotropic phase in the isotropic matrix, figures 79 and 80.

The $(\beta_0 + \gamma'_D)$ and $(\beta_0 + \gamma_D)$ sides of the two-phase field showed similar plate-like precipitates where either phase is equally distributed throughout the alloy, figures 81 and 82.

Apart from $(\gamma'_D + \gamma_D)$ two phase field along the Cu-Fe binary edge, the rest of the alloys at 1000°C were all single phase solid solutions of (Pt,Fe,Cu), thus they all showed normal grain structures with some evidence of annealing twins and were all based on a disordered f.c.c. structure.

The most unusual microstructures were observed for the alloys in the Cu-rich side of the system,i.e., alloys 38,37,36, 33,34,32,31 and 29. The coarse grains were all divided by narrow parallel bands which in some cases were also subdivided by much finer units. Identical microstructures were also observed for the ion-beam etched alloys,figures 87 and 88.

Although these alloys were all single phase solid solutions and apparently did not undergo any compositional or structural change during either the homogenization or slow cooling treatments,some stresses could have been created upon the formation of the solid solution, considering the atomic size differences of the constituent species(Iron and copper differ from platinum in atomic diameter by 8.3% and 7.9% respectively).It is possible that as a result of suitable thermal treatment self-recovery by means of dislocation rearrangements and subsequent subgrain formation have occurred in order to reduce the configurational free energy.

To establish the isothermal section at 600°C the homogenized specimens were slowly cooled to 600°C and were kept there for further period of six months and finally quenched in iced water. Such heat treatment did not allow detailed analysis of any phase decompositions.

The observed microstructures as the result of different precipitations, can be summarized as follows;

a)- Plate-like (Widmanstätten)

b)- Cellular

c)- Grain boundary (continous or discontinous)

d)- Basket-weave like

e)- Plates or particles on the matrix original twinned bands

f)- Eutectiod-type reactions.

The combination of the aforementioned precipitation mechanisms were more pronounced in the two-phase field which surrounded the β_0-phase. The single phase or two-phase structures at 1000°C were further decomposed to produce a variety of microstructures depending on the kinetics and the driving forces available for a given reaction.

On the whole it appears that different precipitation reactions have been operating on slow cooling from 1000°C to 600°C. For example, when the phase decomposition is taking place by a cellular precipitation, certain sets of conditions like specific driving force, time for nucleation and growth and finally a suitable thermal treatment must be observed for such a mechanism to proceed. Now, if these are partially observed, i.e., after initial nucleation and growth the conditions are altered due to change of temperature, it is possible that the rates of the transformation have decreased drastically and such a mechanism may proceed no further. On the other hand the phase separation must take place in order to reduce the free energy of the system. Thus another mechanism, for example plate-like precipitation would take over if the set of the required conditions are fulfilled for such a reaction .

The plate-like precipitation does not necessarily follow the cellular decomposition in this sequence and these two reactions are merely mentioned to explain the nature of the possible transitional phases which have arisen under given sets of conditions, time and temperature upon slow cooling.

The effect of the ordering transformations in these alloys should also be taken into consideration, although it is not very clear as to how they contribute to the phase separation. Due to ordering, additional energies are provided for any possible compositional or structural changes, but at the same time, stresses are also created in the material which could make a positive contribution to the free-energy of formation of the new phase. In the following paragraph these effects in some of the alloys in this two-phase field will be discussed.

The occurrence of the peculiar microstructural changes of the alloys 6,7,8,10,11 and 12 on slow-cooling may be explained in terms of the classical nucleation and growth mechanisms. Attention must be drawn to the elastic stresses contribution to the free energy of formation of the embyro of the growing nucleus in the solid matrix.These stresses can be taken into account by adding to the equation that gives the change of free-energy due to the formation of the nucleus a term representing the elastic energy.

$$F = F_v + F_s + F_e \qquad \ldots\ (25)$$

Here F_v is the value of the difference between the volume free energy in the new phase and that of the old-phase; F_s is the surface energy and F_e is the total elastic energy in the nucleus and its surroundings. For the sake of simplicity the shape factor or mass and other relevant coefficients in the equation (25) are ignored.

In the nucleation and growth reactions (where the elastic stresses are ignored), it is the interplay of the F_v and F_s terms which could determine whether a given transformation would take place or not. In other words, if a) $F_s > F_v$, then the second phase embryo would dissolve back in the matrix and may need greater undercooling to initiate the possible phase separations, and b) $F_s < F_v$, where in this case the free-energy of the formation is negative, consequently making it possible that the nucleation and growth of the second phase can proceed under the given conditions.

For the given shape of the nucleus of the second phase particles, F_e is proportional to, a) the volume and rigidity of the second phase and b) volume and rigidity of the surrounding. Thus the elastic stresses have an effect as if the free energy of the formation of the new phase were increased by the elastic energy.

The probability of occurrence of a new phase in this case is dependent on the magnitude of the elastic stresses and the surface energy contributions to the free-energy formation of the new phase(s),i,e. if only $F_s + F_e < F_v$, then the formation of the second phase is thermodynamically possible.

One way in which the surface energy term can be reduced is for the nucleus to form coherently with the matrix at least in the early stages of the growth.

Having considered the effects of the elastic stresses and its contributions to the free-energy formation of the new phase, it appears that the elastic stresses due to the ordering reaction at the central regions of these alloys are so high that their contribution to equation 25 would increase the free-energy of the formation of a new-phase, i.e., thermodynamically the formation of the phase(s) may be totally suppressed. However under such conditions the central region is still unstable and another reaction(s) is required to reduce the energy of the system. Based on the experimental observation the stress-induced recrystallization (primary or secondary) incorporated with the deformation twins appeared to be the natural choice of the stoichiometric or off- stoichiometric Pt_2FeCu. So in the central regions of the two-phase alloys(6,7,8,10,11 and 12) a similar mechanism occurs in order to reduce the energy of the system considering that there is no change in chemical composition, structural changes are needed in the case of the self-diffusion of the components in Pt_2FeCu.

The outside region of the alloys are under less stress than the central regions, therefore making it possible that the F_e contribution to equation (25) is quite small. In this case the free-energy of the formation is negative and the nucleation and growth of the new phase can take place when lowering the temperature to 600°C.

It is quite clear then, that the ordering reactions can greatly alter the kinetics of a given transformation, i.e. the nucleation and growth of the second phase can be suppressed at the central regions and at the same time would assist the recrystallization mechanism by providing an additional driving force.

It was stated before that some contribution from the binary compound PtCu to the ternary system was expected at 600°C, but it was proved otherwise, no indications were found of any extra phase field based on the PtCu into the interior part of the isothermal section. While it is naturally more difficult to provide conclusive evidence for the absence of an effect than its presence, attempts are made to clarify the situation, by taking different factors into consideration where they all arise due to the uncertainty in the Pt-Cu binary system around the CuPt compound.

a) If the disorder f.c.c transformation to the rhombohedral single phase field based on the stoichiometric CuPt is truly a classical ordering transformation [79][80] and taking the fact that the transition between phases of the different symmetry cannot occur in a continuous manner [81] also into consideration, one can immediately doubt the validity of the currently accepted Cu-Pt [27] binary system around the CuPt compound. In other words, there should be a two-phase field of rhombohehral plus f.c.c phases around the CuPt binary compound in the similar manner to that of the AuCu [82,84] PtCo [83] and FePt. Therefore based on the

aforementioned binary systems it is possible to assume Figure 116 for the Cu-Pt binary system around CuPt compound.

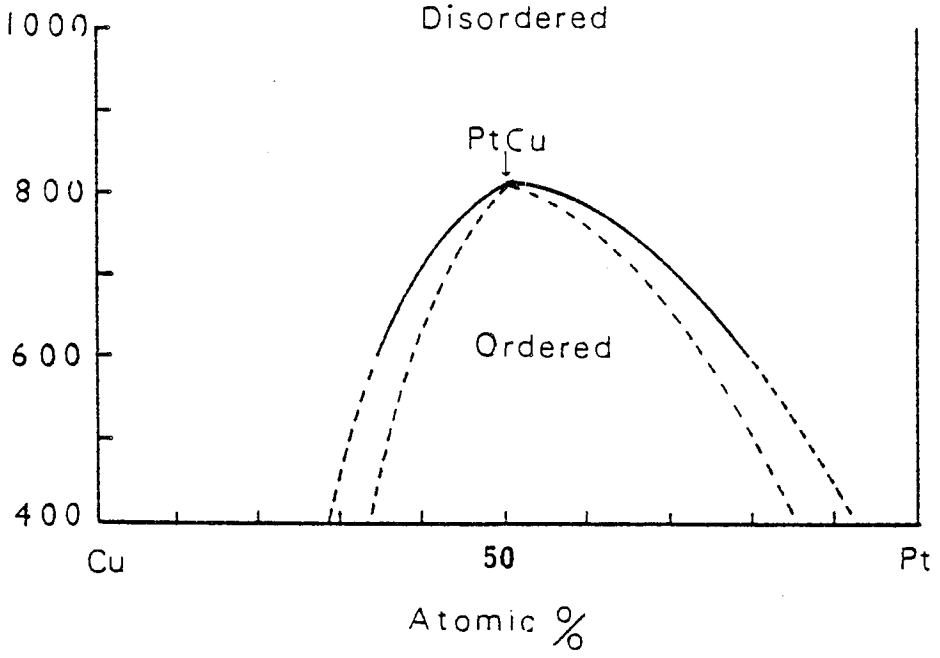

Figure 116 - Proposed binary Pt-Cu alloy system around PtCu.

Irani et al [37] proposed a similar two-phase field for the Cu-rich side, but no published report has dealt with the Pt-rich side of the CuPt

If the above assumption is correct, then one would expect to observe a similar contribution (phase expansion) to that of FePt to the ternary system and the ternary system near the CuPt ought to look like figure 117.

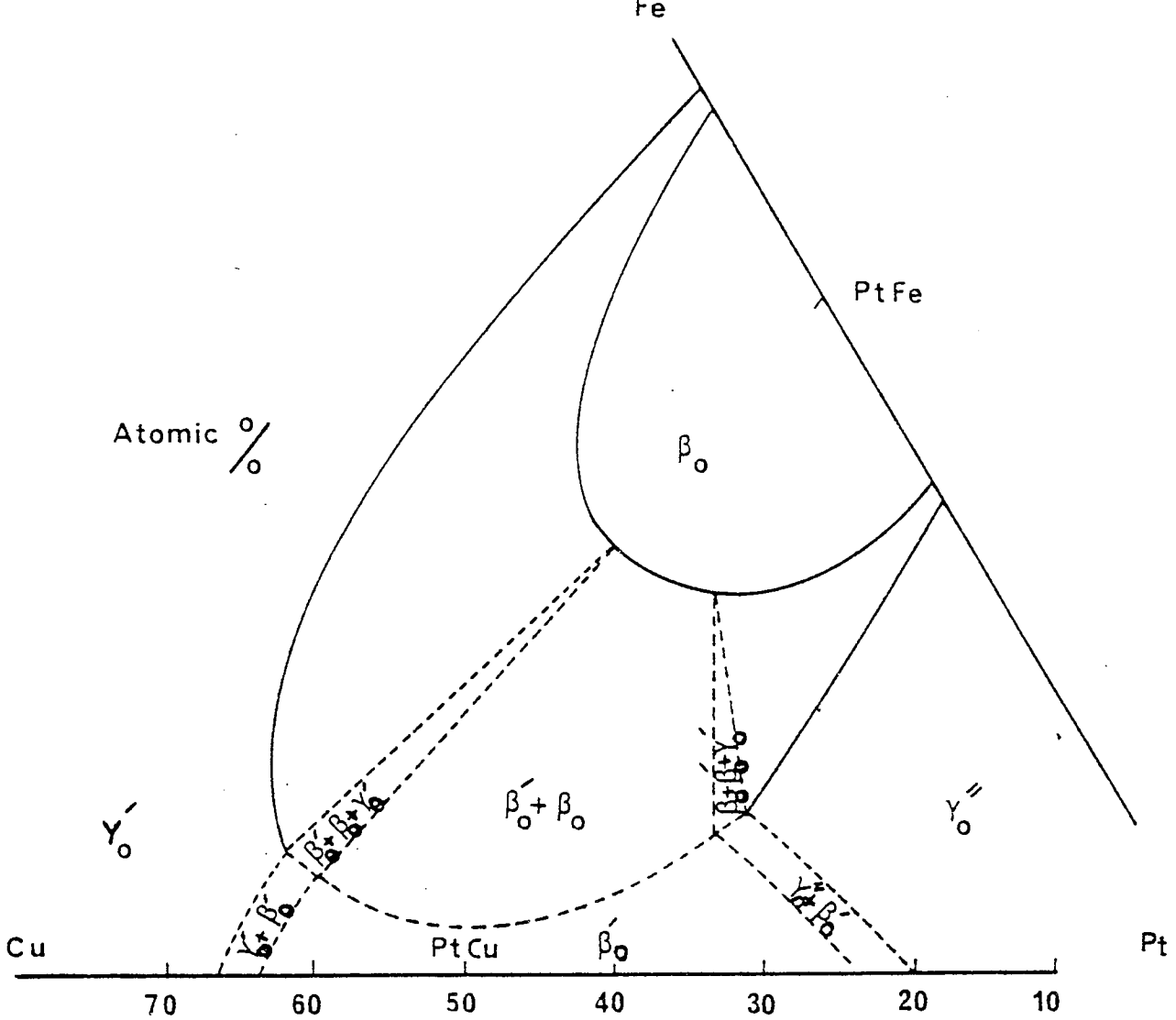

Figure 117 - Possible contribution of stoichiometric CuPt to the interior part of the Pt-Fe-Cu system.

Such phase relationships would indicate that some of the alloys in the ($\beta_o + \gamma'_o$) side of the two-phase field, should have had an additional set of lines belonging to the rhombohedral structure, i.e., splitting of (111) reflections. Close examination of the x-ray diffractometer traces of alloys number 6,7,8,10,11 and 12 proved it to the contrary. At this point it is worth recalling the fact that, a) the second phase particles were the minor phases ($\sim<$ 3%), b) the phase separations have occurred around the edges of the samples and finally the phases of $<3\,\mu m$ were not being analysed by the E.P.M.A. Therefore making it possible that the third phase was not detected by either x-ray diffraction or E.P.M.A. If so, then

figure 117 should be considered as the correct phase relationships in this region of the ternary system.
b) If the transformation is not a true reaction (where figure 2. implies) the structure of the PtCu can be considered as a pseudo-cubic. Thus it is quite possible that an addition of any amount of iron up to $\sim$2% would only replace the Cu atoms in the PtCu crystal lattice. In this case no contribution from the PtCu to the interior part of the ternary system is expected.

During the construction of the isothermal section at 600°C, it was noticed that some minor assumptions based on the phase rules had to be made in order to represent the sections. Such a problem was encountered due to lack of sufficient number of alloys where appropriate. Thus the phase boundary(s) which are shown by the dotted lines in figure 89, are drawn based on a) the $\gamma \longrightarrow \alpha$ transformation in the Pt-Fe binary system and b) due to change of ordered to disordered structures at Cu-rich corner.

The whole aspect of the phase transformation between 1000°C and 600°C can be shown by means of a three dimensional model. Figure 118 is the Fe-rich corner of the Pt-Fe-Cu ternary system. It shows the continuous shifts of the three phase field which is based on the binary eutectiod and also the occurrences of the two,two phase fields on its sides. Fig, 119 shows the formation and compositional shifts of the

of the ordered f.c. tetragonal phase which is based on the corresponding phase fields in the Pt-Fe binary system.

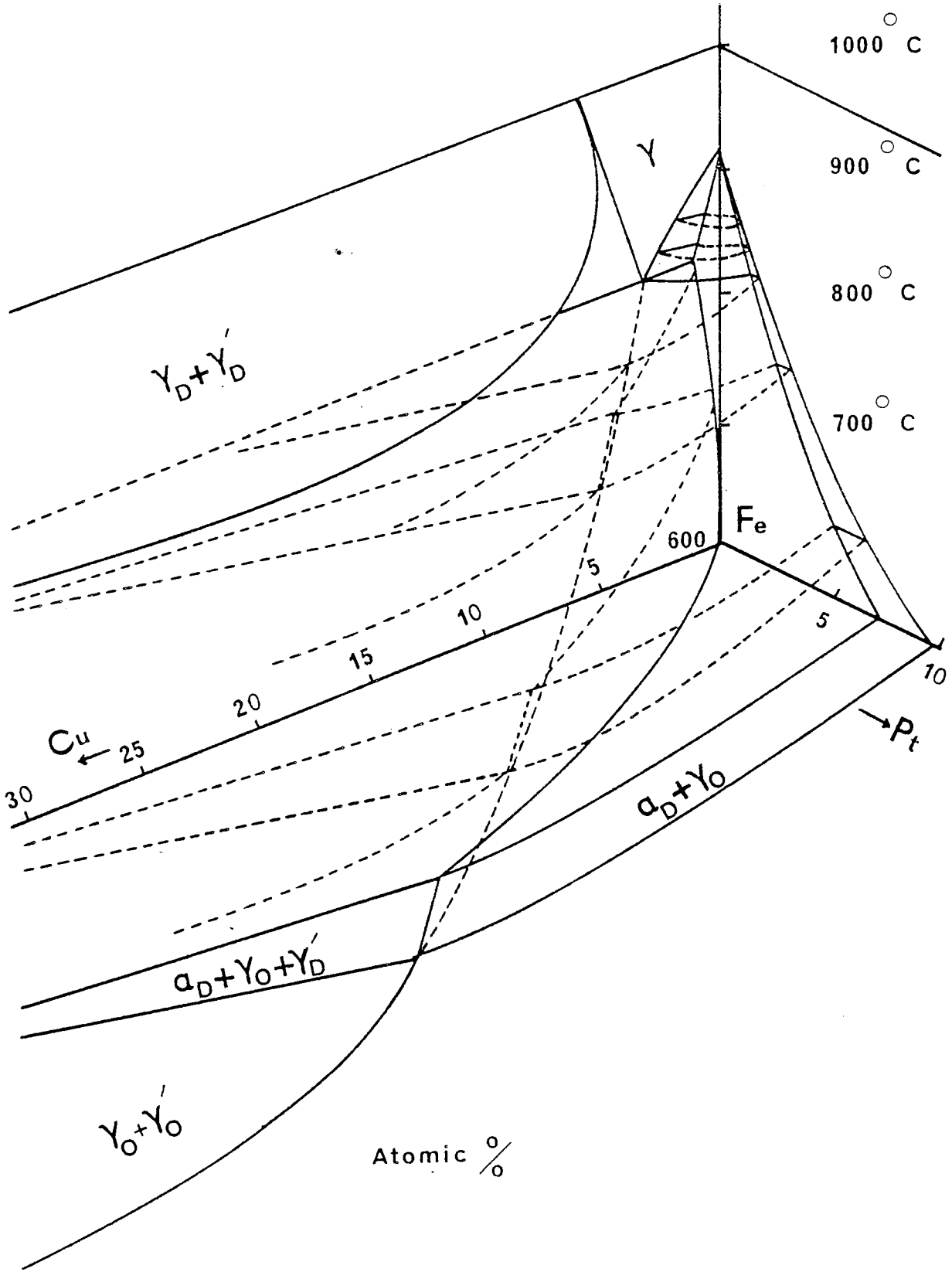

Figure 118 - Space model of the Fe-rich corner of the Pt-Fe-Cu ternary system between 1000°C and 600°C.

Figure 119 - Space model of the ordered tetragonal single phase field based on binary FePt compound and its compositional shifts of the two-phase field between 1300°C - 600°C.

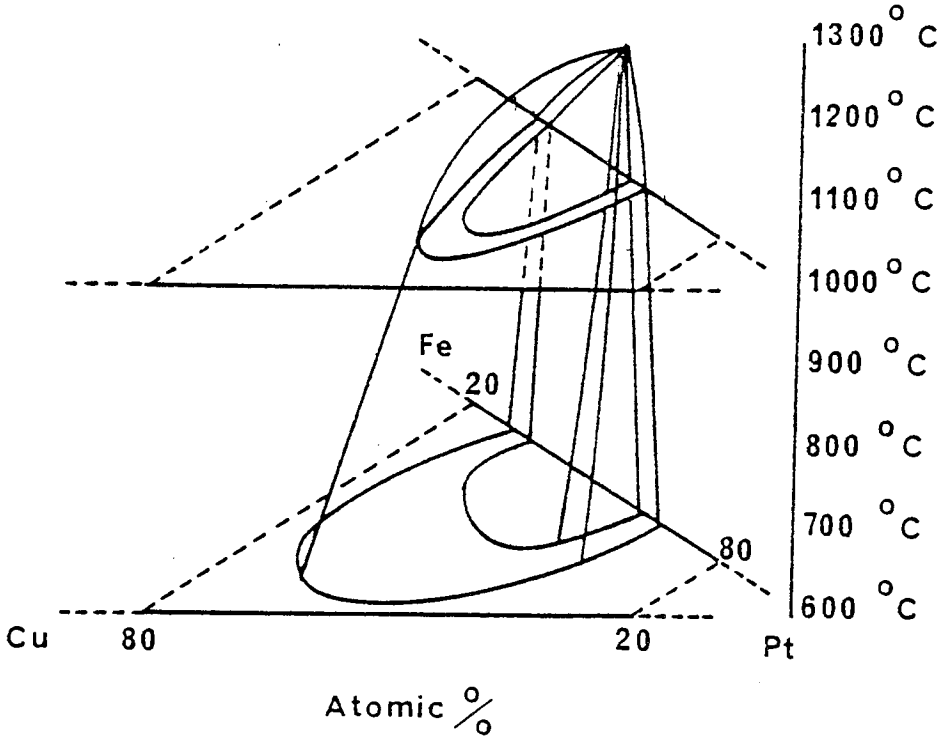

5. CONCLUSIONS

1. At 50% Pt, 25% Fe and 25% Cu there exists a ternary compound in the Pt-Fe-Cu ternary diagram(Tulameenite, Pt_2FeCu).
2. It transforms from a disordered f.c.c. structure(a= 3.793 A^o) to an ordered f.c.t. structure (a = b = 3.895 A^o c = 3.595 A^o , c/a = 0.92) between 1176°C-1146°C.
3. The ordering reaction in the Pt_2FeCu is due to tendency of the platinum atoms to form a periodic arrangement with either iron or copper atoms in the crystal lattice.
4. Iron and copper atoms are randomly distributed on the $(\frac{1}{2}0\frac{1}{2})and(o\frac{11}{22})$ sites of the crystal lattice of the Pt_2FeCu, while platinum atoms occupy the (000), $(\frac{11}{22}0)$ atomic sites.
5. The ordering transformation takes place via a rapid nucleation and growth mechanism of the ordered tetragonal phase, possibly martensitic in charactor.
6. The growth of the ordered tetragonal domains in the isotropic matrix give rise to stresses which are partially relieved by the adoption of special domain arrangements.
7. The domains are produced as fine twins which have a common $\{101\}$ composition plane in the f.c.t. lattice. Such twinning sets the c-axes of neighbouring domains approximately at right angles so that the macroscopic shape change is zero.
8. Due to such an arrangement only the $\{111\}$ planes are parallel and there exists some degree of angular disparities for other planes.

9. The ordering stresses are partially relieved by stress-relief twinning in quenched material subjected to heat-treatments below the ordering temperature, T_c.
10. Below T_c, the short-range stresses are relieved by stress-induced recrystallization which produces long-range stresses as the new grains overlap. These long-range stresses are relieved in turn by deformation twinning, grain-boundary fractures, or a new cycle of recrystallization.
11. The recrystallization mechanisms are grain-boundary nucleation and growth of the new grains, nucleations on the twin-intersections, or by a mechanism similar to stress-induced grain-boundary migrations.
12. The growth of the new grains is an orientation-dependent mechanism.
13. The driving force for the S.I.R is provided by a continuing increase in the degree of long-range order in the tetragonal material.
14. The long-range order is a positional dependent parameter.
15. At 1000°C the Pt_2FeCu forms a continuous region of solid-solution with the binary compound PtFe where the copper atoms substitute for Iron atoms in the $(\frac{1}{2}0\frac{1}{2})$ and $(0\frac{1}{2}\frac{1}{2})$ sites of the f.c.t lattice.
16. At all temperatures below 1300°C (T_c for the stoichiometric PtFe) the off-stoichiometric Pt_2FeCu co-exists with either Pt-rich or iron and copper-rich phases of platinum, iron and copper solid-solutions with an ordered or disordered f.c.c structures.

17. At 600°C the β_o-phase contracts and consequently the Pt_2FeCu is no longer a single phase. The decomposition takes place via the formation of grain-boundary or plate-like precipitates only along the free- surface of the specimen.

18. At 600°C, there is a continous region of solid-solution between Fe_3Pt and Cu_3Pt and between $FePt_3$ and $CuPt_3$.

19. The mineral Tulameenite has undergone a high temperature process leading to grain-boundary cracking which is indicative of formation from the magmatic segregation rather than by chemical accretion at near ambient temperatures.

6. FURTHER WORK

Though the initial aim of the project has been successfully completed, the work has at the same time raised a number of questions.

One general investigation would be to attempt to quench the Pt_2FeCu samples by means of ultra-rapid quenching (splat-cooling) to see if the formation of the ordered tetragonal phase can be avoided in this system. If so, there are certain aspects which need clarifying on the subsequent annealing below T_c . Among the more obvious are :

1)- The site of occurrences of the twinned- plate morphology of the ordered domains at the early stages of the ordering transformation.

2)- To investigate whether the disordered f.c.c. $\longrightarrow$ ordered f.c.t. transformation conforms with the phenomenological theory of martensitic transformation.

3)- To study the variation of the hardness measurements with ageing time to see if the so-called stress-relief twins could cause a drop in hardness during formation.

4)- To study the true nature of the deformation twins and subsequently the superlattice dislocation configurations in Pt_2FeCu.

Finally, more higher temperature , isothermal sections should be established to study:

a)- The compositional shifts of the β_0-phase and subsequently the temperature of the decomposition of the Pt_2FeCu.

b)- The nature of the complex precipitation mechanisms, especially in the two-phase field surrounding the β_0-phase.

c)- The possible contribution of the other binary compounds to the ternary system where the present work is not explicit.

7. Acknowledgement.

I wish to offer my sincere thanks to Dr. S. Murphy for suggesting this project which was interesting and absorbing throughout and for his ceaseless encouragement and invaluable guidance during the research programme. His dedication as a supervisor and his vision and skill as a scientist has been an inspiration.

I would like to thank Dr. D. Vaughan, my associate supervisor for his reassuring presence and his unstinting helpfulness when required.

Special thanks go to Professor T. Mulvey who out of kindness and friendship found time to read this thesis and offer me the benefit of his superior knowledge and opinion.

I would also like to thank all the technicians for their assistance with the practical work, especially Mr. P. Cox and Mr. R. Howell.

Finally, I would like to thank my wife for her patience, understanding and devotion and without whom this work would not have come into being.

REFERENCES

1. N.S. Kurnakov, S. Zemczuzhy and M. Zasedatelev; J. inst. Metals, 15, 305, (1916)
2. G. Tamman Z. Anorg. Chem. 107, 1, (1919)
3. E.C. Bain Chem. Met. Eng. 28, 65, (1923)
4. W.B. Pearson "A handbook of lattice spacing and structures of metals and alloys" Vol.2 pergamon. Oxford, (1967)
5. W.B. Pearson "Handbook of lattice spacings and structures of metals and alloys" Vol.1, pergamon, London (1958)
6. M. Gantois Comptes Rendus, 256, 3629 (1963)
7. D. Bialas et al Naturwisen, 47, 81 (1960)
8. W. Koster Z. Metallkunde, 50, 716, (1960)
9. M. Hirabayashi, et al J. Phy. Soc. Japan 20,381 (1965)
10. A. Nagasawa J. Phy. Soc. Japan, 21, 955 (1966)
11. W.L. Bragg and E.J. Williams Proc. Roy. soc. 145A, 699 (1934)
12. W.L. Bragg and E.J. Williams Proc. Roy. soc. 151A, 540 (1935)
13. H. Bethe Proc. Roy. soc. 150, 552 (1935)
14. W. Hume-Rothery and H.M. Powell Z. Kirst 91, 23, (1935)
15. W. Hume-Rothery and B.R. Coles In "Atomic theory for student of metallurgy" Institute of Metals (1969)

16. T. Muto Sci. papers. inst. phy. chem. Research (Tokyo), 34, 377 (1938)

17. H. Sato and R.S. Toth phy. rev. 127, 469 (1962)

18. C. Sykes and F.W. Jones proc. Roy. soc. 166A, 376 (1938)

19. R.M. Fisher and M.J. Marcinkowski phil. Mag. 6, 1385, (1961)

20. M.J. Whelan and P.B. Hirsch phil. Mag. 2, 1121, 1303, (1957)

21. H.M. Southworth and B. Ralph phil. Mag. 14, 383 (1966)

22. B. Chakravarti J. Mat. sci 5, 391 (1970)

23. C.G. Shull and S. Siegal phy. Rev. 75, 1008 (1949)

24. S. Ogawa, et al Acta. Cry. 11, 872 (1958)

25. M. Marcinkowski et al Acta. Met 9, 129 (1961)

26. M. Marcinkowski et al J. apply phy, 33, 537 (1962)

27. M. Hanson and K. Anderko Constitution of Binary alloy Macgrow-Hill (1958)

28. C.H. Johansson and J.O. Linde Ann physik. 82, 449 (1927)

29. J.O. Linde Ann. physik, 30, 151 (1937)

30. A. Schneider and U. Esch Z. Elektrochem 50, 290, (1944)

31. Y.C. Tang Acta. Cryst. 4, 377 (1951)

32. R. Muda and D. Watanabe
J. apply. cryst. 50, 7, (1974)

33. N.C. Wu and H, Iwasaki
Trans. J.I.M. 309, 14, (1973)

34. C.B. Walker J. Apply. phys 23, 118 (1952)

35. N.T. Corke and S. Amelinckx
Mat. Res. Bull. 4, 289 (1969)

36. H.G. Paris and B.G. Lefevre
Mat. Res. Bull 7, 1109 (1972)

37. R.S. Irani and R.W. Cahn
J. Mat. sci. 8, 1453 (1973)

38. K. Hisatsune and M. Ohta
Scripta. metall. 12, 983 (1978)

39. Y.E.N. Vlasov and T.P. Sapozhkova
Fiz. Metal. Metalloved 30, 980 (1970)

40. Y.E.N. Vlasov, V.I. Gorbunov, J.A. Komarova and
T.P. Sapozhkova Fiz. Metal Metalloved 34, 959 (1972)

41. J. Crangle and J.A. Shaw
Phil. Mag 7, 207 (1962)

42. E. Isaac and G. Tammann
Z. anorg. chem. 55, 63, (1907)

43. V.A. Nemilov IZvest. Inst. plating 7, 1 (1912)

44. V.A. Nemilov Z. anorg. chem. 204, 49 (1932)

45. H. Lipson, D. Schoenberg and G.V. Ritterg
J. Inst. Metals 67, 333 (1941)

46. L.J. Cabri and C.E. Feather
Can. mineralogist 13, 117 (1975)

47. A. Kussman and G.V.V. Rittberg
Z. Metallkde, 41, 470 (1950)

48. R. Sahman Z. anorg chem. 57, 9 (1908)

49. R. Ruer and R. Klesper
Ferrum, 11, 259 (1914)

50. C.S. Smith and E.W. Palmer
Trans. A.I.M.E. 105, 133 (1933)

51. W.R. Maddock and G.E. Claussen
Iron. steel, inst. spec. Rep.
14, 97 (1936)

52. J.T. Norton Trans A.I.M.E. 116, 386 (1935)

53. A.G.H. Anderson and A.W. Kingsbury
Trans A.I.M.E. 152, 38 (1943)

54. V.A. Nemilov and A.A. Rudnitskii
IZvest Sekt. Fiz-chem. Anal
14, 268 (1944)

55. L.J. Cabri, D.R. Owens and J.H. Gilles Laflamme
Can. min. 12, 21 (1973)

56. M. Shahmiri, S.A. Hamilton, D.J.Vaughan and S.Murphy
proceeding of the 7th European Congress
on Electron Microscopy. Volume 1
460, (1980)

57. N.T. Croke, S. Amelinekx and Van Landuyt
J. Mat. Res. Bull 4, 289 (1969)

58. R.S. Irani and R.W. Cahn
Acta. Met 21, 575, (1973).

59. C.S. Barrett and T.B. Massalski
Structure of metals. 4th edition
(1980), Mcgraw-Hill Book Company

60. H.W. King and T.B. Massalski
J. Inst. of metals 90, 486 (1961-62)

61. P. Duncomb and E.M. Jones
T.I. tech. Rept. 260 (1969)

62. B.D. Cullity Elements of x-ray diffraction (1978)

63. W.L. Bragg Crystal structure determination (1944)

64. A. Guinier X-ray diffraction (1963)

65. J.B. Newkirk, A.H. Geisler, D.L. Martin and R. Smoluchowski
Trans A.I.M.E. 188, 1249 (1950)

66. D.T. Keating and B.E. Warren
J. appl. phys. 22, 286 (1951)

67. R.M. Fisher and M.J. Marcinkowski
phil. Mag 6, 1385 (1961)

68. D.G. Morris phys. stat. sol. (a) 32, 145 (1975)

69. J.S. Bowles and S.A. Malin
J. Aust. inst of metals 5, 131 (1960)

70. J.M. Penisson, A. Bourret and P.H. Eurin
Acta. met. 19, 1195 (1971)

71. M. Hirabayshi and S. Weissmann
Acta. met. 10, 25, (1962)

72. V.S. Arunachalam and R.W. Cahn
J. material sci. 2, 160 (1967)

73. S. Murphy and C.J. Ball
J. inst. of metals, 100, 255 (1972)

74. P.G. Shewmon Transformations in metals (1969)

75. K. Okamura, H. Iwasaki and S. Ogawa
J. phys. soc. Japan 21, 1616 (1966)

76. H.M. Finnston (edited)
"Structural characteristics of materials"
Elsevier materials science series (1971)

77. A. Kelly and G.W. Groves
"Crystallography and Crystal Defects"
Longman (1970)

78. I.I. Kornilov "Intermetallic compounds", J.H. Westbrook (edited). Wiley, New York (1967)

79. I.I. Kornilov in "Order-disorder transformations in Alloys" edited: H. Warlimont Spring Verlay (1974)

80. N.S. Kurnakov, S.F. Zhemchuzhny and M.I. Zasedateley
IZvestia St. Peterburgskogo politekhnicheskogo instituta 22, 487 (1914)

81. K. Landau and I.M. Lifshitz
Statistical physics, third edition
Pergamon press (1979)

82. F.W. Jones and C. Sykes
proc. Roy. soc. 166, 375 (1938)

83. F.N. Rhines and J.B. Newkirk
Trans. Amer. soc. metals 45, 1029 (1953)

84. J.L. O'Brien and G.C. Kuczynski
Acta. met. 7, 803 (1959)

85. P. Cotterill and P.R. Mould
"Recrystallization and grain growth in metals" Surrey University press, (1976)

86. F. Cattaneo, I.E. Germagnoli and F. Crasso
phil. Mag. 80, 1373 (1962)

87. T.E. Marder, E.L. Dubinin, A.I. Timofeev and A.L. Shunin
Severcllovsk Mining Institute,
UDC 669.2 (1962)

88. J. Kuceba and B. Million
phys. stat. sol. (a) 31, 275 (1975)

89. R.E. Reed-Hill "Physical Metallurgy Principles"
Van Nostrand Reinhold Company (1979)

90. J. Burke "Kinetics of phase transformation in metals"

91. L.H.Bennett " Theory of alloy phase formation "
The Metallurgical Society of A.I.M.E.
p.228. (1980).

92. S.A. Toma and S.Murphy
Can. Min. 15, 59, (1977).